

The University Of Sheffield.

A Graph-Theoretical Analysis of Ring Currents

Joseph Andrew Clarke

February 12, 2018

A thesis submitted in partial fulfilment of the requirements for the degree of Doctor of Philosophy

Department of Chemistry

Faculty of Science

The University of Sheffield

Supervised by:

Prof. P.W.Fowler, FRS

Abstract

Conjugated-circuit (CC) models are simple and efficient approaches for approximating the aromaticity of a system, as described via application of the magnetic criterion by the presence of ring currents. Unfortunately, this class of current model is often inferior to the well-established Hückel-London model, failing to account for non-Kekuléan, bond-fixed or charged systems. The Aihara variant of the Hückel-London model is employed as a tool to examine cycle contributions and provides a useful understanding of observed ring current effects based on orbital occupancy. Detailed analysis of the Aihara formalism allowed examination of heterocyclic monocycles, indicating that current is robust against changes in electronegativity. Variation in current maps for perylene and related structures, in *ipsocentric*, pseudo-π, Hückel-London and conjugated-circuit models was also rationalised. The major inconsistency in conjugated circuit current maps is identified as the result of inherent exclusion of important non-conjugated contributions. To address various shortcomings, two extended 'conjugated-circuit' models are proposed to reproduce Hückel-London accurate maps. The first involves a parameterised contribution from circuits in Dewar structures, representing the contribution from first-excited structures to a given cycle. The second (the Myrvold-Fowler models) involves ratios of coefficients from the characteristic polynomials of the graph and cycle-removed graph, inspired from the Aihara model. Both models offer a way to include, for the first time, non-Kekuléan systems in CC models, resulting in more accurate current maps. The Adjusted Myrvold-Fowler model is found to 'best' approximate Hückel-London current magnitudes for a variety of benzenoid systems.

Contents

Abstract . . . . . **I**

Abbreviations . . . . . **IV**

Acknowledgements . . . . . **V**

1 Introduction **1**
1.1 The Aromaticity Argument 1
1.2 The Magnetic Criterion of Aromaticity 4
1.3 Ring-Currents 9
1.4 Research Question and Thesis Plan 18

Part I:
Introduction and Theory **20**

2 *Ab initio* Methods and Modifications **21**
2.1 *Ab initio* methods 21
2.2 Implementation of the Ring-Current models 27
2.3 Customisation of Current Density Calculations 30

3 Cyclic Partition of Current in the Hückel-London Model **39**
3.1 Introduction 39
3.2 The Essentials of Graph Theory 40
3.3 Aihara Hückel-London ring current model 42
3.4 Case Studies 47
3.5 Consequences of the Aihara Formulation 53
3.6 Comparison with CC models 56
3.7 Conclusion 59

4 Analytical Expressions for the Hückel-London Ring Current **60**
4.1 Introduction 60
4.2 Mono-Vertex-Altered Mono-Heterocycles 62
4.3 Bi-Vertex-Altered Mono-Heterocycle 78
4.4 *Ipsocentric* Ring Currents 87
4.5 Consequences of the Matrix Analysis 90
4.6 Conclusion 94

Part II:
Application and Investigation of Conjugated-Circuit Models **95**

5 Equiaromaticity and Ring Currents in Antikekulene and Derivatives 96
5.1 Introduction 96
5.2 Conjugated-Circuit Ring-Current analysis 103
5.3 Alternative Ring-Current Models 120
5.4 Conclusion 125

6 Problematic Perylenes 126
6.1 Introduction 126
6.2 The Different Bicycles 130
6.3 Extensions of Perylene 137
6.4 Conclusion 157

Part III:
The Future of Conjugated-Circuit Models **159**

7 The Use of Dewar Structures 160
7.1 Introduction 160
7.2 Dewar-Based Pauling Bond Order 164
7.3 Dewar Structures in Ring-current Calculations 170
7.4 Ring-Current Examples 172
7.5 Conclusion 183

8 The Myrvold-Fowler Model 184
8.1 Introduction 184
8.2 Examination of Ring-Current Models 189
8.3 Conclusion 200

Part IV:
Summary, Future Work and Bibliography **201**

9 Summary and Future Work 202

Bibliography 207

Abbreviations

AO	Atomic Orbital
ASE	Aromatic Stabilisation Energy
BL	Bond Length
BR	Number of Biradical Positions
BRE	Bond-Resonance Energy
CBO	Coulson Bond Order
CC	Conjugated-Circuit
CCMRE	Conjugated-Circuit Model Resonance Energy
CHF	Coupled Hartree Fock
COT	Cyclooctatetraene
CRE	Circuit Resonance Energy
CTOCD-DZ	Continuous Transformation of Current Density - Diamagnetic Zero
CTOCD-PZ	Continuous Transformation of Current Density - Paramagnetic Zero
DFT	Density Functional Theory
DS	Dewar Structure
$\boldsymbol{F}_{\mathrm{N}}$	N^{th} Fibonacci Number
HL	Hückel-London
HLPM	Hückel-London-Pople-McWeeny
HOMO	Hightest Occupied Molecular Orbital
$\boldsymbol{j}_{\mathbf{max}}$	Maximum modulus of current density in the plotting plane
K	Kekulé Structure
$\mathbf{K}^{(\mathbf{2})}$	Biradical Structure
MF	Myrvold-Fowler
$\boldsymbol{L}_{\mathrm{N}}$	N^{th} Lucas Number
LUMO	Lowest Unoccupied Molecular Orbtial
MO	Molecular Orbital
MRE	Magnetic Resonance Energy
N-AC	N-sized AntiCOT
N-AK	N-sized Antikekulene
N-CB	N-sized Cyclic 'Benzenoid'
NBO	Non-Bonding Orbital
NICS	Nucleus Independent Chemical Shift
NMR	Nuclear Magnetic Resonance
RD	Randić-Dewar equation (7.11)
PAH	Polycyclic Aromatic Hydrocarbon
PBO	Pauling Bond Order
TRE	Topological Resonance Energy

Acknowledgements

Primarily, I would like to thank my supervisor Prof. Patrick Fowler for his continued guidance and assistance throughout the entirety of my PhD. Furthermore, the work performed would not have been possible without the help of Prof. Wendy Myrvold, who provided essential programs and insight into the field. I would also like to thank Prof. Leonardus Jenneskens and other collaborators I have worked with over the past three years.

I also want to thank Dr Chris Gibson and previous members of the Fowler group for their prior work which has contributed to the research I have performed, and assistance offered over the years. I would also like to thank Dr Grant Hill and Dr Anthony Meijer for their additional assistance at various points throughout my PhD. I am also grateful to the University of Sheffield and the EPSRC for funding my research and providing opportunities to gain skills outside of my PhD.

I would also like to thank the other members of the theory cluster in Sheffield for support throughout my time studying here, including Dr Theo Keane, Emily Slate, Matt Dwyer, Stella Kritikou and Robert Shaw.

Finally, I need to thank Rachel Mowll for her continued support at all times.

Chapter 1

Introduction

1.1 The Aromaticity Argument

Aromaticity is a feature that is ubiquitous in chemistry, although there is still considerable debate surrounding the criterion, or criteria, that best describe it. The aim of this introduction is not to encapsulate all of the vast literature, but to provide a broad background to the topic of aromaticity and to introduce ideas and models that are important in subsequent chapters. A simple literature search highlights the extensive nature of research in the field of aromaticity and identifies a plethora of models and indices intent on measuring a system's supposed aromaticity. Reviewing each in detail would be an exercise in futility, but the reader is referred to the many reviews and journal special issues dedicated to aromaticity for further information.[1–5]

The modern concept of aromaticity originates with the isolation of benzene by Faraday in 1825.[6] However, it was not until 1865 that the famous structure was proposed by Kekulé as a closed loop[7] with alternating single and double bonds.[8] This was not the only structure proposed, and one that will feature in the present work is the Dewar structure[9] (for a review of the discovery of benzene, see [10]). Nowadays, benzene is synonymous with the Clar sextet circle,[11] which itself has an interesting history.[12] Although named after Clar, its first documented use was in 1925 by Armit and Robinson.[13] It was after its adoption by Clar in the 1970's that this depiction of a sextet gained popularity, and the circle now denotes sets of six π-electrons, particularly in graph-theoretical discussions.

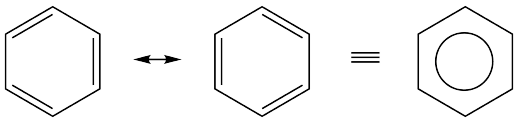


Figure 1.1: The Kekulé structures of benzene, left and middle structures, existing in the form of cyclohexatriene and right the conventional structure featuring a Clar sextet to denote the resonance between pairing Kekulé structures, symbolising the delocalisation of six π-electrons.

However, for such a pervasive chemical phenomenon, aromaticity is surrounded in controversy. The definition of aromaticity varies according to an author's field of research. For instance, one organic textbook emphasises chemical reactivity:[14]

> *"Aromatic compounds are characterised by a special stability and undergo substitution reactions more easily than addition reactions."*

This distinction does not allow for the observed preferential addition reactions of anthracene[15] and phenanthrene,[16] to name just two examples. Alternatively, Schleyer and Jiao consider a variety of properties:[17]

> *"Compounds which exhibit significantly exalted diamagnetic susceptibility are aromatic. Cyclic electron delocalisation also may result in bond length equalisation, abnormal chemical shifts and magnetic anisotropies, as well as chemical and physical properties which reflect energetic stabilisation."*

The description of aromaticity has evolved over the years, and has been influenced by the advent of new technology. The rise of Nuclear Magnetic Resonance (NMR) led to attempts to tie aromaticity to experimental chemical shifts.[18] With the evolving description, more systems become associated with aromaticity that, in the eyes of some authors,[19] tarnishes the description of what makes a system aromatic. This has even led to some, in this case Binsch, to despair:[20]

> *"It is indeed suspicious how often magic rules had and have to serve as an alibi for creating an aura of intellectual respectability for chemical research which is on the verge of turning stale."*

This viewpoint is held by many authors in the literature and often centres on the extension of aromaticity beyond the typical carbon-based benzene-analogue. Indeed, the definition of aromaticity has many sub-fields, each of which could be the focal point of a substantial research project. These include extensions to encompass heteroatomic systems,[21] probed using a multitude of indices,[22–25] including the infamous case of borazine, often proclaimed as the 'inorganic benzene';[26] homoaromaticity,[27] where cyclic conjugation is broken by unsaturated carbon atoms; transition states of both Diels-Alder

reactions and monocycle substituent migrations;[28] non-planar aromaticity, including spherical aromaticity of fullerenes[29,30] and the Möbius strip;[31,32] and more recently the contentious topic of all-metal aromaticity.[33,34]

One of the more important refinements of aromaticity was introduced by Breslow to define those systems showing opposite trends to those of the $4n + 2$ systems. He noted the high chemical reactivity and thermodynamic instability of cyclopropenyl anion, cyclobutadiene and cyclopentadienyl cation. Breslow coined the term 'antiaromatic' for these systems.[35] This category, combined with the concept of aromaticity, leads to a scale of aromaticity and the possibility of one system being "more aromatic" than another.

However, not all have warmed to these extensions; in particular, Hoffmann states:[19]

> *"... labelling of molecules [..] as aromatic [..] appears to be less motivated by an intellectual desire to probe what aromaticity means than by reaching for distinction."*

Specifically, Hoffmann highlights the growing study of all-metal aromaticity, and suggests returning to a simpler definition of aromaticity. Similar opinions were voiced by Bultinck, who attributes the plethora of new aromaticity indices to the basic ambiguity in the definition:[36]

> *"... the problem remains that aromaticity does not have a conclusive definition, which opens the door to many 'magic' rules to quantify aromaticity or to the use of the word aromaticity with an* ***ad hoc*** *meaning."*

Schleyer is more accepting of the new features, noting:[37]

> *"Historically, aromaticity has been a time-dependent phenomenon. Aromatic implies various features, properties, or behaviours to chemists with different backgrounds."*

Ultimately, the ambiguities associated with aromaticity arise from the use of four main criteria to recruit molecules into the aromatic club. In-depth discussions of each criterion can be found elsewhere in the many reviews that include examinations of the various models within the chemical,[17] structural,[38] energetic[39,40] and finally magnetic criteria.[41] For the purpose of the present research project, only the magnetic criterion will be discussed in depth.

1.2 The Magnetic Criterion of Aromaticity

The magnetic criterion of aromaticity is often cited as the 'best' assessment of the aromaticity, although this assessment is by no means universal.[42,43] The magnetic criterion relies on a measurement or prediction of the response of the system to the presence of an external magnetic field (Figure 1.2).

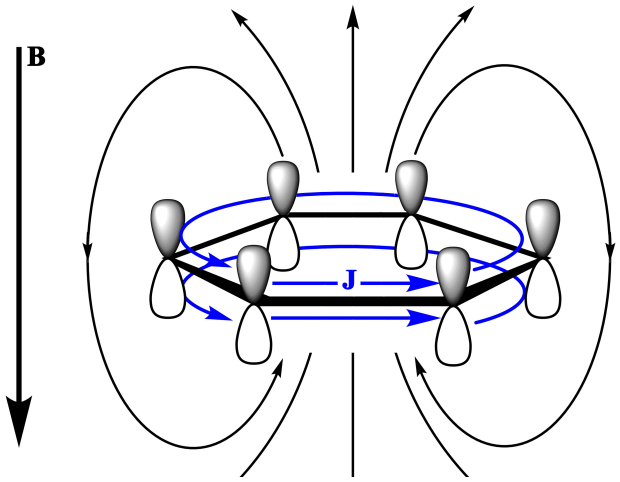


Figure 1.2: The influence of an external magnetic field on benzene. Application of external magnetic field **B** establishes the ring current **J**, which gives rise to the induced field that, in benzene, opposes the external magnetic field. The sense of this induced ring current can serve to distinguish aromatic and antiaromatic systems. Diagram adapted from [44,45]

A detailed history and examination of all aspects of the magnetic criterion is beyond the scope of this introduction. Instead, the reader is directed to the various books and reviews dedicated to the topic.[44–47] The more common interpretations of the magnetic criterion will be discussed and relate to the magnetic susceptibility, proton chemical shifts or the manifestation of ring currents.

1.2.1 Magnetic Susceptibility: Anisotropy and Exaltation

To describe the response to an external magnetic field, several magnetic quantities can be defined, one of which is the magnetic susceptibility tensor, χ, which is:[48–50]

$$\mathbf{M}_{\alpha} = \chi_{\mathrm{V}_{\alpha,\beta}}\ \mathbf{B}_{\beta} \tag{1.1}$$

where $\mathbf{M}$ is the induced magnetic dipole moment generated by induced currents; $\mathbf{B}$ is the external magnetic field; χ_{V} is the susceptibility per unit volume, and α and β are directions for the magnetisability and applied fields respectively. An arguably more useful tensor is the molar magnetic susceptibility, which is related by:

$$\chi_{\mathrm{M}} = \left(\frac{m}{d}\right)\ \chi_{\mathrm{V}} \tag{1.2}$$

where m is the relative molecular mass and d is the density. It is the molar magnetic susceptibility which forms the basis of aromaticity criterion based on either the anisotropy or exaltation of this property. Positive χ_{M} indicates the establishment of an induced field that *reinforces* the applied magnetic field. Conversely, negative χ_{M} indicates the establishment of an induced field that *opposes* the applied magnetic field.

Considering benzenoid and similar polycyclic aromatic hydrocarbons (PAH), the molar susceptibility is the average over the three tensor components along the principal x, y and z axes.[51]

$$\bar{\chi}_{\mathrm{M}} = \frac{1}{3}\left(\chi_{\mathrm{M}_{xx}} + \chi_{\mathrm{M}_{yy}} + \chi_{\mathrm{M}_{zz}}\right) \tag{1.3}$$

where $\chi_{\mathrm{M}_{xx}}$, $\chi_{\mathrm{M}_{yy}}$ and $\chi_{\mathrm{M}_{zz}}$ are the x, y and z components of the molar magnetic susceptibility. The *anisotropy* index of aromaticity relies on the fact that the components of the susceptibility along the principal axes are not equal and the response to the field is strongest along the axis perpendicular to the molecular plane. The anisotropy of the susceptibility is therefore:

$$\Delta\chi_{\mathrm{M}} = \chi_{\mathrm{M}_{zz}}\ - \frac{1}{2}\left(\chi_{\mathrm{M}_{xx}} + \chi_{\mathrm{M}_{yy}}\right) \tag{1.4}$$

Anisotropy is often dominated by the presence of mobile electrons. However, it also has contributions from local effects[52] and significant anisotropies can be present without a ring-current.[53]

Alternatively, *exaltation* of the magnetic susceptibility is defined as the difference between the molar susceptibility and an estimation of the susceptibility of a structurally similar system without ring currents. For PAH systems, the comparison is between the

'aromatic' system and a reference cyclopolyene. The exaltation, Λ is then:

$$\Lambda = \bar{\chi}_{\mathrm{M}} - \chi_{\mathrm{M}}{}' \tag{1.5}$$

where $\chi_{\mathrm{M}}{}'$ refers to a reference susceptibility. Magnetic susceptibilities of reference systems can be estimated via the Pascal System of constants. As pointed out by Musher,[54] and Dauben et al.[55] this method involves the sum of contributions from the magnetic susceptibilities of individual atoms:

$$\chi_{\mathrm{M}}{}' = \sum_i \chi_i + \sum \lambda_{\mathrm{X-Y}} \tag{1.6}$$

where $\sum_i \chi_i$ and $\sum \lambda_{\mathrm{X-Y}}$ are the sums of the Pascal atomic and bond susceptibilities for a given system.[46] Whilst the absolute magnitude of the exaltation has been proposed as an aromaticity criterion,[55,56] the dependence of the exaltation on the ring area suggests a normalised index should be used.[44]

1.2.2 Ring Current Connection

M arises from orbital currents and so χ also describes the induced ring current, **J**. Since **J** is established on application of the external magnetic field, it can be formulated as:[57,58]

$$\mathbf{J} = \frac{c\,\chi\,\mathbf{B}}{S} \tag{1.7}$$

where c is the speed of light, and S is the signed area. The induced ring current will distinguish between aromatic and antiaromatic systems. A molecule is aromatic, if the π component of the ring current is in the diamagnetic sense, and hence is indicative of a local field which *opposes* the applied external field. The converse defines antiaromatic systems where a paramagnetic current is established to *reinforce* the applied external field.

1.2.3 NMR and NICS

Nuclear Magnetic Resonance Spectroscopy provides indirect experimental evidence for ring currents through their effect on ^{1}H NMR spectra. The experimental differences in the hydrogen chemical shifts between benzene and ethene were connected to the pre-existing

model of ring-currents by Pople in 1956.[59] In this paper, the chemical shifts of the -CH_3, -CH_2 and aromatic protons were rationalised using the predicted diamagnetic currents previously described by Pauling.[60] Nowadays ^{1}H NMR chemical shifts in the region of 7 to 10 ppm are taken to be synonymous with 'aromatic' protons.[61] However, peaks in this region can also be attributed to other functional groups, meaning experimental NMR data is instead supplementary, for example: in defining the aromaticity of coronene and corannulene, paracyclophanes,[62] and various charged benzenoids and non-benzenoids.[63]

The utility of NMR shifts extends beyond ^{1}H NMR. Further examples include the calculation of lithium NMR chemical shifts of Li^+ complexed systems, which are reportedly shifted due to the presence of ring-currents.[17] A positive chemical shift indicates antiaromaticity, for example calculated at 9.2 ppm for cyclobutadiene, and negative shifts indicate aromaticity, for example calculated at -6.9 ppm for cyclopentadienyl anion.[64] Furthermore, ^{15}N NMR chemical shifts, both observed and calculated, have been investigated by Katritzky et al. relating to the suspected multidimensionality of aromaticity.[65]

One of the most commonly reported interpretations of the magnetic criterion is the calculation of the NICS, Nucleus-Independent-Chemical-Shift, index. Originating back in 1996 for five-membered rings,[66] a full and detailed history can be found in [47,67]. NICS is based on the calculation of the shielding of a non-interacting H nucleus placed at the ring centre (or other defined position). The NICS value is the negative of this shielding, where negative NICS values are taken to denote aromatic systems, and positive NICS values are taken to denote antiaromatic systems.

Over the past decade, the NICS method has undergone many modifications. The original method is now referred to as NICS(0) to signify the evaluation of the quantity at the ring centre in the molecular plane.[66] However, the consenus in the literature is that NICS(0) is affected by a mixture of σ and π effects. It has been usual to perform the calculation a height of 1 Å above the molecular plane to isolate π-effects.[68] However, the NICS quantity presently considered to be the best diagnostic of aromaticity is $\mathrm{NICS}(0)_{\pi zz}$, representing the π contribution to the zz component of the chemical shift tensor at the

ring centre in the defined molecular plane.[69]

However, NICS has received attention in a negative light too. Aihara has cast doubt on applicability of NICS for polycyclic systems, stating that NICS calculations may over-exaggerate or falsely indicate aromaticity when compared to other indices: Topological Resonance Energy (TRE) and Bond Resonance Energy (BRE).[70–72] In addition, Fowler and Steiner have expressed their dissatisfaction with NICS, noting the loss of orbital information that was present in the *ipsocentric* method (to be discussed in Chapter 2).[73] Finally, Lazzeretti has taken an extreme view of NICS, suggesting its abandonment in favour of other experimentally determined aromaticity methods.[74]

One answer to these criticisms was proposed by Stanger as an alternative more detailed NICS model, referred to as the NICS-Scan.[75] In brief, this method involves the calculation of chemical shifts at multiple heights above the molecular plane allowing the definitive separation of π- and σ- components as the z-height is 'scanned'. Additionally, the newer variant known as the NICS(x,y)-Scan 'scans' the system across the x and y planes.[76] The supposed advantage of this method is that the local and global patterns of aromaticity can now be identified in polycyclic systems, a feat not available to the standard NICS calculation. Currently unpublished work by the Sheffield group has compared NICS-Scan and *ipsocentric* current density maps for polyacenes and heterocyclic polyacenes, finding good agreement in the overall predictions about local diatropicity of current-density in the maps.

1.3 Ring-Currents

The manifestation of ring-currents on application of an external magnetic field is the feature underlying all magnetic criteria of aromaticity. Ring-currents have been inferred from both experiment, via the application of the Pople model,[59] and from calculated quantities such as NICS. An arguably simpler method involves the direct evaluation of the ring current or current density. Two types of ring-current calculation will be used, one resulting in spatial depictions of the induced current density as in the *ab initio ipsocentric* model, (to be discussed in Chapter 2) and the other as bond currents in a more schematic model. The latter type lends itself to treatment with graph-theoretical methodology, the pinnacle of which is the Hückel-London model.

In a quantum mechanical treatment, the Schrödinger equation for the molecule in the field must be solved. The Hamiltonian operator must be modified to account for the external magnetic field, by introducing the vector potential $\mathbf{A}$. $\mathbf{A}$ is related to $\mathbf{B}$ through:

$$\mathbf{B} = \nabla \times \mathbf{A}. \tag{1.8}$$

Equation (1.8) immediately leads to the Maxwell equation $\nabla \cdot \mathbf{B} = 0$, via the relation $(\nabla\cdot)(\nabla\times) \equiv 0$.[50] Many choices of $\mathbf{A}$ give the same $\mathbf{B}$. This physical phenomenon is known as *gauge invariance*. However, invariance is not found for calculations in a finite basis set, leading to an unphysical dependence on the gauge origin.[77] The problem of the ring-current model then revolves around the creation of gauge-invariant orbitals, or by mitigating the gauge variance.

1.3.1 Hückel-London Theory

In 1937, London[78] proposed a quantum-mechanical extension of the classical ring-current model devised the year earlier by Pauling.[60] London's suggestion was to use a linear combination of gauge-including atomic orbitals (ϕ_n) to form molecular orbitals (ψ_n), within the Hückel method.

$$\psi_n = \sum_i \mathrm{C}_i{}^n \phi_i \tag{1.9}$$

where the basis function has an explicit gauge factor

$$\phi_i = \exp\left(-\frac{ie}{\hbar c}\,\mathbf{A_i}\,.\,\mathbf{r}\right)\phi_i{}^{(0)} \tag{1.10}$$

where $\phi_i{}^{(0)}$ is the p_π atomic orbital on atom i and $\mathbf{A_i}$ is the vector potential on atom i at position $\mathbf{r}$. The extension to the calculation of ring-currents was made by Pople and McWeeny, both in 1958.[79,80] There exist three equivalent but conceptually different versions of the combined Hückel theory and London MO theory.

The most important variant related to the work in the present thesis is the cycle decomposition approach proposed by Aihara, which proceeds via the computation of characteristic polynomials. Owing to the significance of this model for the present work, the full account and interpretation is reserved for Chapter 3.

Another method that features heavily in the work by Mallion and co-workers, is a further extension of McWeeny's ring-current model.[80] The model was elaborated over a series of publications[81–83] and eventually culminated in the so-called *Master Equation*:[84]

$$\begin{aligned}\left(\frac{\mathrm{J_C}}{\mathrm{J_0}}\right) = 9 \times \sum_{(\mu)} \left(P_{(\mu)} + \beta\bar{\pi}_{(\mu)(\mu)}\right) S_{(\mu)}\delta^{\mathrm{C}}{}_{(\mu)} + \\ 9 \times \sum_{(\mu<\nu)} \sum_{(\nu)} \beta\bar{\pi}_{(\mu)(\nu)} \left(S_{(\mu)}\delta^{\mathrm{C}}{}_{(\nu)} + S_{(\nu)}\delta^{\mathrm{C}}{}_{(\mu)}\right)\end{aligned} \tag{1.11}$$

where $\mathrm{J_C}$ and $\mathrm{J_0}$ are the ring-currents of ring C and the benzene molecule; μ and ν are circuit-completing bonds which yield C when added to the chosen spanning tree; $P_{(\mu)}$ is the Coulson Bond Order;[85] β is the standard bond resonance integral; $\bar{\pi}_{(\mu)(\mu)}$ and $\bar{\pi}_{(\mu)(\nu)}$ are the self- and mutual-imaginary bond-bond polarisabilities respectively; $S_{(\mu)}$ is the signed area of the μ-completing circuit; and $\delta^{\mathrm{C}}{}_{(\mu)}$ is a topological value depending on the properties of μ: 0 if C is not involved in the μ^{th}-completing circuit; +1 (-1) if the circuit will contribute diatropic (paratropic) current.

The final method of Hückel-London theory is based on a finite perturbation method. In the form implemented in the Sheffield programs, the problem is solved using a Hamiltonian matrix of double dimension to solve the real and imaginary parts of the perturbed eigenvalues,[86] a method also described by Salem.[48] From McWeeny,[80] only the off diagonal resonance integrals are changed upon application of the external magnetic

field. Assuming atoms i and j are bonded, the resonance integral in the presence of $\mathbf{B}$ is:

$$\beta_{ij} = \beta_{ij}{}^{(0)} \exp\left(\frac{ie}{\hbar c}\,(\mathbf{A_i} - \mathbf{A_j})\,.\,(\mathbf{R_i} - \mathbf{R_j})\right) \tag{1.12}$$

$$= \beta_{ij}{}^{(0)} \exp\left(\frac{ie}{\hbar c}\,\mathbf{B}.\,\boldsymbol{S}_{ij}\right) \tag{1.13}$$

where $\boldsymbol{S}_{ij}$ is the signed area of the triangle formed between points i, j and the origin.[48] By defining the magnetic flux, f_{ij}, as:

$$\mathrm{f}_{ij} = \frac{e}{hc}\,\mathbf{B}.\,\boldsymbol{S}_{ij}, \tag{1.14}$$

equation 1.13 can be simplified to:

$$\beta_{ij} = \beta_{ij}{}^{(0)} \exp\left(2i\pi\,\mathrm{f}_{ij}\right). \tag{1.15}$$

The ring current calculated by this method is then the derivative of the total energy with respect to the magnetic flux. This allows the current arc from site $\mathbf{R_i}$ to $\mathbf{R_j}$ to be expressed in terms of the occupied eigenvectors, C_i^n, of the Hamiltonian matrix.[87] Performing the differentiation numerically, as devised by Haddon,[86] avoids complex arithmetic. The through-bond current can be obtained from the derivative of energy with respect to the magnetic flux.[88]

$$\mathrm{J}_{ij} = -\frac{e}{h}\,\frac{\partial E}{\partial\,\mathrm{f}_{ij}} \tag{1.16}$$

$$= \left[\sum_n (C_i^n)^* C_i^n\right] \exp\left(\frac{ie}{\hbar c}\,\mathbf{B}.\,\boldsymbol{S}_{ij}\right) \tag{1.17}$$

Ring currents calculated through the Hückel-London model obey Kirchhoff's law of current conservation,[89] which states that the magnitude of current flowing *into* a vertex is equal to the magnitude of current flowing *out* of the vertex. This extends to all other graph theoretical models in which current traverses bonds only. The finite perturbation approach was used previously by the Fowler group, prior to the new in-depth understanding of the Aihara formalism generated here.

1.3.2 Conjugated-Circuit Models

The present research centres on conjugated-circuit (CC) ring-current models, which are used to approximate the total induced current as the sum of contributions from conjugated circuits. The concept of CC is known to all chemists. One specific example is the Clar sextet of benzene (see Figure 1.1), a compact representation of the existance of two alternating Kekulé structures. In the general case, a conjugated circuit has been defined in two different ways in the literature. The first was proposed by Randić[90–92] and used by Mallion:[93]

> *"Conjugated-circuits are those circuits within an individual Kekulé structure with a regular alternation of carbon-carbon single and double bonds."*

Alternatively, a more graph theoretical approach defines conjugated circuits as:[94]

> *"A cycle C is a conjugated circuit in molecular graph G if both G and G-C (the graph G with the vertices and edges of C removed) have perfect matchings (Kekulé structures)."*

An example illustrating these definitions is illustrated in Figure 1.3.

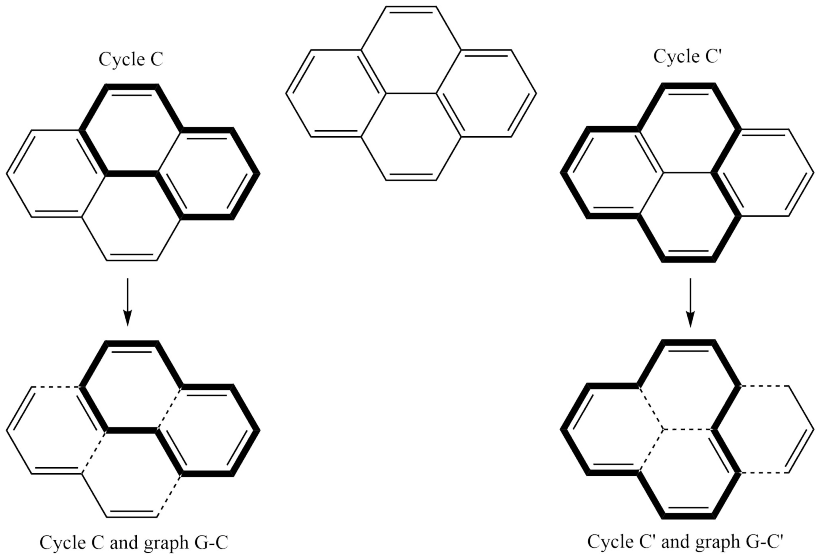


Figure 1.3: An example of a conjugated circuit in pyrene. The left illustration shows cycle C and the corresponding graph G-C, C is considered conjugated by conforming to both CC definitions. The right illustration shows cycle C′ and graph G-C′, considered non-conjugated due to the absence of Kekulé structures in G-C′.

For small examples, the identification of CCs can be performed by a rudimentary pencil-and-paper method. However, as found by Gutman and Randić, the total number of CCs for a graph with K(G) Kekulé structures is equal to:[95]

$$\frac{\mathrm{K(G)}\,[\mathrm{K(G)}-1]}{2}, \tag{1.18}$$

which includes disjoint conjugated circuits, where multiple independent circuits can be identified within a single Kekulé structure. Consequently, as the system size increases, computer programs are soon needed for calculations.[96] The Sheffield group uses programs written by Prof. W. Myrvold and her group as part of a long-standing collaboration.

Conjugated circuits fall into one of two categories depending on the number of carbon vertices. The two categories are analogous to the famous Hückel rules for monocycles,[97–99] in which those circuits with $4n$+2 or $4n$ vertices, where n represents an integer, respectively denote stabilising, aromatic circuits, or destabilising, antiaromatic circuits. Indeed, the combination of these circuits has led to an aromaticity index based on the number of circuits from each class,[100] and even to the claim by Randić to have solved the application of Hückel theory for polycyclic systems.[101]

1.3.2.1 Resonance Energy

The concept of conjugated circuits originated as a model for the energetic criterion of aromaticity in the Conjugated-Circuit Model Resonance Energy (CCMRE), found by the summation of numerical quantities for all possible $4n + 2$ and $4n$ circuits.[90] This resonance energy is defined as:[102]

$$\mathrm{CCMRE} = \frac{1}{\mathrm{K(G)}} \sum_{n} \left(r_n R_n + q_n Q_n\right) \tag{1.19}$$

where r_n and q_n denote the numbers of R_n and Q_n circuits in the system; R_n (Q_n) denotes an energy contribution for a circuit of size $4n + 2$ ($4n$). Values of the R_n parameters are the result of empirical fitting for linear polyacenes,[90] and Q_n parameters were estimated from a plot of R_n vs N, the number of carbon vertices in the circuit.[92] In terms of resonance energy models, CCMRE has not been adopted as widely as the more popular Aromatic Stabilisation Energy, ASE.[103]

1.3.3 Conjugated Circuit Ring-Current Models

The use of CCs was extended to the calculation of ring currents by assigning each class of circuit a directionality. The aromatic $4n + 2$ circuits are given diatropic currents, and conversely the $4n$ antiaromatic circuits are given paratropic currents.[104] This essentially is an *ad hoc* addition to the theory, to give agreement with the results of *ab initio* MO calculations, with a rationale based on orbital nodal characteristics.[105] Weightings of circuits differ according to the four literature models. While the models are formulaically similar, their differences include: a varying dependence on ring area; normalisation; and choice of conjugated circuits. The total ring current of a given face is expressed as the sum of relevant cycle contributions, with bond currents found similarly.[106]

1.3.3.1 Randić CC model

Arguably the simplest model is that known as the Randić model, which was first described briefly in 2003,[107] before being revisited in 2010.[100] Mathematically the weighting of each circuit, C, in this model can be formulated as:[94]

$$\mathrm{J_C} = \pm 2[m\,(\mathrm{G} - \mathrm{C})]^2 \tag{1.20}$$

where the $\pm$ denotes the sign used to differentiate between the two classes of circuits, positive for $4n + 2$, negative for $4n$; the factor of 2 arises from the inclusion of both pairs of compared matchings; $m\,(\mathrm{G} - \mathrm{C})$ is the number of perfect matchings in graph $\mathrm{G} - \mathrm{C}$; the square arises because of the inclusion of disjoint conjugated-circuits. The simplicity of this model arises from its independence of cycle area. Subsequent papers have included a normalisation of the weighting to the order of the number of conjugated-circuits, namely multiplication of $1/\left[\mathrm{K}(\mathrm{K} - 1)\right]$.[96,108,109]

1.3.3.2 The CC model proposed by Ciesielski et al.

The next model to be discussed is that proposed by the Polish group, Ciesielski, Krygowski, Cryański, Dobrowlski and the Japanese chemist Aihara.[110] In the general

formulation, the contribution of cycle C to the bond currents is:[94]

$$\mathrm{J_C} = \pm[m\,(\mathrm{G}-\mathrm{C})]^2 \left|\frac{S_\mathrm{C}}{S_0}\right| \tag{1.21}$$

where $|S_\mathrm{C}/S_0|$ represents the area of circuit C in terms of standard benzene ring. A consequence of inclusion of area as a numerator naturally means that larger circuits tend to contribute larger weightings than smaller circuits. In addition, each pair of circuits is only counted once. Again, no normalisation is included in the original model, but has been added in subsequent iterations as: $1/\left[\mathrm{K}(\mathrm{K}-1)\right]$,[111] or $2/\left[\mathrm{K}(\mathrm{K}-1)\right]$.[94]

1.3.3.3 Mandado CC model

The third model to be considered is that proposed by Mandado, as an elaboration of the resonance energy model discussed earlier.[112] In this model, two formulae exist for circuit weighting depending on the *shape* of the circuit. The general formula is:[94]

$$\mathrm{J_C} = \pm 2[m\,(\mathrm{G}-\mathrm{C})]/\left(\left|\frac{S_\mathrm{C}}{S_0}\right|\mathrm{K(G)}\right). \tag{1.22}$$

with a parameterised alternative accounting for circuit shape of the form:

$$\mathrm{J_C} = \pm 2[m\,(\mathrm{G}-\mathrm{C})]/\left(\left|\frac{S_\mathrm{C}}{S_0}\right| a^2\mathrm{K(G)}\right) \tag{1.23}$$

where the parameter a is an empirically determined parameter calculated from correlation with Dewar Resonance Energy, DRE, resulting in $a = 0.78$ for circuits constructed from three or more linear hexagons and $a = 1$ otherwise.

One will notice that both equations (1.22) and (1.23) are of order one in $[m\,(\mathrm{G}-\mathrm{C})]$. This reflects the exclusion of the disjoint circuits, implied in the text of the paper and confirmed in examination of the supplementary information.[112] Normalisation to the order of the number of Kekulé structures, rather than number of conjugated circuits, is implicitly included in equations (1.22) and (1.23).

1.3.3.4 The CC model proposed by Gomes and Mallion

Perhaps the most complicated of the four CC models was that proposed, incidently in one of the earliest papers relating to conjugated-circuits, by Mallion and Gomes.[93] While

first appearing in 1979, the model has not achieved vast recognition, indeed sparking some debate over recognition for the notion of conjugated-circuits. Consequently, the model was restated in 2011, which clarified the original paper and offered a comparison to the other CC models as well as the *ab initio* pseudo-π method (to be detailed later).[111] A less attractive feature of this method is the reliance on area-corrected numerical estimates for [N]annulenes, calculated in 1967 by Baer et al.,[113] which correlate to the N-sized CC.

Mathematically, the ring-current contribution from a single ring r is formulated as:[93]

$$\mathrm{J}_r = \frac{1}{\mathrm{K(G)}} \sum_{\text{CCs of } r} \mathrm{J_N} \left(\frac{S^{(n)}}{S_\mathrm{N}} \right) \tag{1.24}$$

where $\mathrm{J_N}$ is the ring-current intensity calculated by Baer for the [N]annulene; and $\left(S^{(n)}/S_\mathrm{N}\right)$ are the idealised ring-areas for the regular n-sized conjugated circuit of equivalent size to the regular [N]annulene. Despite the inclusion of area identical to the Ciesielski et al. model, the dependence on area acts as a denominator due to the reduced intensity of $\mathrm{J_N}$ as N increases. In the original paper, disjoint circuits were excluded from the calculation, but these were later incorporated into the calculation. Therefore, comparisons between models must account for this change in the formulation. Expressing this model in terms of $m\,(\mathrm{G-C})$, the form including disjoint circuits is:[94]

$$\mathrm{J_C} = \pm 2[m\,(\mathrm{G-C})]^2 \left| \frac{S_\mathrm{C}}{S_0} \right| j_\mathrm{C} / \left(\mathrm{K(G)}\right) \tag{1.25}$$

where j_C corresponds to the area-normalised current calculated by Baer et al. In the confines of the thesis, this model will not be discussed further.

1.3.4 Pauling Bond Order

An aside should be introduced here about the concept of the Pauling Bond Order, PBO, which is related to the conjugated-circuit approach. PBO was established in 1935 as a simple valence-bond method evaluating the number of times a given bond is double over all Kekulé structures.[114] Mathematically, the bond order for an edge connecting vertices r and s is:[115]

$$\mathrm{PBO}_{rs} = \frac{m_{rs}}{\mathrm{K(G)}} \tag{1.26}$$

where m_{rs} is defined as the matching number of the edge connecting vertices r and s. PBO has been connected to the calculation of ring currents in two different ways. The first, by Randić, introduced the idea of ring bond orders, building on Clar sextets.[116] More recently, work by Fowler, Myrvold, Bird and Jenkinson has shown that PBO is explicitly connected to the currents in the conjugated-circuit models owing to the connection with the alternation between single and double bonds. Qualitatively, the Randić perimeter current for any benzenoid can be found by:

$$\mathrm{J}_{rs} = +2\,\mathrm{K(G)}^2\,\mathrm{PBO}_{rs}\,(1 - \mathrm{PBO}_{rs}) \tag{1.27}$$

It should be noted that in addition to PBO, there are many other definitions of bond orders, and comparisons between them are common in the literature.[117–119] One of the more well-known examples based on MO theory is the Coulson Bond Order.[85]

1.4 Research Question and Thesis Plan

The bulk of this thesis centres on the conjugated-circuit ring-current models and their interpretation of ring-current maps.

Conjugated-circuit models can give a rapid graph-theoretical calculation of the ring current, interpreted as the contribution from the 'most important' cycle. While this may be an appropriate assumption, there are many systems where a conjugated-circuit method inevitably fails. By definition, conjugated circuits relate only to Kekuléan graphs, thereby excluding a large proportion of chemical graphs. Additionally, CC models do not incorporate any interpretation of orbital occupancy and hence have no natural way to account for charged systems. Randić has attempted to include these systems by an expansion or contraction of the charged vertex,[120–122] and Mandado has used weighted Kekulé structures in the charge-deleted fragments.[123] However, neither idea is yet to translate into a well defined ring current model. For example, the cyclopentadiene anion is one example currently outside of the definitions of the CC models. The combination of an odd sized ring and the necessity of a charged state means that CC models would predict, at best, non-aromaticity, despite the general consensus of aromaticity.[124]

There are additional problems associated with the CC models which are beyond the scope of the thesis. A comparison of all models by Dickens, Gomes and Mallion found that the Randić model best approximates the accurate current models for the single isomer of coronene investigated.[111] However, this is in contrast to the conclusion by Fowler and Myrvold who found the Gomes and Mallion models were 'best' through comparion of ring currents in linear polyacenes.[94] The problem of which method is 'best' is epitomised by butalene[125] where the Randić, Ciesielski et al. and Mandado models predict butalene is non-aromatic, aromatic and antiaromatic respectively. Clearly further investigation into the 'best' method is needed.

The present thesis is concerned with addressing some of these criticisms of the CC models in an attempt to answer the following research question:

Can the conjugated-circuit ring-current models be expanded to incorporate systems previously excluded, more specifically non-Kekuléan or locally non-conjugated systems or rings, in order to give better approximations to accurate ring-current models?

Of paramount importance are those systems where maps differ significantly between the various models.

To address this research question, the thesis is split into four parts. Part I details the theoretical background, introducing the methodologies of calculations used in subsequent chapters. Chapter 2 details methodologies for the calculation of current-density via the *ab initio ipsocentric* approach. Chapter 3 details the cyclic decomposition Hückel-London model referred to as the Aihara formalism, which is then implemented to calculate analytical ring currents for monocyclic-heterocycles in Chapter 4.

Part II investigates the implementation and limitations of the conjugated-circuit methods. Chapter 5 derives analytical ring-current equations for systems related to antikekulene, where Kekulé structures are functions of the Fibonacci and Lucas number sequences. Chapter 6 highlights two sets of systems, derived from perylene, where the conjugated-circuit models fail to accurately account for the ring current. This chapter also discusses the strange ring-current maps that can appear through the MO methods, for which an explanation is offered through an occupied orbital approach.

Part III presents two potential improvements of the conjugated-circuit models. The first, in Chapter 7 details the inclusion of additional structures known as the Dewar first-excited structures into the conventional Randić equation. The second in Chapter 8 details an alternative method derived as an analogy to the Aihara Hückel-London model. Finally, Part IV summarises the major conclusions, future work and references for the whole thesis.

Part I

Introduction and Theory

The first part of the thesis details the theoretical background of the high accuracy methods used in later chapters. The first method, is an *ab initio* approach referred to as the *ipsocentric* method, which partitions current density according to available occupied-to-unoccupied virtual transitions in the magnetic field. Within the confines of the present work, this method is mainly used as a tool for comparison with the graph-theory models. The next model to be discussed is the Aihara-variant of the Hückel-London model, which partitions current according to occupied orbitals and cyclic contributions. This method is described in full, and offers insight into phenomena related to the occupation of select molecular orbitals. Finally in Chapter 4, this Hückel-London model is applied to mono-cyclic heterocycles. The Aihara formalism allows for the analytical derivation of ring currents, performed here for mono- and bi-vertex-altered heterocycles.

Chapter 2

Ab initio Methods and Modifications

In addition to the graph theoretical models, two *ab initio* methods will be used. These are used primarily for comparison and calibration of the simpler models. This chapter seeks to inform the reader about the theory behind the *ab initio* approach and to report an analysis of the calculation parameters.

2.1 *Ab initio* methods

The following section details the fundamentals of the *ab initio* method, originating from approaches proposed by Keith and Bader in 1993.[126,127] Their model was then recast into an analytic derivative form by Lazzeretti et al.[128] before being adopted by Steiner and Fowler in 2001, and reformulated in terms of orbital contributions.[129]

For an N-electron system in state Ψ, the charge density, $\rho(\mathbf{r})$, and the current density, $\mathbf{J}(\mathbf{r})$, are given by:

$$\rho(\mathbf{r}) = e\mathrm{N}\int \Psi^*\Psi \mathrm{d}\tau' \tag{2.1}$$

$$\mathbf{J}(\mathbf{r}) = \frac{e}{m_e}\mathbf{A}\,\rho(\mathbf{r}) - \frac{e\hbar\mathrm{N}}{2im_e}\int \left(\Psi^*\nabla\Psi - \Psi\nabla\Psi^*\right) d\tau' \tag{2.2}$$

where, conventional symbols denote fundamental constants, and $\mathrm{d}\tau'$ indicates that the integration is carried out over spins and spatial coordinates of all electrons except the electron at coordinates $\mathbf{r}$. $\mathbf{A}$ is the magnetic vector potential, seen earlier as part of Maxwell's equations (1.8). For a constant uniform external magnetic field, the simplest form of $\mathbf{A}$ is

$$\mathbf{A}(\mathbf{r}) = \frac{1}{2}\,\mathbf{B} \times (\mathbf{r} - \mathbf{d}) \tag{2.3}$$

where $\mathbf{d}$ is the gauge origin.

In the absence of an external magnetic field, the molecular Hamiltonian for a fixed

geometry is:

$$\hat{\mathrm{H}}_0 = -\frac{\hbar^2}{2m_e}\sum_{i=1}^{\mathrm{N}} {\nabla_i}^2 + V \tag{2.4}$$

where V is the potential energy function. Upon application of the external magnetic field, the first-order Hamiltonian is then:

$$\hat{\mathrm{H}} = \hat{\mathrm{H}}_0 + \frac{e}{2m_e}\hat{\mathbf{L}}(\mathbf{d})\,.\,\mathbf{B} \tag{2.5}$$

$\hat{\mathbf{L}}$ is the angular momentum operator for rotation about $\mathbf{d}$ and is a sum of one-electron terms. The present cases are concerned with a closed-shell ground state Ψ_0, and by perturbation theory, the first-order correction is:

$${\Psi_0}^{(1)} = -\frac{e}{2m_e}\sum_{\mathrm{I}\neq 0}\Psi_{\mathrm{I}}\,\frac{\langle\Psi_{\mathrm{I}}|\hat{\mathbf{L}}(\mathbf{d})\,.\,\mathbf{B}|\Psi_0\rangle}{\mathrm{E_I}-\mathrm{E_0}} \tag{2.6}$$

with a first-order correction to the current density of:

$$\begin{aligned}\mathbf{J}^{(1)}(\mathbf{r}) &= \frac{e}{2m_e}\mathbf{B}\,\times\,(\mathbf{r}-\mathbf{d})\,\rho(\mathbf{r}) + \frac{ie\hbar\mathrm{N}}{m_e}\int\left(\Psi_0\nabla{\Psi_0}^{(1)} - {\Psi_0}^{(1)}\nabla\Psi_0\right)d\tau' \\ &= \mathbf{J}^{(\mathrm{d})}(\mathbf{r}) + \mathbf{J}^{(\mathrm{p})}(\mathbf{r})\end{aligned} \tag{2.7}$$

corresponding to a split into diamagnetic (diatropic) and paramagnetic (paratropic) current densities. $\mathbf{J}^{(\mathrm{d})}(\mathbf{r})$ is the conventional diatropic contribution and $\mathbf{J}^{(\mathrm{p})}(\mathbf{r})$ is the paratropic contribution, a typical sum-over-states property dependent on the accessibility of excited states via rotational transitions.

Discussion now returns to the gauge-dependence. Physically, $\mathbf{J}^{(1)}(\mathbf{r})$ must be independent of the origin $\mathbf{d}$ in the vector potential. When $\mathbf{d}$ is changed, $\mathbf{J}^{(\mathrm{d})}(\mathbf{r})$ and $\mathbf{J}^{(\mathrm{p})}(\mathbf{r})$ will both change, but their form remains constant. However, in a calculation with an incomplete basis, the changes in $\mathbf{J}^{(\mathrm{d})}(\mathbf{r})$ and $\mathbf{J}^{(\mathrm{p})}(\mathbf{r})$ no longer cancel correctly. This is the problem of unphysical gauge-dependence and affects all response properties including the current density. The question then arises as to the 'best' choice of $\mathbf{d}$. Various choices have been proposed, (for summaries see [46,47]) notably GIAO, Gauge Including Atomic Orbitals, (previously known by the misnomer of Gauge Independent Atomic Orbitals)[130,131] and IGLO, Individual Gauge for Localised Orbitals.[132,133] The method of dealing with the gauge dependence that is of interest in the present work, is that of

the *ipsocentric* method.

2.1.1 The *Ipsocentric* Method

Beginning with the CSGT, Continuous Set of Gauge Transformations, proposed by Keith and Bader in 1993,[126,127] the origin $\mathbf{d}$ was described as a distribution by a continuous function, $\mathbf{d}(\mathbf{r})$. The induced current density $\mathbf{J}^{(1)}(\mathbf{r})$ is then computed with respect to $\mathbf{d}(\mathbf{r})$ as the origin. Refinement of the CSGT method was made by Lazzeretti and the Modena group who converted it to an analytical derivative method[128] at the coupled Hartree-Fock level.[134] It was then retitled by Lazzeretti and co-authors as the CTOCD-DZ (Continuous Transformation of Origin of Current Density - Diamagnetic Zero) method. Later, Fowler and Steiner adopted this method, and again renamed it to the *ipsocentric* method to draw attention to the fact that each point serves as its own origin. This model reflects the choice $\mathbf{d}(\mathbf{r}) = \mathbf{r}$, and the right-hand side of equation (2.7) simplifies to

$$\mathbf{J}^{(1)}(\mathbf{r}) = \frac{ie\hbar \mathrm{N}}{m_e}\left[\int \left(\Psi_0 \nabla {\Psi_0}^{(1)} - {\Psi_0}^{(1)} \nabla \Psi_0\right) d\tau'\right]_{\mathbf{d}=\mathbf{r}} \tag{2.8}$$

The angular momentum operator, $\hat{\mathbf{L}}$, can be written as:

$$\hat{\mathbf{L}}(\mathbf{d}) = \hat{\mathbf{L}}(\mathbf{0}) - \mathbf{d} \times \hat{\mathbf{P}} \tag{2.9}$$

where $\hat{\mathbf{L}}(\mathbf{d})$ is the operator for rotation about the point $\mathbf{d}$; $\hat{\mathbf{L}}(\mathbf{0})$ refers to the rotation about the origin of the coordinates; and $\hat{\mathbf{P}}$ is the N-electron linear momentum operator. Therefore, choosing *any* coordinates of $\mathbf{d}$ results in the separation of the wavefunction into paratropic and diatropic components, based on sums over occupied-to-unoccupied virtual transitions.

$$\begin{aligned} {\Psi_0}^{(1)} &= \frac{e}{2m_e}\left[\sum_{\mathrm{I}\neq 0} \Psi_\mathrm{I} \frac{\langle \Psi_\mathrm{I}|\hat{\mathbf{L}}(\mathbf{0})|\Psi_0\rangle}{\mathrm{E_I} - \mathrm{E_0}}\right].\mathbf{B} + \frac{e}{2m_e}\left[\mathbf{d} \times \sum_{\mathrm{I}\neq 0} \Psi_\mathrm{I} \frac{\langle \Psi_\mathrm{I}|\hat{\mathbf{P}}|\Psi_0\rangle}{\mathrm{E_I} - \mathrm{E_0}}\right].\mathbf{B} \\ &= {\Psi_0}^{(\mathrm{p})} + {\Psi_0}^{(\mathrm{d})} \end{aligned} \tag{2.10}$$

If the system has a non-trivial point group, $\hat{\mathbf{L}}(\mathbf{0})$ and $\hat{\mathbf{P}}$ will have the symmetry of the system. The two series will obey 'symmetry rules' based on symmetries of the states and operators. Writing ${\Psi_0}^{(1)}$ in terms of one-electron operators allows the construction

of states from an occupied orbital, $\psi_n(n \leq \mathrm{N}/2)$, to a virtual unoccupied orbital, $\psi_p(p > \mathrm{N}/2)$. The first-order current density becomes a sum of orbital contributions:[129]

$$\mathbf{J}^{(1)}(\mathbf{r}) = 2\sum_{n=1}^{\mathrm{N}/2} \mathbf{J}_n{}^{(1)}(\mathbf{r}) \tag{2.11}$$

where the orbital densities are:[73]

$$\begin{aligned} \mathbf{J}_n{}^{(1)}(\mathbf{r}) &= -\frac{e^2}{2m_e}\mathbf{B} \times (\mathbf{r}-\mathbf{d})\ \psi_n^2 + \frac{ie\hbar}{m_e}\left[\psi_n \nabla \psi_n{}^{(1)} - \psi_n{}^{(1)} \nabla \psi_n\right] \\ &= \mathbf{J}_n{}^{(\mathrm{d})} + \mathbf{J}_n{}^{(\mathrm{p})}. \end{aligned} \tag{2.12}$$

Neglecting self-consistency corrections, and assuming that ψ_n are eigenfunctions of the one-electron Hamiltonian with eigenvalues ϵ_n then,[135]

$$\begin{aligned} \psi_n{}^{(1)}(\mathbf{r}) &= -\frac{e}{2m_e}\left[\sum_{p>\mathrm{N}/2} \psi_p(\mathbf{r})\, \frac{\langle\psi_p|\hat{\mathbf{l}}(\mathbf{0})|\psi_n\rangle}{\epsilon_p - \epsilon_n}\right].\mathbf{B} \\ &\quad + \frac{e}{2m_e}\left[\mathbf{d} \times \sum_{p>\mathrm{N}/2} \psi_p(\mathbf{r})\, \frac{\langle\psi_p|\hat{\mathbf{p}}|\psi_n\rangle}{\epsilon_p - \epsilon_n}\right].\mathbf{B} \\ &= \psi_n{}^{(\mathrm{p})} + \psi_n{}^{(\mathrm{d})} \end{aligned} \tag{2.13}$$

Therefore, the orbital current is wholly determined by the accessibility of unoccupied from occupied molecular orbital transitions.

Furthermore, the computational cost is mitigated by the rather modest dependence on the basis set, offering rapid convergence at the 6-31G** level,[136,137] a dependence discussed further in Section 2.3. The methodology allows for partitioning into non-redundant orbital contributions, meaning current-density can be analysed shell-by-shell to give chemical insight into calculations.[73]

Variants of the conventional CTOCD-DZ method also exist which differ in choice of $\mathbf{d}(\mathbf{r})$. One such is the CTOCD-PZ (Continuous Transformation of Origin of Current Density - Paramagnetic Zero) also known as the allocentric method,[138] where the local paramagnetic sum has been eliminated.[139] The advantages of this method lie in the calculations of nuclear shieldings and magnetisability, and will not be discussed further here. Other, *ad hoc* modifications exist. In the -DZ2 and -PZ2 methods, for any point $\mathbf{r}$ close to a nucleus, $\mathbf{d}(\mathbf{r})$ 'jumps' to the position of the nucleus. However, comparisons

between all four models identifies little difference between current maps (calculated in the $1a_0$ plane) with variation to the level of 1%.[138,139] Comparisons have also been performed between the monocentric method, where **d** is a fixed single point, and the *ipsocentric* method, defining multiple points of origin.[73] In addition to the superior convergence and physically realistic maps, the *ipsocentric* choice is unique amongst origin distributions in that it leads to orbital contributions that do not re-mix under application of the field.

Selection Rules

A key feature of the *ipsocentric* method is that calculated currents are governed by a series of selection rules.[105] In general, there are three factors which determine the strength and existence of contributions from occupied-to-unoccupied transitions: symmetry, spatial distribution, and energy. In these rules, $\mathrm{R}_{||}$ and $\mathrm{T}_{\perp}$ represent rotations around the field direction and translations at right angles to the field; and $\Gamma(\psi)$, $\Gamma(\mathrm{R}_{||})$, $\Gamma(\mathrm{T}_{\perp})$ and Γ_0 denote representations of the orbital, the rotation and translations and the totally symmetric representation respectively. The rules state that a transition $\psi_n \rightarrow \psi_p$ has:[105]

1. A diatropic contribution to $\mathbf{J}_n{}^{(1)}$ if the direct product $\Gamma(\psi_n) \times \Gamma(\psi_p) \times \Gamma(\mathrm{T}_{\perp})$ contains Γ_0.

2. A paratropic contribution to $\mathbf{J}_n{}^{(1)}$ if the direct product $\Gamma(\psi_n) \times \Gamma(\psi_p) \times \Gamma(\mathrm{R}_{||})$ contains Γ_0.

3. Both a paratropic and diatropic contribution to $\mathbf{J}_n{}^{(1)}$ if both the direct products $\Gamma(\psi_n) \times \Gamma(\psi_p) \times \Gamma(\mathrm{T}_{\perp})$ and $\Gamma(\psi_n) \times \Gamma(\psi_p) \times \Gamma(\mathrm{R}_{||})$ contain Γ_0.

4. No contribution to $\mathbf{J}_n{}^{(1)}$ if neither of the direct products $\Gamma(\psi_n) \times \Gamma(\psi_p) \times \Gamma(\mathrm{T}_{\perp})$ and $\Gamma(\psi_n) \times \Gamma(\psi_p) \times \Gamma(\mathrm{R}_{||})$ contain Γ_0.

In addition to these selection rules, there exists an explicit energetic relationship. The energy difference $\epsilon_p - \epsilon_n$ in equation (2.13) implies that orbitals with similar energies will result in stronger allowed transitions. In turn, this suggests the dominance of frontier

orbitals near the HOMO-LUMO level. These rules will be of importance later in Chapter 6 where the orbital contributions of perylene are examined.

2.1.2 The Pseudo-π Model

One model that can be used to obtain results close to *ab initio* quality has become known as the pseudo-π model.[140] This model is based on two approximations.

1. The N-carbon framework of the π-manifold is replaced by an N-pseudo-hydrogen framework with identical spatial positions. This relies on the one-to-one relationship between the Hückel molecular orbitals of the carbon $2p_z$ π-system and combinations of the hydrogen 1s σ-orbital. Both are defined by the same eigenvectors of the adjacency matrix of the framework.

2. Calculations are performed using the *ipsocentric* formulation for the N-electron, N-basis-function system. The typical 6-31G** basis-set for the full CHF calculation is therefore reduced to a single STO-3G basis function per hydrogen atom.

The required atomic positions can be determined in various ways, including using experimental data, taking optimised geometries, or considering idealised geometries, with bond lengths fixed to 1.4 Å. The minimal basis set and small number of electrons in the pseudo-molecule results in a faster calculation, without sacrificing numerical accuracy. Variation of the standard STO-3G prescription will be tested later in Section 2.3. The selection rules of the *ipsocentric* method carries over to this model. In fact, the symmetries of the π and σ-orbitals are related by equation (2.14).

$$\Gamma(\sigma) = \Gamma(\pi) \times \Gamma_z \tag{2.14}$$

where $\Gamma(\sigma)$ is the symmetry for the set of hydrogen atoms; $\Gamma(\pi)$ is the symmetry of the set of π molecular orbitals for the full-carbon parent; and Γ_z is the symmetry of the translation perpendicular to the molecular plane.

The eigenvalues of the C_π and H_σ adjacency matrices are identical and it happens that the effective resonance integrals $\beta_{\pi\pi}$ and $\beta_{\sigma\sigma}$ are numerically similar for a distance of 1.4 Å.

As a result, numerical results are also strikingly similar, corresponding to current-density maps that are near-indistinguishable,[84,141,142] and are typically qualitatively comparable to the HL models.[143,144] In terms of molecular orbitals, there is a strong correspondence between the C_N π-MOs and the H_N σ-orbitals, with identical nodal patterns and similar orders of energy. This model will be utilised when systems are large and potentially computationally expensive for instance in the investigation of perylene in Chapter 6.

2.2 Implementation of the Ring-Current models

The implementation of the full *ipsocentric* method will now be demonstrated using the example of benzene. The convention applied in these calculations is to use optimised geometries, calculated at the DFT/B3LYP/6-31G** level of theory. The optimised structure is then used with the *ipsocentric* method in calculations at the CHF/6-31G** level of theory, and currents are plotted at a height of $1\,a_0$ above a defined molecular plane. It is often useful to analyse current maps using three subsets of occupied molecular orbitals: the full set, and the full σ or π sets.

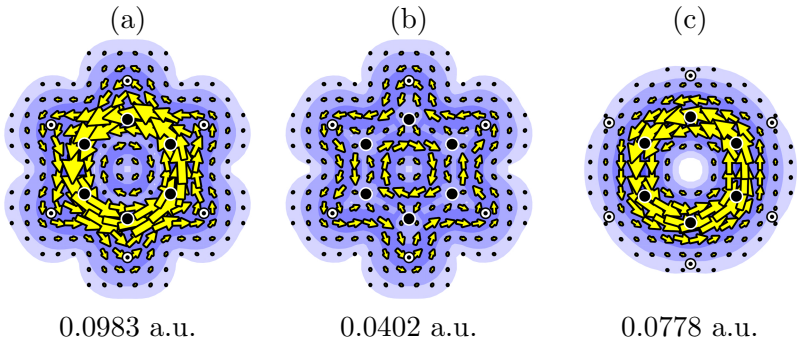


Figure 2.1: The current maps of benzene formed from: (a) combination of all molecular orbitals; (b) combination of the σ-orbitals; and (c) combination of the π-orbitals. Orbitals are identified by their behaviour under reflection in the molecular plane. Black filled circles correspond to carbon atoms and dotted circles correspond to hydrogen atom positions.

Current-density maps are quantified using the value $j_{\max}$, corresponding to the maximum modulus of current density in the plotting plane, which can act as a rough numerical scale of the current strength. Figure 2.1 demonstrates the construction of the Total map, the combination of all molecular orbitals; the σ-map, the contribution of all

σ-orbitals including carbon-carbon and carbon-hydrogen single bonds; and finally, the π-map, representing the contribution from all π-orbitals, i.e. those antisymmetric under the reflection in the molecular plane. The latter map is arguably the most informative of the three. Many other subsets can be constructed to include the contributions from individual user-defined orbitals. Taking for example the occupied π-orbitals of benzene, which are of A_{2u} and doubly degenerate E_{1g} symmetries, the individual current densities are shown in Figure 2.2.

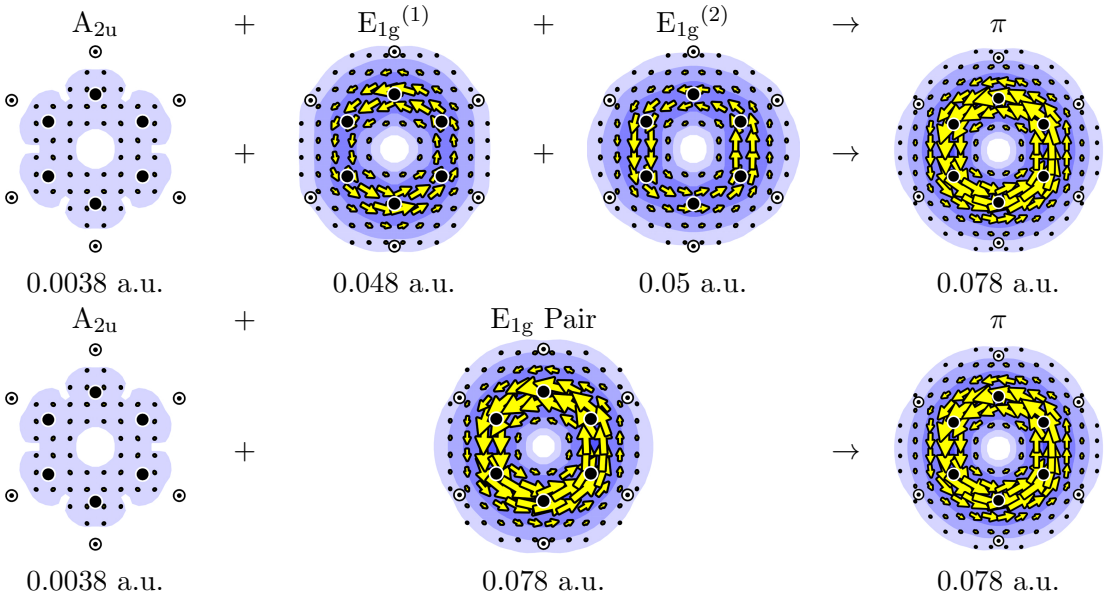


Figure 2.2: The combinations of the three different orbitals and individual j_{max} values which contribute to the overall π-current of benzene. The largest contributors to the total current are the doubly degenerate E_{1g} orbitals, which are combined in the E_{1g} pair map. The A_{2u}, the lowest lying π-orbital, is a relatively weak current contributor.

Figure 2.2 illustrates an inevitable feature of maps for degenerate sets. The Total map for benzene has C_{6h} symmetry. However, the components of the E_{1g} shell give different maps dependent on the choice of the two orthogonal symmetry-adapted linear combinations for this representation. Only, the combined E_{1g} shell is required to carry the full C_{6h} rotational π-current symmetry (Figure 2.2). These maps also highlight the frontier-orbital effect described earlier. The π-current is near-indistinguishable from the combined E_{1g} shell (even j_{max} values are identical to two significant figures). The two

categories of aromaticity and antiaromaticity correspond to opposite senses of circulation in the map. Current flowing clockwise in a closed loop is paratropic, and in a monocycle, would be associated with molecular antiaromaticity (described in graph-theory by negative current values). In contrast, current flowing anticlockwise in a closed loop, would be associated with aromaticity (denoted by positive current values in graph-theory models). The two archetypes can be seen in Figure 2.3.

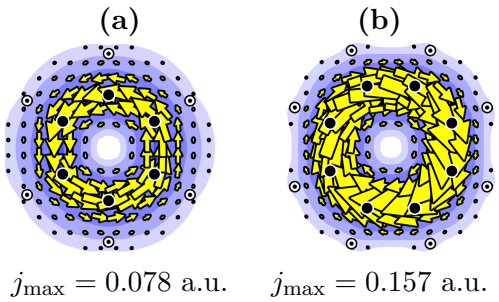


Figure 2.3: The ring-current maps and $j_{\max}$ of the π manifold for the archetypes of aromaticity and antiaromaticity, (a) benzene and (b) planar cyclooctatetraene respectively. The maps are reported at a height of $1\,a_0$ above the defined molecular plane.

One can identify a systematic difference between 'aromatic' and 'antiaromatic' $j_{\max}$ values. Paratropic currents are typically stronger than diatropic magnitudes owing to the energy denominator in equation (2.13). The ring current of cyclooctatetraene originates from the rotationally allowed HOMO-LUMO transition in which initially degenerate orbitals in D_{8h} symmetry have undergone Jahn-Teller splitting to the D_{4h} symmetry.[145,146] The reduced energy gap in the COT system results in a strongly paratropic HOMO-LUMO transition, partially cancelled by the weaker underlying [HOMO-1]-LUMO and HOMO-[LUMO+1] diatropic contributions. In contrast, the HOMO-LUMO transition in benzene is from orbital sets with different angular momenta and different numbers of nodes, and have separated energy levels.

Combining *ab initio* and the topological Hückel-London calculations allows for useful comparisons. Such comparisons have been performed previously and have highlighted the qualitative equivalence of ring-current maps, for instance: corazulene and cornaphthalene[147,148] and phenylenes.[149]

2.3 Customisation of Current Density Calculations

The standard *ipsocentric* approach described earlier assumes a plotting height of $1\,a_0$ above the molecular plane, and a 6-31G** basis set. Here, the choices of plotting height and basis set are investigated for the example of benzene. The largest set of data presented here is for benzene, but similar conclusions have been reached for anthracene, coronene and corrannulene. For this section, results reported correspond to current-density calculations of only the occupied π-molecular orbitals in the *ipsocentric* calculation, or all occupied molecular orbitals in the pseudo-π analogue.

2.3.1 Plotting Plane Height

Consider the conventional 6-31G** *ipsocentric* calculation (abbreviated to AI in figure legends), and its pseudo-π analogue (abbreviated to PP). The effect of choice of plotting plane height between 0 and $3\,a_0$ above the defined plane is shown in Figure 2.4.

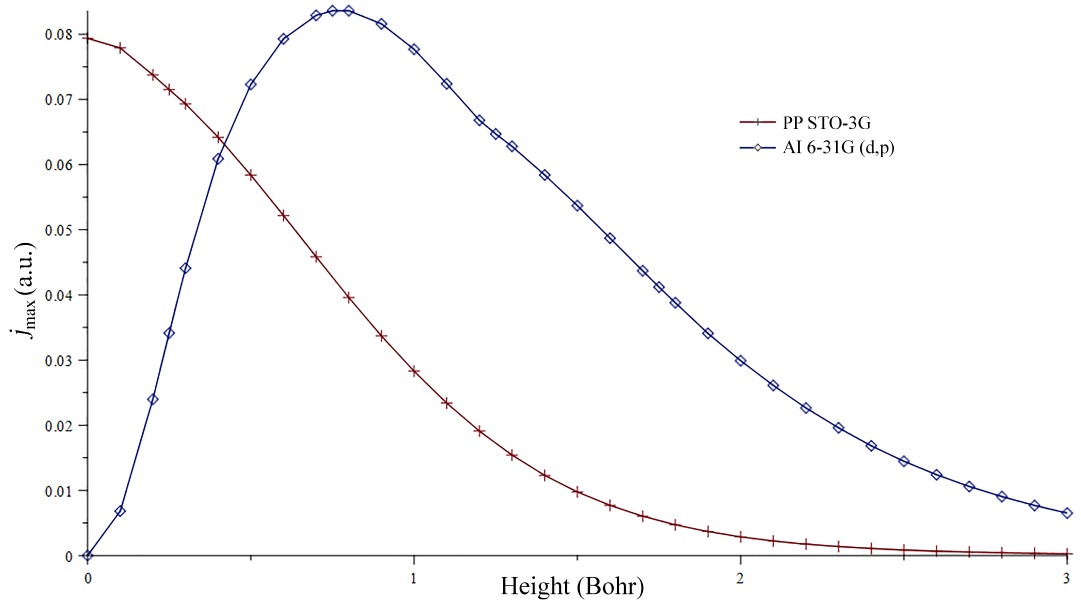


Figure 2.4: The dependence of the plotted height above the defined molecular plane on the j_{max} current magnitudes for the CHF/6-31G** *ab initio* method, labelled as AI 6-31G(d,p), and the CHF/STO-3G pseudo-π method, labelled as PP STO-3G.

Figure 2.4 shows the overall profile of the π-current is as expected, with the magnitude falling to zero in the nodal plane, maximising in the region of $0.75\,a_0$, and tailing off at

large heights above the plane. The current maximises at $0.75\,a_0$, but is only reduced by 5% when the standard plotting height of $1\,a_0$ is taken. Likewise the pseudo-π current has the expected decline in $j_{\max}$ as the plotting height is raised. The figure also shows a good numerical match between the largest pseudo-π current and the true-π current (0.079 a.u. vs 0.078 a.u. respectively). The comparison justifies the simple use of $1\,a_0$ and $0\,a_0$ as the plotting heights in the *ipsocentric* and pseudo-π calculations, respectively.

2.3.2 Basis Set Dependence

Next, the dependence of calculated currents on basis set is scrutinized. This dependence has been investigated previously,[137] using a small selection of basis-sets. However, the present investigation will extend the discussion to include a wider range of Pople and Dunning style basis sets and compare the height profiles of each.

CHF *ipsocentric* method

The CHF *ab initio* calculations were carried out on benzene using a fixed geometry calculated at the DFT/B3LYP/6-31G** level of theory. The standard 6-31G** basis set in the CHF calculation was changed to: STO-3G, 4-31G, 4-31G**, 6-31G, 6-31G*, 6-31G**, 6-311G**, 6-31+G**, 6-31++G**, 6-311+G**, 6-311++G**, cc-pVDZ and cc-pVTZ.[150–152] This selection provides a variety of different basis sets which incorporate: 'zeta' changes; inclusion of polarisation functions; addition of diffuse functions and switching from Pople-style to Dunning-style basis sets.[153] Plotted between 0 and $2\,a_0$ above the defined plane, the $j_{\max}$ dependence for each basis set is displayed in Figure 2.5.

One can identify three distinct families of curves corresponding to the types of basis set used. The smallest basis-set, STO-3G, maximises higher than the 6-31G** and, at most heights, lies below $j_{\max}$ values of the larger basis sets.

The second family includes the two split-valence basis sets 4-31G and 6-31G. These initially follow the rise of the STO-3G curve and again maximise at greater heights above the molecular plane, but eventually merge with curves for the larger basis sets.

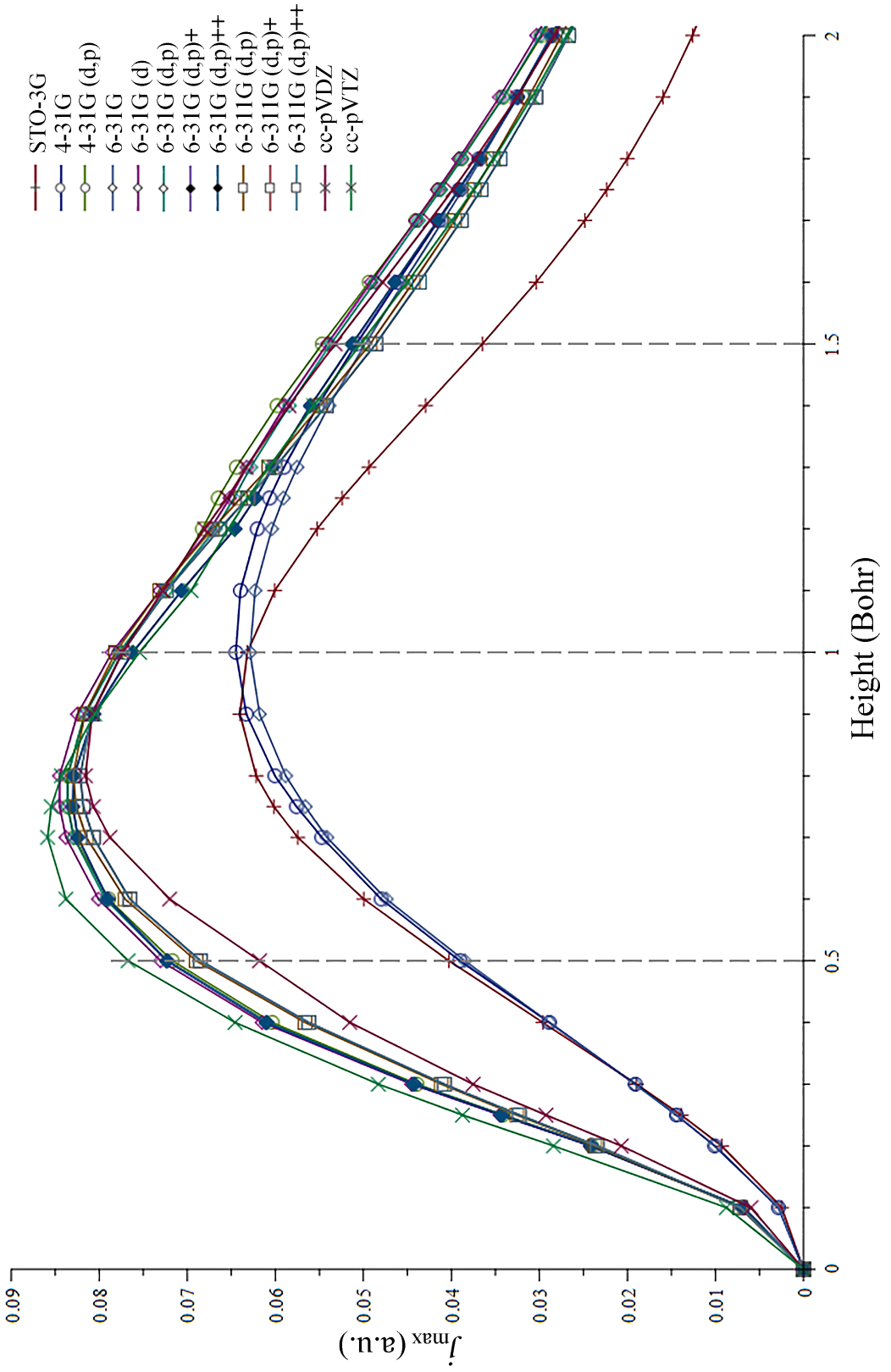


Figure 2.5: Calculated $j_{\max}$ values, in a.u., at various heights above the molecular plane using a wide range of basis sets for the CHF calculation of benzene. $1\,a_0$ above the plane is the standard choice for the plotting height in typical procedures.

Comparison of the other curves of Pople-style basis sets shows a significant effect on inclusion of polarisation functions, but little effect on inclusion of diffuse functions. Strikingly, all Pople-style sets that include polarisation functions yield $j_{\max}$ values that are similar to within 3%, when plotted at a height of $1\,a_0$ above the molecular plane. Inclusion of the Dunning basis sets increases this variation to 4%, and the DZ and TZ Dunning sets bracket the polarisation including Pople sets for the plotted heights of $0 - 0.75\,a_0$ above the molecular plane.

One can also assess the current maps from a qualitative perspective. A selection is shown in Figure 2.6 calculated at $1\,a_0$ above the molecular plane. Smaller basis-sets such as the STO-3G, 4-31G and 6-31G are evidently not sufficient, with current maps that are clearly distinguishable from the larger basis sets. In addition, use of basis sets larger than 6-31G** show no additional changes, suggesting that the basis-set limit has indeed been reached. Similar conclusions are reached for the other systems mentioned earlier. The conclusion here is simple: 6-31G** is sufficient for calculations.

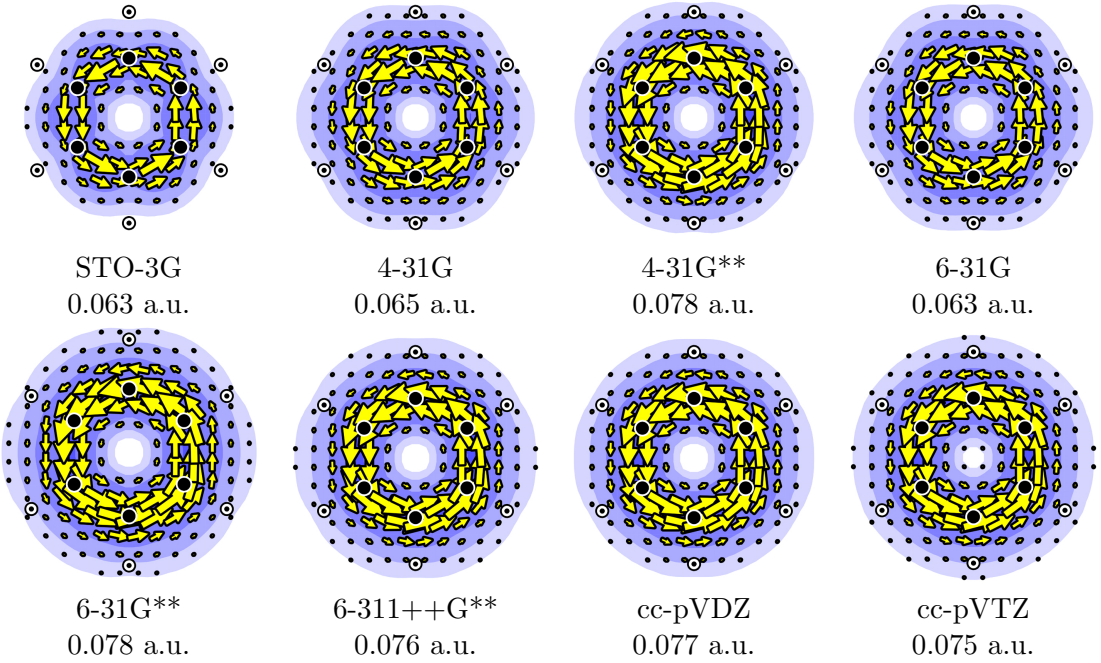


Figure 2.6: A selection of current maps and corresponding $j_{\max}$ values plotted $1\,a_0$ above the plane calculated using different basis sets at the CHF level of theory. The basis set used in current-density calculations is indicated below each map.

DFT *ipsocentric* Method

The *ipsocentric* method can also be used with Density Functional Theory, DFT, using a version of the GAMESS-UK[154] computational package.[155] Previous investigations have shown that current maps are similar overall at the CHF and DFT levels.[156]

Plotting $j_{\max}$ values against the height above the plane yields Figure 2.7. One can easily observe similarities between Figure 2.5 (the CHF calculation) and Figure 2.7 suggesting a similar overall conclusion on basis set utility: those sets that do not include polarisation functions should be discarded.

Again, Dunning and polarisation including Pople-style basis sets can be seen to cluster. For DFT calculations, there is a variation of 6% in $j_{\max}$ values for this cluster compared to the CHF 4%. Equivalence between CHF and DFT levels is not limited to benzene, it has been noted in other instances,[155,157] and in the other systems mentioned earlier. Furthermore, current maps for altered basis sets are qualitatively comparable. A selection of current maps calculated using the basis sets: STO-3G, 4-31G*, 6-31G, 6-31G**, 6-311G**, cc-pVDZ and cc-pVTZ at a height of $1\,a_0$ above the molecular plane, are shown in Figure 2.8 (the background colour is altered to distinguish levels of theory, blue for CHF maps, and green for DFT maps). Once again there are qualitative similarities in the current densities calculated using basis-sets which include polarisation parameters, and current-density maps are indistinguishable when calculated using the larger Pople and Dunning basis sets. Again, the conclusion is that the use of the 6-31G** basis set is sufficient.

It should also be noted that DFT implementation allows further customisation. Prior work has investigated the effect of changing the functional; from the standard B3LYP, to PBE,[155] KT3, optimised effective potential (OEP) and Wu-Yang coupled cluster singles and doubles (WY-CCSD) functionals.[158] This investigation found negligible changes in the diatropicity of benzene and a minor qualitative difference in the paratropicity of COT.

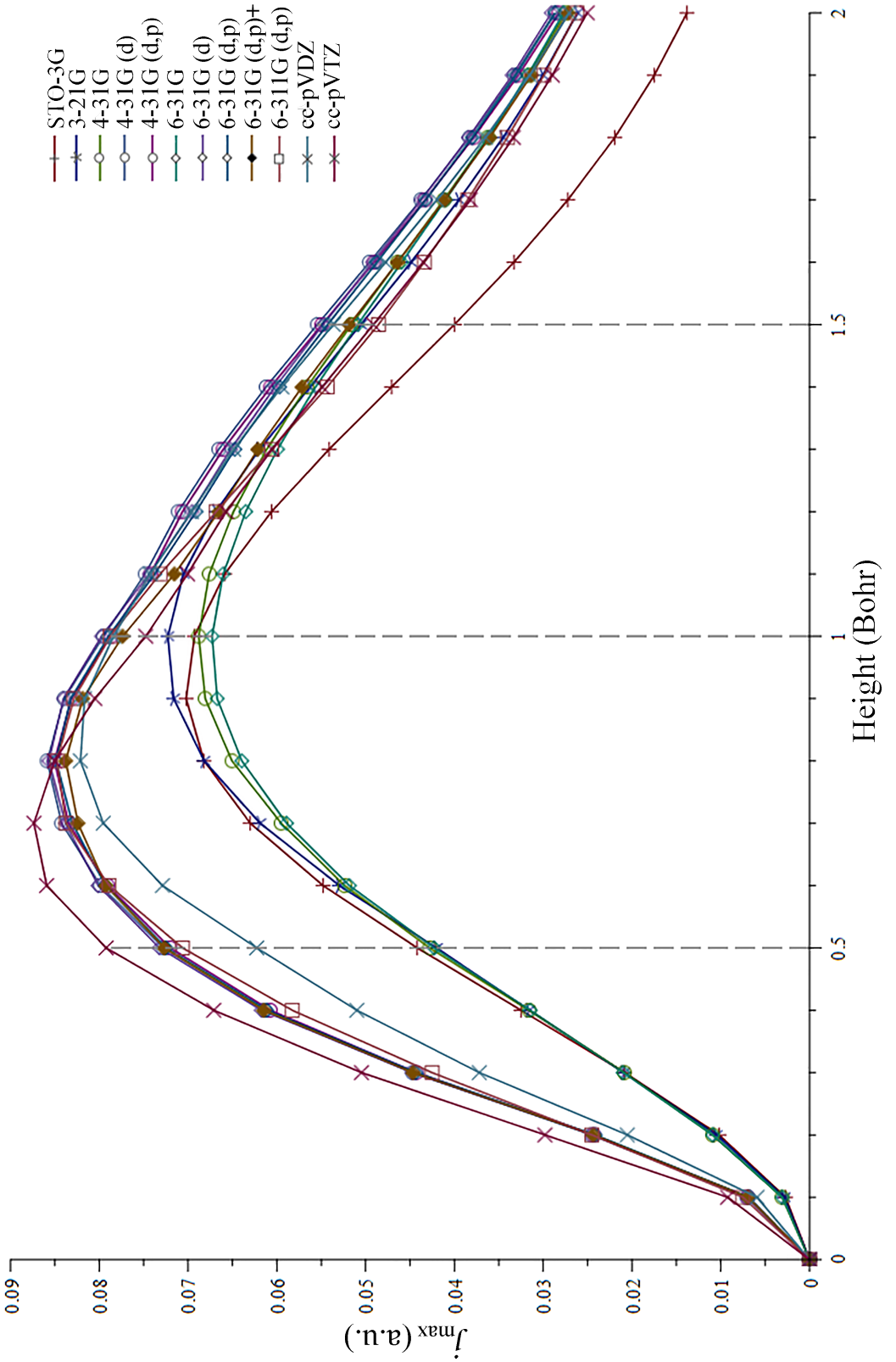


Figure 2.7: Calculated $j_{\max}$ values in a.u. at various heights above the molecular plane using a wide range of basis sets for the DFT/B3LYP calculation of benzene. $1\,a_0$ above the plane is the standard choice for the plotting height in typical procedures.

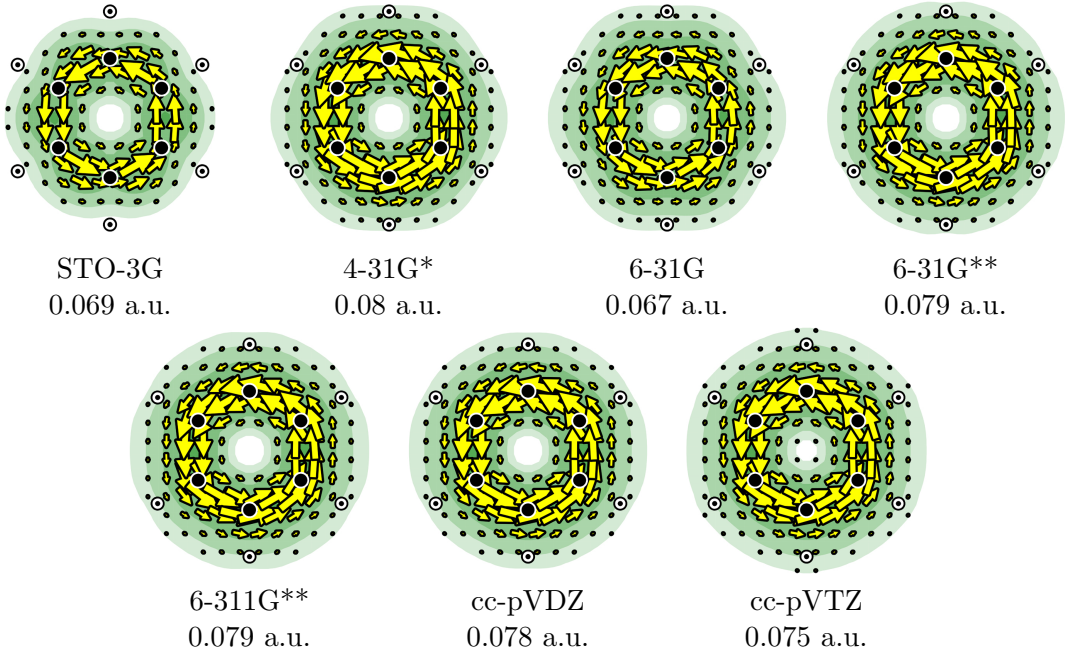


Figure 2.8: A selection of current-density maps and $j_{\max}$ values plotted $1\,a_0$ above the plane calculated using different basis sets at the DFT level of theory using the B3LYP functional.

The Pseudo-π model

Finally, consider the pseudo-π model. The standard procedure for the pseudo-π approach is to replace the N-carbon framework with an N-pseudo hydrogen framework and reduce the basis set to a single 1s STO-3G basis function per hydrogen centre. As discussed earlier, the optimal plotting plane for the generation of *ab initio* comparable results, is in the molecular plane. It is appropriate to investigate the effect changing this single basis function to a larger basis set has on this conclusion. The minimal STO-3G was altered to 4-31G, 6-31G and 6-31G**, yielding the plot shown in Figure 2.9. As can be seen, only the minimal basis STO-3G gives the quantitative reproduction of the $1\,a_0$ full CHF/6-31G** result. The crude choice of a simple STO-3G basis set is therefore close to optimal for this procedure. In addition, current-density maps calculated using the full carbon framework at the CHF/6-31G** level, and the pseudo-π model at the STO-3G level are qualitatively similar in shape (see Figure 2.10) and quantitatively comparable.

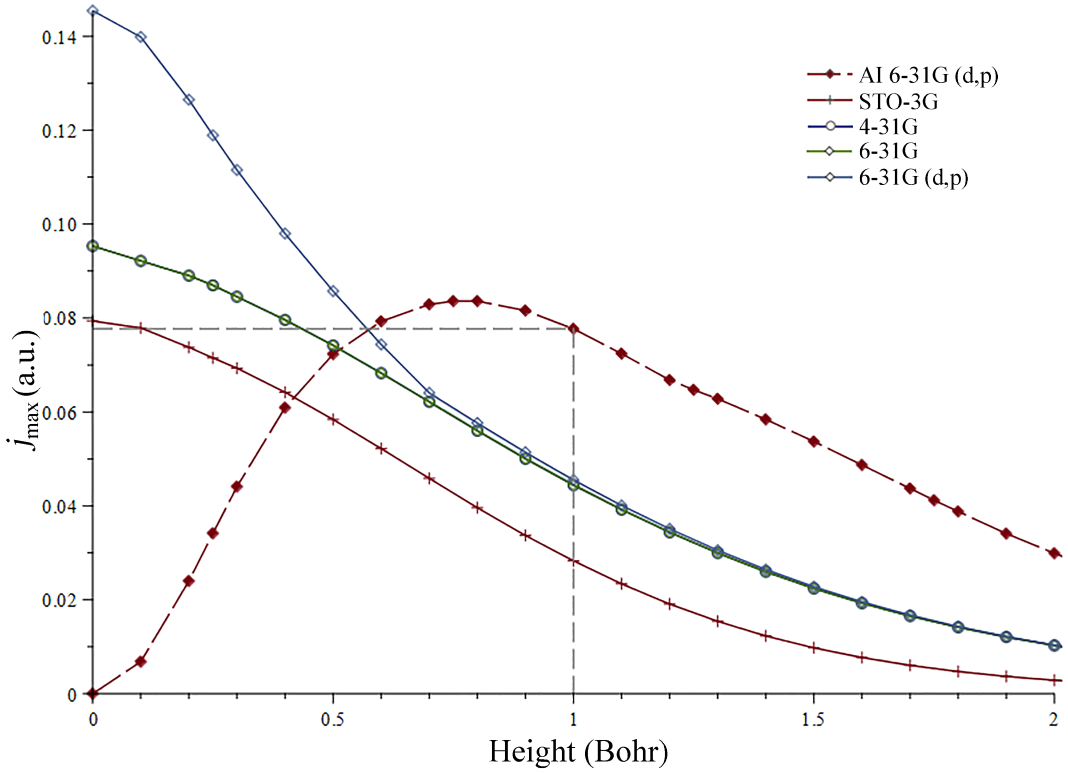
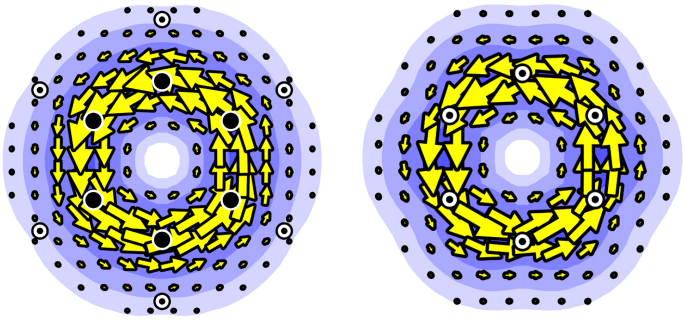


Figure 2.9: A plot of the j_{max} values in a.u. at various heights above the plane performed using several different basis sets for the calculation of benzene using the pseudo-π model. Comparisons are made to the full *ipsocentric* method, shown as the AI 6-31G(d,p) line.

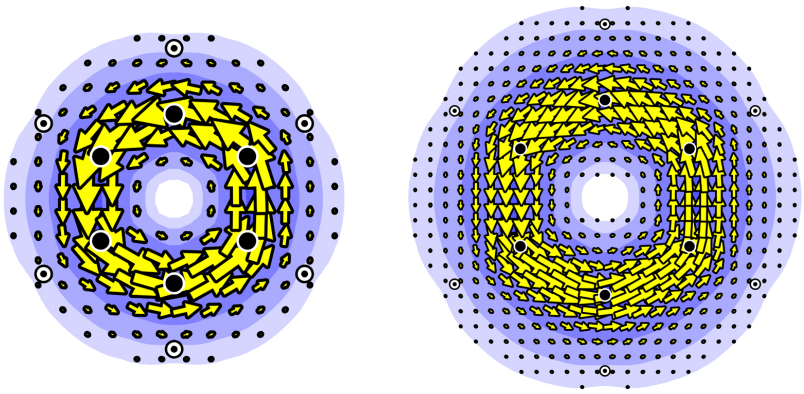


$j_{max} = 0.078$ a.u. $j_{max} = 0.079$ a.u.

Figure 2.10: The ring current maps and j_{max} values of benzene calculated as (left) the π manifold at the CHF/6-31G** level and (right) the total orbital manifold at the pseudo-π/STO-3G level. Plotting conventions are as discussed in the text.

2.3.3 Dependence on the plotting grid

The method for evaluation of the $j_{\max}$ value relies on the computation of the current density as a mesh of grid points. This grid can also be customised, whereby a reduction of mesh size can increase the precision of $j_{\max}$ values. Typically, the current density is calculated assuming a standard grid size of $32\,a_0$ by $32\,a_0$ with 40 points on each axis for the current modulus and 100 points on each axis for the current contours. A simple reduction to $16\,a_0$ by $16\,a_0$ with the same number of points per axis, leads to more precise $j_{\max}$ values, and thus in some sense, more accurate current maps. This effect can be visualised in Figure 2.11.



Box size	$32\,a_0$ by $32\,a_0$	$16\,a_0$ by $16\,a_0$
$j_{\max}$	0.0777 a.u.	0.0783 a.u.

Figure 2.11: The effect of altering the plotting density grid on the $j_{\max}$ and current maps for benzene. The difference is small at less than 2%.

As can be seen from the $j_{\max}$ values, increasing the precision offers only marginal improvement ($< 2\%$) offset by the detrimental effect of degrading the current map by an over abundance of arrows. Therefore, the physical space of $32\,a_0$ by $32\,a_0$ (with a 40/100 mesh, as defined above) is adequate for the computation of maps for molecules of this size. Unless stated otherwise, all current-density maps correspond to this choice, and values of $j_{\max}$ will typically be quoted to three decimal places.

Chapter 3

Cyclic Partition of Current in the Hückel-London Model[1]

3.1 Introduction

Discussion now returns to the Hückel-London model discussed briefly in Chapter 1. In addition to the methods defined in Chapter 1, a third approach needs to be discussed that is integral to future discussions in this thesis. This method is known as the *Aihara formalism*. This method can provide specific insight into the connection between current and electronic structure, and offers useful comparisons with *ab initio* and conjugated-circuit model results.

The Aihara formalism is conceptually different to the finite-field approach, typically employed by the Sheffield group, and the perturbation method based on bond-bond polarisabilities, typically employed by Mallion and co-workers,[84] both discussed previously in section 1.3. All three methods have an identical origin in the literature, relying on the combination of Hückel theory (a graph theoretical model of electronic structure) and London theory (accounting for the perturbation of molecular orbitals in the presence of an external magnetic field).[48,94] As a result, all three methods must give identical numerical results for calculation of the total current.

The Aihara formalism employs ideas from algebraic graph theory and seemingly has not been widely adopted by other workers in the field. This may in part be due to the scattered presentation of literature spanning several decades and published in a multitude of journals. Several 'reviews' published by Aihara exist (see for example [159,160]), but each has focused on a different aspect of the model.

[1] The work in the present chapter is adapted from that performed in collaboration with Prof. Wendy Myrvold and Parminder Kaur. It will be reprinted in full in an upcoming paper: Myrvold. W., Kaur. P., Clarke. J., and Fowler. P.W., *In Preparation*.

The present chapter begins with a step-by-step exposition of the basic graph-theoretical background and chemical ideas. Then two examples are explicitly detailed: anthracene and acridine to show the detailed workings of the model. This then leads into a comparison of cycle contributions between this model and the published CC models. The formalism also allows the derivation of theorems concerning the contribution of molecular orbitals to current; these apply to bipartite systems such as benzenoids and highlight the role of non-bonding orbitals.

3.2 The Essentials of Graph Theory

Before the specifics of the Aihara formalism are addressed, it is useful to recap some essentials from graph theory. The basis for the Hückel-London model relies on the combination of Hückel and London[78] theories.

In the simple Hückel molecular orbital approximation, only the π-electrons are treated. The carbon and hydrogen nuclei, core-electrons and set of localised σ-bonds are assumed to move in a fixed potential, and are therefore treated separately. From the secular equations, derived by application of the variation principle, with an ansatz of molecular orbitals described by linear combinations of N-atomic π-orbitals one per centre, the secular determinant is:

$$\begin{vmatrix} H_{11} - ES_{11} & H_{21} - ES_{21} & \cdots & H_{\mathrm{N}1} - ES_{\mathrm{N}1} \\ H_{12} - ES_{12} & H_{22} - ES_{22} & \cdots & H_{\mathrm{N}2} - ES_{\mathrm{N}2} \\ \vdots & \vdots & \ddots & \vdots \\ H_{1\mathrm{N}} - ES_{1\mathrm{N}} & H_{2\mathrm{N}} - ES_{2\mathrm{N}} & \cdots & H_{\mathrm{NN}} - ES_{\mathrm{NN}} \end{vmatrix} = 0 \tag{3.1}$$

Two parameters are now introduced, α, the *Coulomb integral*, and β, the *resonance integral*. Orthonormality of the atomic orbital basis is assumed. For diagonal entries in matrix (3.1):

$$\begin{aligned} H_{rr} &= \alpha, \\ S_{rr} &= 1 \end{aligned} \tag{3.2}$$

and for off-diagonal entries:

$$\begin{aligned} H_{rs} = H_{sr} &= \beta \text{ if r and s are } \sigma \text{ bonded} \\ &= 0 \text{ otherwise} \\ S_{rs} = S_{sr} &= 0 \end{aligned} \tag{3.3}$$

This is equivalent to defining the Hamiltonian matrix as: $\mathbf{H} = \alpha\mathbf{1_N} + \beta\mathbf{A_N}$, where $\mathbf{1_N}$ is the N-dimensional unit matrix and $\mathbf{A_N}$ is the adjacency matrix of the graph; and the AO overlap matrix as: $\boldsymbol{S} = \mathbf{1_N}$. Hence from (3.1),

$$\det\left|E\mathbf{1_N} - \alpha\mathbf{1_N} - \beta\mathbf{A_N}\right| = 0 \tag{3.4}$$

which can be reduced to:

$$\det\left|\frac{(E-\alpha)}{\beta}\mathbf{1_N} - \mathbf{A_N}\right| = 0 \tag{3.5}$$

and hence, $\lambda = (E-\alpha)/\beta$ is an eigenvalue of $\mathbf{A_N}$ and the orbital energy is $E = \alpha + \lambda\beta$. These eigenvalues then form the basis of the characteristic polynomial $\phi_{\mathrm{G}}(x)$

$$\begin{aligned} \phi_{\mathrm{G}}(x) &= \prod_{k=1}^{\mathrm{N}} (x - \lambda_k) \\ &= \det|x\mathbf{1_N} - \mathbf{A_N}| \end{aligned} \tag{3.6}$$

In effect, α and $|\beta|$ denote the origin and scale for the orbital energy spectrum and hence can conveniently be taken to be 0 and 1, respectively, for carbon. β is a negative energy and therefore positive λ denote the lowest orbital energies. Heteroatoms can be incorporated into the system through scaling of α_{X} and β_{XC} or β_{XY} in terms of the standard α and β parameters. This is illustrated in section 3.4 and is investigated further in Chapter 4.

In the case of benzene for example, matrix (3.1) reduces to an N by N matrix where N= 6.

$$\begin{vmatrix} \alpha - E & \beta & 0 & 0 & 0 & \beta \\ \beta & \alpha - E & \beta & 0 & 0 & 0 \\ 0 & \beta & \alpha - E & \beta & 0 & 0 \\ 0 & 0 & \beta & \alpha - E & \beta & 0 \\ 0 & 0 & 0 & \beta & \alpha - E & \beta \\ \beta & 0 & 0 & 0 & \beta & \alpha - E \end{vmatrix} = 0 \tag{3.7}$$

and with $x = (E - \alpha)/\beta$, matrix (3.7) reduces to:

$$\begin{vmatrix} x & -1 & 0 & 0 & 0 & -1 \\ -1 & x & -1 & 0 & 0 & 0 \\ 0 & -1 & x & -1 & 0 & 0 \\ 0 & 0 & -1 & x & -1 & 0 \\ 0 & 0 & 0 & -1 & x & -1 \\ -1 & 0 & 0 & 0 & -1 & x \end{vmatrix} = 0. \tag{3.8}$$

with solutions $x = +2, +1, +1, -1, -1, -2$ and thus represent the eigenvalues of the cycle.

3.3 Aihara Hückel-London ring current model

The Aihara formalism of Hückel-London theory was developed and refined over a long series of papers from 1976 to the present by J-I. Aihara of Shizuoka University. The main concept of his model connected Hückel and London theories to a characteristic polynomial treatment through the use of Sachs graphs. These graphs are defined as all sub-graphs of G containing cycles and/or complete graphs with two vertices, which are then used in the Sachs Theorem[161] to compute coefficients of the characteristic polynomial of G.[162] Application of London approximations is established through manipulation of characteristic polynomials.[163,164] A key feature is that current densities can be expressed in terms of ratios to the response of benzene in the same magnetic field, meaning that only simple (field-free) characteristic polynomials are required.[58]

An eigenvalue, λ_k, that appears m_k times is said, in chemistry, to have m_k-fold degeneracy, and is said to form a *shell*. In the simple Hückel model, an eigenvector of

the adjacency matrix corresponds to the molecular orbital and eigenvalues to the orbital energies. For a graph of order N with N electrons (using the assumption of a single π-electron per heavy atom) the occupancy of molecular orbitals is designated through application of the Aufbau, Pauli and Hund's rules until all electrons have been assigned to a molecular orbital. Here, N_k will denote the number of electrons assigned to the k^{th} shell. If all N_k are either $2m_k$ or 0 the system is said to be *closed-shell*. Otherwise the system is *open-shell* and there will be some orbital/orbitals with $0 < N_k < 2m_k$. In these cases, the approximation of fractional occupation is employed, in which a fraction N_k/m_k of the electrons is assigned to each orbital in the shell.

The first quantity to be discussed in the Aihara formalism is known as the *Circuit-Resonance-Energy*, denoted here CRE_C. This quantity represents an approximate resonance energy contribution for the cycle,[165] interpreted as an energy gain or loss from cyclic conjugation along the C^{th} circuit.[166] This quantity has appeared in multiple papers, often with different notations, such as RE^C and A_C.[166,167] It is defined as:[168]

$$\text{CRE}_\text{C} = 2 \sum_{k=1}^{\text{N}}{}' \frac{N_k}{m_k} f_k(\lambda_k) \tag{3.9}$$

where f_k is a function that is dependant on the multiplicity of eigenvalue λ_k; the prime on the summation indicates that the sum runs over distinct values λ_k (each distinct eigenvalue is counted once, irrespective of multiplicity, i.e. over shells). In the Aihara formalism, cycle C is defined as *any* possible cycle in the graph, conjugated or not. In future sections the cycles will be called *Aihara cycles* to distinguish them from conjugated circuits.

The function f_k in (3.9) is defined differently according to the multiplicity of the eigenvalue. If $m_k = 1$, f_k is simply equal to:

$$f_k(x) = \frac{\phi_{\text{G-C}}(x)}{\phi_\text{G}{}'(x)} \tag{3.10}$$

where $\phi_{\text{G-C}}(x)$ is the characteristic polynomial of graph G$-$C, defined as graph G with the vertices and edges of cycle C removed, and the presence of a prime on a characteristic polynomial indicates taking the first derivative with respect to x. It is useful to note

that $\mathrm{CRE_C}$ is independent of the molecular geometry: it is a purely graph theoretical quantity. For systems with $m_k \neq 1$ the contributions to the CRE must account for the splitting induced within the set by the presence of an external magnetic field. In such cases, f_k is then:[169]

$$f_k(x) = \frac{1}{(m_k-1)!}\left\{\frac{d^{m_k-1}}{dx^{m_k-1}}\frac{\phi_{\text{G-C}}(x)}{U_k(x)}\right\}_{x=\lambda_k} \tag{3.11}$$

where U_k is defined as:

$$\begin{aligned} U_k(x) &= \frac{\phi_{\mathrm{G}}(x)}{(x-\lambda_k)^{m_k}} \\ &= \prod_{\lambda_{k'}\neq\lambda_k}(x-\lambda_{k'}) \end{aligned} \tag{3.12}$$

Therefore, $U_k(x)$ is the result of factoring out all contributions from the shell with eigenvalue λ_k from the characteristic polynomial. In the case of $m_k = 1$, equation (3.11) can also be used (although it is clearer to use equation (3.10)). By taking d^0/dx^0 as the formal identity operation, equation (3.11) reduces to equation (3.10) since, for $m_k = 1$, the polynomial $U_k(x)$ is identical to ${\phi_{\mathrm{G}}}'(x)$. From (3.12),

$$\phi_{\mathrm{G}}(x) = U_k(x) \times (x-\lambda_k)^{m_k} \tag{3.13}$$

$${\phi_{\mathrm{G}}}'(x) = {U_k}'(x) \times (x-\lambda_k)^{m_k} + U_k(x) \times (x-\lambda_k)^{m_k-1} \tag{3.14}$$

For $m_k = 1$, equation (3.14) reduces to

$${\phi_{\mathrm{G}}}'(x) = {U_k}'(x) \times (x-\lambda_k) + U_k(x). \tag{3.15}$$

When evaluated at $x = \lambda_k$ the right hand side of (3.15) reduces to,

$${\phi_{\mathrm{G}}}'(x) = U_k(x) \tag{3.16}$$

The sum of $\mathrm{CRE_C}$ values over *all* cycles of graph G is proposed as the aromaticity index *Magnetic Resonance Energy*, MRE, defined as:[165]

$$\mathrm{MRE} = \sum_{\mathrm{C}}^{\mathrm{G}} \mathrm{CRE_C} \tag{3.17}$$

Aihara has argued for the universal applicability of MRE as an aromaticity index, owing to the independence of cycle size. Hence is, in Aihara's eyes, superior to the definition of

ring-current aromaticity. One example he used to support this is for pentalene and the variation of its tropicity with charge.[72] Aihara also advocates for the use of *Topological Resonance Energy*[23,170] as an indicator of aromaticity. This resonance energy method corresponds to the difference in the total π-electron energy between the conjugated molecule and a hypothetical reference structure, commonly an acyclic derivative. Aihara reports the typically linear relationship between TRE and MRE that, supposedly, validates Magnetic Resonance Energy as an index of aromaticity applied through the magnetic criterion.[159,166]

Individual circuit resonance energies represent a sum of contributions taken over all occupied eigenvalues for one cycle. Through manipulation of the HL expression for magnetic susceptibility (equation (1.7)), each $\mathrm{CRE_C}$ can be converted into a Hückel-London *cycle-current*.[58] The contribution from cycle C to the total HL current, denoted $\mathrm{J_C}$, is formulated as:

$$\mathrm{J_C} = \left(\frac{9}{2}\right) \mathrm{CRE_C}\ \mathrm{J_0} \left(\frac{S_\mathrm{C}}{S_0}\right) \tag{3.18}$$

where $\mathrm{J_0}$ is the HL current for a benzene molecule in the standard geometry;[58] and S_C and S_0 are the areas of cycle C and the benzene hexagon respectively. In what follows, the HL current will be expressed as the ratio $\mathrm{J/J_0}$. Both the cycle and the hexagon are assumed to be constructed from regular polygons with sides of a normal carbon-carbon bond length, 1.4 Å. The area of a regular n-vertex polygon is then formulated as:

$$\frac{S_n}{S_0} = \frac{n\sqrt{3}\cot\left(\pi/n\right)}{18} \tag{3.19}$$

The total Hückel-London current map is then found from edge-by-edge summation over contributing cycles that pass through the given edge, to give *bond-currents* for the graph. Alternatively, *ring-currents* can be calculated by the summation over all cycles that enclose a particular face, with the resulting quantity denoted as $\mathrm{J_{Face}}$.

Minor modification of the adjacency matrix of G can account for the presence of heteroatoms. This method was detailed in full in 2007[24] and then reviewed to include a more extensive catalogue of calculations in 2008.[166] Parameterisation for heteroatom inclusion is achieved through simple alteration of the Coulomb and resonance integrals,

α and β, as defined by Van-Catledge.[171] Equation (3.18) must be modified to account for the change in β parameters, becoming:

$$\frac{\mathrm{J_C}}{\mathrm{J_0}} = \left(\frac{9}{2}\right)\left(\prod_{\mathrm{i}=1}^{|\mathrm{C}|}\frac{\beta_\mathrm{i}}{\beta_0}\right)\left(\frac{S_\mathrm{C}}{S_0}\right)\mathrm{CRE_C} \tag{3.20}$$

where β_i is the resonance integral of the i^{th} edge of cycle C, and β_0 is the usual carbon resonance integral.

Bringing all the terms together, the Aihara current will be denoted by the following generalised formula

$$\frac{\mathrm{J_C}}{\mathrm{J_0}} = 9\left(\prod_{\mathrm{i}=1}^{|\mathrm{C}|}\frac{\beta_\mathrm{i}}{\beta_0}\right)\left(\frac{S_\mathrm{C}}{S_0}\right)\sum_{k=1}^{\mathrm{N}}{}'\frac{N_k}{m_k}\frac{\phi_{\text{G-C}}(\lambda_k)}{\phi_\mathrm{G}{}'(\lambda_k)} \tag{3.21}$$

Modifications will be made on an *ad hoc* basis for those orbitals with $m_k \neq 1$ by the use of equation (3.11) replacing the ratio of polynomials. Therefore, the total face current, defined as the sum of all cycle contributions for a given face, is defined as:

$$\frac{\mathrm{J_{Face}}}{\mathrm{J_0}} = \sum_{\mathrm{C}}^{\mathrm{Face}} 9\left(\prod_{\mathrm{i}=1}^{|\mathrm{C}|}\frac{\beta_\mathrm{i}}{\beta_0}\right)\left(\frac{S_\mathrm{C}}{S_0}\right)\sum_{k=1}^{\mathrm{N}}{}'\frac{N_k}{m_k}\frac{\phi_{\text{G-C}}(\lambda_k)}{\phi_\mathrm{G}{}'(\lambda_k)} \tag{3.22}$$

Application of equation (3.22) allows the possibility to partition HL current according to both cycle and occupied molecular orbital levels. It should be noted that HL theory does not obey the frontier-orbital approach discussed in Chapter 2. Instead, all occupied orbitals have a significant contribution to the HL current with cancellation or reinforcement from lower lying orbitals resulting in the total HL map.

3.4 Case Studies

Two case studies will be considered. The first deals with anthracene, a molecule composed of three linearly fused hexagons for which all currents can be expressed analytically. The second deals with acridine, three linear fused hexagons for which a single nitrogen atom substitutes a carbon atom in the central hexagon. In both cases, the unique property of partitioning into cyclic currents will be made explicit.

3.4.1 Anthracene

The first step is to find the eigenvalues from the roots of the characteristic polynomial. From a graph theory approach, the characteristic polynomial for this graph is:

$$\begin{aligned}\phi_{\mathrm{G}}(x) &= x^{14} - 16x^{12} + 98x^{10} - 296x^8 + 473x^6 - 392x^4 + 148x^2 - 16 \\ &= (x-2)(x+2)(x-1)^2(x+1)^2\left(x^2+2x-1\right)\left(x^2-2x-1\right)\left(x^2-2\right)^2\end{aligned} \tag{3.23}$$

Roots of this polynomial are equal to the eigenvalues of the adjacency matrix, corresponding to the bonding and antibonding orbitals. The occupied orbitals of neutral anthracene, with 14 π-electrons, have eigenvalues, λ_{B}, where

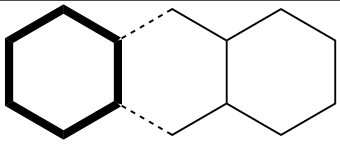
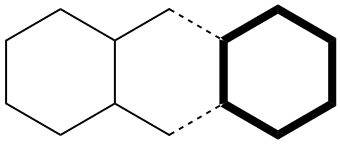
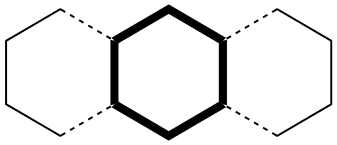
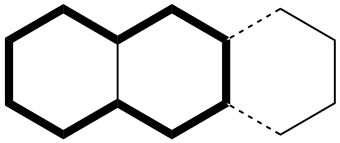
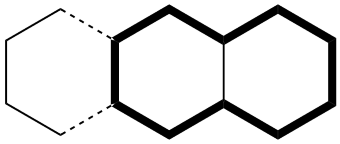
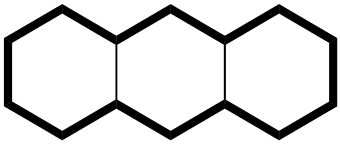
$$\{\lambda_{\mathrm{B}}\} = \left\{1+\sqrt{2}, 2, \sqrt{2}, \sqrt{2}, 1, 1, -1+\sqrt{2}\right\}$$

Thus, anthracene has doubly degenerate occupied orbitals at $\lambda_{\mathrm{B}} = \sqrt{2}$ and 1. From the pairing theorem for bipartite graphs, the unoccupied orbitals corresponding to antibonding orbitals have eigenvalues, λ_{AB}, of the opposite sign to λ_{B}, where

$$\{\lambda_{\mathrm{AB}}\} = \left\{1-\sqrt{2}, -1, -1, -\sqrt{2}, -\sqrt{2}, -1-\sqrt{2}\right\}$$

Next, one must find all possible cycles. For anthracene there are a total of six: three correspond to the individual faces; two result from the fusion of two hexagonal faces; and the final cycle is the result of fusion of all three faces. All cycles and the corresponding characteristic polynomials are reported in Table 3.1.

Table 3.1: The individual circuits and the corresponding $\phi_{\text{G-C}}(x)$ and S_{C}/S_0 for all cycles of anthracene. Bold lines represent edges in C, and removal of bold and dashed lines yields the graph G-C.

Label	**Cycle Diagram**	$\boldsymbol{\phi_{\text{G-C}}(x)}$	$\boldsymbol{\frac{S_{\text{C}}}{S_0}}$
C_1		$\left(x^4-2x^3-2x^2+3x+1\right)\times$ $\left(x^4+2x^3-2x^2+3x+1\right)$	1
C_2		$\left(x^4-2x^3-2x^2+3x+1\right)\times$ $\left(x^4+2x^3-2x^2+3x+1\right)$	1
C_3		$\left(x^2+x-1\right)^2\left(x^2-x-1\right)^2$	1
C_4		$\left(x^2+x-1\right)\left(x^2-x-1\right)$	2
C_5		$\left(x^2+x-1\right)\left(x^2-x-1\right)$	2
C_6		1	3

Calculation effort can be reduced by addressing the symmetry of the system, and identifying equivalent cycles. In anthracene, instead of six calculations, only four are needed as $C_1 = C_2$ and $C_4 = C_5$.

Circuit resonance energies can be calculated through application of equation (3.9) with $f_k(x)$ calculated using equations (3.10) for non-degenerate eigenvalues or (3.11) for the degenerate eigenvalues $\lambda_{\text{B}} = \sqrt{2}$ or 1. For all occupied shells, $N_k/m_k = 2$. The values of CRE_{C} are reported in Table 3.2. It should be noted that Table 3.2 identifies an apparent cycle size dependence, where larger circuits contribute smaller CRE_{C} values.

This apparent trend cannot be attributed to a direct formulation of cycle area, since equation (3.9), calculating $\mathrm{CRE_C}$, is independent of such terms.

Table 3.2: $\mathrm{CRE_C}$ values calculated for the individual cycles in anthracene, given as an analytical expression and a (rounded) numerical value. Analytical $\mathrm{CRE_C}$ expressions are split into: (left) the contributions from each orbital in order of occupation, lowest to highest; (right) a simplified compact expression.

Label	**$\mathrm{CRE_C}$**		
	Formula		**Value**
$\mathrm{C_1}$	$\left(\frac{53+38\sqrt{2}}{2128+1512\sqrt{2}} + \frac{19}{252} + \frac{-83\sqrt{2}}{392} + \frac{13}{36} + \frac{53-38\sqrt{2}}{1512\sqrt{2}-2128}\right)$	$= \left(\frac{55}{126} - \frac{12\sqrt{2}}{49}\right)$	0.0902
$\mathrm{C_3}$	$\left(\frac{153+108\sqrt{2}}{2128+1512\sqrt{2}} + \frac{-25}{252} + \frac{-113\sqrt{2}}{392} + \frac{17}{36} + \frac{153-108\sqrt{2}}{1512\sqrt{2}-2128}\right)$	$= \left(\frac{47}{126} - \frac{43\sqrt{2}}{196}\right)$	0.0628
$\mathrm{C_4}$	$\left(\frac{9+6\sqrt{2}}{2128+1512\sqrt{2}} + \frac{-5}{252} + \frac{85\sqrt{2}}{392} + \frac{-11}{36} + \frac{9-6\sqrt{2}}{1512\sqrt{2}-2128}\right)$	$= \left(\frac{25\sqrt{2}}{98} - \frac{41}{126}\right)$	0.0354
$\mathrm{C_6}$	$\left(\frac{1}{2128+1512\sqrt{2}} + \frac{-1}{252} + \frac{-57\sqrt{2}}{392} + \frac{5}{36} + \frac{1}{1512\sqrt{2}-2128}\right)$	$= \left(\frac{17}{126} - \frac{15\sqrt{2}}{196}\right)$	0.0267

Conversion of the $\mathrm{CRE_C}$ values into a cycle current, $\mathrm{J_C}$, is achieved through application of equation (3.18). These values are summarised in Table 3.3.

Table 3.3: The cycle currents, $\mathrm{J_C}$, for the unique individual cycles in anthracene calculated with values for the S_C/S_0 and $\mathrm{CRE_C}$ from Tables 3.1 and 3.2. $\mathrm{J_C}$ is reported in terms of the standard benzene value, $\mathrm{J_0}$.

Label	**$\mathrm{J_C}$**	
	Formula	**Value**
$\mathrm{J_1}$	$\left(\frac{55}{28} - \frac{54\sqrt{2}}{49}\right)$	0.4058
$\mathrm{J_3}$	$\left(\frac{47}{28} - \frac{387\sqrt{2}}{392}\right)$	0.2824
$\mathrm{J_4}$	$\left(\frac{225\sqrt{2}}{98} - \frac{41}{14}\right)$	0.3183
$\mathrm{J_6}$	$\left(\frac{51}{28} - \frac{405\sqrt{2}}{392}\right)$	0.3603

Now it is convenient to discuss the significance of the calculated values. In the Aihara formalism, the largest cyclic contributor (or contributors) to the total HL current can be identified. In the case of anthracene, these correspond to the terminal hexagon faces. Notice here the inequivalence between $\mathrm{J_1}$ and $\mathrm{J_3}$. This will be discussed further when the comparisons are made between CC and HL models. From Table 3.3, the total ring

currents in the faces are sums of contributing cyclic currents, as listed in Table 3.4.

Table 3.4: Face ring currents of anthracene, J_{Face}, found through summation of cyclic contributions as defined in Table 3.3 for the terminal and central faces of anthracene. J_{Face} is reported in terms of the standard benzene value, J_0.

Face	**Contribution**	**J_{Face}**	
		Formula	**Value**
Terminal	$J_1 + J_4 + J_6 = J_2 + J_5 + J_6$	$\left(\frac{6}{7} + \frac{9\sqrt{2}}{56}\right)$	1.0844
Central	$J_3 + J_4 + J_5 + J_6$	$\left(\frac{18\sqrt{2}}{7} - \frac{33}{14}\right)$	1.2794

Finally, Figure 3.1 displays the ring-current maps, showing the raw and scaled ring currents. These are of course identical to maps calculated through application of the other versions of HL theory.

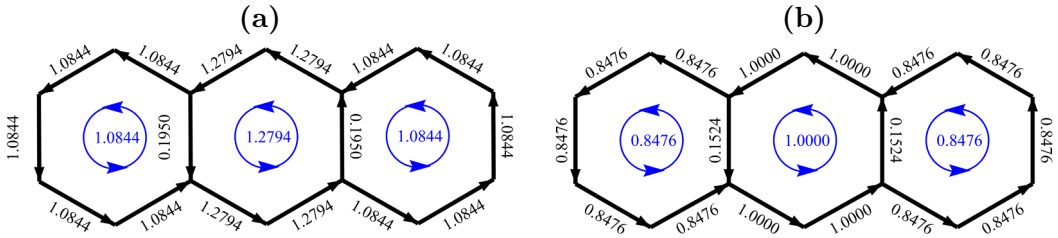


Figure 3.1: Hückel London ring-current maps for anthracene calculated using the Aihara formalism for a) raw current and b) current scaled to the largest magnitude.

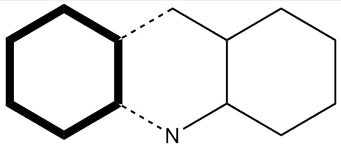
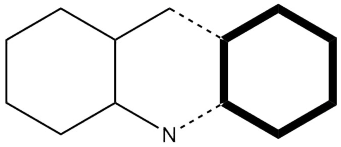
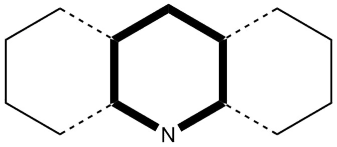
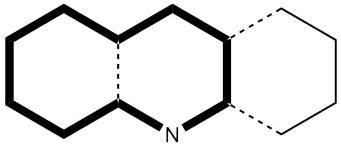
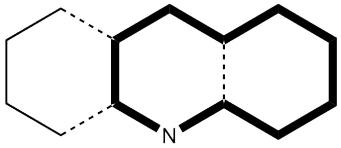
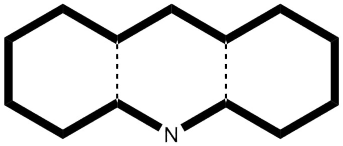
3.4.2 Acridine

Next consider heterocyclic acridine, formally derived from anthracene by a single nitrogen substitution in the central ring (see Table 3.5). Standard carbon parameters are replaced by α_N and β_{CN} representing the Coulomb integral of nitrogen and resonance integral of a carbon-nitrogen bond respectively. This essential change for a heterocyclic system leads to additional complication in the evaluation of the characteristic polynomials, with $\phi_G(x)$ becoming:

$$\begin{aligned}\phi_G(x) =&(x-2)(x+2)(x-1)^2(x+1)^2\left(x^2-2\right)\\ &\left(x^6-\alpha_N x^5-\left(2{\beta_{CN}}^2+6\right)x^4+6\alpha_N x^3+\left(8{\beta_{CN}}^2+5\right)x^2-5\alpha_N x-2{\beta_N}^2\right)\end{aligned} \tag{3.24}$$

Thus, $\phi_{\mathrm{G}}(x)$ and $\phi_{\text{G-C}}(x)$ will now be functions containing both α_{N} and β_{CN} parameters, and will no longer necessarily factor into simple polynomials. The polynomials for G−C are reported in Table 3.5.

Table 3.5: The individual circuits and the corresponding $\phi_{\text{G-C}}(x)$ in acridine. Bold edges in the cycle diagrams indicate the cycle under consideration and dashed arrows indicate the bonds removed in order to lead to the graph G-C.

Label	Cycle Diagram	$\boldsymbol{\phi_{\text{G-C}}(x)}$
C_1		$x^8 - \alpha_{\mathrm{N}}x^7 - \left(\beta_{\mathrm{CN}}{}^2 + 7\right)x^6 + 7\alpha_{\mathrm{N}}x^5 + \left(5\beta_{\mathrm{CN}}{}^2 + 13\right)x^4$ $-13\alpha_{\mathrm{N}}x^3 - \left(6\beta_{\mathrm{CN}}{}^2 + 7\right)x^2 + 7\alpha_{\mathrm{N}}x + \beta_{\mathrm{CN}}{}^2$
C_2		$x^8 - \alpha_{\mathrm{N}}x^7 - \left(\beta_{\mathrm{CN}}{}^2 + 7\right)x^6 + 7\alpha_{\mathrm{N}}x^5 + \left(5\beta_{\mathrm{CN}}{}^2 + 13\right)x^4$ $-13\alpha_{\mathrm{N}}x^3 - \left(6\beta_{\mathrm{CN}}{}^2 + 7\right)x^2 + 7\alpha_{\mathrm{N}}x + \beta_{\mathrm{CN}}{}^2$
C_3		$\left(x^2 + x - 1\right)^2\left(x^2 - x - 1\right)^2$
C_4		$\left(x^2 + x - 1\right)\left(x^2 - x - 1\right)$
C_5		$\left(x^2 + x - 1\right)\left(x^2 - x - 1\right)$
C_6		1

Now the $\mathrm{CRE_C}$ and $\mathrm{J_C}$ values can be calculated. The equations for $\phi_{\mathrm{G}}(x)$ and $\phi_{\text{G-C}}(x)$ Using numerical values[171] of $\alpha_{\mathrm{N}} = 0.51$ and $\beta_{\mathrm{CN}} = 1.02$, the characteristic polynomial equation (3.24) is solved numerically to calculate eigenvalues. Input into the Aihara equation (3.21), and accounting for orbital degeneracy at $\{\lambda_{\mathrm{B}}\}$ means values for $\mathrm{CRE_C}$

and J_C can be calculated. Noting again the symmetrical equivalence of $C_1 = C_2$ and $C_4 = C_5$, CRE_C and J_C values of the symmetry-distinct cycles are reported in Table 3.6.

Table 3.6: The symmetry-distinct CRE_C, S_C/S_0 and J_C values in acridine. Due to the inclusion of α_N and β_{CN} parameters, analytical expressions for these quantities cannot be evaluated. Values from the numerical calculations are reported to four decimal places. J_C is reported in terms of the standard benzene value, J_0.

Label	CRE_C	$\frac{S_C}{S_0}$	J_C
C_1	0.0929	1	0.4182
C_3	0.0604	1	0.2717
C_4	0.0341	2	0.3066
C_6	0.0258	3	0.3486

Again the face current maps can be constructed, and are given in Figure 3.2. Therefore, the overall effect of heteroatom inclusion, in the case of acridine, is to reduce the intensity of all ring currents. From both *ab initio* and scaled HL current maps, the current of acridine is similar to anthracene.

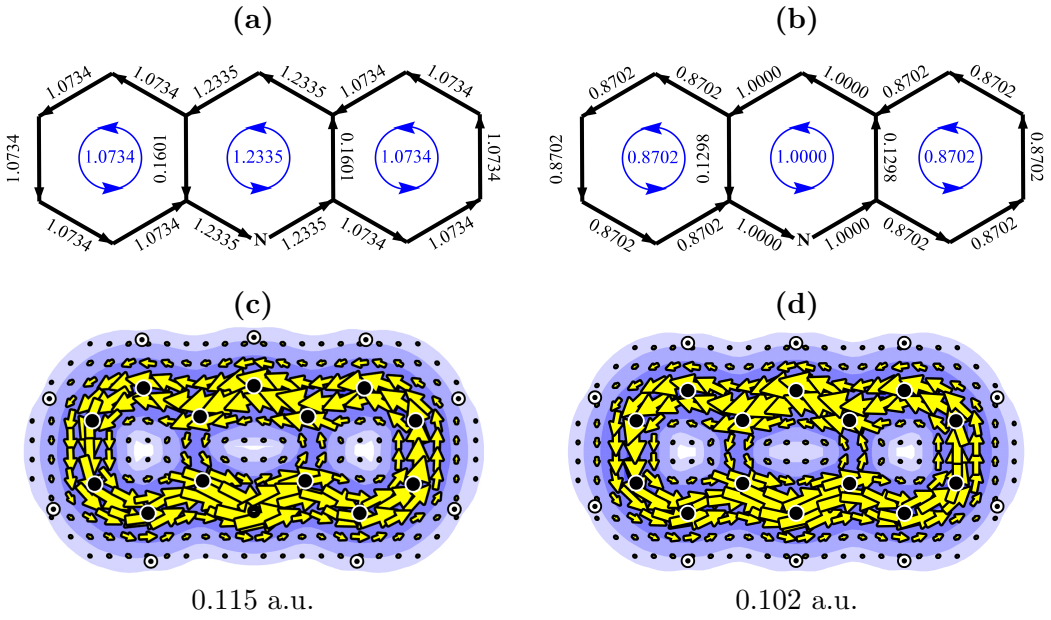


Figure 3.2: Hückel-London and *ab initio* current maps for acridine. (a) the raw HL current; (b) the HL current scaled to the largest magnitude on the graph; (c) the current-density map for acridine and (d) the comparative current-density map for anthracene with j_{max} values listed below the two *ab initio* maps.

3.5 Consequences of the Aihara Formulation

The Aihara formalism leads to some chemically significant results based on orbital occupancy. Bipartite graphs obey the Pairing theorem.[172,173] For eigenvalues listed in decreasing order, the theorem shows that:

$$\lambda_i = -\lambda_{n-i+1} \tag{3.25}$$

where n is the order of the graph. A consequence of equation (3.25) is that every bipartite graph has equal numbers of bonding and antibonding levels, and the number of zero eigenvalues (the nullity of the graph, η) has the same parity as n. Contributions of occupied orbitals to the HL current are governed by theorem 3.5.1.

Theorem 3.5.1 *The contribution per electron to the Hückel-London current from an occupied orbital with eigenvalue λ_i in a bipartite graph, is of equal magnitude and opposite sign to the contribution per electron from an orbital with eigenvalue λ_{n-i+1}.*

Hence, removal of an electron from an orbital with λ_i has the same effect on the HL current map as addition of an electron to an orbital with λ_{n-i+1}.

For any shell multiplicity, the HL current contribution from a given eigenvalue can be represented by modification of the general equation (3.22). Reversing the order of summation of the Aihara formalism from a sum over occupied eigenvalues to a sum over cycles which contribute to a face, the contribution to a given face current from a single eigenvalue λ_k is represented by:

$$\frac{\mathrm{J_{Face}}(\lambda_k)}{\mathrm{J}_0} \propto \sum_{\mathrm{C}}^{\mathrm{Face}} \frac{S_{\mathrm{C}}}{S_0} \frac{1}{(m_k-1)!} \left\{ \frac{d^{m_k-1}}{dx^{m_k-1}} \frac{\phi_{\text{G-C}}(x)}{U_k(x)} \right\}_{x=\lambda_k} \tag{3.26}$$

From the pairing theorem, the eigenvalues of the graph are related by equation (3.25), thus, for theorem 3.5.1 to be true:

$$\mathrm{J_{Face}}(\lambda_k) = -\mathrm{J_{Face}}(\lambda_{n-k+1}) \tag{3.27}$$

To show that equation (3.27) is true, it is sufficient to show that:

$$\left\{ \frac{d^{m_k-1}}{dx^{m_k-1}} \frac{\phi_{\text{G-C}}(x)}{U_k(x)} \right\}_{x=\lambda_k} = -\left\{ \frac{d^{m_k-1}}{dx^{m_k-1}} \frac{\phi_{\text{G-C}}(x)}{U_{n-k+1}(x)} \right\}_{x=\lambda_{n-k+1}} \tag{3.28}$$

Equation (3.28) will therefore be true if and only if the fractional expressions of polynomial numerators and denominators is of odd order in x. $\phi_{\text{G-C}}(x)$ and $U_k(x)$ both have well-defined parities in x, and hence so does the fraction $\phi_{\text{G-C}}(x)/U_k(x)$. By an extension of the pairing theorem, the multiplicity of the shell with eigenvalue λ_k will be equal to the multiplicity of the shell with eigenvalue λ_{n-k+1}. Therefore, the parities of the terms on both sides of equation (3.28) will be identical. Each differentiation of any function of a fixed parity reverses that parity. Taking all the possible parities, it is seen that the $(m_k - 1)^{\text{th}}$ derivative is always odd in x.

Table 3.7: The parities of all functions appearing in equation (3.28).

N	m_k	ϕ_{G}	$\phi_{\text{G-C}}$	U_k	$\frac{\phi_{\text{G-C}}}{U_k}$	Number of Differentiations	Differentiated Function
Even	odd	even	even	odd	odd	even	odd
	even	even	even	even	even	odd	odd
Odd	odd	odd	odd	even	odd	even	odd
	even	odd	odd	odd	even	odd	odd

As seen by Table 3.7 the order of the resultant differentiated function in all cases is odd. Hence, equation (3.27) is true and the theorem is proved.

Two specific cases follow immediately from theorem 3.5.1:

Lemma 3.5.1.1 *Electrons in non-bonding orbitals of a bipartite graph G make no contribution to the Hückel-London current map.*

Lemma 3.5.1.2 *The Hückel-London current maps for the +q cation and -q anion of a bipartite graph G are identical.*

To illustrate the case in lemma 3.5.1.2, take the chemically relevant removal of electrons from the HOMO level and electron insertion into the LUMO level. From the general Aihara formalism (equation (3.21)), the cycle current contribution can be separated into each individual eigenvalue.[174]

$$\frac{\text{J}_{\text{C}}}{\text{J}_0} \propto \left(\frac{\phi_{\text{G-C}}(x)}{{\phi_{\text{G}}}'(x)}\right)_{x=\lambda_1} + \left(\frac{\phi_{\text{G-C}}(x)}{{\phi_{\text{G}}}'(x)}\right)_{x=\lambda_2} + \left(\frac{\phi_{\text{G-C}}(x)}{{\phi_{\text{G}}}'(x)}\right)_{x=\lambda_3} + \dots$$

Three ring-current equations for the contribution for cycle C can then be constructed for the cationic, neutral and anionic systems.

$$\mathrm{J_C(cationic)} \propto \left(\sum_i^{\mathrm{N}-1} \left(\frac{\phi_{\text{G-C}}(x)}{\phi_{\mathrm{G}}{}'(x)} \right)_{x=\lambda_i} \right)$$

$$\mathrm{J_C(neutral)} \propto \left(\sum_i^{\mathrm{N}-1} \left(\frac{\phi_{\text{G-C}}(x)}{\phi_{\mathrm{G}}{}'(x)} \right)_{x=\lambda_i} \right) + \left(\frac{\phi_{\text{G-C}}(x)}{\phi_{\mathrm{G}}{}'(x)} \right)_{x=\lambda_j}$$

$$\mathrm{J_C(anionic)} \propto \left(\sum_i^{\mathrm{N}-1} \left(\frac{\phi_{\text{G-C}}(x)}{\phi_{\mathrm{G}}{}'(x)} \right)_{x=\lambda_i} \right) + \left(\frac{\phi_{\text{G-C}}(x)}{\phi_{\mathrm{G}}{}'(x)} \right)_{x=\lambda_j} + \left(\frac{\phi_{\text{G-C}}(x)}{\phi_{\mathrm{G}}{}'(x)} \right)_{x=\lambda_{j+1}}$$

where λ_j and λ_{j+1} refer to the HOMO and LUMO eigenvalues of the neutral system, respectively. By theorem 3.5.1,

$$\left(\frac{\phi_{\text{G-C}}(x)}{\phi_{\mathrm{G}}{}'(x)} \right)_{x=\lambda_j} = - \left(\frac{\phi_{\text{G-C}}(x)}{\phi_{\mathrm{G}}{}'(x)} \right)_{\lambda_{j+1}}$$

because $\lambda_j = -\lambda_{j+1}$, and thus, $\mathrm{J_C(cationic)} = \mathrm{J_C(anionic)}$. This extends to other orbital occupancies and arbitrary multiplicity.

However, it should be noted that theorem 3.5.1 and lemmas 3.5.1.1 and 3.5.1.2, are derived specifically for *bipartite* graphs and are typically not true for non-bipartite graphs. For example, the non-bonding orbital in pentalene dianion has a significant contribution to the overall HL map, contradicting lemma 3.5.1.1.

3.6 Comparison with CC models

Analogies can be drawn between the Aihara variant of Hückel-London theory and the three main Conjugated-Circuit models for ring-currents. This section will compare the cyclic contributions to the total ring-current map for anthracene and then discuss other examples where HL theory is apparently superior. For anthracene, and all other linear chain of benzenoids, all Aihara cycles are conjugated-circuits. Therefore, like-for-like comparison between the Aihara HL model and CC models identifies where improvements to the latter are necessary.

Scaled current maps depicting the current in anthracene from the Aihara, Randić, Ciesielski et al., and Mandado models are shown in Figure 3.3. The total current can be partitioned into cyclic contributions, which are shown in Table 3.8.

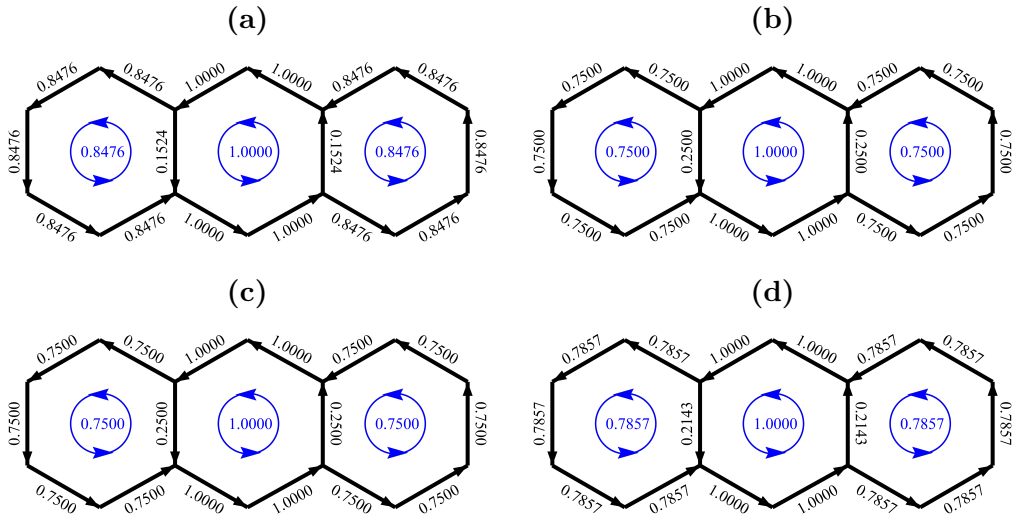


Figure 3.3: The ring-current maps scaled to the largest current magnitude calculated using (a) the Aihara Hückel-London model and the three main conjugated-circuit models, (b) the Randić model; (c) the Ciesielski et al. model; and (d) the Mandado model.

Table 3.8: The individual cycles in anthracene and the corresponding contributions to a total ring-current from the Aihara HL model and the CC models. Bracketed ring currents reported below the raw current are scaled to the largest total magnitude of the specific current model. Cycle labels are identical to the notation in Table 3.1.

Label	HL	Conjugated-Circuit Models		
	Aihara	Randić	Ciesielski et al.	Mandado
$\mathbf{C_1}$	0.4058	2	1	0.5
	(0.3172)	(0.25)	(0.125)	(0.5)
$\mathbf{C_2}$	0.4058	2	1	0.5
	(0.3172)	(0.25)	(0.125)	(0.5)
$\mathbf{C_3}$	0.2824	2	1	0.5
	(0.2207)	(0.25)	(0.125)	(0.5)
$\mathbf{C_4}$	0.3183	2	2	0.25
	(0.2488)	(0.25)	(0.25)	(0.25)
$\mathbf{C_5}$	0.3183	2	2	0.25
	(0.2488)	(0.25)	(0.25)	(0.25)
$\mathbf{C_6}$	0.3603	2	3	0.1667
	(0.2816)	(0.25)	(0.375)	(0.1667)

It is immediately clear where some of the problems with the CC models lie. Compare the individual hexagon faces, C_1 to C_3. As expected C_1 is equivalent in all models to C_2. In the CC models, $C_1 = C_2 = C_3$. However, in the Aihara model, the central cycle C_3 is not equivalent to C_1, again this could be expected from the different environments in the system. Also of note is the overall weak dependence on cycle area in the Aihara model. Both the largest and smallest contributors to the current are cycles with the smallest area. This is clearly at variance with the trends in the models by Mandado and Ciesielski et al.

Considering the overall current maps, all models are qualitatively similar. The major feature being the larger magnitude of current in the central ring compared to the terminal rings. The current-density map calculated using the *ab initio ipsocentric* approach also shows this feature (see Figure 3.2).

Anthracene and other linear benzenoids are a set of systems where current maps are qualitatively similar between HL and CC models. This is in part due to the fact that all

Aihara cycles are also conjugated circuits. However, there exist a whole host of other systems for which there are more severe discrepancies between the two models. One such example is perylene, see Figure 3.4, where the conjugated-circuit model gives an exaggerated depiction of the current modulus: current in the central ring is completely absent, whereas both HL and *ab initio* maps indicate some current in that region. Improvement of the CC models will be a recurring theme in upcoming chapters, which discuss CC/ HL comparisons further.

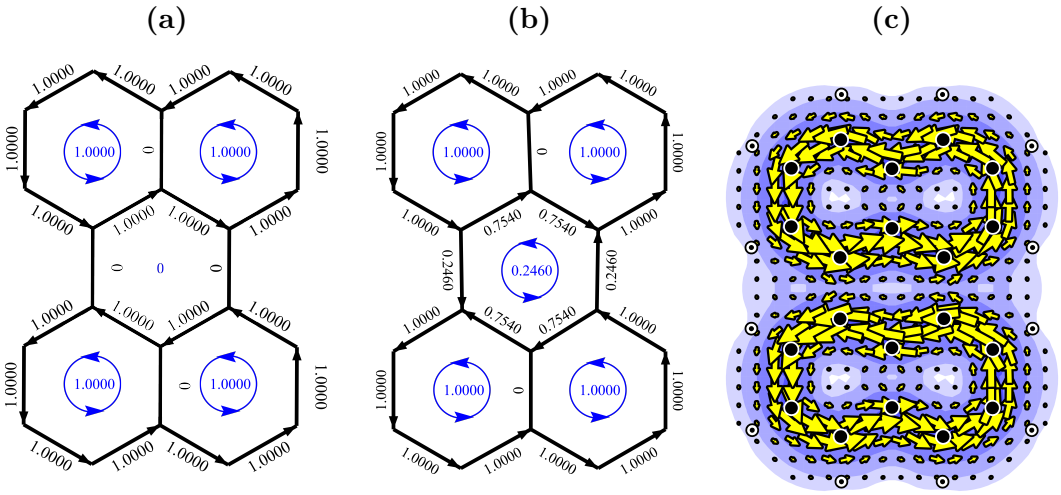


Figure 3.4: Scaled ring-current maps for perylene for (a) the Randić model and (b) the Aihara formalism, with current magnitudes scaled to the largest magnitude. (c) the *ipsocentric* model current-density map, $j_{\max} = 0.090$ a.u.

3.7 Conclusion

The Aihara formalism gives the possibility of reducing a Hückel-London calculation to a summation of cyclic contributions, and in so doing, invites comparison with the conjugated-circuit models and a way of assessing their internal approximations. Through manipulation of characteristic polynomials, the Aihara method offers the partitioning of current into either individual eigenvalue or cycle contributions, and can be interpreted as either a local and global dissection of the HL current. Furthermore, the Aihara method makes it possible to obtain fully analytical solutions for the Hückel-London current. This feature will be explored further in the next chapter discussing trends in heterocyclic systems.

When compared with the published conjugated-circuit models, the Aihara Hückel-London model identifies situations where the CC models systematically fail. In the example of anthracene, the Randić model does not distinguish between the contributions of different cycles. Despite the inability to distinguish local currents to the level of HL theory, CC models lead to a qualitative representation of the HL current maps. In contrast, the example of perylene identifies a profound difference between the two methods, rationalised by the lack of any conjugated circuits containing the central ring. Although in this particular case, one can argue that the *ab initio* model indicates a pattern of ring-currents closer to the CC model. However, the systematic absence of current results in wildly different current maps later in the benzenoid series, as shall be seen in Chapter 6.

Chapter 4

Analytical Expressions for the Hückel-London Ring Current[1]

4.1 Introduction

It is possible, in classical Hückel theory, to construct a graph theoretical model to predict the ring current of a general mono- or bi-vertex-altered heterocycle. These systems are based on an [N]annulene, where one or two CH vertices are replaced by X, a generalised heteroatom. This chapter is concerned with predicting the aromaticity of heterocycles, with ring-currents calculated using the Hückel-London model.

There exist a multitude of publications by many different authors who have investigated the aromaticity of polycyclic and mono-cyclic heterocycles using models based on various aromaticity criteria. To highlight just a few, there exist models based on the structural criteria, such as HOMA[175] for Heterocyclic Electron Delocalisation;[176] those based on resonance energy, including work by Aihara describing Magnetic Resonance Energy[24] and his early efforts on devising a unified Hückel-London model using Sachs graphs of heterocycles;[162] Topological Resonance Energy;[23] the unified aromaticity index proposed by Bird;[177] and finally those models based on the magnetic criteria such as maps of *ipsocentric* ring currents[25] and maps of Hückel-London ring currents in boron clusters.[178] Perhaps one of the most notorious heterocycles is borazine where models disagree on whether this system is aromatic[26] or non-aromatic,[135,179] a confusion that highlights the care that must be taken when considering heterocycles.

For the systems most relevant to those discussed in the present chapter, there are several publications addressing the aromaticity of mono-cyclic heterocycles. The

[1]Prof. Leonardus Jenneskens is thanked for his contribution to discussions and input for this chapter, part of which forms the basis of an upcoming paper, Bean D., Clarke J., Havenith R., Jenneskens L., Lillington M., Rogowska A., and Fowler. P.W., *In Preparation.*

most notable of these is by Schleyer *et al.* comparing ASE[17,44,103] with NICS(0) for the 5-membered heterocycles.[66,180] This was later extended to include 6-membered heterocycles.[181] The presence and sense of magnetic-field-induced ring-currents, has also been discussed by Aihara.[166]

The approach to ring-current calculations here takes a more general approach where instead of numerical parameterisation, the modelling of a heteroatom uses undefined parameters. To achieve this, the parameter η represents the electronegativity of the heteroatom as a vertex weight, and hence alters the characteristic polynomial of a graph,

$$\phi_{\mathrm{G}}(x) = \det\left|E\mathbf{1_N} - \mathbf{H}\right|, \tag{4.1}$$

where: E is the eigenvalue of the graph; $\mathbf{1_N}$ is the N×N identity matrix; and $\mathbf{H}$ is the Hamiltonian matrix, containing elements altered when a CH unit is replaced with X. The effect is to change α_{C} to $\alpha_{\mathrm{C}} + \eta\beta_{\mathrm{CC}}$, where α_{C} and β_{CC} are the carbon Coulomb and bond resonance integrals respectively, and η is an electronegativity parameter, positive for X more electronegative than carbon. In principle, heteroatomic substitution will alter the C-X bond strength too, and hence β_{CX}, but, this effect is neglected in the first approximation by taking $\beta_{\mathrm{CX}} = \beta_{\mathrm{CC}} = \beta$.

Orbital energies are obtained from the roots of the characteristic equation $\phi_{\mathrm{G}}(x) = 0$. In a system where, by convention $\alpha_{\mathrm{C}} = 0$ and $\beta_{\mathrm{C_1C_2}} = 1$ if $\mathrm{C_1}$ and $\mathrm{C_2}$ share an edge, otherwise $\beta_{\mathrm{C_1C_2}} = 0$, E becomes $(E - \alpha)/\beta = x$ and so $\phi_{\mathrm{G}}(x, \eta)$, the characteristic polynomial as a function of x and η is:

$$\phi_{\mathrm{G}}(x,\eta) = \det\left|x\mathbf{1_N} - \mathbf{H}\right| = \begin{vmatrix} x-\eta & -1 & 0 & \cdots & -1 \\ -1 & x & -1 & \cdots & 0 \\ 0 & -1 & x & \cdots & 0 \\ \vdots & \vdots & \vdots & \ddots & \vdots \\ -1 & \cdots & 0 & -1 & x \end{vmatrix} \tag{4.2}$$

The ring-current behaviour and orbital spectra, for both mono- and bi-vertex-altered mono-heterocycles, are discussed using this simplified η-altered model. The two types of alteration will be considered independently.

4.2 Mono-Vertex-Altered Mono-Heterocycles

First, consider a mono-vertex η-altered heterocycle. The characteristic polynomial for the general $C_{N\text{-}1}H_{N\text{-}1}X$ system, $\phi_G(x,\eta)$, can be summarised as:[161]

$$\phi_G(x,\eta) = \phi_{C_N}(x) - \eta\phi_{P_{N-1}}(x) \tag{4.3}$$

where $\phi_{C_N}(x)$ is the characteristic polynomial of the N-sized cycle; $\phi_{P_{N-1}}(x)$ is the characteristic polynomial of the path on N−1 vertices. Both characteristic polynomials can be calculated using the adjacency matrices of the path and cycle via the expansion of (4.2)

$$\det|x\mathbf{1_N} - \mathbf{H}| = \det|x\mathbf{1_N} - \mathbf{A_{C_N}}| - \eta\det|x\mathbf{1_N} - \mathbf{A_{P_{N\text{-}1}}}|, \tag{4.4}$$

where $\mathbf{A_{C_N}}$ and $\mathbf{A_{P_{N\text{-}1}}}$ are the adjacency matrices of the cycle and path respectively. Explicitly for N=6, the characteristic polynomial for N=6 mono-vertex altered heterocycle is:

$$\begin{aligned}\det|x\mathbf{1_6} - \mathbf{H}| &= \begin{vmatrix} x & -1 & 0 & 0 & 0 & -1 \\ -1 & x & -1 & 0 & 0 & 0 \\ 0 & -1 & x & -1 & 0 & 0 \\ 0 & 0 & -1 & x & -1 & 0 \\ 0 & 0 & 0 & -1 & x & -1 \\ -1 & 0 & 0 & 0 & -1 & x \end{vmatrix} - \eta \begin{vmatrix} x & -1 & 0 & 0 & 0 \\ -1 & x & -1 & 0 & 0 \\ 0 & -1 & x & -1 & 0 \\ 0 & 0 & -1 & x & -1 \\ 0 & 0 & 0 & -1 & x \end{vmatrix} \\ &= \left(x^6 - 6x^4 + 9x^2 - 4\right) - \eta\left(x^5 - 4x^3 + 3x\right) \\ &= \left(x^2 - 1\right)\left(x^4 - x^3\eta - 5x^2 + 3x\eta + 4\right).\end{aligned} \tag{4.5}$$

The orbital energies of this system are found by setting equation (4.5) equal to 0. It turns out the roots fall into two categories: those dependent on η and those that are not. This observation can be rationalised through symmetry arguments. In a system with $\eta = 0$ the maximum symmetry of the C_NH_N cycle is D_{Nh}. In the system with $\eta \neq 0$ this is reduced to C_{2v}, which implies a factorisation into two functions that are symmetric and antisymmetric under reflection in the mirror plane perpendicular to the molecular plane.

Functions of each type can be isolated within the characteristic polynomial, defined as ϕ^a and ϕ^s for the antisymmetric and the symmetric components, respectively. Using

this notation equation (4.3) can expanded as

$$\phi_{\mathrm{G}}(x,\eta) = \phi_{\mathrm{C_N}}(x)^a \; \phi_{\mathrm{C_N}}(x)^s - \eta \, \phi_{\mathrm{P_{N-1}}}(x)^a \; \phi_{\mathrm{P_{N-1}}}(x)^s \tag{4.6}$$

The antisymmetric roots of the path and cycle are identical. Thus equation (4.6) can be further simplified

$$\phi_{\mathrm{G}}(x,\eta) = \phi_{\mathrm{C_N}}(x)^a \left[\phi_{\mathrm{C_N}}(x)^s - \eta \, \phi_{\mathrm{P_{N-1}}}(x)^s\right] \tag{4.7}$$

and hence

$$\begin{aligned} \phi_{\mathrm{G}}(x,\eta)^a &= \phi_{\mathrm{C_N}}(x)^a \\ \phi_{\mathrm{G}}(x,\eta)^s &= \phi_{\mathrm{C_N}}(x)^s - \eta \, \phi_{\mathrm{P_{N-1}}}(x)^s \end{aligned} \tag{4.8}$$

The orders of the polynomials with respect to x can be summarised as:

Table 4.1: The order of the components of the general characteristic polynomial of a mono-vertex-altered monocycle. In this notation symmetric and antisymmetric components are labelled according to the reflection in the mirror plane perpendicular to the molecular plane in the reduced $\mathrm{C_{2v}}$ point group.

	Symmetric	**Antisymmetric**
N= $2p+1$	$p+1$	p
N= $2p$	$p+1$	$p-1$

These symmetry arguments will be important later when the orbital spectrum is discussed and orbital energies evaluated.

4.2.1 The Orbital Energies

Before the eigenvalue spectrum is considered in detail and the limiting cases discussed, it is useful to recall some results from linear algebra. Gerschgorin's theorem states:[182,183] (see also the textbooks [184,185])

> *"Let λ be an eigenvalue of an arbitrary $N \times N$ matrix $\boldsymbol{A} = [a_{jk}]$. Then for some integer j $(1 \leq j \leq N)$ we have:*
> $|a_{jj} - \lambda| \leq |a_{j1}| + |a_{j2}| + \cdots + |a_{jj-1}| + |a_{jj+1}| + \cdots + |a_{jN}|$"

In the present cases, this theorem defines the location of the eigenvalues of the graph. All eigenvalues lie in unit *Gerschgorin discs* located in the complex plane centred on

points on the real axis, with the whole spectrum, $\{\lambda_i\}$, found in the union of all such discs. As the matrix is Hermitian, all eigenvalues are real and hence are found on the real axis. The radius of each disc is the sum of all elements of the corresponding row in matrix **A**, except for the diagonal element which denotes the origin of the disc and the eigenvalue. A useful extension of this theorem states:[184]

> *"If p Gerschgorin discs form a set S that is disjoint from the N − p other discs of a given matrix **A**, then S contains precisely p eigenvalues of **A** (counted with their degeneracy)."*

Applied to the mono-η-altered systems, N-1 of the discs are identical, all centred on the origin with radii of 2β. The final disc is centred on η, and at a critical value of $|\eta| > 4\beta$ separates from the other, with the η-centred disc carrying a single eigenvalue along with it (as implied by the extension to Gerschgorin's theorem). The superposition of N-1 origin-centred Gerschgorin discs correspond to the spectral range circle used in the Frost-Musulin construction[186] and always contains at least N-1 roots of the characteristic polynomial. Using N=6 as an example, the Gerschgorin theorem and its extension are illustrated in Figure 4.1.

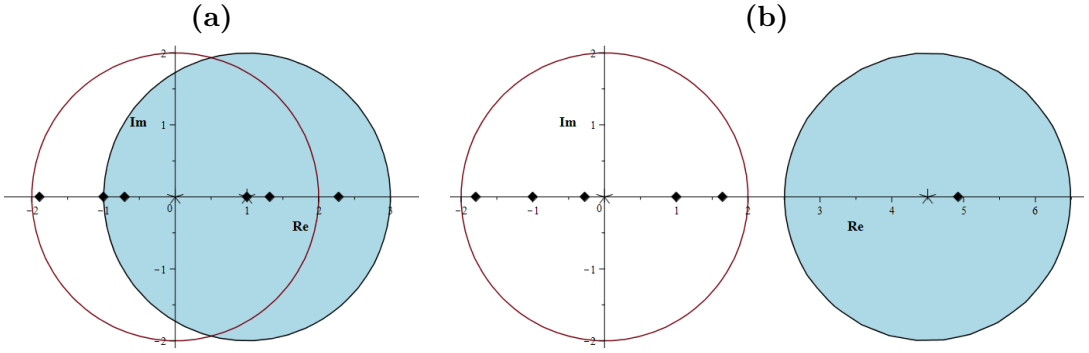


Figure 4.1: Illustrations of the Gerschgorin theorem and its extension in the case of N=6. A Gerschgorin disc centred on the origin is generated for each row of the adjacency matrix $\mathbf{A_N}$. Five of the Gerschgorin discs are superimposed on the origin (unfilled circle), with one (blue circle) centred on the point $(\eta, 0)$. Asterisks denote the origin of the discs and diamonds denote eigenvalues, note all eigenvalues are along the real axis. The two graphs show the changes in η: (a) $\eta = 1\beta$ the discs overlap, (b) $\eta = 4.5\beta$ the two discs separate and one eigenvalue is separated from the five others.

Using the Gerschgorin theorem, two limiting cases can be identified for which roots of the characteristic polynomial have an easy form: $\eta = 0$ and $|\eta| = \infty$. When $\eta = 0$, the solutions are those for the unmodified [N]annulene, for which $\phi_{\mathrm{G}}(x, 0) = \phi_{\mathrm{C_N}}(x)$, and can be expressed as a Chebyshev polynomial of the first kind:[161]

$$\phi_{\mathrm{C_N}}(x) = 2\mathrm{T_N}\left(\frac{x}{2}\right) - 2, \tag{4.9}$$

where $\mathrm{T_N}(x) = \cos\left[\mathrm{N}\arccos x\right]$. The roots of $\phi_{\mathrm{G}}(x, 0)$ are

$$\lambda_{\mathrm{G}} = \lambda_{\mathrm{C_N}} = 2\cos\left(\frac{2\pi k}{\mathrm{N}}\right) \text{ for } k = 0, \ldots, \mathrm{N}-1 \text{ and } E = \alpha + \lambda\beta \tag{4.10}$$

At $|\eta| = \infty$ the X centre is effectively decoupled from the remainder of the ring by electron localisation on centre X ($\eta = +\infty$), or on the carbon framework ($\eta = -\infty$). Therefore the solutions are those for a single isolated vertex and the path on N-1 vertices, the characteristic polynomial of which can be expressed as a Chebyshev polynomial of the second kind:[161]

$$\phi_{\mathrm{P_{N\text{-}1}}}(x) = 2\mathrm{U_N}\left(\frac{x}{2}\right), \tag{4.11}$$

where $\mathrm{U_N}(x) = \left(1 - x^2\right)^{-1/2} \sin\left[(\mathrm{N}+1)\arccos x\right]$. The roots of $\phi_{\mathrm{G}}(x, \infty)$ are,

$$\begin{aligned} &\lambda_{\mathrm{X}} = \eta && \text{for } k = 0 && \text{and } E = \alpha + \lambda\beta \\ &\lambda_{\mathrm{P_{N\text{-}1}}} = 2\cos\left(\frac{\pi k}{\mathrm{N}}\right) && \text{for } k = 1, \ldots, \mathrm{N}-1 && \text{and } E = \alpha + \lambda\beta \end{aligned} \tag{4.12}$$

Depending on the sign of η, the lowest occupied (positive η) or highest unoccupied (negative η) molecular orbital will localise fully on X at the infinite limit. Graphically these limits can be depicted on a modified Frost-Musulin diagram (Figure 4.2), where N-1 roots travel on the circle with the final root travelling towards infinity. Using the two defined limits as the start and end positions, the intermediate region where $0 < |\eta| < \infty$ can be defined knowing the direction of travel for each eigenvalue.

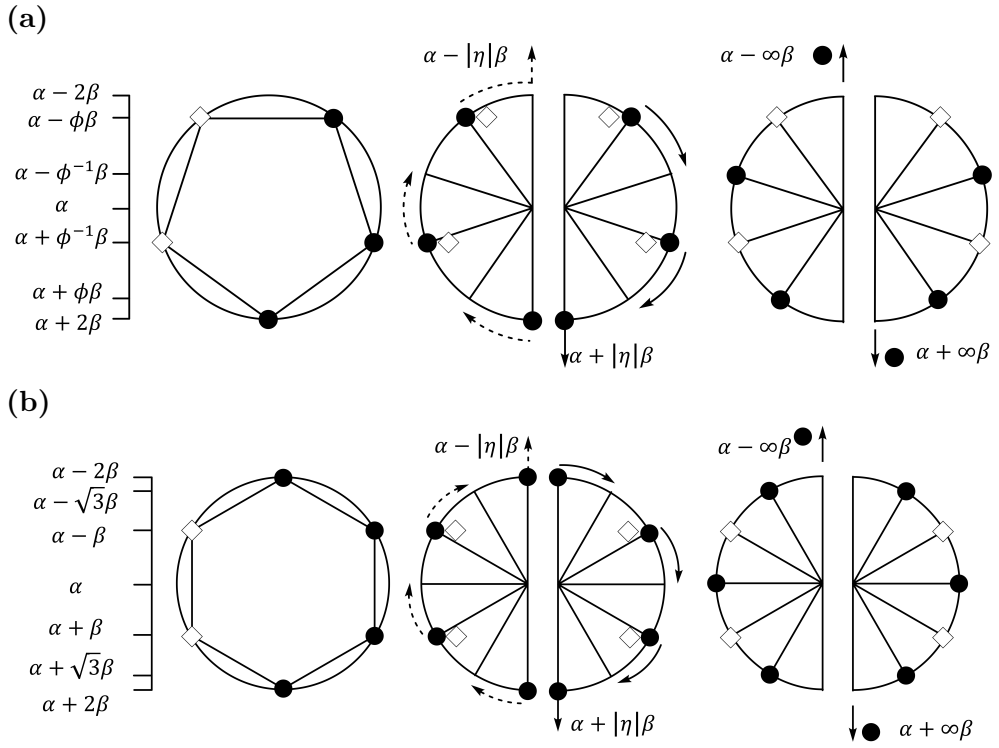


Figure 4.2: Mathematical constructions for the Hückel orbital energy spectrum for the $C_{N-1}H_{N-1}X$ mono-heterocycle with (a) N=5 and (b) N=6, for the [N]annulene (left), the [N]heterocycle with an arbitrary η value (middle), and the [N-1]polyene limit (right). For the heterocycle in the middle diagram, the annulene and polyene Frost-Musulin constructions are combined, to indicate the starting and final positions of the energies as $|\eta|$ sweeps from 0 to ∞. Left and right semicircles denote $\eta < 0$ and $\eta > 0$ respectively. White-filled diamonds denote orbital energies independent of η, black-filled circles denote those orbital energies dependent on η. Full arrows show the variation in energies as η runs through positive values from 0 to ∞, and dashed arrows show the variation in energies as η runs through negative values from 0 to $-\infty$. The quantities $\phi \approx 1.618$ and $\phi^{-1} \approx 0.618$ are the golden ration and its reciprocal, respectively.

As seen in Figure 4.2, the heterocycle Frost-Musulin construction is the combination of both the annulene and path diagrams. For N=5 and N=6, the constructions have a straightforward chemical interpretation. In the limit of large positive η, the π system of the mono-heterocycle can be described as a superposition of a π electron pair localised on atom X and a 4π electron C_4H_4 (N=5) or $C_5H_5^+$ (N=6) polyene-like fragment. Conversely, at the negative η limit, the π system can be described as a 6π electron $C_4H_4^{2-}$ or $C_5H_5^-$ polyene-like fragment.

Some energy levels are fixed at positions derived from the cycle (white-filled diamonds). These correspond to the solutions of $\phi_G(x, \eta)^a$ resulting from the reduction in symmetry to

C_{2v} as derived from equation (4.8), and are not sensitive to the weight on the heteroatom as they are antisymmetric. The solutions for these orbitals are simple to quantify, and form a subset of solutions derived in equation (4.7):

$$\begin{aligned} {\lambda_{\mathrm{G}}}^{a} = {\lambda_{\mathrm{C_N}}}^{a} = 2\cos\left(\frac{2\pi k}{\mathrm{N}}\right) \quad & k = 1, \ldots, p \qquad \text{for N } = 2p+1 \\ & k = 1, \ldots, p-1 \quad \text{for N } = 2p \end{aligned} \tag{4.13}$$

Black-filled circles denote orbital energies that move as a function of η, ultimately ending up at positions of an [N-1]polyene path with an isolated vertex. Behaviour of orbital energies in the intermediate region are difficult to evaluate analytically when energies are the roots of cubic or higher order equations (when N > 3, see Table 4.1), but can easily be seen from a plot of numerical solutions.

Those orbitals symmetric in the mirror plane can be separated into two cases. The energy of the orbital that localises on X is isolated within its own Gerschgorin disc and converges rapidly to $\alpha + \eta\beta$; from below for negative η and above for positive η. The remaining orbitals change slowly with η, as each orbital energy moves through an angle of $2\pi/\mathrm{N}$ on the Frost-Musulin diagram (see Figure 4.2). Variation of these orbitals with η is shown graphically in Figure 4.3.

For even N, the energy level diagrams for positive and negative η are related by inversion through the origin (E= α and $\eta = 0$). The $\eta \leftrightarrow -\eta$ inversion also applies to the two halves of the respective Frost-Musulin construction (Figure 4.2). For odd N, this inversion symmetry is attained only at the infinite limit. However, a range of $-3 \leq \eta \leq 3$ is more than sufficient to cover the chemically realisable X groups.

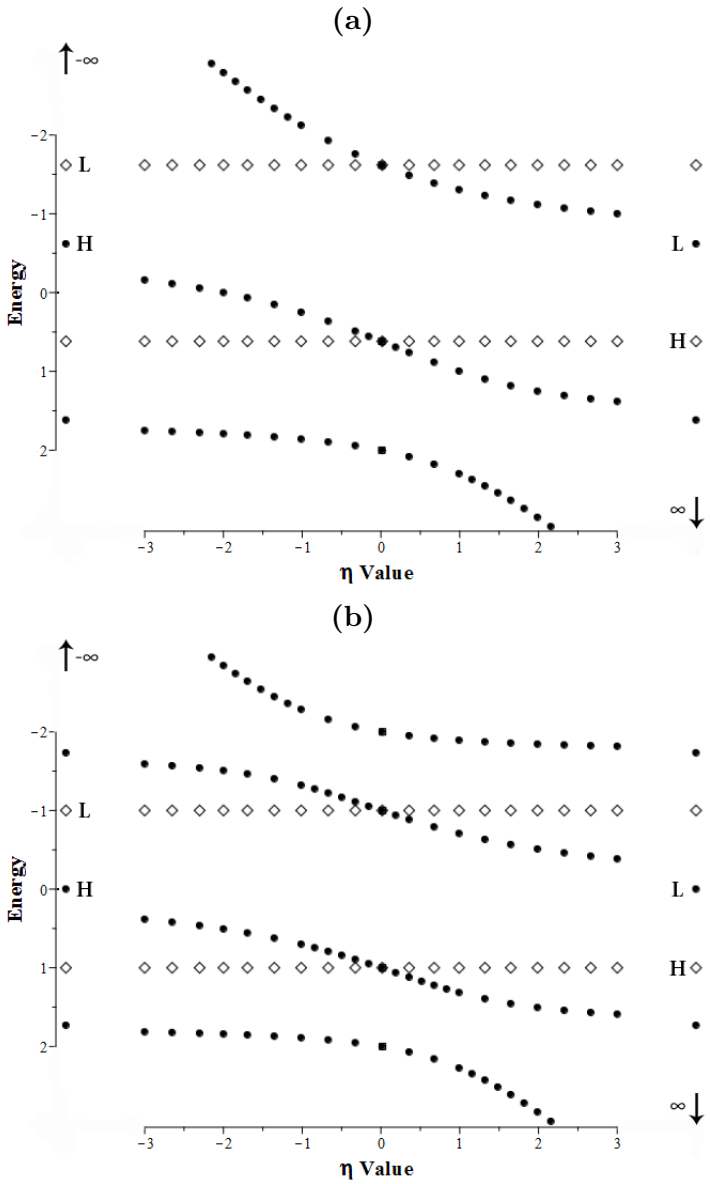


Figure 4.3: The variation of the π-orbital energies, in units of β, with a chemically relevant change in η for (a) N=5 and (b) N=6. Symbolic representation of the orbitals dependence on η is identical to those in Figure 4.2. H and L labels denote the labelling of the HOMO and LUMO respectively. The solo dots, at the extremes of the diagram, show the energies calculated at the limit of $|\eta| \to \infty$. Squares at $\eta = 0$ denote orbital energies of the benzene standard.

Variation of η leads to a narrowing of the HOMO-LUMO gap in both the electropositive or electronegative directions. Either the HOMO energy level is fixed, and the LUMO energy drops (as seen for the positive η in both N=5 and N=6), or the LUMO energy is fixed and the HOMO is raised in energy (negative η). For N=5 the gap shrinks from $\sqrt{5}\beta$ to a limiting value of β for negative η and $\left(\sqrt{5}-1\right)\beta$ for positive η. For N=6 the HOMO-LUMO gap shrinks from 2β to a limiting value of β for both positive and negative η.

4.2.2 The Orbital Overlap

The behaviour of the orbital energies will have consequences for calculated ring-current based aromaticity. Through the *ipsocentric* formulation, there will be two competing effects. These arise from changes in the HOMO-LUMO gap, which shrinks as η is altered, and the changes in angular momentum parentage of the orbitals, as for $\eta \neq 0$ occupied and virtual orbitals will no longer be pure eigenfunctions of angular momentum. Both of these effects result in a cancellation of diatropic current in $4n + 2$ π-systems. The mixing will also introduce competing paratropic virtual excitations which are magnified, along with remaining diatropic currents, by a reduction in the HOMO-LUMO gap.[187] Therefore, the ring-current calculated through the *ipsocentric* approach is expected to decrease in magnitude compared to $\eta = 0$. Ring-current behaviour at the two limits is clear. At $\eta = 0$ the ring-current will be identical to the unperturbed cycle, and as $|\eta| \to \infty$ the current will tend to 0.

The overlap of orbitals can be modelled in the simplified Hückel picture. In the Hückel model, the overlap of two orbitals can be calculated from the coefficients of the vertices:

$$S_{kk'} = \sum_r c_r^k d_r^{k'} \tag{4.14}$$

where c_r^k and $d_r^{k'}$ are the coefficients of vertex r of the cycle and the composite path-with-an-isolated-vertex respectively; k and k' are eigenvectors of the cycle and the path and vertex systems respectively. Normalisation ensures that $\sum_{k'} {S_{kk'}}^2 = 1$. S^2 values are reported to map the overlap between the cycle orbitals with the path orbitals and thus

illustrate how orbital appearance changes as $|\eta|$ sweeps from 0 to ∞. The matrix of S^2 values of the cycle and path-with-an-isolated-vertex are shown in Figure 4.4 for cycle MOs calculated when $\eta = 0$, and in Figure 4.5 for cycle MOs at $|\eta| = 1$, both illustrating the examples of N=5 and N=6.

Entries where ${S_{kk'}}^2 = 1$ show the (antisymmetric) orbitals that are independent of η. For other (symmetric) orbitals the picture is more complicated. For intermediate values of η, each orbital is a mixture of all others within the same symmetry class in the reduced C_{2v} point group. At $\eta = 0$ the mixing does not give an obvious indication of the shape of the orbital at the limit of $|\eta| = \infty$. Along the pathway to $|\eta| \to \infty$, orbital overlap values will change. Within the range of chemical relevance, the changes in ${S_{kk'}}^2$ values are slow. For example, consider the LOMO of N=5 as η sweeps to $+\infty$. At $\eta = 0$ this orbital has 20% square overlap with the isolated-vertex orbital; at $\eta = 1$ the overlap has increased to 43%; and by $\eta = 2.5$ ${S_{kk'}}^2 = 76\%$. Additional values of the orbital overlap for $|\eta| = 1$ are shown in Figure 4.5. These show that as η is changed the parent orbital changes to become more like the $|\eta| = \infty$ solution.

Overall, the combination of energy and orbital-overlap factors suggest an initially rather weak variation in the induced current-density in η. Hence, over the range of 6π electron mono-heterocycles there is a tendency to *retain* magnetic aromaticity within the chemically relevant η range.

(a)

η = −∞	Negative η					η = 0	Positive η					η = ∞
∞	40	0	58	0	2	LUMO	2	0	58	0	40	LUMO
LUMO	0	100	0	0	0	LUMO	0	0	0	100	0	HUMO
HOMO -1	0	0	0	100	0	HOMO	0	100	0	0	0	HOMO
HOMO	40	0	38	0	22	HOMO	22	0	38	0	40	HOMO -1
LOMO	20	0	4	0	76	LOMO	76	0	4	0	20	-∞

(b)

η = −∞	Negative η						η = 0	Positive η						η = ∞
∞	17	77	0	5.5	0	0.4	HUMO	0.4	0	5.5	0	77	17	HUMO
LUMO	0	0	100	0	0	0	LUMO	0	0	0	100	0	0	LUMO +1
LUMO +1	33	21	0	44	0	1.5	LUMO	1.5	0	44	0	21	33	LUMO
HOMO	33	1.5	0	44	0	21	HOMO	21	0	44	0	1.5	33	HOMO -1
HOMO -1	0	0	0	0	100	0	HOMO	0	100	0	0	0	0	HOMO
LOMO	17	0.4	0	5.5	0	77	LOMO	77	0	5.5	0	0.4	17	-∞

Figure 4.4: The values of S^2 calculated from equation (4.14) and reported to the nearest percentage point for the overlap between the molecular orbitals of the parent cycle with $|\eta| = 0$ and the path-with-an-isolated-vertex for (a) N=5 and (b) N=6. The middle column shows the $\eta = 0$ orbitals, left and right of this show the matrix of S^2 values with the corresponding path orbital at the head of the column for negative and positive η changes respectively. The extreme left and right denote the nomenclature of the orbital at the infinite limit. Filled boxes indicate those path orbitals to which the cycle converges at the positive or negative infinite η.

(a)

η = −∞	Negative η					|η| = 1	Positive η					η = ∞
∞	59	0	38	0	2	LUMO	2	0	74	0	24	LUMO
LUMO	0	100	0	0	0	LUMO	0	0	0	100	0	HUMO
HOMO -1	0	0	0	100	0	HOMO	0	100	0	0	0	HOMO
HOMO	31	0	60	0	9	HOMO	48	0	18	0	33	HOMO -1
LOMO	9	0	2	0	89	LOMO	50	0	7	0	43	-∞

(b)

η = −∞	Negative η						|η| = 1	Positive η						η = ∞
∞	42	47	0	11	0	1	HUMO	0	0	3	0	90	7	HUMO
LUMO	0	0	100	0	0	0	LUMO	0	0	0	100	0	0	LUMO +1
LUMO +1	27	52	0	21	0	1	LUMO	1.4	0	66	0	8	25	LUMO
HOMO	25	1.4	0	66	0	8	HOMO	52	0	21	0	1	27	HOMO -1
HOMO -1	0	0	0	0	100	0	HOMO	0	100	0	0	0	0	HOMO
LOMO	7	0	0	3	0	90	LOMO	47	0	11	0	1	42	-∞

Figure 4.5: The values of S^2, reported to the nearest percentage point for the overlap between the molecular orbitals of the parent cycle with $|\eta| = 1$ and the path-with-an-isolated-vertex for (a) N=5 and (b) N=6. The middle column shows the $\eta = 0$ orbitals, left and right of this show the matrix of S^2 values with the corresponding path orbital at the head of the column for negative and positive η changes respectively. The extreme left and right denote the nomenclature of the orbital at the infinite limit. Filled boxes indicate those path orbitals to which the cycle converges at the positive or negative infinite η.

4.2.3 Hückel-London results

The Hückel-London currents were calculated analytically using the Aihara formalism. To re-cap, the general Aihara ring-current equation (discussed in detail in Chapter 3) is:

$$\frac{\mathrm{J_C}}{\mathrm{J_0}} = 18. \left(\prod_{\mathrm{i}=1}^{|\mathrm{C}|} \frac{\beta_\mathrm{i}}{\beta_0} \right) \left(\frac{S_\mathrm{C}}{S_0} \right) \left(\sum_{k=1}^{\mathrm{occ}} \frac{\phi_{\mathrm{G\text{-}C}}\left(\lambda_k\right)}{\phi_\mathrm{G}{}'\left(\lambda_k\right)} \right) \tag{4.15}$$

where symbols are as defined in Chapter 3. In this instance, the summation runs over λ_k representing the roots of $\phi_\mathrm{G}(x,\eta)$ running from lowest to highest occupied eigenvalue, assuming all orbital shells are fully occupied.[166] For the mono-vertex-altered graphs, the derivative $\phi_\mathrm{G}{}'(x,\eta)$ is a simple function that can be calculated directly from the differentiation of equation (4.3).

$$\begin{aligned} \phi_\mathrm{G}{}'(x,\eta) &= \phi_{\mathrm{C_N}}{}'(x) - \eta\phi_{\mathrm{P_{N\text{-}1}}}{}'(x) \\ &= \mathrm{N}\phi_{\mathrm{P_{N\text{-}1}}}(x) - \frac{\mathrm{N}\eta\left(\phi_{\mathrm{C_N}}(x)+2\right) - x\eta\phi_{\mathrm{P_{N\text{-}1}}}(x)}{(x^2-4)} \end{aligned} \tag{4.16}$$

However, for the present systems, equation (4.15) can be simplified. To the first approximation, all $\beta_\mathrm{i} = 1$. There is also only one cycle to consider, thus $\phi_{\mathrm{G\text{-}C}}(x) = 1$. Finally, assuming graph G and the benzene standard are regular polygons with the standard benzene bond length, S_C/S_0 reduces to:

$$\frac{S_\mathrm{C}}{S_0} = \frac{\mathrm{N}\sqrt{3}\cot(\pi/\mathrm{N})}{18} \tag{4.17}$$

Therefore, equation (4.15) reduces to the calculation of $\mathrm{J_G}/\mathrm{J_0}$:

$$\frac{\mathrm{J_G}}{\mathrm{J_0}}\left(\mathrm{C_N},\eta,q\pi\right) = \left(\mathrm{N}\sqrt{3}\cot(\pi/\mathrm{N})\right)\left(\sum_{k=1}^{\mathrm{occ}} \frac{1}{\phi_\mathrm{G}{}'\left(\lambda_k\right)}\right), \tag{4.18}$$

where the ring-current is expressed using the notation of $\mathrm{J_G}/\mathrm{J_0}\left(\mathrm{C_N},\eta,q\pi\right)$ to denote the current, relative to benzene, of a $\mathrm{C_N}$-based $\mathrm{C_{N\text{-}1}H_{N\text{-}1}X}$ mono-heterocycle modelled with electronegativity parameter η and a total of $q\pi$-electrons.

Numerical solutions to equation (4.18) can always be found. However, the use of the Aihara formalism implies the possibility of generating an analytical ring-current expression in terms of η. For large N and $\eta \neq 0$ this is not always possible, owing to the

difficulty of expressing eigenvalues from the symmetric component of the characteristic polynomial, $\phi_{\mathrm{G}}(x,\eta)^s$. Furthermore, this component soon becomes impossible to evaluate fully, because of the increasing order of the equation, (see Table 4.1). Note, in the case where $\eta = 0$, orbitals become degenerate and the ring-current is calculated using continuity. Alternatively, the general Aihara formalism, modified with equation (3.11), could be used.

However, for some special values of N and η the ring current can be expressed in a compact analytical form. For instance, a complete solution can be found for N=3 with 2 π-electrons.

$$\frac{\mathrm{J_G}}{\mathrm{J_0}}\,(\mathrm{C}_3,\eta,2\pi) = \frac{6}{\eta^2-2\eta+9+(\eta+3)\sqrt{\eta^2-2\eta+9}} \tag{4.19}$$

For larger N, closed-form expressions are only possible for $\eta = 0$, $\eta = \infty$ and special η values in between. For example, it turns out that at $\eta = 2\beta$ for N = 6, $\phi_{\mathrm{G}}(x,\eta)$ can be simplified to:

$$\begin{aligned}\phi_{\mathrm{G}}(x,2) &= x^6 - 2x^5 - 6x^4 + 8x^3 + 9x^2 - 6x - 4 \\ &= (x-1)(x+1)(x^2 - x - (3-\sqrt{5}))(x^2 - x - (3+\sqrt{5}))\end{aligned} \tag{4.20}$$

with the roots being, in order lowest occupied to highest unoccupied:

$$\frac{1+\sqrt{13+4\sqrt{5}}}{2},\ 1,\ \frac{1+\sqrt{13-4\sqrt{5}}}{2},\ \frac{1-\sqrt{13-4\sqrt{5}}}{2},\ -1,\ \frac{1-\sqrt{13+4\sqrt{5}}}{2}$$

The Hückel-London current is then evaluated from the substitution of the three occupied orbital energies into the Aihara equation (4.18), which for N=6 simplifies to $\mathrm{J} = 18/\phi'(\lambda)$. In this case the HL ring-current for $\eta = 2\beta$ (and incidentally that of $\eta = -2\beta$) is:

$$\begin{aligned}\frac{\mathrm{J_G}}{\mathrm{J_0}}\,(\mathrm{C}_6,2,6\pi) &= \frac{9}{712}\left((13+4\sqrt{5})\sqrt{13-4\sqrt{5}} + (13-4\sqrt{5})\sqrt{13+4\sqrt{5}}\right) \\ &\approx 0.799\end{aligned} \tag{4.21}$$

Further examples where factorisation can be achieved are: $\eta = 1\beta$ and -2β for N=5.

For a general η, the ring current can be represented graphically (Figure 4.6) for the general $\mathrm{C_{N\text{-}1}H_{N\text{-}1}X}$ mono-heterocycle. The magnitudes of the ring-current for N=5, 6 and 7 are all normalised to the value for $\eta = 0$. Current is maximised for $\eta = 0$, i.e. for the

all-carbon system, and falls off slowly with η.

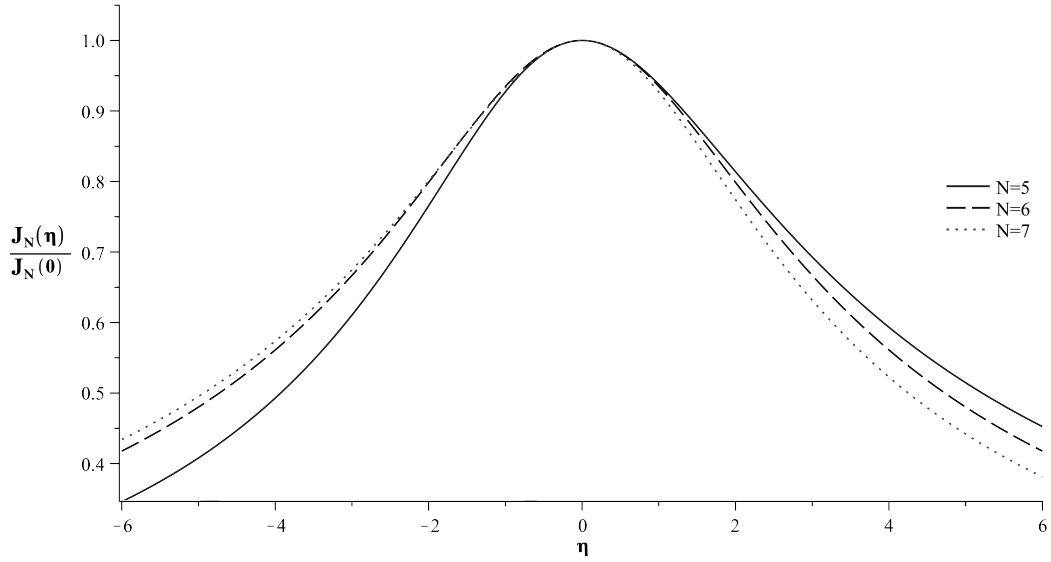


Figure 4.6: The Hückel-London ring-currents calculated for N=5, 6 and 7 for the single η-altered mono-heterocycle. Ring-currents, J have been normalised to that calculated when $\eta = 0$. Calculations assume a uniform occupancy of six π-electrons.

From Figure 4.6, it is clear that the ring-current survives largely unaltered when the perturbation caused by changes in η, is small. Experimentally, the similarity in aromaticity between benzene and other heteroatoms has been shown from NMR data,[188] although this is debated and a general trend of reduced aromaticity is commonly noted.[189] From Figure 4.6, it is clear $|\eta|$ must be changed to a large value, well beyond the chemically relevant range, to result in a significant reduction in the ring-current in this model. The η values necessary to reduce the current to 80% and 50% of $J_G/J_0\,(C_N, 0, 6\pi)$ are reported in Table 4.2.

Table 4.2: The values of positive and negative η necessary to reduce the Hückel-London current to (a) 80% and (b) 50% of $J_G/J_0\,(C_N, 0, 6\pi)$ for $N = 5, 6$ and 7. η values are reported in units of β.

(a)

	Positive η	**Negative η**
N = 5	2.11	−1.80
N = 6	1.99	−1.99
N = 7	1.84	−2.01

(b)

	Positive η	**Negative η**
N = 5	5.22	−3.93
N = 6	4.73	−4.73
N = 7	4.25	−4.91

From Table 4.2a, to reduce the HL magnitude to 80% of the J_0 current, η must be changed to approximately 2β. From numerical parameters, from Praiser-Parr-Pople calculations, proposed by Van Catledge,[171] this value of η excludes the majority of relevant p-block elements, and thus, the majority of mono-heterocycles will retain diatropic currents of moderate strength.

In the case of N = 6, and in general all even N, there is a reflection symmetry in the curve of current, $J_N(\eta) = J_N(-\eta)$, which is not present for odd N. This symmetry was noted earlier when considering the Frost-Musulin constructions (Figure 4.2) and orbital spectrum (Figure 4.3). To rationalise the inversion one must consider a property of bipartite graphs, the pairing theorem,[172,173] which for unweighted graphs is

$$\lambda_i = -\lambda_{n-i+1}. \tag{4.22}$$

This can be adapted to the present case, where one vertex weight $\eta \neq 0$:

$$\lambda_{(i,\eta)} = -\lambda_{(n-i+1,-\eta)} \tag{4.23}$$

At full occupancy, all current will vanish as there are no $\pi - \pi^*$ virtual transitions available. This is true at any value of η for any system size. In general, for any occupation and vacancy of molecular orbitals:

$$\mathrm{J}(\eta, \lambda_{\mathrm{Occ}}) + \mathrm{J}(\eta, \lambda_{\mathrm{NBO}}) + \mathrm{J}(\eta, \lambda_{\mathrm{Unocc}}) = 0 \tag{4.24}$$

in a notation where $\mathrm{J}(\eta, \lambda_{\mathrm{Set}})$ is the contribution of doubly occupied molecular orbitals in the set $\{\lambda_{\mathrm{Set}}\}$. Shown by lemma 3.5.1.1 for bipartite graphs, $\mathrm{J}(\lambda_{\mathrm{NBO}}) = 0$. So,

$$\begin{aligned} \mathrm{J}(\eta, \lambda_{\mathrm{Occ}}) &= -\mathrm{J}(\eta, \lambda_{\mathrm{Unocc}}) \\ \mathrm{J}(-\eta, \lambda_{\mathrm{Occ}}) &= -\mathrm{J}(-\eta, \lambda_{\mathrm{Unocc}}) \end{aligned} \tag{4.25}$$

From the generalised Aihara formalism, $\mathrm{J} \propto 1/{\phi_{\mathrm{G}}}'(x, \eta)$. The derivative of ϕ leads to a function with different orders in η, with terms proportional to $x^z\eta$. For even N (a necessity for the mono-cycle G to be bipartite), all exponents z are even. At an occupancy of N/2 molecular orbitals, $1/\phi'_{\mathrm{G}}(x, \eta)$ at $x = \lambda$, is identical to $1/\phi'_{\mathrm{G}}(x, -\eta)$ at $x = -\lambda$.

Hence,

$$\begin{aligned} \mathrm{J}(\eta, \lambda_{\mathrm{Occ}}) &= -\mathrm{J}(-\eta, \lambda_{\mathrm{Unocc}}) \\ \mathrm{J}(-\eta, \lambda_{\mathrm{Occ}}) &= -\mathrm{J}(\eta, \lambda_{\mathrm{Unocc}}) \end{aligned} \tag{4.26}$$

and in combination with (4.25) leads to:

$$\mathrm{J}(\eta, \lambda_{\mathrm{Occ}}) = \mathrm{J}(-\eta, \lambda_{\mathrm{Occ}}) \tag{4.27}$$

In contrast for $\eta = 0$ non-bipartite graphs, the order of exponents z in the terms $x^z\eta$ from ${\phi_{\mathrm{G}}}'(x, \eta)$ are a mixture of odd and even. The absence of a pairing theorem means analogous conclusions cannot be drawn. As such equation (4.27) does not hold for odd N, and consequently there is no inversion of both current or orbital energies until the graph becomes bipartite at the $|\eta| = \infty$ limit.

The qualitative conclusion from this simple ring-current model is that the current can survive significant changes in electronegativity, provided β_{CX} is not significantly altered. From a chemical point of view, a diatropic ring-current is expected in all $\mathrm{C_{N\text{-}1}H_{N\text{-}1}X}$ mono-heterocycles with $4\mathrm{n} + 2$ π-electrons, where X can be taken from a wide range of elements in the periodic table, and so the heterocycles should be considered aromatic systems.

4.3 Bi-Vertex-Altered Mono-Heterocycle

Now consider a bi-vertex-altered heterocycle, with a general formula $C_{N-2}H_{N-2}X_2$. If two vertices from a cycle are altered by the electronegativity parameter η, the orbital spectrum and Hückel-London ring currents can be evaluated in analogous ways to the mono-vertex-altered systems. The major difference is that bi-vertex-alteration allows for isomerisation. For N=6 these isomers are ortho, meta and para, illustrated in Figure 4.7.

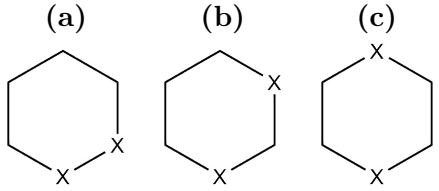


Figure 4.7: The three isomers for a bi-vertex-alteration heterocycle in the example of N=6: (a) ortho, (b) meta, (c) para.

The question then is how this will affect the characteristic polynomials, eigenvalue spectra, and Hückel-London ring currents. Each of these will be considered in turn.

4.3.1 Characteristic Polynomials

The characteristic polynomials of the bi-vertex-altered graphs can be expressed by a partition breakdown of the determinant. For each of the three isomers of N=6, an individual polynomial can be constructed:

$$\begin{aligned}
{\phi_G}^{\text{Ortho}}(x,\eta) &= \phi_{C_6}(x) - 2\eta\phi_{P_5}(x) + \eta^2\phi_{P_4}(x) \\
&= x^6 - 2\eta x^5 + (\eta^2-6)x^4 + 8\eta x^3 + (9-2\eta^2)x^2 - 6\eta x - 4 \\
&= \left(x^3 - (\eta+2)x^2 + (\eta-1)x + \eta + 2\right) \times \\
&\quad \left(x^3 - (\eta-2)x^2 + (\eta+1)x + \eta - 2\right)
\end{aligned} \tag{4.28}$$

$$\begin{aligned}
{\phi_G}^{\text{Meta}}(x,\eta) &= \phi_{C_6}(x) - 2\eta\phi_{P_5}(x) + \eta^2\phi_{P_3}(x)\,\phi_{P_1}(x) \\
&= x^6 - 2\eta x^5 + (\eta^2-6)x^4 + 8\eta x^3 + (9-2\eta^2)x^2 - 6\eta x(\eta^2-4) \\
&= \left(x^2 - \eta x - 1\right)\left(x^4 - \eta x^3 - 5x^2 + 2\eta x + 4\right)
\end{aligned} \tag{4.29}$$

$$\begin{aligned}\phi_{\mathrm{G}}{}^{\mathrm{Para}}(x,\eta) &= \phi_{\mathrm{C}_6}(x) - 2\eta\phi_{\mathrm{P}_5}(x) + \eta^2\phi_{\mathrm{P}_2}(x)^2 \\ &= x^6 - 2\eta x^5 + (\eta^2-6)x^4 + 8\eta x^3 + (9-3\eta^2)x^2 - 6\eta x(\eta^2-4) \\ &= (x-1)(x+1)\left(x^2-(\eta+1)x+\eta-2\right)\left(x^2-(\eta-1)x-\eta-2\right)\end{aligned} \tag{4.30}$$

It turns out that for *any* vertex weighted graph, the characteristic polynomial can be formulated by separating each weighted vertex and the polynomial of G with the vertex removed. Thus, for a general altered heterocycle:[161,190]

$$\begin{aligned}\phi_{\mathrm{G}}(x,\eta) =& \phi_{\mathrm{C_N}}(x) - \sum_r \eta_r\left(\phi_{\mathrm{C_N}-v_r}(x)\right) + \sum_{r<s}\eta_r\eta_s\left(\phi_{\mathrm{C_N}-v_r-v_s}(x)\right) - \\ & \sum_{r<s<t}\eta_r\eta_s\eta_t\left(\phi_{\mathrm{C_N}-v_r-v_s-v_t}(x)\right) + \ldots\end{aligned} \tag{4.31}$$

where r, s, t are vertex labels, η_i corresponds to the η modification to the i^{th} vertex, labelled as v_i. Characteristic polynomials $\phi_{\mathrm{C_N}-v_i}(x)$ can also be represented as the product of several path polynomials, as in the example of (4.29).

4.3.2 The Orbital Energies

The Gerschgorin theorem can also be applied here to rationalise the orbital spectrum. For two η-altered vertices, two clear limits can again be identified.

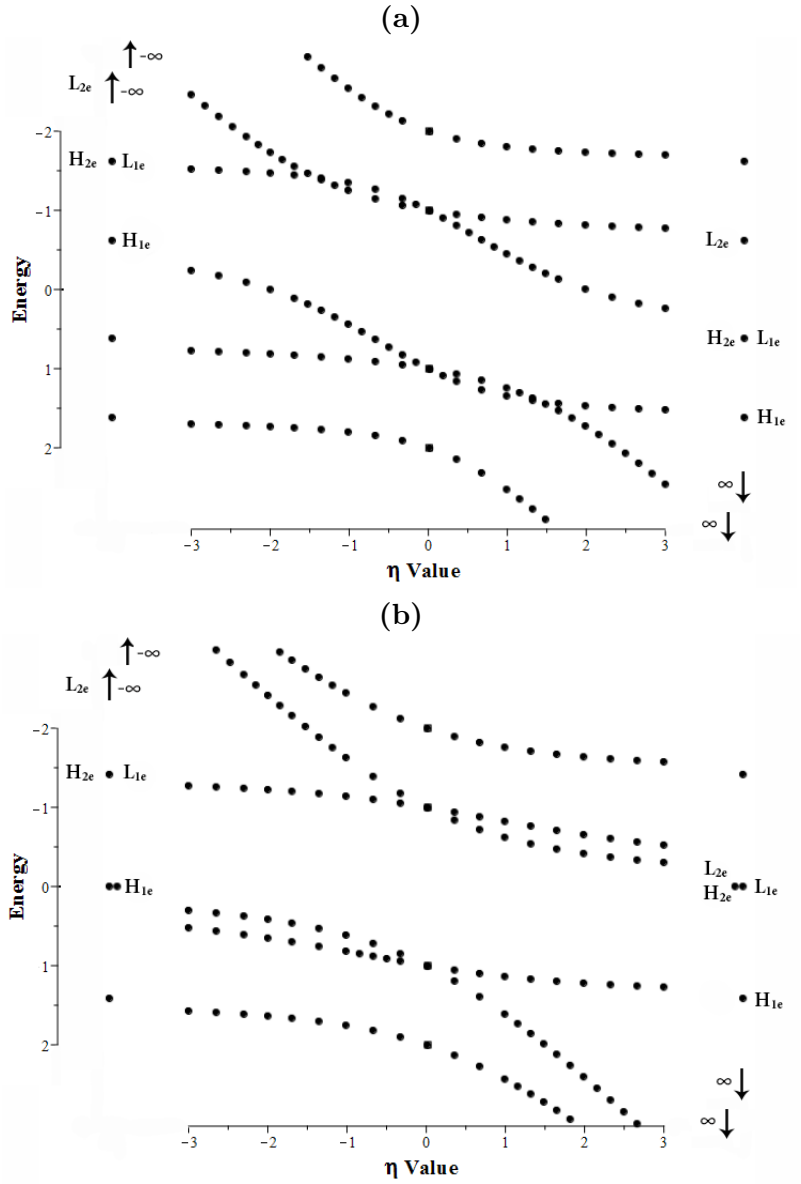
At $\eta = 0$ the orbital energies are those of the unmodified [N]annulene, with roots formulated in equation (4.10). At the infinite limits, both the X centres are effectively decoupled from the remainder of the cycle. However depending on the isomer in question, there will be fragments of different sizes left. The roots of $\phi_{\mathrm{G}}(x,\eta)$ can still be separated into two cases. Two solutions are those of the two vertices which tend to infinity as $|\eta| \to \infty$.

$$\lambda_{\mathrm{G}} = \eta$$

Solutions of all remaining vertices are from those of a generic path polynomial. For N=6 and ortho, this is the path on four vertices; meta, the path on a single and three vertices; and para, leads to two paths on two vertices. For a generic path, denoted as $\mathrm{P_{N-}}_{v_i}$, where $\mathrm{N} - v_i$ is the length of path formed from the removal of v_i vertices, the eigenvalues are:

$$\lambda_{\mathrm{P}_{\mathrm{N}-v_i}} = 2\cos\left(\frac{\pi k}{\mathrm{N}-v_i+1}\right) \text{ for } k = 1,\ldots,\mathrm{N}-v_i \tag{4.32}$$

Orbital energies between the limits are difficult to evaluate analytically but are simple to depict graphically as an eigenvalue spectrum. For the range of $-3 \leq \eta \leq 3$, the orbital spectra for the ortho, meta and para bi-vertex-altered heterocycles show little variation in energy (see Figure 4.8).



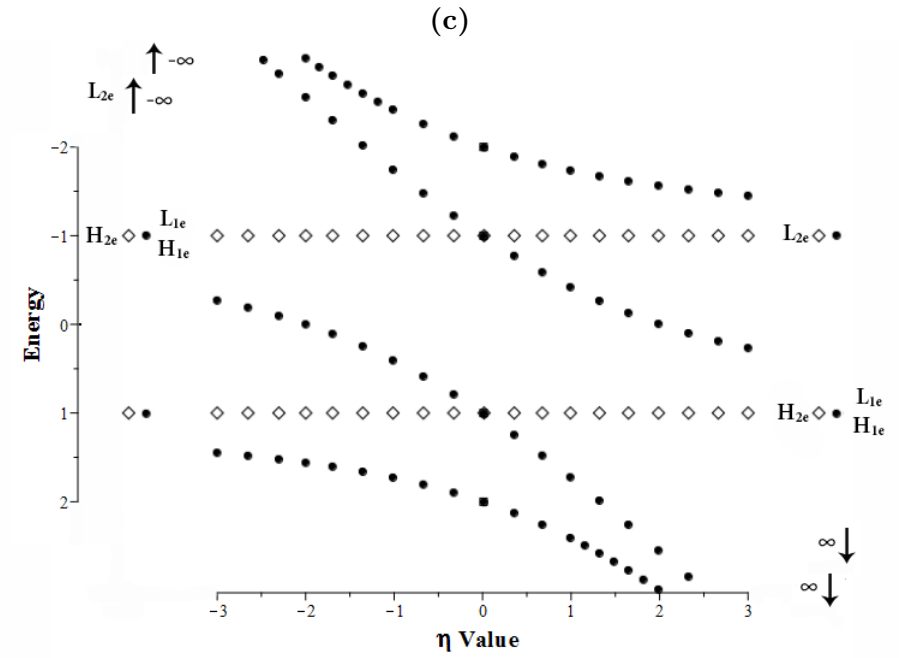


Figure 4.8: Orbital spectra, in units of β, of the three isomers of N=6 of a bi-vertex-altered mono-heterocycle: (a) ortho, (b) meta, (c) para. Orbital energies are dependent on the electronegativity parameter η on the X centres of the $C_{N\text{-}2}H_{N\text{-}2}X_2$. Squares denote the locations of the eigenvalues for $\eta = 0$. Orbital energies are displayed from lowest eigenvalue (positive y-values) to highest eigenvalue (negative y-values) denoting the order of occupying orbitals. Labels of H and L denote HOMO and LUMO energy levels assuming atom X is a 1- or 2-π-electron donor.

Of note is the absence of η-independent orbital energies in the case of ortho and meta isomers of the N=6 heterocycle. The symmetry groups for both are C_{2v}, but no non-trivial symmetry element passes through both X-centres. In the case of the para isomer, D_{2h} symmetry is attained and $\phi_G(x,\eta)$ can be decomposed into the antisymmetric, $\phi_G(x,\eta)^a$, and symmetric, $\phi_G(x,\eta)^s$, polynomials as a C_2 axis and mirror plane bisects both X positions.

$$\phi_G(x,\eta) = \phi_{C_N}(x)^a\phi_{C_N}(x)^s - 2\eta\phi_{P_{N\text{-}1}}(x)^a\phi_{P_{N\text{-}1}}(x)^s + \eta^2\phi_{P_{(N/2)\text{-}1}}(x)^a\phi_{P_{(N/2)\text{-}1}}(x)^s \quad (4.33)$$

For even N, the antisymmetric components are all equal to the polynomial $\phi_{P_{(N/2)\text{-}1}}(x)$. Thus the characteristic polynomial for the para bi-vertex-altered heterocycle simplifies to:

$$\phi_G(x,\eta) = \phi_{P_{(N/2)\text{-}1}}(x)\left[\phi_{C_N}(x)^s - 2\eta\phi_{P_{N\text{-}1}}(x)^s + \eta^2\phi_{P_{(N/2)\text{-}1}}(x)\right] \quad (4.34)$$

This symmetry breakdown is only possible in the para isomer. The consequence of this absence in the other two isomers is that factorisation of the characteristic polynomial is less obvious. For the three isomers of N=6, the characteristic polynomial can be factored into functions of x that are at most quartic equations, and thus roots can be obtained analytically if desired.

It should also be noted that in the case of ortho bi-vertex-alteration, an apparent 'accidental' degeneracy is introduced, in addition to the degeneracy at $\eta = 0$. For two specific values of η the HOMO and LUMO are independently degenerate. At $\eta = \sqrt{2}$ and $-\sqrt{2}$ orbital degeneracy is present at $\lambda_{\mathrm{G}}(\eta = \sqrt{2}) = \sqrt{2}$, and $\lambda_{\mathrm{G}}(\eta = -\sqrt{2}) = -\sqrt{2}$. Degeneracy is also observed in N=5 at $\eta = 1$, $\lambda_{\mathrm{G}}(\eta = 1) = 1$.

Bi-vertex-alteration will also impact on the number of contributing electrons from the heteroatoms. For even N, an overall neutral system can support both one π and two π-electron heteroatom donors per X centre. Consequently, the total number of π-electrons will be 6 or 8. Using Hückel 4n+2 or 4n rules of aromaticity, the two types of donors will be expected to lead to different ring-current behaviour.

Now, it is useful to discuss the HOMO-LUMO gap and its implications for the *ipsocentric* ring-current analysis. Any change in η leads to an alteration of the HOMO-LUMO gap. For the six π-electron N=6 heterocycle, HOMO and LUMO curves are labelled on the extremes of Figure 4.8. The N/2 occupancy of orbitals leads to an inversion of orbital energies, for reasons similar to those operating in the mono-vertex-altered case. Thus, the HOMO-LUMO gap at positive η is equivalent to the gap at negative η. The gap decreases from 2β at $\eta = 0$ to limiting values of β for the ortho isomer; $\sqrt{2}\beta$ for the meta isomer; and finally 0β for the para isomer.

For ortho and meta isomers both HOMO and LUMO energy levels vary with η. For the para isomer at positive η, the HOMO remains fixed and the LUMO energy varies with η, at negative η the opposite effect is observed where the LUMO is fixed and the HOMO varies. From an *ipsocentric* methodology, the η parameter will mix values of angular momentum for the orbitals introducing cancelling paratropic contributions. In all isomers, the HOMO-LUMO gap narrows. As in the mono-vertex-altered case, this

will result in the amplification of both paratropic and diatropic contributions, ultimately resulting in a reduction of current magnitude.

Perhaps more interesting is alteration in the HOMO-LUMO gap for the eight π-electron mono-cycle. In all isomers for N=6 and negative η, the orbitals still located on a Frost-Musulin circle are occupied. Thus, the HOMO-LUMO gap increases for all isomers; from 0β at $\eta = 0$ to $\infty\beta$ at $\eta = -\infty$. At positive η, the HOMO-LUMO gap increases from 0β to $(\sqrt{5}-1)\beta$ for the ortho isomer; remains unchanged for the meta isomer; and increases to 2β for the para isomer. As with the mono-vertex-altered heterocycles, the gap in the region between the limiting values of η is difficult to define analytically. Orbital angular momentum mixing will also be introduced here by the changes in η, and cancelling diatropic current density is introduced. An increase in the HOMO-LUMO gap will result in the weakening of existing current contributions. The effect will be an expected sharp decline in the current magnitude with increasing $|\eta|$.

4.3.3 Hückel-London ring-currents

In discussing the ring current of the $C_{N\text{-}2}H_{N\text{-}2}X_2$ heterocycles, the two types of electron donor must be considered separately. In both electronic configurations, analytical expressions for the ring current are either simpler or as complicated as those in the mono-vertex-altered heterocycle, depending on the isomer investigated. However, the derived expressions are not as simple as the example of N=3 with 2 π-electrons. Analytical expressions are complicated in the cases of ortho and meta isomers, where roots of the characteristic polynomials arise from quartic or cubic factors. The para isomer has a straightforward set of eigenvalues which can be expressed analytically for a general η value. However, simple numerical evaluation is used in the following section to report the Hückel-London ring currents using the simplified Aihara equation (4.18).

4.3.3.1 One-π-electron donors

First, the X centres contributing one-π-electron are considered. Ring-current magnitudes for the three bi-vertex-altered isomers of N=6, normalised to $\eta = 0$, are displayed in Figure 4.9.

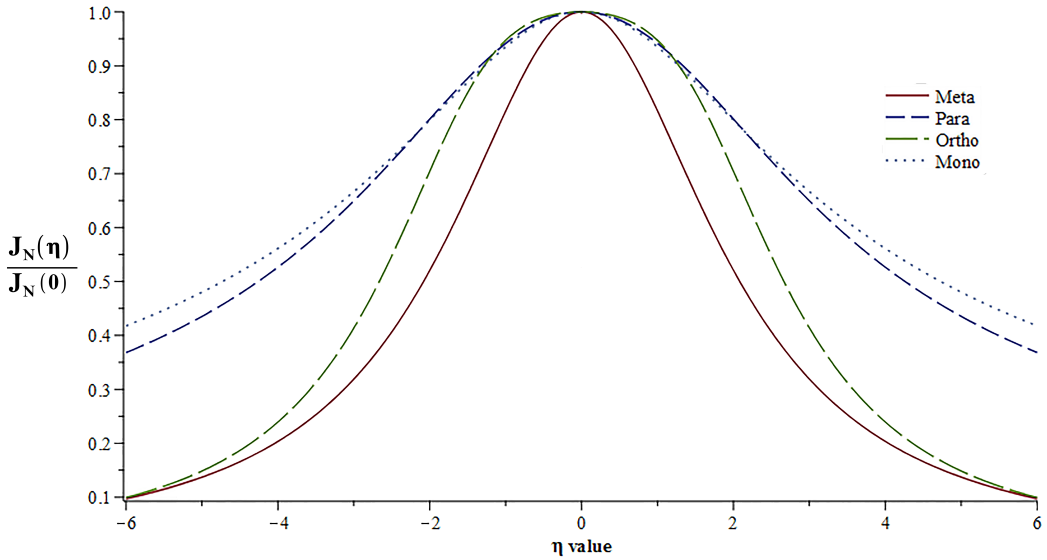


Figure 4.9: Hückel-London currents calculated for the three isomers of N=6 bi-vertex-altered $C_{N\text{-}2}H_{N\text{-}2}X_2$. Also shown is the HL current of the mono-vertex-altered N=6 heterocycle. Calculations assume an occupancy of 6π-electrons.

From this graph it is clear that the ring-current magnitudes of the bi-vertex-altered heterocycles are more susceptible to changes in η than the mono-vertex-altered heterocycle. In particular, the ortho and meta isomers show a much faster decrease, falling to just over 50% of $J_G/J_0\,(C_N, 0, 6\pi)$ within the defined chemically relevant range. The η values necessary to reduce the HL magnitude to 80% and 50% of $J_G/J_0\,(C_N, 0, 6\pi)$ are reported in Table 4.3.

Table 4.3: The values of positive and negative η necessary to reduce the Hückel-London current to (a) 80% and (b) 50% of $J_G/J_0\,(C_N, 0, 6\pi)$ for the three isomers of the bi-vertex-altered heterocycle, and the mono-vertex-altered heterocycle for N = 6.

	(a)			(b)	
	Positive η	**Negative η**		**Positive η**	**Negative η**
Mono	1.99	-1.99	**Mono**	4.73	-4.73
Ortho	1.69	-1.69	**Ortho**	2.66	-2.66
Meta	1.05	-1.05	**Meta**	2.08	-2.08
Para	2.01	-2.01	**Para**	4.26	-4.26

From these values, it is clear that ortho and meta isomers suffer rapid decline in current magnitudes. For these two isomers, the decline is much faster than in the mono-

vertex-altered case retaining roughly half the magnitude of $J_G/J_0\,(C_N, 0, 6\pi)$ at $\eta \approx 2$. However, both meta and ortho isomers maintain a moderate strength diatropic current for the majority of p-block heteroatoms in the chemically relevant η range.[171,191] The para isomer retains a diatropic ring-current of moderate strength on a par with that of the mono-vertex-altered heterocycle. Also, the symmetry of the current ($\eta \leftrightarrow -\eta$), from an extension of the pairing theorem, is also present in the bi-vertex-altered system.

4.3.3.2 Two-π-electron donors

Next, the two-π-electron donors are considered. One can consider the X centres to be analogous to the nitrogen in pyrrole, where the lone pair is involved in the π-manifold. In the present case, as the orbital energies approach degeneracy, i.e. as $|\eta| \to 0$, $J \to -\infty$. This is a consequence of how standard Hückel-London theory deals with open-shell systems. The closed shell occupancy for $\eta \neq 0$ is replaced at $\eta = 0$ with an open shell triplet, represented by the fractional occupation of the suddenly degenerate HOMO-LUMO levels. As the orbital energies approach degeneracy, the HOMO-LUMO gap decreases resulting in an exponential growth of current modulus. As such the behaviour of the ring current for these systems in this area is inferred from continuity. This seems physically correct, especially in view of the likely Jahn-Teller distortion at the degeneracy.[192]

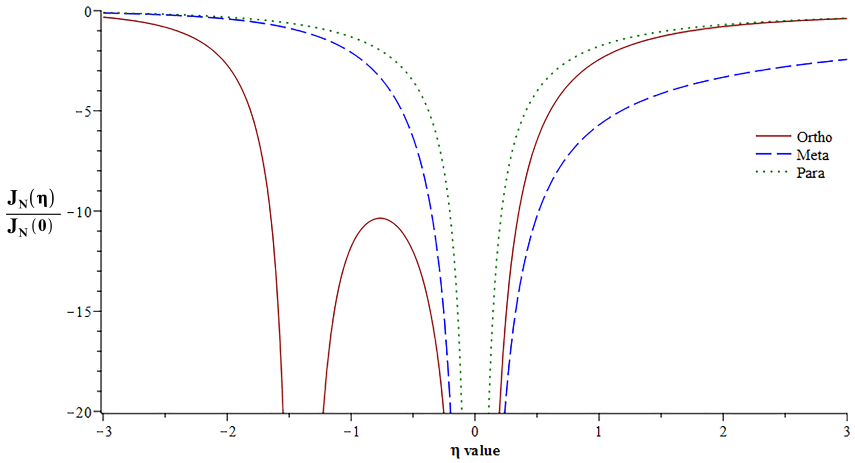


Figure 4.10: Hückel-London currents calculated for the three isomers of N=6 bi-vertex-altered $C_{N-2}H_{N-2}X_2$. Calculations assume an occupancy of eight π-electrons.

It turns out that there are two zones where continuity must be used to infer the ring-current behaviour. The first is at $\eta = 0$ where the degeneracy of the orbitals at $\lambda = 1$ leads to an increase in the Hückel-London ring-current. The second is present only in the ortho bi-vertex-altered isomer, where 'accidental' degeneracy is introduced at $\eta = \sqrt{2}$, $\lambda = \sqrt{2}$. Typically, the degenerate Aihara equation (3.11) is used to evaluate the ring-current at these zones. However, the general underlying Hückel-London theory is unable to properly deal with the partial occupancy of degenerate orbitals.

Paratropic ring-currents in the two π-electron donor case are more susceptible to η changes, a fact that has been noted previously.[193] For η approaching 0, a strong paratropic current is observed. As seen in Figure 4.10, the smallest alteration in η results in a significant weakening of the paratropic current, with all isomers displaying similar reductions in magnitude as $\eta \to \infty$. Although, it should be noted that $\mathrm{J}(\eta) \neq \mathrm{J}(-\eta)$, owing to the difference in orbital occupation at equivalent $|\eta|$.

In addition, $\mathrm{J}(-\eta)$ is more susceptible to changes in η . From earlier, the HOMO-LUMO gap at negative η changes from 0β to $\infty\beta$ between the two limits. The result is an expected rapid decline in current magnitude for negative η vs positive η. An exception is the ortho isomer. As seen in Figure 4.8(a), the LUMO levels tend to $\infty\beta$ but over a larger η range than the other isomers. The smaller increase in HOMO-LUMO gap at positive η leads to an overall drop in the Hückel-London current magnitude as $\eta \to \infty$.

4.4 *Ipsocentric* Ring Currents

Current-density maps calculated through the *ipsocentric* method, as discussed in detail in Chapter 2, should now be used to compare the Hückel-London predictions from the η-only model. Current-density calculations utilise structures optimised at the DFT/B3LYP/6-31G** level of theory, with currents calculated at the CHF/6-31G** level.

A selection of p-block elements will be used to represent the X centres: N, O, P and S, which contribute either 1π-electron per X centre (Figure 4.11), or 2π-electrons per X centre (Figure 4.12), each with an appropriate charge. The selection of these heteroatoms covers two rows of the periodic table and the most common heteroatoms in chemistry.

Ab initio calculations give currents that are not restricted to edges of a molecular graph. However, Figures 4.11 and 4.12 both show that the *ipsocentric* ring-current approach leads to current-density maps similar to those expected from Hückel-London maps using the simple $4n$, $4n + 2$ electron counting rules.

Heteroatoms that donate one π-electron to an N= 6 mono- or bi-vertex-altered heterocycle, lead to a system consisting of six π-electrons. The current-density maps show all heterocyclic systems to be aromatic, sustaining diatropic ring-currents of a similar magnitude to benzene ($j_{\max} \approx 0.08$ a.u.). If the heteroatom is a two-π-electron donor, closed-shell occupations are only possible in bi-vertex-altered heterocycles. The total of eight π-electrons leads to the assignment of antiaromaticity, sustaining paratropic currents with magnitudes comparable with cyclooctatetraene ($j_{\max} \approx 0.12$ a.u.) with some notable exceptions. Meta-bi-vertex-alteration leads to the strongest paratropic currents, and para-bi-vertex-alteration leads to the weakest. This is in disagreement with the conclusions established earlier from the Hückel-London model where the opposite trend was observed. However, the simpler Hückel-London model does not include any deviations from ideal geometry, and accounts for changes only in electronegativity, not bond-bond polarisability. Ultimately, an over-arching qualitative conclusion can be drawn: the ring-currents in heteroatomic systems are robust against changes to electronegativity, whether calculated at the *ab initio* or more primitive graph-theoretical level.

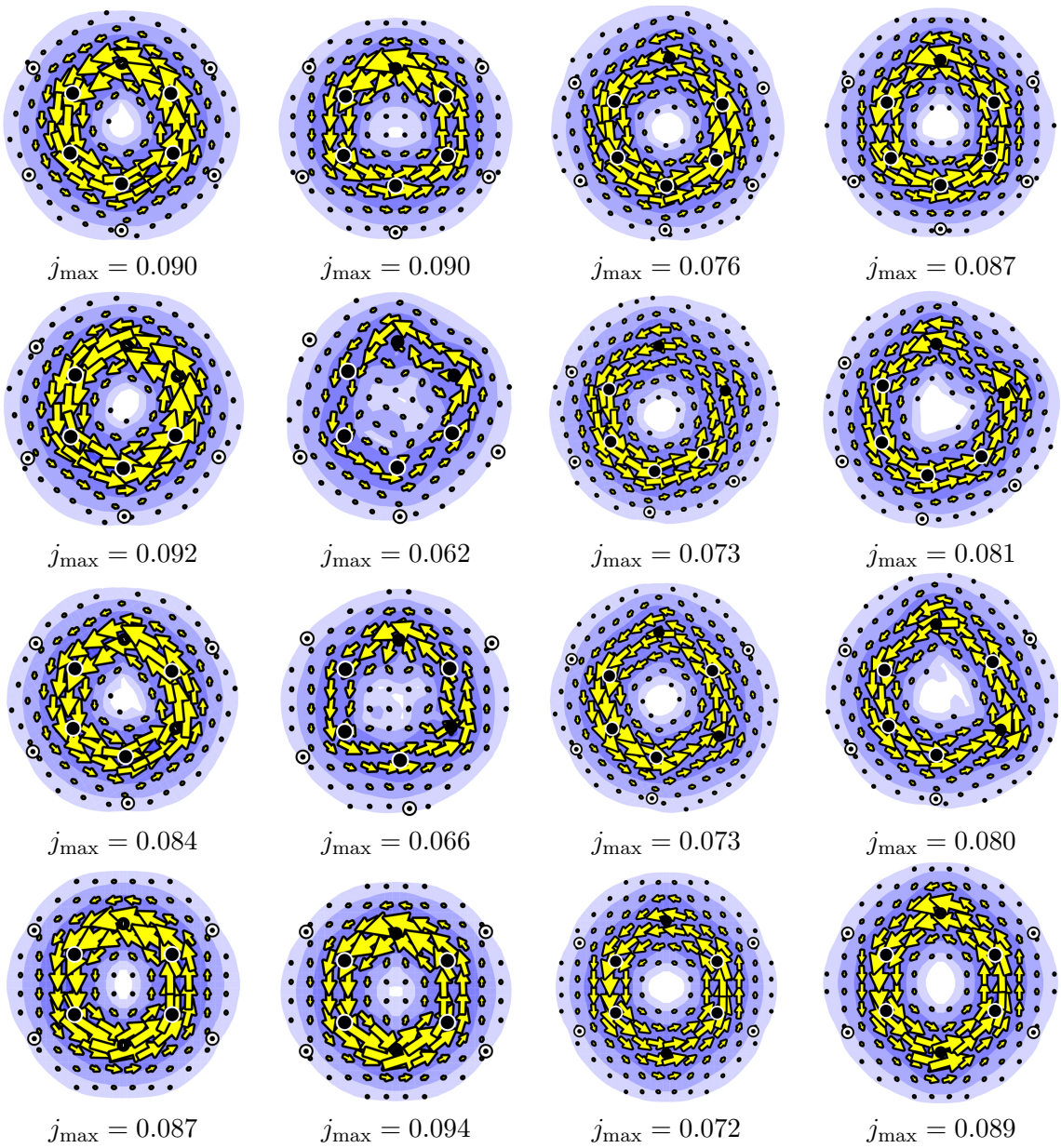


Figure 4.11: The current maps for the C_5H_5X heterocycle (row 1) and the three isomers of $C_4H_4X_2$ heterocycle: ortho (row 2), meta (row 3) and para (row 4). All X centres contribute one π-electron to the total π manifold. The four columns identify heteratomic alteration with X = N (column 1), O (column 2), P (column 3) and S (column 4). j_{max} values are all reported in units of a.u.

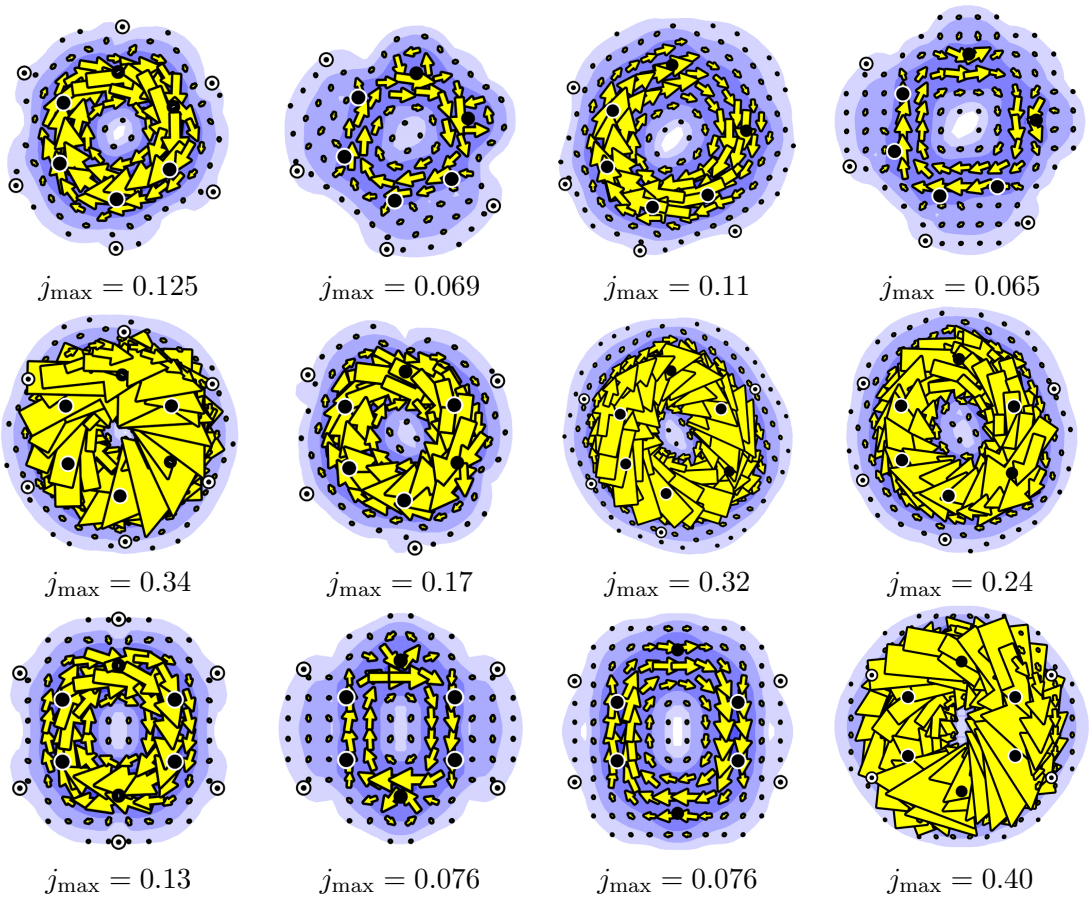


Figure 4.12: The current maps for the three isomers of $C_4H_4X_2$ heterocycle: ortho (row 1), meta (row 2) and para (row 3). All X centres each contribute two π-electrons to the total π-manifold. The four columns identifies heteratomic alteration with X = N (column 1), O (column 2), P (column 3) and S (column 4). j_{max} values are all reported in units of a.u.

4.5 Consequences of the Matrix Analysis

Consider the adjacency matrix (4.2) for a general heterocycle. The η values modelling the heteroatoms can be considered numerically distinguishable from the carbon atoms, for which α_C is set to 0. Now, imagine a bipartite system where this notation is inverted, and the original N-M carbon atoms are altered to heteroatoms, and the original M heteroatoms are altered to carbons. This process will define two systems, the 'parent' (M,N)-heterocycle and an 'inverted' (N-M,N)-heterocycle with nomenclature defined as any M-substitution of heteroatoms in an N-monocycle. The following section explores the idea of symmetry and relationship of eigenvalues between these two systems.

First, to simplify the analysis, the ring size will be set to N= 6 for these exploratory calculations. There are seven distinct patterns of substitution which can be imagined: one corresponds to the mono-vertex-altered cycle; three to the three isomers of a bi-vertex-altered cycle; and three to the three isomers of the tri-vertex-altered cycle. The parent and inverted heterocycles are shown in Figure 4.13.

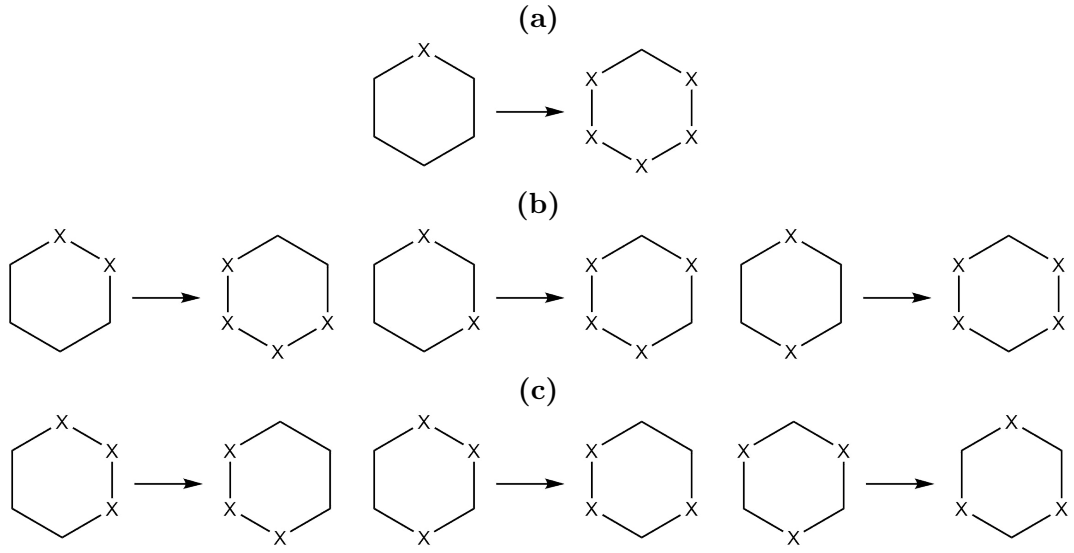


Figure 4.13: The seven unique conversions, for a 6 membered ring, of the 'parent' heterocycle, left of the arrow, to the 'inverted' systems where carbon and heteroatomic vertices are swapped. (a) the mono-vertex-altered case; (b) the three bi-vertex-altered cases; (c) the three tri-vertex-altered cases.

For the moment only the bi-vertex-altered para isomer will be discussed in detail as

this isomer has the simplest expressions for its roots (see equations (4.5) and (4.28) - (4.30)). Roots of the characteristic polynomial can readily be expressed analytically for the para isomer, since the largest order of the polynomial is quadratic. For the other isomers, the roots are a mixture of cubic and quartic equations. In such cases, analytical roots can be calculated, but these expressions are too complicated to present in detail here. Finally the tri-substituted isomers are not treated here owing to the trivial isomeric rotational relationship between the 'parent' and 'inverted' systems.

The eigenvalues of the 'parent' para-(2,6)-heterocycle can be calculated from roots of the characteristic polynomial that, for this section, are denoted ϕ_{G}(N-M,N),

$$\begin{aligned}
\phi_{\mathrm{G}}(2,6) &= \det\left|x\mathbf{1_6} - \mathbf{A_{(2,6)}}\right| \\
&= \begin{bmatrix} x-\eta_1 & -1 & 0 & 0 & 0 & -1 \\ -1 & x & -1 & 0 & 0 & 0 \\ 0 & -1 & x & -1 & 0 & 0 \\ 0 & 0 & -1 & x-\eta_1 & -1 & 0 \\ 0 & 0 & 0 & -1 & x & -1 \\ -1 & 0 & 0 & 0 & -1 & x \end{bmatrix} \\
&= (x-1)\,(x+1)\left(x^2-(1+\eta_1)x+(\eta_1-2)\right)\left(x^2-(\eta_1-1)x-(2+\eta_1)\right).
\end{aligned} \tag{4.35}$$

Now consider the inverse system, namely the para-(4,6)-heterocycle, with carbon and heteroatomic vertices exchanged.

$$\begin{aligned}
\phi_{\mathrm{G}}(4,6) &= \det\left|x\mathbf{1_6} - \mathbf{A_{(4,6)}}\right| \\
&= \begin{bmatrix} x & -1 & 0 & 0 & 0 & -1 \\ -1 & x-\eta_2 & -1 & 0 & 0 & 0 \\ 0 & -1 & x-\eta_2 & -1 & 0 & 0 \\ 0 & 0 & -1 & x & -1 & 0 \\ 0 & 0 & 0 & -1 & x-\eta_2 & -1 \\ -1 & 0 & 0 & 0 & -1 & x-\eta_2 \end{bmatrix} \\
&= (x-1-\eta_2)\,(x+1-\eta_2)\left(x^2-(1+\eta_2)x-2\right)\left(x^2-(\eta_2-1)x-2\right)
\end{aligned} \tag{4.36}$$

The polynomials $\phi_{\mathrm{G}}(4,6)$ and $\phi_{\mathrm{G}}(2,6)$ can be considered as two particular solutions of the general matrix, defined by $\mathbf{M_6}$. The trace of this matrix is non-zero, which has an impact on the summation of eigenvalues. However, η_1 and η_2 values can be chosen to lead to $\mathrm{Tr}(\mathbf{M_6}) = 0$: $-2\eta_1 = \eta_2$.

$$\mathbf{M_6} = \begin{bmatrix} x-\eta_1 & -1 & 0 & 0 & 0 & -1 \\ -1 & x-\eta_2 & -1 & 0 & 0 & 0 \\ 0 & -1 & x-\eta_2 & -1 & 0 & 0 \\ 0 & 0 & -1 & x-\eta_1 & -1 & 0 \\ 0 & 0 & 0 & -1 & x-\eta_2 & -1 \\ -1 & 0 & 0 & 0 & -1 & x-\eta_2 \end{bmatrix} \tag{4.37}$$

The roots of $\phi_{\mathrm{G}}(2,6)$ and $\phi_{\mathrm{G}}(4,6)$ can be expressed analytically:

$\boldsymbol{\lambda}$	**Bi-alteration**	**Tetra-alteration**
λ_1	1	$\eta+1$
λ_2	-1	$\eta-1$
λ_3	$\frac{1}{2}\left(\eta+1+\sqrt{\eta^2-2\eta+9}\right)$	$\frac{1}{2}\left(\eta+1+\sqrt{\eta^2+2\eta+9}\right)$
λ_4	$\frac{1}{2}\left(\eta+1-\sqrt{\eta^2-2\eta+9}\right)$	$\frac{1}{2}\left(\eta+1-\sqrt{\eta^2+2\eta+9}\right)$
λ_5	$\frac{1}{2}\left(\eta-1+\sqrt{\eta^2+2\eta+9}\right)$	$\frac{1}{2}\left(\eta-1+\sqrt{\eta^2-2\eta+9}\right)$
λ_6	$\frac{1}{2}\left(\eta-1-\sqrt{\eta^2+2\eta+9}\right)$	$\frac{1}{2}\left(\eta-1-\sqrt{\eta^2-2\eta+9}\right)$

Simple inspection of these eigenvalues for both systems leads to the identification of functions that map eigenvalues from the bi-vertex-altered system, λ_{Bi}, to the tetra-substituted system, λ_{Tetra}, and vice versa.

$$\lambda_{\mathrm{Bi}}(\eta) = \lambda_{\mathrm{Tetra}}(-\eta) + \eta \tag{4.38}$$

$$\lambda_{\mathrm{Tetra}}(\eta) = \lambda_{\mathrm{Bi}}(-\eta) + \eta \tag{4.39}$$

Inspection of the orbital spectra for both systems confirms this relationship.

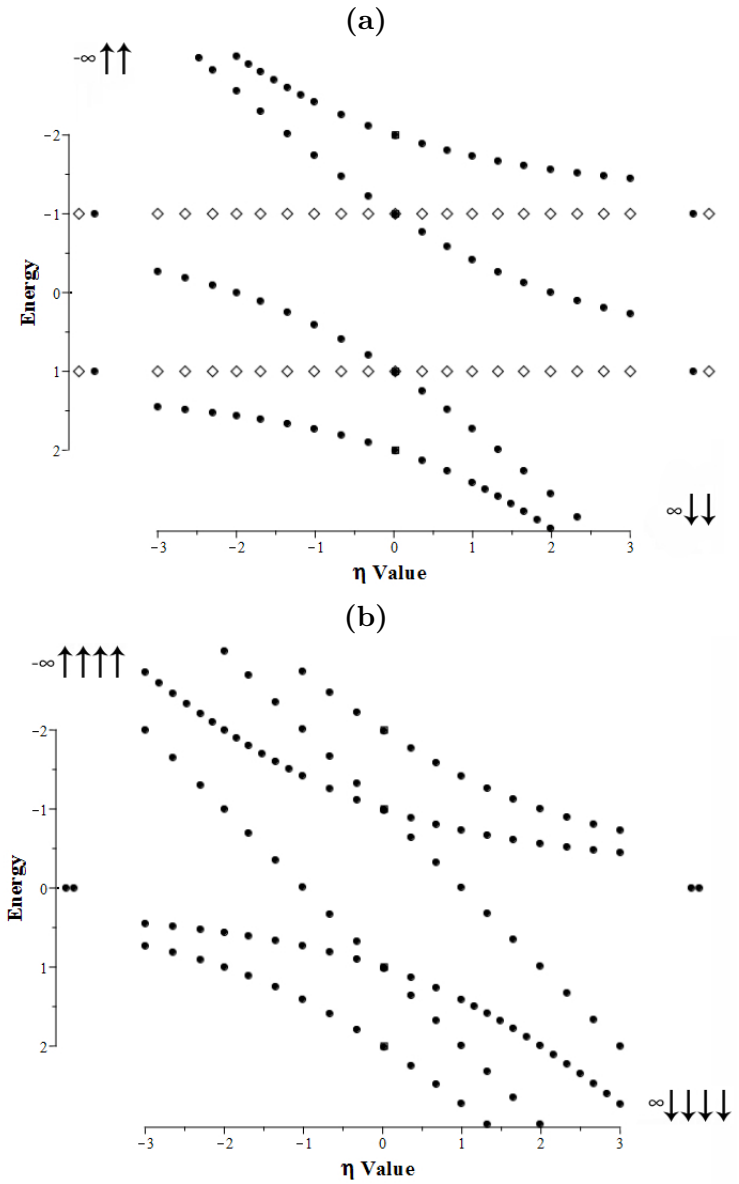


Figure 4.14: The orbital spectra of eigenvalues, in units of β, for (a) the 'parent' para-(2,6)-heterocycle, and (b) the 'inverse' para-(4,6)-heterocycle. Orbital spectra are related by the functions defined in equations (4.38) and (4.39).

As can be seen, the graphical relationship between eigenvalues resembles that of the functions in equations (4.38) and (4.39). Eigenvalues are reflected through the y-axis and then offset by $+\eta$.

4.6 Conclusion

Using only a simple model where α parameters in the adjacency matrix are altered, ring-currents can be calculated using the Aihara-Hückel-London method. In this method, $\alpha_{\mathrm{X}} = \alpha_{\mathrm{C}} \pm \eta\beta_{\mathrm{CC}}$ models the change in electronegativity upon alteration of carbon to a heteroatom X. The ring current in both mono- or bi-vertex-altered heterocycles were found to be robust against chemically relevant changes to the electronegativity parameter η.

In the mono-vertex-altered systems, where only one CH unit is replaced with X, each vertex donates one π-electron. Within the realm of chemical relevance, $-3 \leq \eta \leq 3$, the predicted ring current remains above 50% of the value at $\eta = 0$. Furthermore, simple analytical formulae of the HL ring current could be formed for small N in the cases where λ could also be found analytically.

In the bi-vertex-altered heteroatomic systems, where two CH units are replaced with X, there is the possibility of multiple isomers. For N= 6, there are three such isomers. In the HL model, the para isomer sustains a stronger current over the relevant η range. Ring currents in this set of heterocycles decrease over the same η range more quickly than in the mono-vertex-altered systems. Both X centres donate one or two electrons. One π-electron donors sustain diatropic currents of moderate strength and two π-electron donors sustain strong paratropic currents. Paratropic currents are more susceptible to alterations in η, and diatropic currents were sustained over the majority of the chemically relevant η range.

Comparison of *ab initio ipsocentric* current-density maps with Hückel-London current maps showed similarities, with 1e donors supporting diatropic currents and 2e donors supporting paratropic currents. Minor differences exist between the two models. For example, the heterocycle j_{max} values indicate increased current-density for the *ab initio* approach compared to the all-carbon system. This trend is not observed at the HL level. In addition, the ordering of magnitudes for the three bi-vertex-altered isomers differs between the two levels of theory. The overall conclusion is that ring-currents are robust against changes in electronegativity and sustain current-density magnitudes close to those in the full carbon system.

Part II

Application and Investigation of Conjugated-Circuit Models

The second part of the thesis details two families of systems with interesting conjugated-circuit model ring currents. First, the Randić conjugated-circuit model is applied to derivatives and homologues of the antikekulene systems where ring-currents are functions of the Fibonacci sequence. Second, the conjugated-circuit models are applied to perylene and related extensions and bicycles, with resultant ring currents compared to those calculated through the Hückel-London and *ab initio* models. In this family of systems, a detailed analysis of the latter two approaches is detailed, in order to explain deviations from conjugated circuit results.

Chapter 5

Equiaromaticity and Ring Currents in Antikekulene and Derivatives[1]

5.1 Introduction

Antikekulene is a system that has eluded synthetic chemists for decades but seems constantly on the cusp of synthesis. The structure of antikekulene is formed through construction of alternating squares and hexagons around the perimeter of a 12-membered ring (see Figure 5.1). In this sense, it can be regarded as the 'antiaromatic twin' of kekulene.

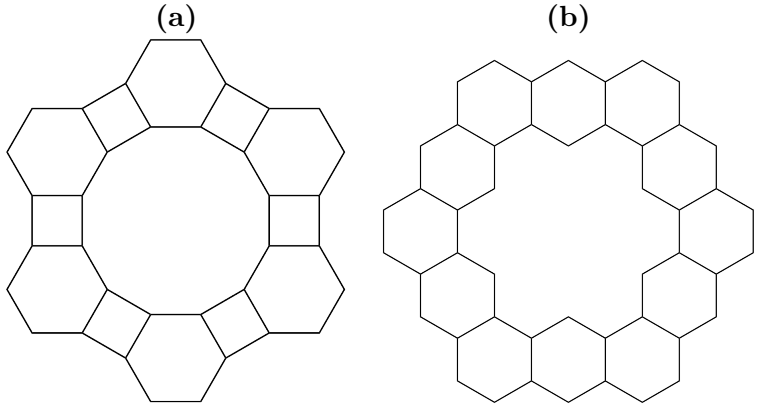


Figure 5.1: The structures of antikekulene, **(a)**, and kekulene, **(b)**, double bonds of the sp^2 carbon vertices have been removed for simplicity.

The aromaticity of antikekulene and kekulene have been evaluated with a multitude of theoretical models over various papers spanning many decades. These include, but are not limited to, TRE, Topological Resonance Energy;[23,170] CCMRE, Conjugated-Circuit Model Resonance Energy;[102] HLPM, the Hückel-London-Pople-McWeeny method,[81–83]

[1]Dr Chris Gibson is thanked for prior work on some of the *ab initio* calculations that appear in this chapter. Details of this work also form the basis of the in preparation research paper: Clarke. J., Gibson. C., Myrvold. W., and Fowler. P.W., *In Preparation.*

and NICS, Nucleus-Independent-Chemical-Shift.[66] The general consensus indicates that kekulene is aromatic, as qualified by a TRE value of $1.5688|\beta|$;[194] the presence of negative NICS values in the perimeter benzenoids;[70,195] the manifestation of diatropic ring currents;[70,196] as well as many others,[197,198] In contrast, antikekulene is antiaromatic, as manifested by a TRE value of $-0.710|\beta|$;[194,198] the presence of paratropic ring currents in the HLPM model, of magnitudes -1.393, -0.609 and -1.660[199] for the centre, hexagon and square faces, respectively, implying antikekulene is fully antiaromatic and NICS(1)[68] values of +2.5, -5.2 and +2.1 for the same respective faces, implies locally aromatic hexagons and antiaromatic squares and centre rings;[200] finally the CCMRE model calculates a value of -0.006 which indicates non-aromaticity.[201]

The failure to synthesise antikekulene is perhaps one of the strongest indicators of antiaromaticity. This is in direct contrast to the sucessful synthesis of kekulene.[202] Although structures which are likely to be precursors to antikekulene have been synthesised, this has not yet materialised into a full synthetic route.[203] Difficulty in synthesis could be interpreted as a property of an antiaromatic system.[204] The presence of a short-lived ^{1}H NMR peak suspected to belong to antikekulene is considered the most promising synthetic lead. However, as no firm evidence is available, the existance of antikekulene should be regarded with caution.[203]

Literature is both sparse and conflicted with regards to the local or global nature of antiaromaticity in antikekulene. The present chapter will address some of these inconsistencies in the supposed antiaromaticity of antikekulene and extend the discussion to some derivatives of antikekulene, as defined from the literature.

5.1.1 Antikekulene homologues and derivatives

In 1993 Gutman and Cyvin discussed the Kekulé structures for a series of cyclic phenalenes, defined as non-alternant, non-benzenoid graphs constructed from alternating squares and hexagons around a central polygonal ring.[205] The antikekulene homologues, denoted as N-antikekulenes, are constructed from N squares, N hexagons and one 2N-sided central ring, see Figure 5.2.

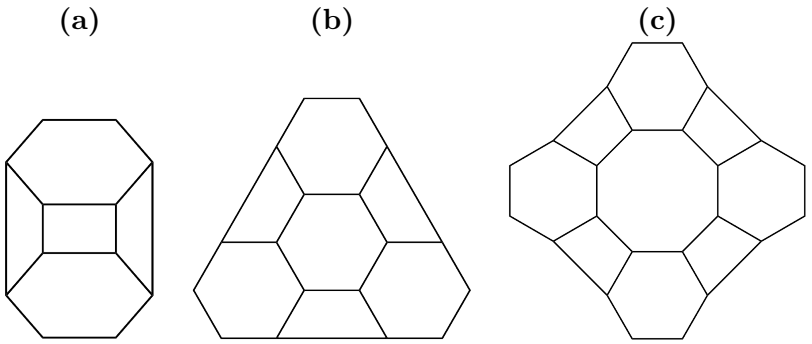


Figure 5.2: The first three homologues of antikekulene defined as N-antikekulenes where N is an integer defined as 1/2 the number of vertices of the central ring. a) 2-antikekulene, b) 3-antikekulene, c) 4-antikekulene.

The number of Kekulé structures of an N-antikekulene is:[205]

$$\begin{aligned} \mathrm{K(N)} &= F_{2\mathrm{N}+1} + F_{2\mathrm{N}-1} + 2 \\ &= L_{2\mathrm{N}} + 2 \end{aligned} \tag{5.1}$$

where F_{N} is the N^{th} Fibonacci number and L_{N} is the N^{th} Lucas number. Fibonacci and Lucas numbers fall into two well-known number sequences, where each entry is formed from the sum of the two preceding numbers conforming to the general formula:

$$\begin{gathered} G_{\mathrm{N}} = G_{\mathrm{N}-1} + G_{\mathrm{N}-2} \\ \text{with } F_0 = 0 \text{ and } F_1 = 1 \\ \text{with } L_0 = 2 \text{ and } L_1 = 1 \end{gathered} \tag{5.2}$$

However, equation (5.1) is not limited to N-antikekulenes. These equations are applicable for any antikekulene derivative, modified through the addition or removal of two vertices from any external cycle so long as this face remains a cycle. The rationale for this assertion is that two additional vertices will support any pattern of single-double bond alternation necessary to support Kekulé structures.

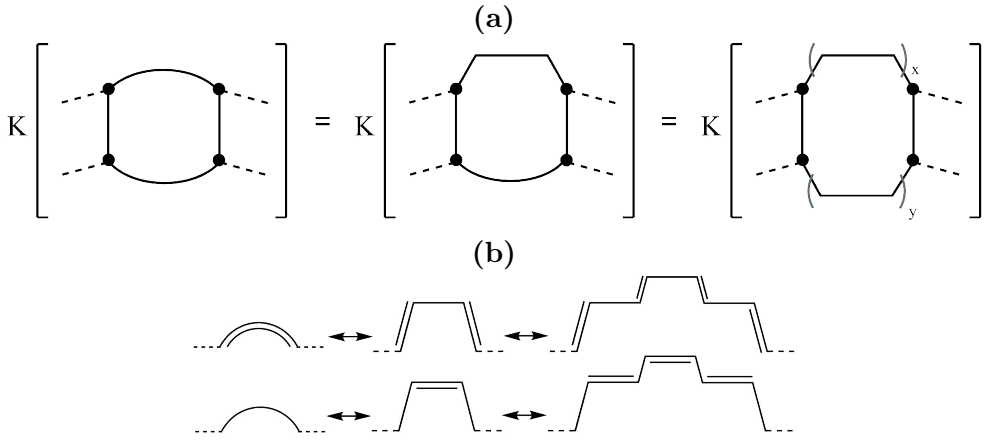


Figure 5.3: (a) Illustrations of the dependence of Kekulé valence structures on the number of spacers in a macrocycle. In the general case, right, as long as an even number of vertices are added, i.e. x and y are integers, the number of Kekulé valence structures will be preserved. (b) Examples of the vertex addition and deletion in the cases where the joining bond is double, top, and single, bottom.

Using the general construction, Figure 5.3a (right), several symmetric structures can be drawn. If only the square face in the parent antikekulene is modified, x=0, y=0 results in the N-antikekulene series, hereafter referred to as N-AK. x=1, y=0 leads to the so-called N-cyclic 'benzenoid' series, hereafter referred to as N-CB. Finally, x=1, y=1 leads to the N-antiCOT series consisting of alternating octagon and hexagon faces around a centre ring of size 4N, hereafter referred to as N-AC. The sets of structures in the case of N=6 are shown in Figure 5.4. Similar to homologues of the N-AK series, the size of the centre ring will be altered in all derivatives.

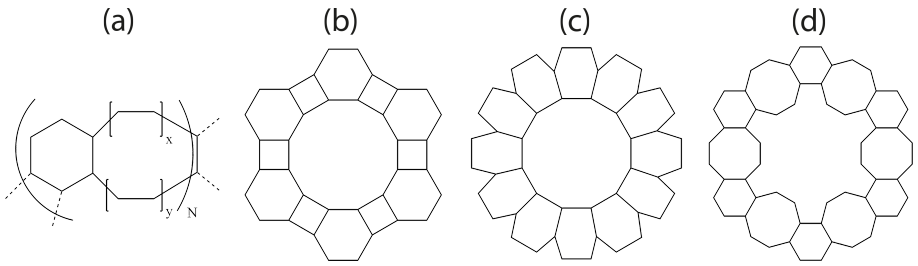


Figure 5.4: The structures of the three types of systems discussed in the present chapter showing (a) the general formula for an N-antikekulene derivative, and then three N=6 cycles: (b) 6-Antikekulene, (c) 6-cyclic 'benzenoid' and (d) 6-AntiCOT.

Since the Kekulé structure count can be formulated as an analytical expression, it

should also be possible to formulate expressions for the conjugated-circuit models, which are explicitly dependent on counting Kekulé structures. Such expressions have previously been established for the ring current and number of Kekulé structures in other families. For example, in a linear chain a linear polyacenes of N-benzenoids, the number of Kekulé structures, K(N), and the Randić ring current in ring Q, J(N, Q), are:[94]

$$\mathrm{K(N)} = \mathrm{N} + 1 \tag{5.3}$$

$$\mathrm{J(N}, Q) = 2Q\,(\mathrm{N} - Q + 1) \tag{5.4}$$

Likewise for a fibonacene, a kinked chain of N-benzenoids with no linear segment containing more than two hexagons, the equivalent quantities are:[104]

$$\mathrm{K(N)} = F_{\mathrm{N}+2} \tag{5.5}$$

$$\mathrm{J(N,}\, Q) = 2F_{\mathrm{N}-Q+2}F_{\mathrm{N}-Q+1}F_{Q+1}F_{Q} \tag{5.6}$$

The question then arises as to whether the ring currents in the antikekulene homologues and derivatives, identified in Figures 5.2 and 5.4, can be analogously represented as analytical formulae. Furthermore, the effect of system alteration, through the addition of a spacer unit (Figure 5.3), on the CC ring current map will be explored.

5.1.2 Cyclic Partition

Before the ring currents are analysed, it is useful to discuss some nomenclature used here and in future sections. To rationalise the ring currents in the antikekulene homologues and derivatives, it is useful to categorise conjugated circuits according to the faces involved. Four different classes of circuits can be envisaged according to degree of incorporation of the centre face, with each circuit belonging to only one class. These categories encompass all derivatives and homologues considered in this chapter. Class (A) circuits do not contain the centre face; class (B) circuits contain the centre face; a class (C) circuit contains all faces of the cycle; and finally a class (D) circuit contains only the centre faces of the system. The latter class is only important when considering the ring current of the centre face. Examples of the four classes are illustrated in Figure 5.5.

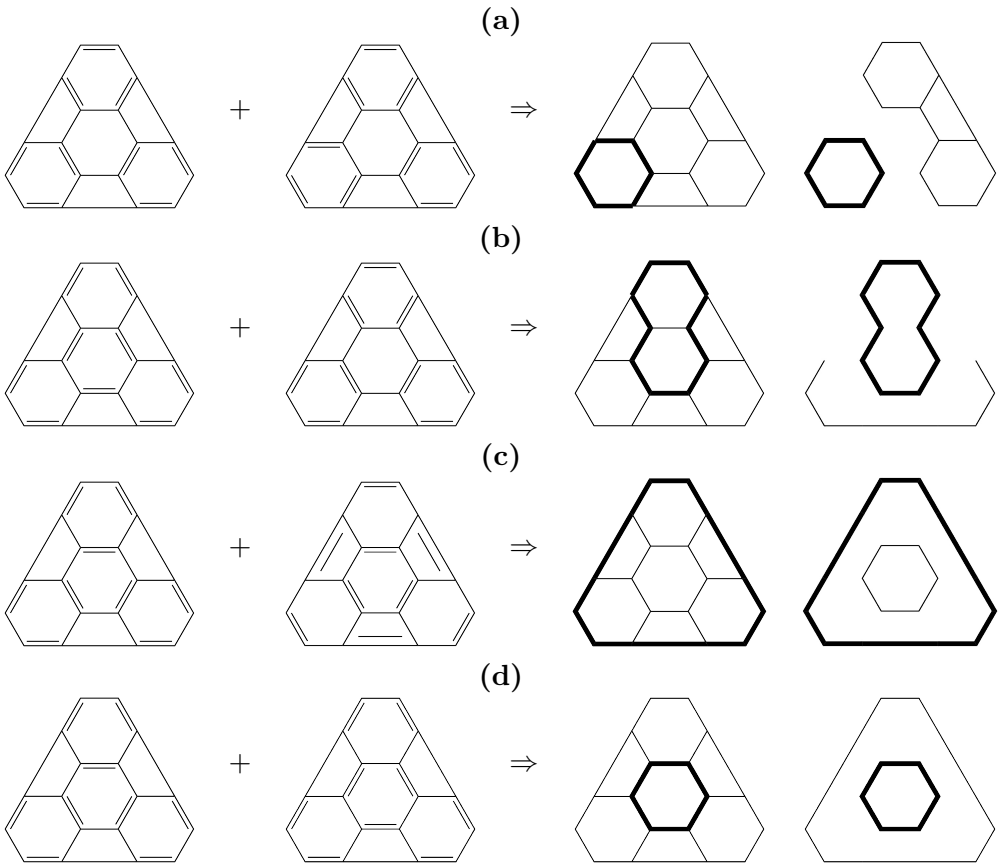


Figure 5.5: Examples of the four different classes of conjugated-circuits for 3-AK which can also be applied to all other systems in the chapter. The four classes of circuit are: a) class (A), conjugated-circuits do not contain the centre ring; b) class (B), conjugated-circuits contain the centre ring; c) class (C), the perimeter conjugated-circuit; and d) class (D), the centre face circuit. Columns 1 and 2 show the two Kekulé structures which correspond to the conjugated-circuit, in column 3 highlighted in bold. Column 4 shows the circuit, in bold, and the resulting graph G − C obtained through removal of all vertices and edges involved in C.

The ring-current model of significance in this section is the Randić model defined in full in Chapter 1.3.3.1. The current contribution of cycle C to the total current map is:

$$\mathrm{J_C} = \pm 2\left[m\left(\mathrm{G}-\mathrm{C}\right)\right]^2 \tag{5.7}$$

Here, a connection to the Fibonacci sequence can be established. $m\left(\mathrm{G}-\mathrm{C}\right)$, the number of Kekulé structures in graph G−C, will vary amongst the four defined classes of circuits. Using the transformation of Kekulé structures (Figure 5.3), G−C can be shown to have the same number of Kekulé structures as a fibonacene of the same number of faces, see Figure 5.6.

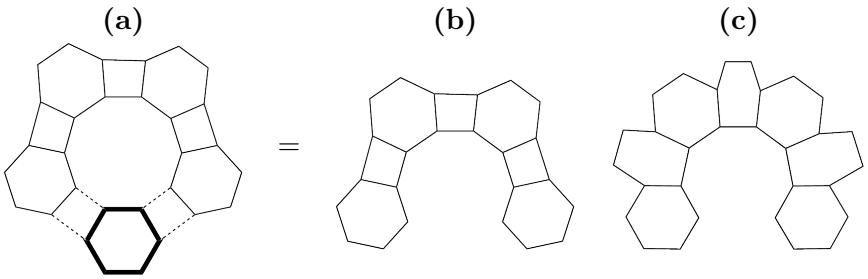


Figure 5.6: The relationship between G − C and a fibonacene. Any cycle has the possibility of preserving cycles in G − C. Using the example of 5-AK, cycle C, highlighted in bold in (a), leads to graph G − C in (b). Graph G−C can then be considered as a pseudo-fibonacene by simple insertion of two extra vertices for each square to result in the 7-fibonacene, (c).

Therefore, m(G − C) follows the formula for the number of Kekulé structures of a fibonacene (equation (5.5)). If h faces are preserved in G − C, the graph is a pseudo h-fibonacene, thus:

$$m(\mathrm{G}-\mathrm{C}) = F_{h+2} \tag{5.8}$$

As evident from Figure 5.5, the four classes lead to different numbers of preserved faces in graph G − C. Class (A) circuits preserve faces depending on the size of $\mathrm{C}_{(\mathrm{A})}$, so $m\left(\mathrm{G}-\mathrm{C}_{(\mathrm{A})}\right) = F_{h+2}$. Class (B) circuits lead to a varying length alkenyl chain in $\mathrm{G}-\mathrm{C}_{(\mathrm{B})}$, so $m\left(\mathrm{G}-\mathrm{C}_{(\mathrm{B})}\right) = F_2 = 1$. Finally, both classes (C) and (D) circuits are consistent over all derivatives due to the preservation of the centre face or perimeter face respectively, thus $m\left(\mathrm{G}-\mathrm{C}_{(\mathrm{C\ or\ D})}\right) = F_3 = 2$. The total current of any perimeter face will then be the sum of the contributions from class (A), (B) and (C) circuits, and any centre face will be the sum of class (B), (C) and (D) circuits.

Finally, the divisibility of circuits must be discussed. For *any* circuit constructed from α faces of size $4n+2$ and β faces of size $4n$; the divisibility of the circuit, will be solely dependent on the value of β.

If β is even, the cycle C is of type 4n + 2.

If β is odd, the cycle C is of type 4n.

5.2 Conjugated-Circuit Ring-Current analysis

5.2.1 Mandado and Ciesielski et al. models

First, a brief mention needs to be made for two of the other published conjugated-circuit models, namely the Mandado[112] and Ciesielski et al.[110] models. A difficulty in the analysis of these models is due to the explicit inclusion of area parameters. To recap from 1.3.3, the Ciesielski et al. model formulates the contribution of a given circuit as:[94]

$$\mathrm{J_C} = \pm \left[m\left(\mathrm{G}-\mathrm{C}\right)\right]^2 \left|\frac{S_\mathrm{C}}{S_0}\right| \tag{5.9}$$

and the Mandado model formulates current as:

$$\mathrm{J_C} = \pm 2\left[m\left(\mathrm{G}-\mathrm{C}\right)\right] / \left(\left|\frac{S_\mathrm{C}}{S_0}\right| \ \mathrm{K(G)}\right) \tag{5.10}$$

where S_C/S_0 denotes the size of circuit C. In both models, C is assumed to be constructed from the fusion of regular n-sized polygons with sides of length 1.4 Å and are normalised to that of a hexagon of the same side length (S_0). In this approximation, the area of each n-polygon is:

$$\frac{n\sqrt{3}\cot\left(\pi/n\right)}{18} \tag{5.11}$$

One can now appreciate the difficulty. For *every* CC identified in an antikekulene-like structure the area must be individually calculated. If a single circuit is defined as (γ, ζ, κ) where γ denotes the numbers of hexagons; ζ denotes the numbers defining rings of derivative (squares in N-AK, for example); and κ accounts for the possible inclusion of the centre face, then the area term for circuit $\mathrm{C}_{(\gamma,\zeta,\kappa)}$ is:

$$\frac{S_{\mathrm{C}_{(\gamma,\zeta,\kappa)}}}{S_0} = \gamma + \zeta\left[\frac{n\sqrt{3}\cot\left(\pi/n\right)}{18}\right] + \kappa\left[\frac{2\mathrm{N}\sqrt{3}\cot\left(\pi/2\mathrm{N}\right)}{18}\right] \tag{5.12}$$

This analysis becomes difficult for the larger antikekulene derivatives where, as N increases so too does the number of conjugated circuits (combine equations (1.18) and (5.1)). Since every circuit will have a different area term, the contribution of each circuit must be taken on a case-by-case basis, in addition to the categorisation necessary for

the type of circuit. It is possible to treat the contributions through the use of matrices, but this leads to cumbersome expressions for both Mandado and Ciesielski et al. models. In the confines of the present chapter, only the simple Randić CC model and its simple accountability of the area will be considered further.

5.2.2 N-Cyclic 'Benzenoids'

The first series to be discussed in detail is the N-CB series, also referred to as 2N-circulenes in the literature.[206] The exact and largest-magnitude-scaled ring currents for the unique hexagon and centre faces of an N-CB, calculated using the Randić model, are reported in Table 5.1. The simplicity of this series is evident when considering the parity of cycles.

Table 5.1: The raw and largest-magnitude-scaled ring currents calculated in the Randić CC model for an N-CB detailing the ring-current magnitude and direction present in the symmetrical distinct hexagon and central faces. 2N corresponds to the size of the central face, and K(G) refers to the number of Kekulé structures in the homologue.

N	K(G)	Raw Current		Scaled Current	
		Hexagon	Centre	Hexagon	Centre
2	9	0	-36	0	-1
3	20	168	80	1	0.4762
4	49	784	-196	1	-0.2500
5	125	6300	500	1	0.0794
6	324	40824	-1296	1	-0.0317
7	845	285948	3380	1	0.0118
8	2209	1943920	-8836	1	-0.0045

Decomposing the total current into contributions from the circuit classes, it is clear that the ring currents are factorisable into simple Fibonacci-like formulae. Each class is considered separately before composed into one function for the ring current of each face.

5.2.2.1 Class (A) circuits

The removal of a class (A) circuit from the N-CB results in a graph which can be represented as a kinked h-faced fibonacene. If C is constructed from 2N−1 faces of the perimeter, this is equivalent to a fibonacene with $h = 0$. Since all faces of G − C are hexagonal, these cycles will always be of type $4n + 2$ for every N-CB.[207]

The total ring-current contribution from all class (A) circuits containing one specific hexagon of the N-CB, is found through application of equation (5.8) to $m\,(\mathrm{G}-\mathrm{C})$. Circuits are of different sizes, with the number of faces encompassed successively increasing from 1 to 2N−1 hexagons. Additionally there are multiple isomers to consider. The number of isomeric circuits of given size is equivalent to the number of perimeter hexagons. This is illustrated in Figure 5.7 where current contributions arise from: one circuit of size one benzenoid; two circuits fused from two benzenoids; three circuits fused from three benzenoids, and so on.

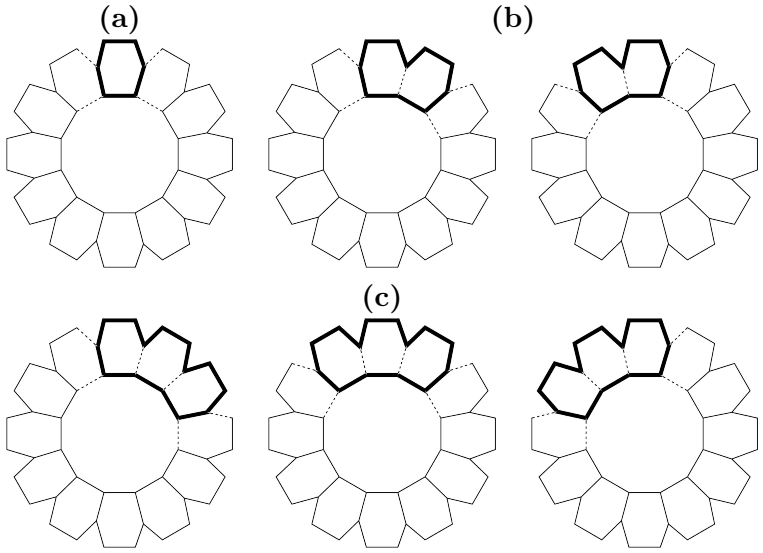


Figure 5.7: Conjugated-circuits in 6-CB involving up to three benzenoid faces indicating the number of isomers and preserved faces. (a) indicates the sole cycle when only one face is involved in the CC; (b) the two isomers of the CC involving two faces; (c) the three isomers of the CC involving three faces.

In general, a circuit constructed from i faces, C_i, of the perimeter will appear i times ranging from 1, a solo cycle, to 2N−1, when all but one face is involved in the circuit. The $m\,(\mathrm{G}-\mathrm{C}_i)$ value for the i^{th} circuit obeys,

$$m\,(\mathrm{G}-\mathrm{C}_i) = F_{2\mathrm{N}-i} \tag{5.13}$$

and so,

$$[m\,(\mathrm{G}-\mathrm{C}_i)]^2 = {F_{2\mathrm{N}-i}}^2 \tag{5.14}$$

The additive contribution from all non-centre circuits is thus,

$$\sum_{i=1}^{2\mathrm{N}-1} i{F_{2\mathrm{N}-i}}^2 \tag{5.15}$$

Since all class (A) circuits in N-CB are of size $4n+2$, all current contributions will be positive. From the Randić equation (5.7), the total ring current contribution from all class (A) circuits, $\mathrm{J}_{(\mathrm{A})}$, is:

$$\mathrm{J}_{(\mathrm{A})} = 2 \times \left[\sum_{i=1}^{2\mathrm{N}-1} i{F_{2\mathrm{N}-i}}^2 \right] \tag{5.16}$$

Or, this can be expressed simply, using proof by induction, as:[208,209]

$$\mathrm{J}_{(\mathrm{A})} = 2 \times \left[{F_{2\mathrm{N}}}^2\right] \tag{5.17}$$

5.2.2.2 Class (B) and (C) circuit contributions to the hexagon

Class (B) and (C) circuits fall into two categories. If the centre face is of size $2\mathrm{N} = 4\mathrm{n}+2$, when N is odd, all centre-containing circuits are of size $4n+2$, the well-known example is the fully hexagonal 3-CB, better known as coronene. Conversely, if the centre ring is of size $2\mathrm{N} = 4\mathrm{n}$, when N is even, all centre-containing conjugated-circuits are of size $4n$. The contribution from these conjugated circuits is the resultant contribution from the total number of conjugated-circuits that contain the centre ring. There are $L_{2\mathrm{N}} - 2$ of these class (B) circuits.

The perimeter class (C) circuit, has $m\,(\mathrm{G}-\mathrm{C}) = F_3 = 2$. In the case of N-CB, the contribution from both these classes of cycles can be combined. Now accounting for divisibility, all class (B) and (C) circuits will be of size $4n$, if N is even, or $4n+2$, if N is odd. Thus, in the Randić model, the contribution to a given hexagon for the two classes of circuits are:

$$\mathrm{J}_{(\mathrm{B})} = 2 \times \left[(-1)^{\mathrm{N}-1}\,(L_{2\mathrm{N}} - 2)\right] \tag{5.18}$$

$$\mathrm{J}_{(\mathrm{C})} = 2 \times \left[(-1)^{\mathrm{N}-1}\,(4)\right] \tag{5.19}$$

with the total contribution from all class (B) and (C) circuits to a given hexagon,

$J_{Centre}(Hexagon)$:

$$J_{Centre}(Hexagon) = J_{(B)} + J_{(C)} = 2 \times \left[(-1)^{N-1} (L_{2N} + 2)\right] \tag{5.20}$$

5.2.2.3 Centre contribution

Changing focus to the manifested ring current in the centre ring, the current is the sum of the contributions from the class (B), (C) and (D) circuits. For *all* circuits, there are two sets of complementary cycles yielding equal bond currents on the perimeter and central rings. This implies a two-to-one ratio in the respective ring currents.

$$J_{Centre}(Centre) = 2J_{Centre}(Hexagon) \tag{5.21}$$

The complementary CC in question involves one that contains the centre ring plus H perimeter rings, and its complement containing the central ring plus the $2N - H$ hexagons not included in the first (see Figure 5.8 for examples). Complementary CC are always of the same divisibility: they are of type $4n + 2$ if N is odd and $4n$ if N is even.

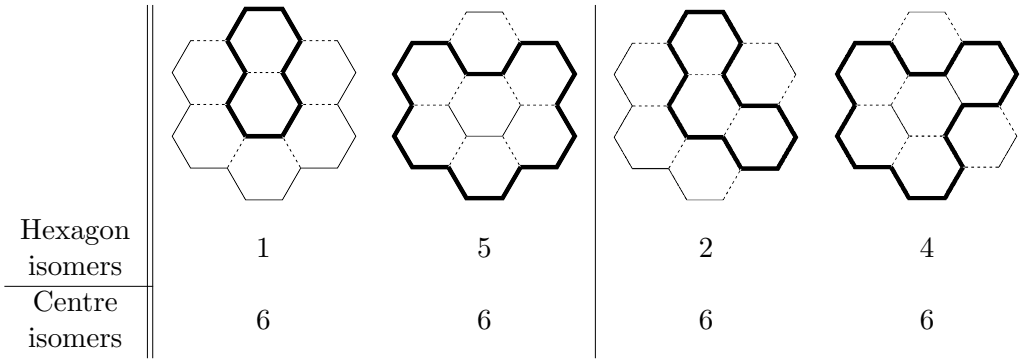


Figure 5.8: Examples of two complementary pairs of centre-containing conjugated-circuits, highlighted in bold, and related number of isomers which contribute to the centre cycle itself and also the hexagon. The number of isomers obeys equation (5.22).

Hence, the currents follow from complementary CC pairs. Labelling any cycle as C_{1+H}, with the subscript referring to the number of faces contained in the CC, the two complementary paired CCs are:

$$\sum_{H=0}^{2N} C_{1+H} + C_{2N+1-H}\,(Centre) = 2 \sum_{H=0}^{2N} C_{1+H} + C_{2N+1-H}\,(Hexagon) \tag{5.22}$$

From this formulation, the class (C) circuit can be seen as a complement of the class (D) circuit. Hence, the contribution from the three classes of circuits are:

$$\mathrm{J}_{(\mathrm{B})} = 2 \times \left[(-1)^{\mathrm{N}-1}\left(2L_{2\mathrm{N}} - 4\right)\right] \tag{5.23}$$

$$\mathrm{J}_{(\mathrm{C})} = 2 \times \left[(-1)^{\mathrm{N}-1}\left(4\right)\right] \tag{5.24}$$

$$\mathrm{J}_{(\mathrm{D})} = 2 \times \left[(-1)^{\mathrm{N}-1}\left(4\right)\right] \tag{5.25}$$

5.2.2.4 Total face currents

The total ring current for each face is then the combination of both formulae. For a hexagon hub face, this is the combination of equations (5.17) and (5.20).

$$\begin{aligned} \mathrm{J}_{\mathrm{Tot}}(\mathrm{Hexagon}) &= \left[\mathrm{J}_{(\mathrm{A})} + \mathrm{J}_{\mathrm{Centre}}(\mathrm{Hexagon})\right] \\ &= 2 \times \left[{F_{2\mathrm{N}}}^2 + (-1)^{\mathrm{N}-1}\left(L_{2\mathrm{N}} + 2\right)\right] \end{aligned} \tag{5.26}$$

and the Randić ring current for the centre circuit is the combination of equations (5.23) - (5.25):

$$\mathrm{J}_{\mathrm{Tot}}(\mathrm{Centre}) = 2 \times \left[(-1)^{\mathrm{N}-1}\left(2L_{2\mathrm{N}} + 4\right)\right] \tag{5.27}$$

Equations (5.26) and (5.27) explain the observed reduction of the centre face current compared to the hexagon face (Table 5.1). At large N, hexagon currents are dominated by the large ${F_{2\mathrm{N}}}^2$ term that rapidly surpasses the centre current.

5.2.3 Ring-currents in Antikekulene homologues

Now focusing on the centrepiece of the chapter, the ring currents in the N-AK series can be considered related to those in the N-CB series. Additional complexity is introduced by the existence of both $4n$ and $4n+2$ faces leading to a mix of conjugated circuits. The exact and largest-magnitude-scaled ring currents calculated using Randić ring-current model for the symmetry distinct hexagon, square and central faces of an N-AK, are reported in Table 5.2. K(G) for a given N-AK is identical to that for a given N-CB.

Once again, the results of the Randić CC ring-current model can be rationalised through partitioning of conjugated circuits into the defined classes of circuits. Each class of circuit will now be considered in turn.

Table 5.2: The raw and largest-magnitude-scaled ring-currents for the hexagon, square and central ring of the N-AK series. 2N corresponds to the size of the central ring and K(G) refers to the number of Kekulé structures of the homologue.

N	K(G)	Raw Current			Scaled Current		
		Hexagon	Square	Centre	Hexagon	Square	Centre
2	9	-8	-20	-20	-0.4	-1	-1
3	20	8	-88	0	0.0909	-1	0
4	49	80	-508	-36	0.1574	-1	-0.0709
5	125	660	-3396	0	0.1943	-1	0
6	324	4568	-23080	-80	0.1979	-1	-0.0035
7	845	31556	-158004	0	0.1997	-1	0
8	2209	216384	-1082508	-196	0.1999	-1	-0.0002

5.2.3.1 Class (A) circuits

Class (A) circuits in the N-AK series will be a mixture of $4n$ and $4n+2$ types. In analogy to Figure 5.7 (for N-CBs), a similar diagram for class (A) circuits in 6-AK can be constructed.

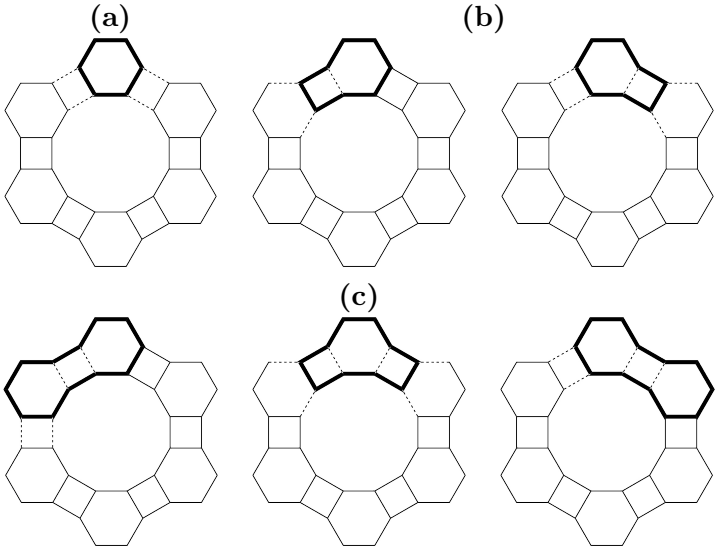


Figure 5.9: Conjugated-circuits in 6-AK involving up to three perimeter faces indicating the number of isomers and preserved faces.

Focusing first on the hexagon common to all circuits in Figure 5.9, one can appreciate the large degree of cancellation between circuits. In the three examples given, the circuits correspond to: one $4n+2$ circuit (Figure 5.9(a)); two $4n$ circuits (Figure 5.9(b)); and

two $4n$ and one $4n+2$ circuit (Figure 5.9(c) left, right and middle respectively). Using previously defined formulae for fibonacenes, the current contribution for the ring current in the hexagon of choice, from the class (A) circuits is:

$$\begin{aligned} \mathrm{J}_{(\mathrm{A})} &= 2 \times \left[{F_{11}}^2 - {F_{10}}^2 - {F_{10}}^2 - {F_9}^2 + {F_9}^2 - {F_9}^2 \ldots \right] \\ &= 2 \times \left[{F_{11}}^2 - 2{F_{10}}^2 - {F_9}^2 + 4{F_8}^2 + {F_7}^2 \ldots \right] \end{aligned} \tag{5.28}$$

Represented over all class (A) circuits, for a general N-AK, the current in a hexagon can be summarised as:

$$\mathrm{J}_{(\mathrm{A})} = 2 \times \left[\sum_{i=0}^{\mathrm{N}-1} (-1)^i \ {F_{2\mathrm{N}-2i-1}}^2 + (-1)^i \ 2i \ {F_{2\mathrm{N}-2i}}^2 \right] \tag{5.29}$$

For a given square, the magnitudes in equation (5.29) are also applicable, but with a sign change owing to the substitution of a $4n$ square in the place of a $4n+2$ hexagon.

$$\mathrm{J}_{(\mathrm{A})} = 2 \times \left[-{F_{11}}^2 - 2{F_{10}}^2 + {F_9}^2 + 4{F_8}^2 - {F_7}^2 \ldots \right] \tag{5.30}$$

$$= 2 \times \left[\sum_{i=1}^{\mathrm{N}} (-1)^i \ {F_{2\mathrm{N}-2i+1}}^2 + (-1)^i \ 2i \ {F_{2\mathrm{N}-2i}}^2 \right] \tag{5.31}$$

Using a proof by induction with well defined Fibonacci and Lucas formulae,[208] the bracketed terms in equations (5.29) and (5.31) can be reduced to:

$$\text{For a Hexagon} \quad \text{If } \mathrm{N} = 2p \qquad \frac{{F_{2\mathrm{N}}}^2}{9} \tag{5.32}$$

$$\text{If } \mathrm{N} = 2p+1 \qquad \frac{{F_{2\mathrm{N}}}^2 + 8}{9} \tag{5.33}$$

$$\text{For a Square} \quad \text{If } \mathrm{N} = 2p \qquad \frac{-5{F_{2\mathrm{N}}}^2}{9} \tag{5.34}$$

$$\text{If } \mathrm{N} = 2p+1 \qquad \frac{-5{F_{2\mathrm{N}}}^2 - 4}{9} \tag{5.35}$$

The largest contributor to the current arises from class (A) circuits owing to the dependence of $m\,(\mathrm{G}-\mathrm{C})$ on the Fibonacci sequence. Equations (5.32) - (5.35) rationalise the observed significant reduction in the Randić ring-current between N-CB and N-AK series (compare the magnitudes of Tables 5.1 and 5.2). Furthermore, equation (5.32) was originally found as a registered number sequence in OEIS.org,[210] (the Online Encyclopedia of Integer Sequences) with other equations found by making minor alterations. This

was important for obtaining the form of the total Randić equation but has now been surpassed by the firm understanding that comes from identifying cycle contributions and deriving equations (5.32) - (5.35).

5.2.3.2 Class (B), (C) and (D) circuits

Next consider the class (B) and (C) circuits. Comparison can again be made to those in the N-CB series, although the necessity to account for divisibility of cycles adds complexity. The equivalence of Kekulé structure counts between N-AK and N-CB series means that the *total* number of conjugated-circuits of the specific classes remains the same. In both series, this number is $L_{2N} - 2$ for the class (B) circuits. In the case of N-AK systems it is necessary to separate the circuits according to type. The number of $4n + 2$ and $4n$ circuits, denoted by m_{4n+2} and m_{4n}, for the hexagon, square and centre are summarised in Table 5.3.

Table 5.3: The number of circuits of the two parities, $4n$ or $4n+2$ which contribute ring currents to the hexagon, square and centre rings.

		Hexagon	**Square**	**Centre**
N = 2p	m_{4n+2}	$\frac{L_{2N} - L_N}{2}$	$\frac{L_{2N} - L_N}{2}$	$L_{2N} - L_N$
	m_{4n}	$\frac{L_{2N} + L_N}{2} - 2$	$\frac{L_{2N} + L_N}{2} - 2$	$L_{2N} + L_N - 4$
N = 2p+1	m_{4n+2}	$\frac{L_{2N} - F_N}{2}$	$\frac{L_{2N} - 3F_N}{2}$	$L_{2N} - 2$
	m_{4n}	$\frac{L_{2N} + F_N}{2} - 2$	$\frac{L_{2N} + 3F_N}{2} - 2$	$L_{2N} - 2$

The total Randić ring current can then be conveniently expressed as the sum of m_{4n+2} and $-m_{4n}$ terms, as, from Figure 5.5, all $m\,(\mathrm{G} - \mathrm{C}) = 1$. First, considering the hexagon:

$$\text{If } N = 2p \qquad J_{(B)} = 2 \times [2 - L_N] \tag{5.36}$$

$$\text{If } N = 2p + 1 \qquad J_{(B)} = 2 \times [2 - F_N] \tag{5.37}$$

and for the square:

$$\text{If N} = 2p \qquad \text{J}_{\text{(B)}} = 2 \times [2 - L_{\text{N}}] \tag{5.38}$$

$$\text{If N} = 2p + 1 \qquad \text{J}_{\text{(B)}} = 2 \times [2 - 3F_{\text{N}}] \tag{5.39}$$

The class (C) circuit retains the $m\,(\text{G} - \text{C}) = 2$ dependence discussed earlier. In addition, since the circuit is always of size $4N$, $m\,(\text{G} - \text{C})^2$ will always occur with a negative sign:

$$\text{J}_{\text{(C)}} = -2 \times [4] \tag{5.40}$$

For the centre face, the ring current contribution for the class (B) circuits is found as the sum of $m_{4\text{n}+2}$ and $-m_{4\text{n}}$ terms in Table 5.3. The class (C) circuit always occurs with a negative sign and obeys equation (5.40). Similar to the N-CB series, the class (D) circuit divisibility varies according to the parity of N. Therefore to summarise:

$$\text{If N} = 2p \qquad \text{J}_{\text{(B)}} = 2 \times [4 - 2L_{\text{N}}] \tag{5.41}$$

$$\text{J}_{\text{(C)}} = -2 \times [4] \tag{5.42}$$

$$\text{J}_{\text{(D)}} = -2 \times [4] \tag{5.43}$$

$$\text{If N} = 2p + 1 \qquad \text{J}_{\text{(B)}} = 0 \tag{5.44}$$

$$\text{J}_{\text{(C)}} = -2 \times [4] \tag{5.45}$$

$$\text{J}_{\text{(D)}} = 2 \times [4] \tag{5.46}$$

In the case of N= $2p$, the relationship in equation (5.22) for the N-CB series, is applicable in this instance (compare equations (5.41) and (5.36)). For N= $2p + 1$, the equality in $m_{4\text{n}+2}$ and $-m_{4\text{n}}$ terms results in exact cancellation of contributions.

5.2.3.3 Total face currents

Finally, summing all relevant contributions from relevant classes of circuits leads to a general analytical ring-current equation for the N-AK. Separating according to the parity of N, if N= $2p$:

$$\mathrm{J_{Tot}(Hexagon)} = 2 \times \left[\frac{{F_{2N}}^2}{9} - L_N - 2 \right] \tag{5.47}$$

$$\mathrm{J_{Tot}(Square)} = 2 \times \left[\frac{-5{F_{2N}}^2}{9} - L_N - 2 \right] \tag{5.48}$$

$$\mathrm{J_{Tot}(Centre)} = 2 \times [-2L_N - 4] \tag{5.49}$$

and if N= $2p + 1$:

$$\mathrm{J_{Tot}(Hexagon)} = 2 \times \left[\frac{{F_{2N}}^2 + 8}{9} - F_N - 2 \right] \tag{5.50}$$

$$\mathrm{J_{Tot}(Square)} = 2 \times \left[\frac{-5{F_{2N}}^2 - 4}{9} - 3F_N - 2 \right] \tag{5.51}$$

$$\mathrm{J_{Tot}(Centre)} = 0 \tag{5.52}$$

Equations (5.47) - (5.52) rationalise observations made in Table 5.2. Comparing scaled currents of the square, hexagon and centre, a general trend can be identified as:

$$\mathrm{J_{Tot}(Square)} \approx 5 \times \mathrm{J_{Tot}(Hexagon)}$$

$$\mathrm{J_{Tot}(Square)} > \mathrm{J_{Tot}(Hexagon)} >> \mathrm{J_{Tot}(Centre)}$$

One caveat is that N must be large enough so the F^2 terms in equations (5.47) - (5.52) dominate, as seen when N> 4.

5.2.4 Ring-currents in N-AntiCOT

Ring currents in the N-AntiCOT systems are simple to rationalise. Two types of N-AC can be imagined. From the general formula in Figure 5.4 (a), one can imagine two cases which support the alternating rim of octagons and hexagons with identical Kekulé structure counts: x=2, y=0 and x=1, y=1. The former is now referred to as N-AC$'$ and the latter the N-AC series. In both cases the perimeter faces alternate between $4n + 2$ and 4n, and the centre face is of type $4n + 2$ for even N and 4n for odd N. Ignoring the

obvious steric strain, both types are shown in Figure 5.10 for the case of N=6.

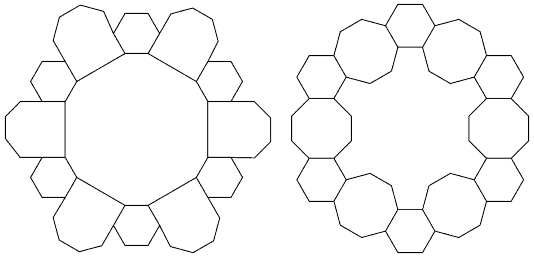


Figure 5.10: Two example constructions of 6-AntiCOT. (Left) x=2, y=0 6-AC′, (right) x=1, y=1 6-AC.

Dealing with the less interesting N-AC′ case, this series obeys identical cycle divisibility rules as the equivalent N-AK. Combined with equivalent Kekulé structures, and consequently the number of conjugated circuits, the Randić ring currents are identical to those in the N-AK series. The increase in the area of the circuit is unaccounted in the Randić model, thus the ring current is identical, obeying equations (5.47) − (5.52).

In the case of N-AC, the addition of 2N vertices to the centre ring results in a change in the cycle type. The size of the centre face now changes from 2N in N-AK to $4n$ in the N-AC series. If N=2p (2p+1) the centre circuit is of type $4n$ $(4n+2)$. This has a profound effect on the ring current values (Table 5.4). For the rest of this section only the N-AC series will be considered.

Table 5.4: The ring currents for the hexagon, octagon and central ring of N-AC′ (x=2, y=0) and N-AC (x=1, y=1): top shows raw Randić current magnitudes and bottom shows currents scaled to the largest magnitude. The number of Kekulé structures, K(G), is identical for both N-AC and N-AC′, where 2N denotes the size of the centre face in N-AC′, and $4n$ denotes the size of the centre face in N-AC.

N	K(G)	N-AC′			N-AC		
		Hexagon	Octagon	Centre	Hexagon	Octagon	Centre
2	9	-8	-20	-20	-8	-20	-20
3	20	8	-88	0	24	-56	0
4	49	80	-508	-36	80	-508	-36
5	125	660	-3396	0	688	-3328	0
6	324	4568	-23080	-80	4568	-23080	-80
2	9	-0.4	-1	-1	-0.4	-1	-1
3	20	0.0909	-1	0	0.4285	-1	0
4	49	0.1575	-1	-0.0709	0.1575	-1	-0.0709
5	125	0.1943	-1	0	0.2067	-1	0
6	324	0.1979	-1	-0.0035	0.1979	-1	-0.035

In order to explain the subtle differences in CC ring-current magnitudes between the N-AC and N-AC′ series, it is useful to discuss an additional series where an alternating ring current is also in effect.

5.2.4.1 Sequential alterations of Antikekulene

Consider the set of sub-structures of an N-antikekulene where the squares are sequentially altered to octagons one-by-one until the corresponding N-antiCOT is obtained. The case in point is the example of 6-AK and the sequential conversion to 6-AC. The ring-current maps of these systems fall into two categories and can be rationalised easily.

6-AK and 6-AC support equivalent Randić ring-current magnitudes in equivalent faces, but this is not true of every N-AK and corresponding N-AC. The Randić ring-current maps of the sub-structures (Figure 5.11 (a)) epitomise the effect of divisibility switching in the circuit class. To clearly differentiate between structures, the sub-structures will be denoted by N-AK(M) which indicates the system is based on the N-AK series with M squares altered to octagons, M can range from 0 to N with N-AK(0) equivalent to N-AK, and N-AK(N) equivalent to N-AC.

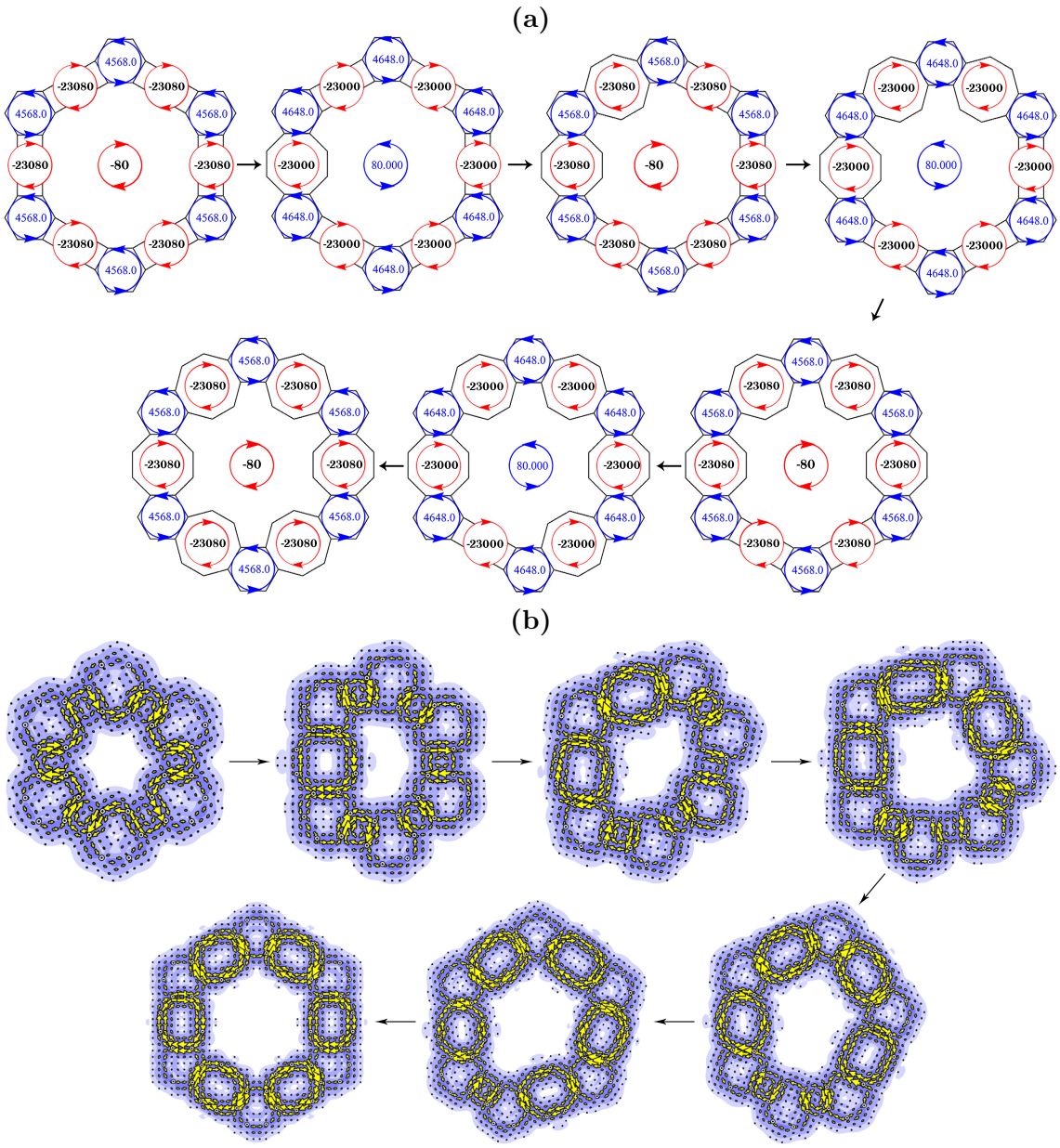


Figure 5.11: The ring currents for the stepwise conversion of 6-AK to 6-AC, as squares are sequentially altered to octagons, starting from 6-AK, top left, until 6-AC is obtained, bottom left, of each individual ring-current model. (a) the Randić based conjugated-circuit model and (b) the *ab initio* pseudo-π ring-current model generated from optimised structures constrained to planarity calculated at the DFT/B3LYP/6-31G** level of theory.

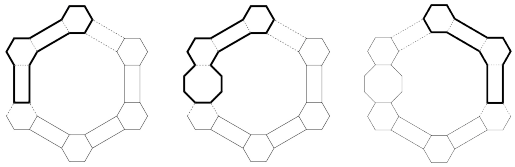
In Figure 5.11(a), two clear alternating sets of ring-current moduli can be observed; differing by magnitude 80 in the octagon and hexagon, and by magnitude 160 in the centre

face as M increases. The first series of ring currents reappear for every 6-AK(M=$2p$), which are all equivalent to those in 6-AK. This is due to the addition of 0, 4 or in general 2M vertices that preserves all cyclic parities. The ring-current magnitudes of the first set are equivalent to the ring currents in 6-AK, as formulated in equations (5.47) − (5.49). In contrast, the ring currents for the 6-AK(M=$2p+1$) systems are not equivalent to 6-AK, and are discussed further later.

Figure 5.11(b) shows the corresponding pseudo-π maps for the changes, demonstrating an increase in current-density within the octagon. Comparison of the hexagon current-density between N-AK(M) maps shows the map is mainly unchanged as M increases. To a lesser extent, this is reproduced in the Randić scaled current. However, as more octagons are added, it becomes clear that octagon faces support stronger paratropic current-densities than the squares. This observation is in direct contrast to the Randić model in which the square and octagon faces are equal, and is rationalised by the decomposition of circuits into the different classes of circuits.

Class (A) circuits

The $4n+2$ or $4n$ type of any class (A) circuit is preserved for any N-AK(M) with respect to the parent N-AK. Consider the three circuits in Figure 5.12 showing: a 6-AK circuit; the corresponding 6-AK(1) circuit containing the octagon; and a 6-AK(1) circuit not containing an octagon. The possible addition (or incidentally removal) of 4 vertices through the cycle expansion (or contraction) to any circuit preserves $4n$ or $4n+2$ types. This effect is also true for the addition of 4 vertices to graph G − C, hence preserving the value of $m\,(\mathrm{G}-\mathrm{C})$ and retaining the parent N-AK circuit class contributions.

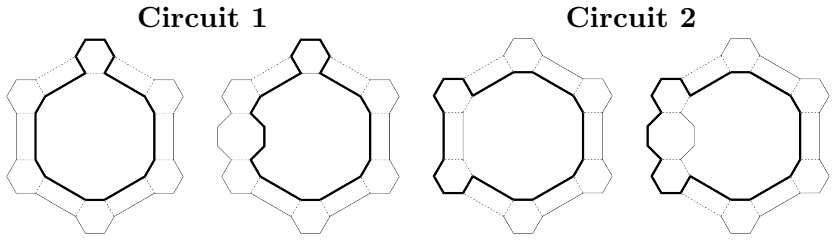


Vertices	14	18	14
Size	$4n+2$	$4n+2$	$4n+2$
m(G − C)	21	21	21

Figure 5.12: Illustrations of three conjugated circuits not containing the centre ring as steps are taken along the pathway from 6-AK to 6-AC by the stepwise alteration of squares to octagons. (left) identifies a circuit in 6-AK, (middle) the equivalent circuit in the single octagon altered system; (right) a circuit where the octagon is not involved. All three circuits have identical m(G − C), and thus an identical Randić current contribution.

Class (B), (C) and (D) circuits

In contrast, the value of M will have an effect on the divisibility of any circuit including the centre ring. For every octagon added, two of the four new vertices are involved in the circuit. Compare the two circuits pairs for the parent 6-AK and 6-AK(1) systems. If the octagon *is not* involved in the conjugated-circuit (circuit 1 Figure 5.13), the circuit will now contain two extra vertices along the y-route (see Figure 5.4), compared to the equivalent AK circuit. If the octagon *is* involved in the circuit (circuit 2 Figure 5.13), only two vertices along the x-route are involved in the circuit, the other two remaining isolated in graph G − C. Each eventuality results in an inversion of the circuit types between an N-AK(M) and N-AK(M+1) series. This rationale applies to both (B), (C) and (D) circuit classes.



Vertices	16	18	18	20
Size	$4n$	$4n+2$	$4n+2$	$4n$
***m*(G − C)**	1	1	1	1

Figure 5.13: Examples of two circuits in 6-AK and the octagon-altered systems. Circuit 1 highlights the effect when a square or octagon is not involved in the circuit; circuit 2 highlights the effect when a square or octagon is involved in the circuit.

The inversion of circuit types explains the alteration observed in Figure 5.11(a). In addition, this alternating magnitude is only small owing to the preservation of class (A) circuits, which, from established current magnitude equations, are the dominant contributors. The central face ring current is fully inverted for each increase in M. This is rationalised by the reversal of all centre containing circuits, i.e. all class (B), (C) and (D) circuits.

5.2.4.2 Ring-currents in N-AntiCOT

Discussion now returns to the original observation. Table 5.4 identifies different current magnitudes between (2p+1)-AK and (2p+1)-AC, but identical magnitudes for (2p)-AK and (2p)-AC. All systems can be considered identical to a corresponding N-AK(M). When N= $2p$, the number of added vertices to all circuits preserves parity thus Randić ring currents obey equations (5.47) - (5.49). In contrast when N= $2p+1$, the types of class (B), (C) and (D) circuits invert resulting in a different set of equations:

$$\mathrm{J_{Tot}(Hexagon)} = 2 \times \left[\frac{{F_{2\mathrm{N}}}^2 + 8}{9} + F_{\mathrm{N}} + 2 \right] \tag{5.53}$$

$$\mathrm{J_{Tot}(Octagon)} = 2 \times \left[\frac{-5{F_{2\mathrm{N}}}^2 - 4}{9} + 3F_{\mathrm{N}} + 2 \right] \tag{5.54}$$

$$\mathrm{J_{Tot}(Centre)} = 0 \tag{5.55}$$

Therefore, the Randić model predicts the presence of diatropic currents in hexagons, strong paratropic currents in the octagons and a weak paratropic current in the centre face. Again, equations (5.53) - (5.55) rationalise the observed differences in the scaled currents seen in Table 5.4. The magnitude of current present in an octagon is five times larger than that in a hexagon, at large N once the F^2 term dominates.

This now completes the analysis of the ring currents using the conjugated-circuit method. Next comparisons are made to the *ab initio* and Hückel-London models to compare the conclusions of this graph-theoretical method with those that have an explicit quantum mechanical form.

5.3 Alternative Ring-Current Models

To test the conclusions of the CC model, other methods of ring current calculation should be employed. These include the Hückel-London and pseudo-π methods, discussed in depth in Chapters 3 and 2, respectively.

5.3.1 The Hückel-London Model

First, the graph-theoretical Hückel-London, HL, model, is employed. The variant of the HL theory used here is based on the Aihara method of partitioning current contributions from all possible cycles:[58,211]

$$\frac{\mathrm{J_C}}{\mathrm{J_0}} = 18. \left(\frac{S_\mathrm{C}}{S_0}\right) \left(\prod_{\mathrm{i}=1}^{|\mathrm{C}|} \frac{\beta_\mathrm{i}}{\beta_0}\right) \left(\sum_{k=1}^{\mathrm{occ}} \frac{\phi_{\mathrm{G\text{-}C}}\left(\lambda_k\right)}{\phi_\mathrm{G}{}'\left(\lambda_k\right)}\right) \tag{5.56}$$

where symbols are defined in Chapter 3, and minor corrections are made for degenerate energy levels. Scaled and raw HL results for the symmetry distinct faces in the N-AK series are reported in Table 5.5.

Table 5.5: The raw and scaled to the largest magnitude Hückel-London ring currents for the N-antikekulene series for the three different sized faces. Raw results are given in terms of the standard benzene result.

N	Raw Current			Scaled Current		
	Hexagon	**Square**	**Centre**	**Hexagon**	**Square**	**Centre**
2	-3.8548	-6.4476	-6.7897	-0.5677	-0.9496	-1
3	-1.7023	-4.1223	-1.9906	-0.4130	-1	-0.4829
4	-1.4538	-2.8020	-2.8812	-0.5046	-0.9725	-1
5	-0.5710	-2.2574	-0.5684	-0.2530	-1	-0.2518
6	-0.6061	-1.6570	-1.3865	-0.3658	-1	-0.8368
7	-0.1635	-1.4760	-0.1687	-0.1108	-1	-0.1143
8	-0.2175	-1.1748	-0.6729	-0.1851	-1	-0.5728

Perhaps not surprisingly, the Hückel-London ring currents are qualitatively and quantitatively different to those calculated using the Randić model. All faces in all N-AK homologues support paratropic currents, indicating global antiaromaticity. Square faces support the strongest current with hexagons supporting, initially, around half the square

current, and decreases as N increases. A major difference is in the strength of the centre current which is, in all cases, as large or larger than the hexagon face.

Attention is now turned to the N-CB series. Comparison of the HL currents in Table 5.6 with the Randić currents in Table 5.1 illustrates qualitative agreement. Comparing scaled currents, both methods identify the hexagon as the strongest contributor with the magnitude of the centre ring current decreasing in intensity as N increases. Furthermore, the two sets of results agree in the regular alternation in tropicity.

Table 5.6: The raw and scaled to the largest magnitude Hückel-London ring currents calculated using the Aihara HL model for the N-cyclic benzenoids for the two distinct faces. Raw results are given in terms of the standard benzene result.

N	**Raw Current**		**Scaled Curret**	
	Hexagon	**Centre**	**Hexagon**	**Centre**
2	0.4113	-2.5448	0.1616	-1
3	1.4593	1.0376	1	0.7110
4	0.9747	-0.6426	1	-0.6593
5	1.2494	0.3134	1	0.2508
6	1.1129	-0.1621	1	-0.1457

HL ring currents for the N-AC series are listed in Table 5.7. The N-AC series supports a global paratropic current with the largest magnitude of current in the octagon. Trends in this series are similar to those in the N-AK series, with the central ring varying in strength according to the parity of N. The HL ring currents of the N-AC′ series, see Table 5.7, indicates the presence of a global paratropic or diatropic system depending on the parity of N. Overall, HL trends for neither N-antiCOT series are reproduced to an acceptable level in the Randić model. For example, the equiaromaticity between N-AC, N-AC′ and N-AK series noted earlier in the Randić series is not present in HL theory. In fact, in HL theory, the two N-AC series differ significantly in both strength and tropicity.

Table 5.7: The raw and scaled to the largest magnitude Hückel-London ring currents calculated using the Aihara HL model for the N-AC series for the three symmetry distinct faces. Raw results are given in terms of the standard benzene result.

N	Raw Current			Scaled Current		
	Hexagon	Octagon	Centre	Hexagon	Octagon	Centre
2	-6.7178	-9.8623	-10.149	-0.6619	-0.9718	-1
3	1.0853	2.2319	0.5542	0.4863	1	0.2483
4	-2.9094	-4.322	-4.6345	-0.6278	-0.9326	-1
5	0.6762	1.1941	0.4555	0.5663	1	0.3815
6	-1.5049	-2.4577	-2.3514	-0.6123	-1	-0.9568

Table 5.8: The raw and scaled to largest magnitude Hückel-London ring currents calculated using the Aihara HL model for the N-AC′ series for the three symmetry distinct faces. Raw results are given in terms of the standard benzene result.

N	Raw Current			Scaled Current		
	Hexagon	Octagon	Centre	Hexagon	Octagon	Centre
2	-4.1856	-6.7182	-5.8311	-0.6230	-1	-0.8680
3	-1.9216	-3.9334	-2.0997	-0.4885	-1	-0.5338
4	-1.5999	-2.7902	-2.3485	-0.5734	-1	-0.8906
5	-0.7965	-2.1121	-0.6098	-0.3771	-1	-0.2887
6	-0.7864	-1.6413	-1.0909	-0.4791	-1	-0.6647

In general, the majority of antikekulene derivatives show discrepancies between the CC and HL models. This is not unexpected due to the exclusion of non-conjugated cycles in the CC models that are included in the Aihara HL model. However, one problem with the Aihara form of the HL model is that it includes ring area based on idealised, sterically unlikely geometries. To an extent, this problem is mitigated by using optimised structures as in the *ab initio* model.

5.3.2 The *ab initio* Methods

Next, consider the pseudo-π and *ipsocentric* methods.[105,129,140] Using optimised geometries, calculated at the DFT, B3LYP/6-31G** level of theory, qualitative current-density maps can be calculated. For the N-AK series, those with small N will be highly distorted. From a previous study, only 6-AK is predicted to be a planar D_{6h} symmetrical

structure, with 4-AK and 5-AK predicted to be bowl-shaped.[212] This is probably due to the ring strain introduced by a small-sized central ring.

The structures of 5, 6 and 7-AK were optimised at the B3LYP/6-31G** level with the Gaussian 09 computational package.[213] Structures of 6 and 7-AK optimised to planarity at the D_{Nh} symmetry. In contrast 5-AK, constrained to D_{5h} symmetry, is a high energy structure with an imaginary frequency at $84.5i$ cm^{-1} corresponding to the breaking of planarity. Current-density maps were generated for the planar D_{Nh} structures at the CHF/6-31G** level for the *ipsocentric* method, and at the CHF/STO-3G level for the pseudo-π method using the SYSMO98 computational package.[214] Ring-current maps for 5, 6 and 7-AK are shown in Figure 5.14.

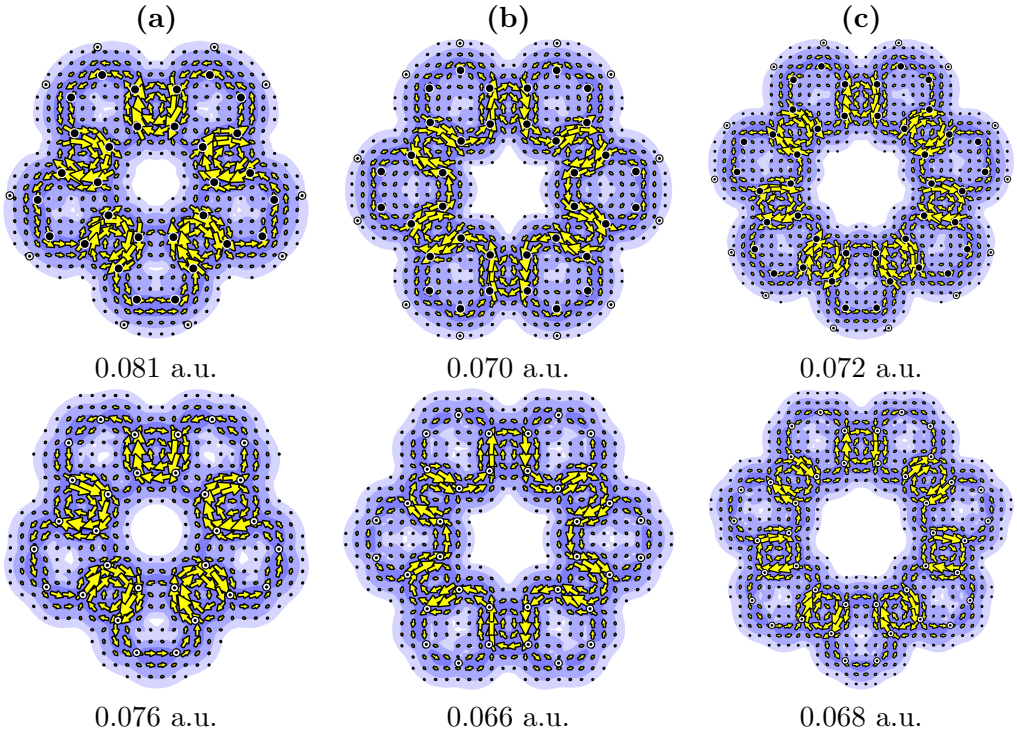


Figure 5.14: Current-density maps for: column a) 5-antikekulene, column b) 6-antikekulene and column c) 7-antikekulene calculated with the full CHF/6-31G** *ipsocentric* method (top) and CHF/STO-3G pseudo-π method (bottom). Geometries of N-AK systems were calculated at the DFT/B3LYP/6-31G** level constrained to the D_{Nh} symmetry. j_{max} values are indicated below the current-density map.

Surprisingly, there is general qualitative agreement between the, presumably, more

accurate *ab initio* methods and the Randić conjugated-circuit maps. From the *ipsocentric* and pseudo-π current-density maps, the squares are strongly paratropic and hexagons are weakly diatropic. Current moduli are high for bonds shared by hexagons and squares owing to vector reinforcement of the diatropic hexagon currents and paratropic square currents.

This predicted pattern of current density differs slightly from the Hückel-London model. Both methods predict paratropicity in squares, supporting the largest modulus of current. However, there is disagreement on the overall tropicity of the hexagonal faces. In addition, the centre current pattern is dependent on the model. From *ab initio* current maps, the central ring appears to support a weak diatropic and paratopic ring current present for the N=2p and N=2p+1 antikekulenes, respectively. This is in direct conflict with the strong paratropic current calculated in the HL model. One possible reason for these differences is the sensitivity of the HL model to the ring area (S_C/S_0), which is calculated using idealised geometries. These geometries are likely to result in large discrepancies, when compared to optimised *ab initio* structures.

Ab initio calculations could not be performed for multiple entries of the N-CB series (with the exception of 3-CB aka coronene) and N-AC series, owing to the difficulties in optimising structures. This is suspected to stem from the ring and bond strain introduced by dictation of specific ring sizes.

5.4 Conclusion

The ring currents of the antikekulene homologues and derivatives were evaluated using a series of models. The homologues of antikekulene are defined as those systems containing alternating squares and hexagons around a central cycle of even size; and the derivatives considered here are where any square has been altered to either a hexagon or an octagon. Whilst the results agree with the general consensus in the literature that antikekulene is antiaromatic, there still exists some ambiguity.

For these molecules, the conjugated-circuit models are shown off to their full potential, providing simple analytical formulae that describe the ring-current magnitudes for the different sized rings. The explicit relationship of Fibonacci and Lucas number sequences to the Kekulé valence structures allows the construction of functions for the ring-current, at least in the Randić CC model.[100] Inclusion of cycle area in the Mandado[112] and Ciesielski et al.[110] models result in a more complicated, though in principle tractable, formulation. Examination of these models suggests that any algebraic approach is cumbersome to give useful explanations owing to the area evaluation necessary for each individual cycle.

Cycle expansion in the antikekulene series has been used to construct a series of derivatives with constant Kekulé count and (in the Randić model) analytical formulae of the ring currents. This has proved useful in rationalising trends observed in ring current magnitudes, and equiaromaticity in the N-AC, N-AC′ and N-AK series.

Comparison of the Randić model with the Hückel-London model demonstrates disparity, especially with the N-AC, N-AC′ series. HL currents predict these series to be very different, with tropicity dependent on the parity of N. This is not reproduced in the Randić model. Unfortunately comparisons with the *ab initio* model can only be made for the N-AK series, owing to the ring and bond strain of structures. For the N-AK series there is agreement between the *ab initio* and Randić models predicting paratropic squares and centre and diatropic hexagons. However, this conclusion, for N-AK, is in direct contrast to the fully paratropic HL model.

Chapter 6

Problematic Perylenes

6.1 Introduction

By construction, a conjugated-circuit method for evaluating ring currents has several limitations. These include: the inability to deal with odd-sized cycles, as found in cyclopentadiene; lack of a clear formulation for inclusion of charge; and finally the exclusion of non-Kekuléan structures. These shortcomings combine to fuel the arguments from authors such as Gutman who advocate abandoning Kekulé-based models altogether.[144,215,216] One further instance epitomising the failure of CC models for systems that, on first inspection appear treatable by CC models, are those with fixed Pauling Bond Orders.[114] This feature was mentioned in passing in an early CC paper,[217] and many documented cases have been presented including, but by no means limited to: chevrons,[218] indacenoids[219] and systems such as fluoranthene[174,220] and zethrene.[221] The phenomenon is commonly referred to as '*empty rings*'.[222–224]

The focus of this chapter is an examination of perylene and its various derivatives with the aim of understanding the ring-current behaviour of both graph theoretical models and *ab initio* methods. An extreme view of the perylene molecule is as two naphthalene '*monomers*' joined together with two fixed single bonds, referred to as '*spoke bonds*', consistent with Pauling Bond Orders (defined earlier in 1.3.4).[215] Ring-current maps for the three main CC models, as well as Hückel-London and *ab initio* methods, are all illustrated in Figure 6.1. All CC models have a total absence of current in the centre ring, a feature which is not reproduced in the graph theoretical HL model. This failure of CC models can be attributed directly to the fixed-single-bond problem.

The current maps calculated through the *ab initio* and pseudo-π methods both show weak but non-zero current along the spoke bonds. Scaling of arrows makes this current

hard to see against the stronger flow in the naphthalene rings, but it is present. HL is a plausible alternative, reproducing the fact that the spoke current is non-zero.

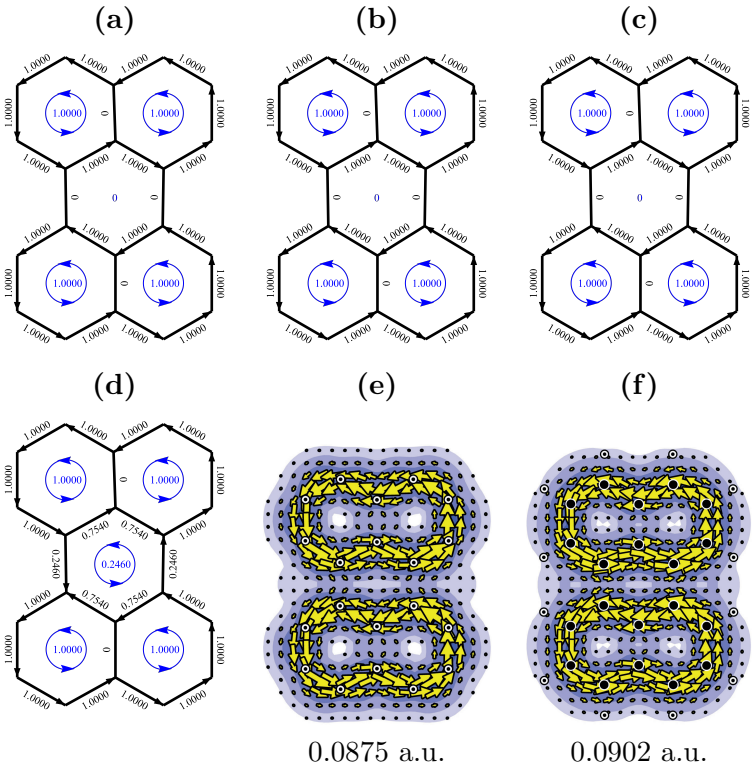


Figure 6.1: The ring current maps of perylene calculated using the various different models. The scaled CC models: (a) the Randić model, (b) the Mandado model, (c) the Ciesielski et al. model; and the models employed as comparative tools (d) the Hückel-London method, (e) the pseudo-π model and (f) the full *ipsocentric* approach. Values below the *ab initio* maps refer to the $j_{\max}$ of the calculation.

The purpose of the present chapter is to discuss pitfalls of the CC models and to rationalise the different ring-current maps that arise from other methods. The approach will be to regard perylene as a limiting case of two different families. If perylene is defined as the construction of two 'monomer' naphthalene rings joined at the 1 and 3 positions, the first set of systems can be constructed with various other bicycles replacing naphthalene. In this sense, naphthalene is changed to pentalene, heptalene or octalene. The effect this alteration has on the ring current is explored in Section 6.2. The second change is through a linear expansion of the monomer unit, from naphthalene to anthracene,

tetracene and beyond, with the addition of more spoke bonds as the chain increases. The effect of this change is discussed in Section 6.3.

6.1.1 Symmetry of orbitals

Before these investigations of the perturbations of perylene are detailed, it is useful to consider a symmetry argument that makes assignment of molecular orbitals easier.

Using the defined construction of the perylene systems as the fusion of two monomers, the symmetries of the molecular orbitals, MOs, in the perylene can be assigned from those of the monomer. For the present section we will consider only pseudo-π orbitals of perylene, in which AOs have s-orbital character. Although, the reasoning can easily be adapted to the π-orbitals (through equation (2.14)).[140] This methodology will be used for all derivatives investigated in this chapter. Illustrating by example in Figure 6.2, two naphthalene LOMO A_g orbitals can overlap in two ways: either both orbitals will have the same phase leading to the constructive combination denoted (+), or orbitals will have opposite phases leading to destructive overlap, denoted (−). These correspond to the two lowest occupied levels of perylene, the (+) combination having A_g symmetry and the (−) combination having B_{1u} symmetry.

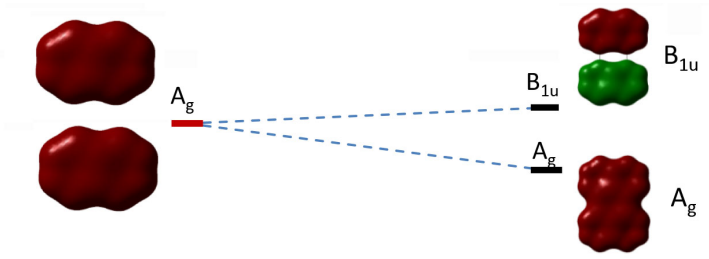
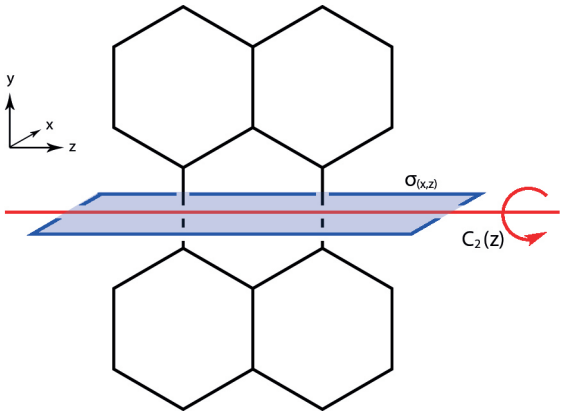


Figure 6.2: Illustrations of the symmetry argument for the formation of perylene MOs from the monomer MOs. Two eventualities of orbital overlap can be envisaged for the monomer molecular orbitals leading to constructive overlap, A_g, or destructive overlap, B_{1u}.

This is true for *all* molecular orbitals of the perylene derivatives and can be understood using the D_{2h} point group of the system. In the D_{2h} point group there are two symmetry operations intersecting the spoke bonds, the $\sigma_{(x,z)}$ and the $C_2(z)$ (Figure 6.3). Across the spoke bonds, the symmetry element for each operation produces a (+) or (−) symmetry-adapted combination. For example, an A_g combination has +1 under both operations

and thus represents a (+)-combination.



D_{2h}	**E**	$\mathbf{C_2(z)}$	$\mathbf{C_2(y)}$	$\mathbf{C_2(x)}$	**i**	$\boldsymbol{\sigma_{(x,y)}}$	$\boldsymbol{\sigma_{(x,z)}}$	$\boldsymbol{\sigma_{(y,z)}}$
$\mathbf{A_g}$	1	1	1	1	1	1	1	1
$\mathbf{B_{1u}}$	1	-1	1	-1	-1	1	-1	1
$\mathbf{B_{2u}}$	1	1	-1	-1	-1	-1	1	1
$\mathbf{B_{3g}}$	1	-1	-1	1	1	-1	-1	1

Figure 6.3: The major symmetry operations across the spoke bond of perylene and the character table for the D_{2h} point group.

Nodal character in the monomer along other axes will be preserved in the combination, thus the only changes needing to be considered are those across the z axis. Therefore, the symmetry conversions can be tabulated indicating the starting monomer symmetry and the final combination orbital symmetry. These are displayed in Table 6.1 (and can be extended to encompass other point groups provided a symmetry operation exists bisecting the spoke bonds).

Table 6.1: The (+) and the (−) combinations of orbitals formed from two of the monomer molecular orbitals.

Monomer MO		**Perylene MO**	
		(−) combination	**(+) combination**
A_g	→	B_{1u}	A_g
B_{1u}	→	B_{1u}	A_g
B_{2u}	→	B_{3g}	B_{2u}
B_{3g}	→	B_{3g}	B_{2u}

6.2 The Different Bicycles

Now, consider the systems where the monomer in perylene is altered to another bicycle. Analogues to perylene can be designed with pentalene, heptalene and octalene monomers. Ordered according to the size of the monomer graph, Figure 6.4 illustrates these cycles, which collectively will be described as the *bicycles of perylene*.

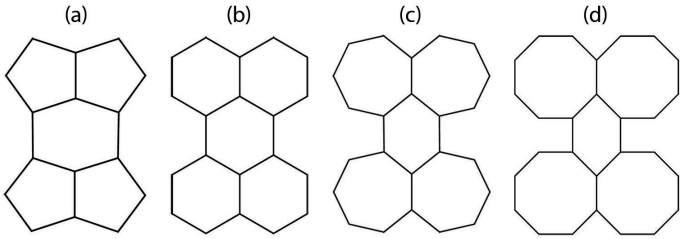


Figure 6.4: The four bicycles of perylene, where the monomer has been changed to a different sized bicycle: (a) dipentalene, (b) perylene, (c) diheptalene and (d) dioctalene.

In principle, the purpose of the present investigation is to discover what, if any, change is observed in the ring current in this series. Since the maximum point group of all bicycles is D_{2h}, simple analogies can be made regarding occupied energy levels and orbital contributions to properties of the current. Particular emphasis will be placed on those cases where current appears or is strong along the spoke bonds. It turns out that changing the size of the monomers has a dramatic effect on the predicted ring current in conjugated-circuit, Hückel-London and *ab initio* methods. Each of these models is now examined.

6.2.1 A Conjugated-Circuit Approach

One obvious feature is that, in the cases of dipentalene and diheptalene, the altered shape of the monomer allows the construction of conjugated circuits involving the central ring. This is a feature applicable to all cases where the monomer is non-alternant. For the specific cases of dipentalene and perylene, the full set of conjugated-circuits is shown in Figure 6.5.

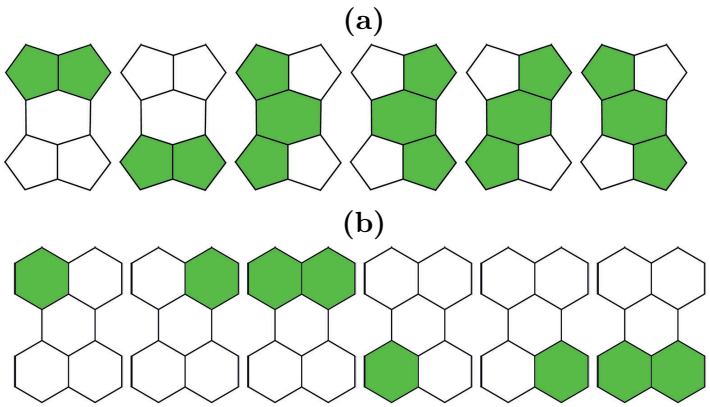


Figure 6.5: All possible conjugated circuits, formed from the shaded faces, for (a) dipentalene and (b) perylene. In both cases analogies can be drawn with other cycles in the series. Other non-alternant graphs will have identically located conjugated circuits to those in (a), the only difference being the size of the monomer faces. Likewise in the case of (b) analogies can be made with the bipartite examples, such as dioctalene.

In the case of the non-alternant graphs, all conjugated circuits are of consistent size: all are classed as 4N cycles. The only difference is in the area enclosed, which affects the prediction in Mandado and Cieselski et al. models. For bipartite graphs, the divisibility of CCs will depend on the size of the monomer. For perylene, all conjugated circuits are of size $4N + 2$; for dioctalene, the conjugated circuits are a mixture of 4N and $4N + 2$ circuits. By symmetry there are two unique ring currents, corresponding to the faces of the monomer and the central ring. The ring currents in these faces, calculated using the three CC methods, are summarised in Table 6.2.

Table 6.2: The total conjugated-circuit ring currents for the two faces of the four bicycles investigated, the monomer face, J_{Mono}, and the centre face, J_{Cen}. Values are the summation of relevant conjugated circuits and are formulated using the three major conjugated circuit models (as described in section 1.3.3). J′ is the scaled ring current where the magnitude is normalised to that of $|J_{Mono}|$.

CC Model	Cycle	Dipentalene	Perylene	Diheptalene	Dioctalene
Randić	J_{Mono}	-12	36	-12	0
	J_{Cen}	-8	0	-8	0
	J'_{Mono}	-1.0	1.0	-1.0	0
	J'_{Cen}	-0.666	0	-0.666	0
Cieselski et al.	J_{Mono}	-9.947	27	-18.784	16.726
	J_{Cen}	-9.298	0	-15.19	0
	J'_{Mono}	-1.0	1.0	-1.0	1
	J'_{Cen}	-0.935	0	-0.809	0
Mandado	J_{Mono}	-0.948	1	-0.497	-0.179
	J_{Cen}	-0.688	0	-0.421	0
	J'_{Mono}	-1.0	1.0	-1.0	-1
	J'_{Cen}	-0.726	0	-0.848	0

From a conjugated-circuit approach the presence of current, or lack thereof, crossing the spoke bonds is easily rationalised. For a bond to support current, it must be involved in a CC (i.e. have $1 > PBO > 0$), and the current must not be removed through cancellation (as it would be in the case of dioctalene in the Randić model). For non-alternant graphs, there exist CCs that involve the central ring and thus induce current in the spoke bond. As, all circuits in these systems are of size 4n, contributions will be paratropic in direction. However, for bipartite graphs, there are no such CCs that involve the spoke bond, and hence there is zero current in the centre face for all CC models.

6.2.2 Hückel-London Model

Evaluation of the Hückel-London ring current using the Aihara formalism (Chapter 3) provides an analogous method for calculating cyclic contributions to the total HL current. There are nine symmetry-distinct cycles, a mixture of conjugated and not conjugated for each bicycle. For the general bicycle, with n referring to the number of carbon atoms of

degree two required to complete the cycle (e.g. for dipentalene, n=2). The set of Aihara cycles is shown in Figure 6.6.

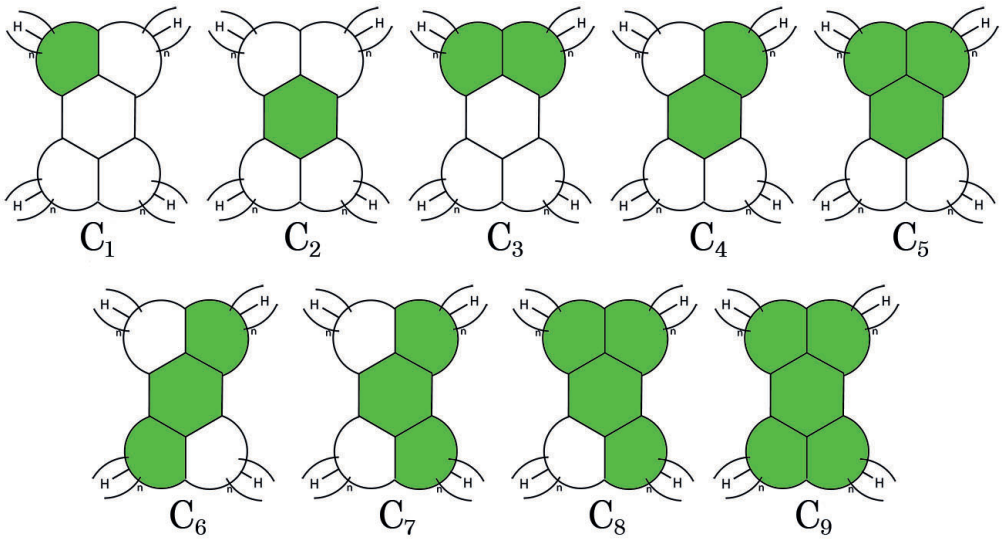


Figure 6.6: The unique Aihara cycles for all the bicycles of perylene, the area of the cycle is highlighted in green. The general case is shown where n refers to the number of degree two carbons: n = 2 (dipentalene), n = 3 (perylene) etc. Numbers below the cycle refer to the labelling convention. Cycles may be present in symmetry-related copies, for example cycle 1 appears four times in the four corner faces.

Using the labelling notation for the Aihara cycles, the individual cyclic-HL contribution for each system is summarised in Table 6.3. Each cycle has multiple 'isomers'. For example there are four equivalent C_1 cycles, but only one will contribute to the given monomer face. The Aihara cycles will be a mixture of conjugated and non-conjugated circuits that differ depending on the bicycle in question. The conjugated cycles are represented by shaded cells in Table 6.3.

Table 6.3: The cyclic Hückel-London contributions from the nine unique cycles, as identified in Figure 6.6. Negative (positive) values indicate paratropic (diatropic) currents. Highlighted cells indicate those Aihara cycles that are also conjugated circuits.

Cycle	Isomers	Dipentalene	Perylene	Diheptalene	Dioctalene
$\mathbf{C_1}$	4	8.448	0.457	7.092	-2.203
$\mathbf{C_2}$	1	-62.292	0.097	-19.853	0.454
$\mathbf{C_3}$	2	-23.057	0.489	-20.585	3.126
$\mathbf{C_4}$	4	88.610	0.039	39.475	-0.403
$\mathbf{C_5}$	2	-61.854	-0.024	-20.306	-0.201
$\mathbf{C_6}$	2	-105.503	0.017	-51.018	0.257
$\mathbf{C_7}$	2	-105.503	0.017	-51.018	0.257
$\mathbf{C_8}$	4	67.916	-0.01	22.880	-0.112
$\mathbf{C_9}$	1	-41.449	0.006	-9.456	0.045

The total HL ring current is calculated as the sum of those cycles enclosing the face in question (see Chapter 3). For the two faces, the total currents are the combinations:

$J_{Mono} = \mathbf{C_1} + \mathbf{C_3} + \mathbf{C_4} + \mathbf{C_5} + \mathbf{C_6} + \mathbf{C_7} + (3 \times \mathbf{C_8}) + \mathbf{C_9}$

$J_{Cen} = \mathbf{C_2} + (4 \times \mathbf{C_4}) + (2 \times \mathbf{C_5}) + (2 \times \mathbf{C_6}) + (2 \times \mathbf{C_7}) + (4 \times \mathbf{C_8}) + \mathbf{C_9}$

The total HL current is then summarised in Table 6.4.

Table 6.4: The total HL currents for the four bicycles investigated, corresponding to the two different faces, the monomer face, J_{Mono}, and the centre face, J_{Cen}. Values are the summation of relevant cyclic HL values (Table 6.3). J' is the scaled ring current where the magnitude is normalised to that of $|J_{Mono}|$.

Cycle	Dipentalene	Perylene	Diheptalene	Dioctalene
J_{Mono}	-36.561	0.970	-37.175	1.215
J_{Cen}	-23.359	0.239	-24.572	-0.039
J'_{Mono}	-1.0	1.0	-1.0	1.0
J'_{Cen}	-0.639	0.246	-0.661	-0.032

Scaled HL ring currents for the non-alternant bicycles are very similar, with the centre cycle current being roughly 2/3 of that of the monomer. Surprisingly there is also agreement between HL and Randić CC models, where an exact 2/3 factor is a straightforward mathematical consequence of the CC model. However, perylene and dioctalene show dissimilar HL currents, rationalised by the further cancellation of aromatic

and antiaromatic contributions in dioctalene. The HL model denotes a centre current roughly 25% of the monomer current for perylene, and roughly 3% for dioctalene, neither of which are present in CC models. Considering the latter molecule, the small size of the central current could be taken at face value as a support for the CC-like models. However, all three models give disparate conclusions (Table 6.2) for the overall tropicity of this molecule. The diatropicity of the monomer face in dioctalene is predicted only in the Ciesielski et al. model.

In a general sense, both non-alternant systems support a global paratropic current, with 66% of the monomer face current arcing across the spoke bond. Bipartite systems are less consistent: perylene and dioctalene support diatropic currents, but only perylene is globally diatropic, whereas dioctalene is locally diatropic within the monomer units. Compare Tables 6.3 and 6.2 for the individual circuits. For bipartite graphs, the currents of largest magnitude are in the conjugated circuits. In the non-alternant systems, other cycle contributions also play a significant role.

6.2.3 *Ab initio* ring current calculations

Next, the *ab initio* current-density maps are considered. In all cases, molecular structures were optimised in Gaussian09 to the DFT/B3LYP/6-31G** level of theory with a constraint of planarity. With the exception of perylene, all planar structures exhibit at least two imaginary frequencies. This is to be expected from considerations of ring strain and steric clashes of exo hydrogen atoms. Pseudo-π current-density calculations were then performed, as described earlier in section 2.1.2.

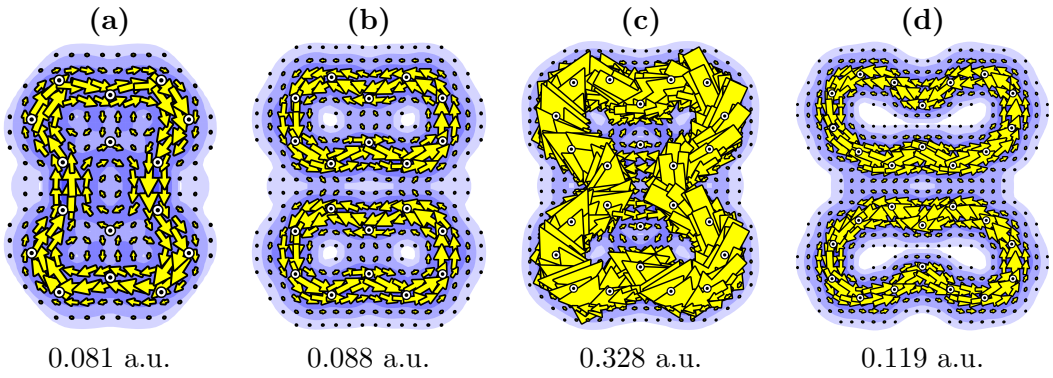


Figure 6.7: Current-density maps for the bicycles of perylene: (a) dipentalene, (b) perylene (c) diheptalene and (d) dioctalene.

As evident in Figure 6.7, an alternating pattern emerges similar to that found with the conjugated-circuit and HL approaches. The alternant bicycles support diatropic currents with predominantly localised monomer-based currents. This observation is consistent with HL and CC models. Non-alternant bicycles show a paratropic current circulating strongly around the perimeter, passing from one monomer to the other. Again, this is consistent with the general conclusions from the graph theoretical methods.

The non-alternant bicycles are highly distorted systems. In the simplest model of π-distortivity, they show large 'Heilbronner' vectors, with negative eigenvalues of larger magnitude than the isolated monomers.[225,226] As a result, current-density calculations of dipentalene and diheptalene are susceptible to molecular geometry and, in the case of dipentalene, the symmetry point group must be dropped from D_{2h} to C_s. This drop in symmetry has had an impact on the ring-current magnitudes and is the reason for the difference in intensities of dipentalene and diheptalene in Figure 6.7. A small HOMO-LUMO gap will result in large paratropic currents, such as those predicted in diheptalene. A similar interface is expected for dipentalene, but the effect has been mitigated by the symmetry drop, where the gap opens up through a 2^{nd} order Jahn-Teller interaction.

6.3 Extensions of Perylene

6.3.1 Nomenclature

Next we consider the cases where monomers of perylene are extended to include longer linear polyacenes. A series can be identified where the number of hexagons of the monomer (the number of faces in the top or bottom rows) varies between 1 and N, thus retaining the D_{2h} point group symmetry. Using this notation, experimentally known systems can then be identified: biphenylene (N= 1), perylene (N= 2) and bisanthrene (N= 3).[227] These systems will be collectively referred to as the *perylene extensions*, with the first four illustrated in Figure 6.8.

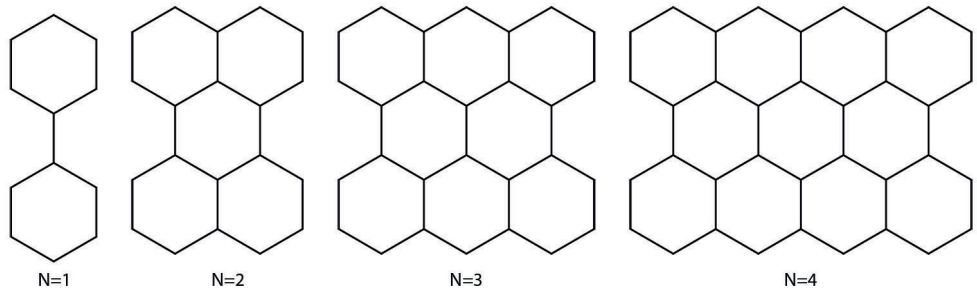


Figure 6.8: The first four of the altered perylene systems investigated in this section. N refers to the number of faces in the top row.

Individual systems are labelled according to the number of faces in each of the three rows. In this notation perylene is denoted as 212-perylene. Furthermore, the faces will be labelled according to the following convention (see Figure 6.9): faces in the top and bottom rows (which are symmetrically equivalent) are labelled **a**, **b**, **c** etc. and faces in the centre row are labelled **i**, **ii**, **iii** etc. After reaching the mid point of each row, labels repeat in reverse order counting down to take into account the symmetry equivalence of corresponding faces. The ring currents from all of the various models are discussed in the following sections with particular emphasis placed on trends.

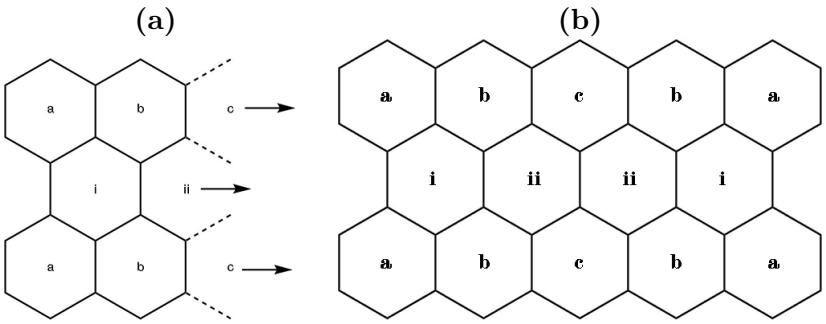


Figure 6.9: The convention of cycle labelling for the general N-extension of perylene, (a) identifies the labels of the different rings which (b) are then used in the example of 545-perylene.

6.3.2 Conjugated-Circuit models

The first method of ring-current calculation to consider is the Kekulé structure-dependent conjugated-circuit model. The lack of conjugated circuits involved in the central ring again results in a ring-current picture devoid of spoke bond current. For this section only the Randić CC model will be reported, but the other CC models also display maps void of central ring current. The ring currents for the first four extensions are shown in Figure 6.10.

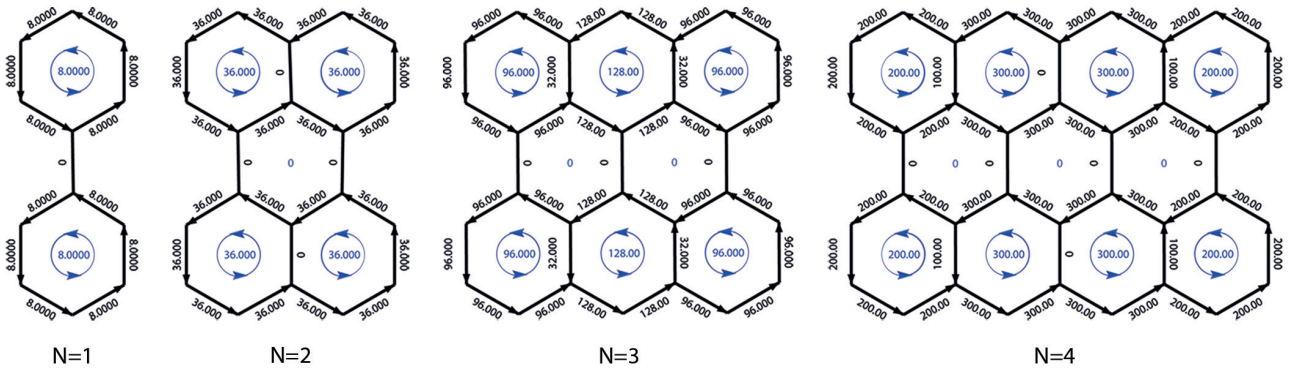


Figure 6.10: The ring currents calculated using the Randić conjugated-circuit model for the first four perylene extensions. Ring currents indicate absence of current in the central ring and across the spoke bonds. Numbers along the bonds denote bond currents, and those at the face centres denote ring currents.

Union of two alternant conjugated linear polyacene 'monomers' means any new rings created will be non-conjugated owing to the enforcement of fixed single spoke bonds. This is a particular example of a previously known phenomenon involving even alternant

hydrocarbons, documented by Dewar.[228] Hence, all CC ring-current models give maps consisting of two localised monomer circulations for *all* N-extensions of perylene. This picture is in sharp disagreement with the prediction of HL and *ab initio* maps.

6.3.3 The Hückel-London model

Next, ring-currents calculated from more accurate models are considered. In this family of molecules, use of the Aihara Hückel-London formalism[159,166] is impractical: as N increases, one can readily appreciate that the number of possible cycles increases rapidly, from 22 cycles at N=2 to 27650 at N=6. Whilst information on the individual HL cyclic contributions could be useful, the analysis soon becomes impractical. However, any HL formalism from the arsenal available can be used to compute the total HL current. The patterns of ring-currents and bond-currents are displayed in Figure 6.11.

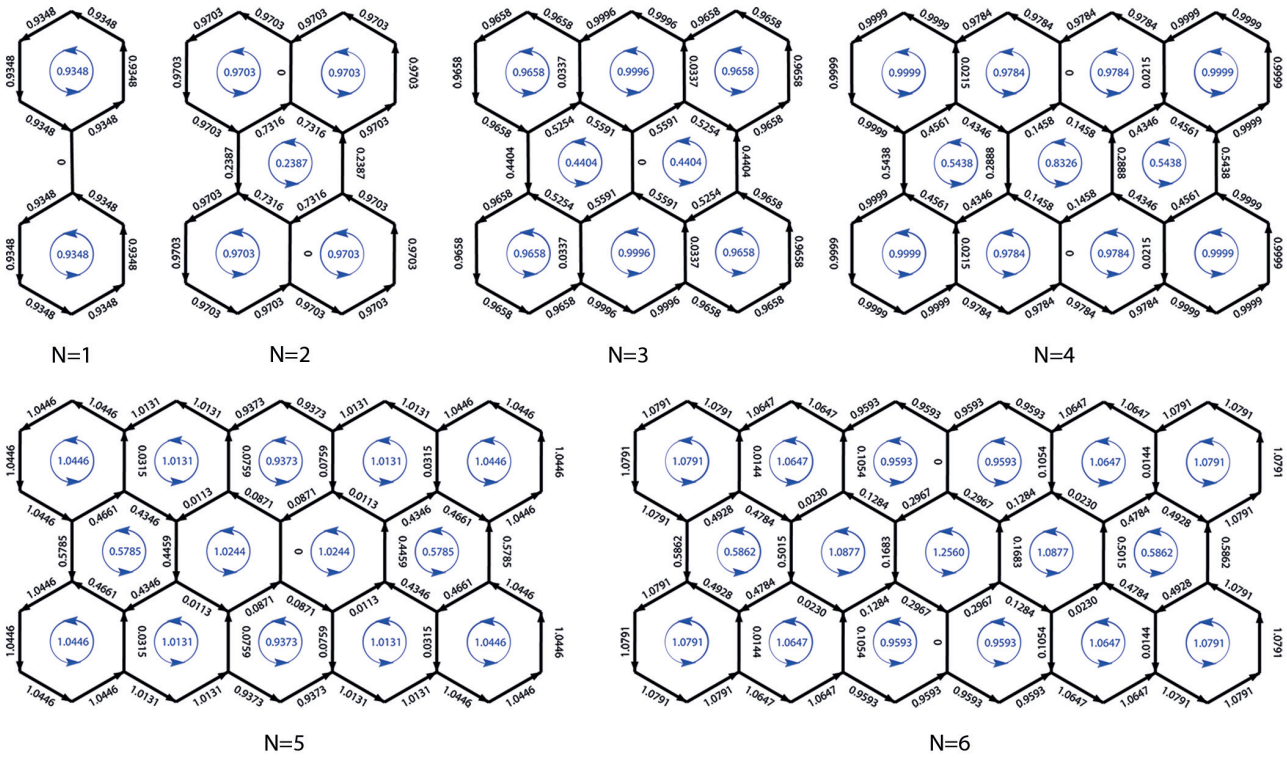


Figure 6.11: Ring-currents calculated using the Hückel-London model. Numbers along the bond denote bond currents, and those in the centre of the faces denote ring-currents.

A changing pattern of ring-currents is noticeable in these systems. In the range

$1 \leq N \leq 3$ the monomer ring-currents are much larger in magnitude than those in the central faces (four times larger in 212-perylene and twice as large in 323-perylene), with the largest magnitude in ring **a** for N=2 and ring **b** for N=3. Outside this range the centre ring current increases in strength becoming closer in magnitude to the top-row currents for N=4 and 5. For $N \geq 6$, the current in the central ring of the centre row, i.e. ring **iii** for N=6, has the largest magnitude. Interpretation and rationalisation of this current will be explained later.

6.3.4 Ab-initio model

Ab initio current-density calculations were performed using the pseudo-π method,[140] owing to the computational speed of calculations at the large N system size. The current-density maps are displayed in Figure 6.12.

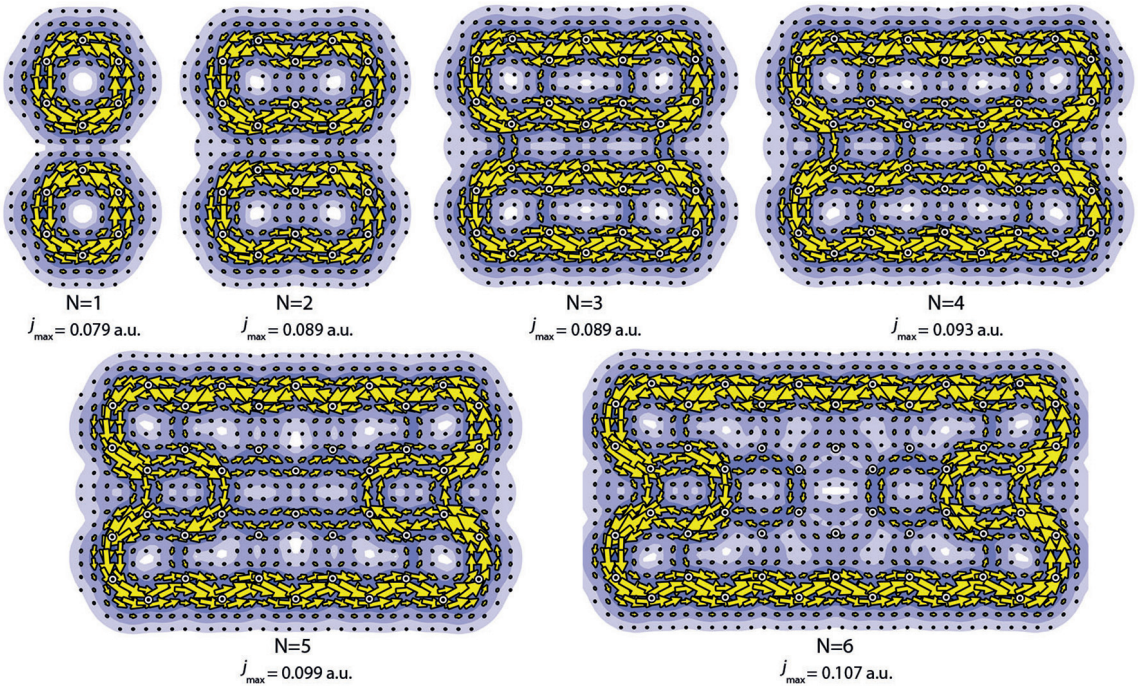


Figure 6.12: Ring-currents calculated using the *ab initio* pseudo-π model. $j_{\max}$ values are reported beneath the relevant cycle.

At first glance, both HL and *ab initio* current maps, give similar overall depictions of the current. Clearly both models show major differences from the CC model, for all

but N=1. For systems in the range $1 \leq N \leq 4$ the total *ab initio* current-density map is dominated by two current patterns essentially identical to the two π-current density maps of the isolated monomers. Perylene extensions in this range have little or no current along spoke bonds.

Beyond this range, the pattern clearly changes to support a strong perimeter current. At N=5 the central rings of the system have significantly weaker currents than the rest of the system. At N=6 ring **iii** appears empty of current. This appears to be the start of a new central-face pattern. For N= $7-9$ the trend continues, moving from the empty ring **iii** (for N=6) to supporting diatropic circulations in rings **iii** and **iv** by N= $7-9$ (see Figure 6.13). In addition, ring **i** and its symmetry counterpart, both continue to appear to support strong paratropic ring-currents.

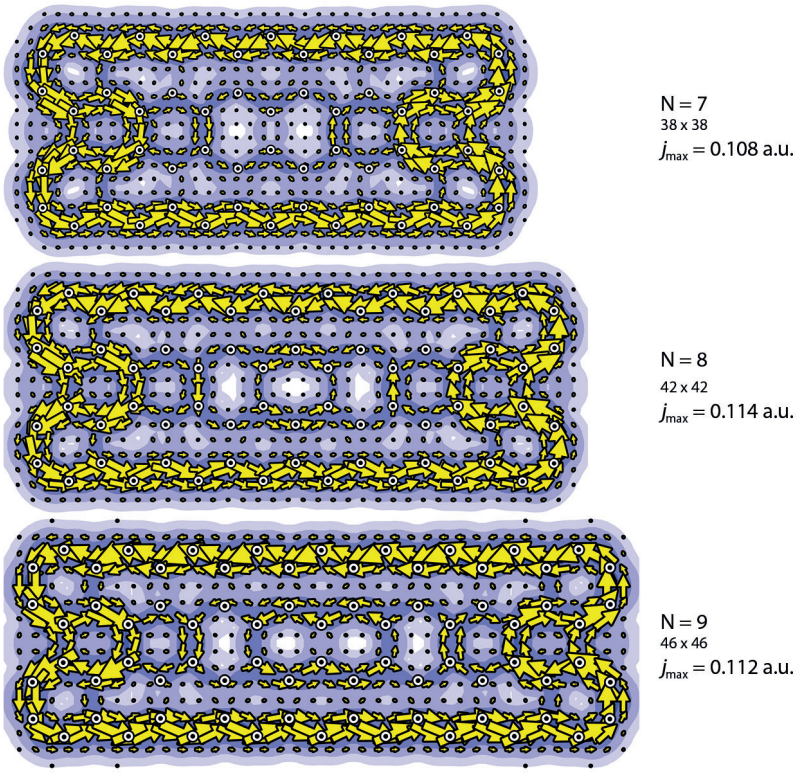


Figure 6.13: Ring-currents calculated using the *ab initio* pseudo-π method. In this case the $j_{\max}$ value is reported beneath the relevant cycle, reported to three significant figures. As the size of the system increases, the box size must be adapted. This affects the precision of the current-density $j_{\max}$ values, as discussed in Chapter 2.

Between N= 7 and N= 9 one can identify, at the heart of the central row, a diatropic linear polyacene-like ring-current starting with naphthalene-like for N= 7 to tetracene-like for N= 9. This observation leads to the following hypothesis for the direction and strength of the ring current.

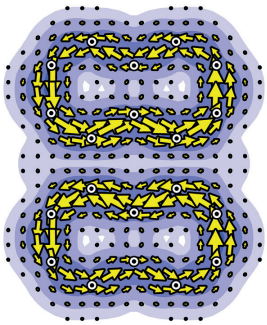
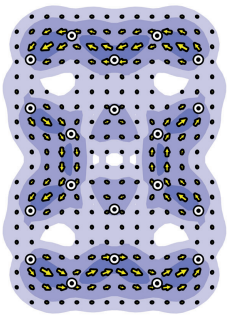
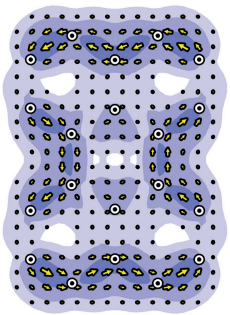
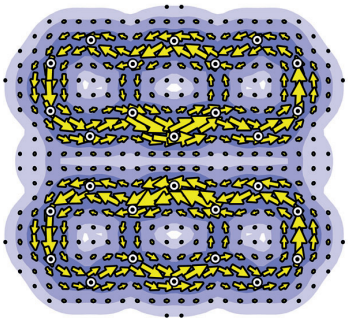
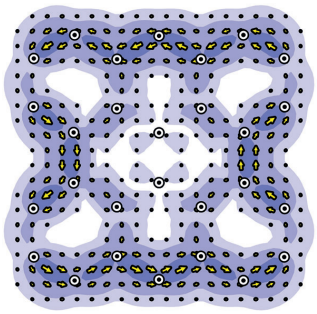
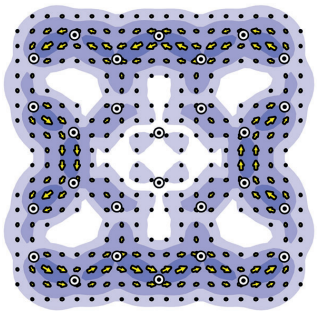
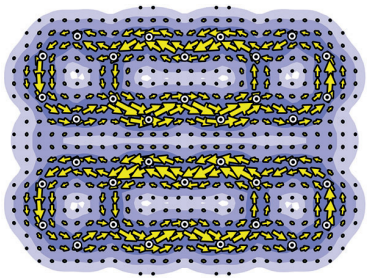
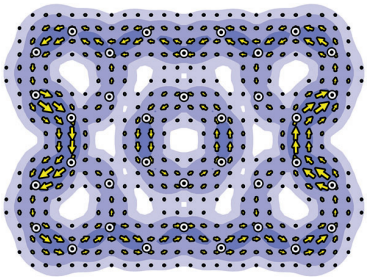
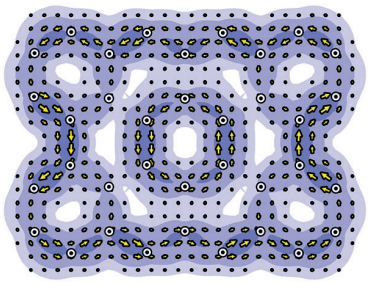
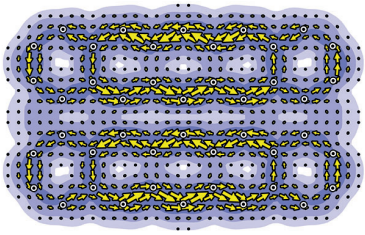
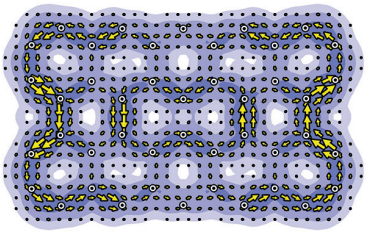
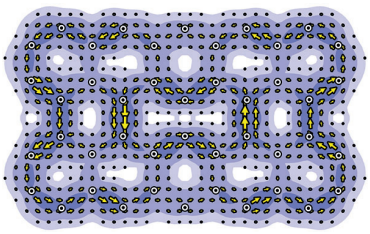
Hypothesis 1: *The change in current-density maps for the centre rings, from monomeric in* $1 \leq N \leq 4$ *to a perimeter dominated current at* $N \geq 5$*, is due to the vector cancellation of the current-density contribution from two subsets: A monomer set localised on the top and bottom rows, and a set corresponding to the centre row.*

The advantage of the *ipsocentric* method is the ability to partition current-density into subsets of molecular orbitals. Hypothesis 1 will be tested using these subsets in an attempt to explain this unusual ring-current.

By the nature of the perturbation expansion (equation (2.13)), those MOs closer to the HOMO-LUMO frontier are more important to the current-density response.[105] The dominant contributions to the ring-current can be identified and then 'mapped' onto an orbital energy diagram.

The total current-density of all perylene derivatives can be broken down into individual canonical-orbital contributions. Two distinct subsets can be identified from all major contributions. The first, '*Monomer MOs*', denote those molecular orbitals with current dominated by a monomer picture; the second, '*Spoke Bond MOs*', denote those MOs which contribute to the spoke bonds in the perylene extension. This final set is further separated into the dominant contributors using a current-density analysis; '*Major Spoke Bond MOs*' are defined as those individual canonical orbitals with $j_{\max} \geq 0.01$ a.u. in the spoke region.

Table 6.5: The current-density maps for the three different sets of molecular orbitals that contribute to the monomer, spoke bond and the major spoke bond (orbitals with $j_{\max} \geq 0.01$ a.u.) subsets. The $j_{\max}$ values for the contributing orbital subsets are reported below the current-density map in units of a.u. Numbers after the molecular orbital indicate denote the orbital number for the particular symmetry.

N	Monomer MOs	Spoke Bond MOs	Major Spoke Bond MOs
2			
	$B_{3g}(2)$, $A_g(3)$, $B_{1u}(3)$ 0.073	$B_{1u}(2)$, $B_{2u}(2)$ 0.027	$B_{1u}(2)$, $B_{2u}(2)$ 0.027
3			
	$B_{1u}(4)$, $B_{2u}(3)$, $B_{3g}(2)$ 0.079	$A_g(4)$, $B_{3g}(3)$ 0.025	$A_g(4)$, $B_{3g}(3)$ 0.025
4			
	$B_{3g}(4)$, $A_g(5)$, $B_{1u}(4)$ 0.069	$B_{1u}(5)$, $B_{2u}(4)$, $B_{3g}(5)$ 0.046	$B_{1u}(5)$, $B_{2u}(4)$ 0.031
5			
	$B_{1u}(6)$, $B_{2u}(5)$, $B_{3g}(4)$ 0.065	$A_g(6)$, $B_{3g}(5)$, $B_{1u}(5)$, $B_{2u}(4)$ 0.06	$A_g(6)$, $B_{3g}(5)$ 0.046

The current-density maps in Table 6.5 show interesting trends. First, consider the Monomer MOs subset current-density maps. The ring-currents present in the monomer rings are essentially identical to those of the linear polyacenes.[94] However, compared to the isolated monomer molecules, current-density strength in the terminal rings is reduced as N increases. This feature coincides with the overall reduction in the uniformity and strength of current, as evident from $j_{\max}$ values.

Secondly, consider the current-density maps of the Spoke Bond MO subset: all MO contributions (middle) and those MOs that are major contributors (right). It is clear that early in the series, $N = 2 - 3$, the contribution to the spoke current is weak and the π-current-density maps (see Figure 6.12) display negligible current passing between the two monomers. Later in the series, $N = 4 - 5$ and beyond, the contribution is stronger leading to the cancellation of the monomer current and the appearance of a perimeter current (see Figures 6.12 and 6.13).

Observations from the maps in Table 6.5 highlight two key questions. First, why does a diatropic ring-current appear in the central rings at $N = 7 - 9$? Secondly, what is the significance of the MOs that are designated as important to the ring-current?

6.3.4.1 Why does the row interface bond-current reverse direction?

This question is ultimately related to Hypothesis 1, which addresses the weakening along the interface between the top and middle rows. In graph-theoretical models, the current magnitude for any perimeter bond is equal to the magnitude of the face ring-current (see Figure 6.11). If a bond is shared between two faces, the magnitude of current is subject to vector addition (or cancellation) of the two face ring-currents.

Comparisons with the Hückel-London model can be made. The HL ring-currents for the extensions, with faces labelled as in Figure 6.9, are reproduced below.

Table 6.6: Hückel-London ring-current magnitudes for individual faces in the perylene extensions.

N	Monomer Rings				Centre Rings			
	a	b	c	d	i	ii	iii	iv
1	0.9348							
2	0.9703				0.2387			
3	0.9658	0.9996			0.4404			
4	0.9999	0.9784			0.5438	0.8326		
5	1.0446	1.0131	0.9373		0.5785	1.0244		
6	1.0791	1.0647	0.9593		0.5862	1.0877	1.256	
7	1.1007	1.1054	1.0043	0.9696	0.5877	1.1037	1.3344	
8	1.1135	1.1314	1.0423	1.0079	0.5888	1.1093	1.3573	1.4207

First, consider the centre ring-currents. As N increases, the magnitude of this ring-current also increases until, at N= 6, it surpasses that of the monomer for ring **iii**. By vector cancellation, the overall pattern from the HL model for N > 5 is then a strong perimeter current with little current traversing the interface between the rows of benzenoids. A side-by-side comparison of the HL and *ab initio* approaches demonstrate this similarity in bond current depiction (Figure 6.14).

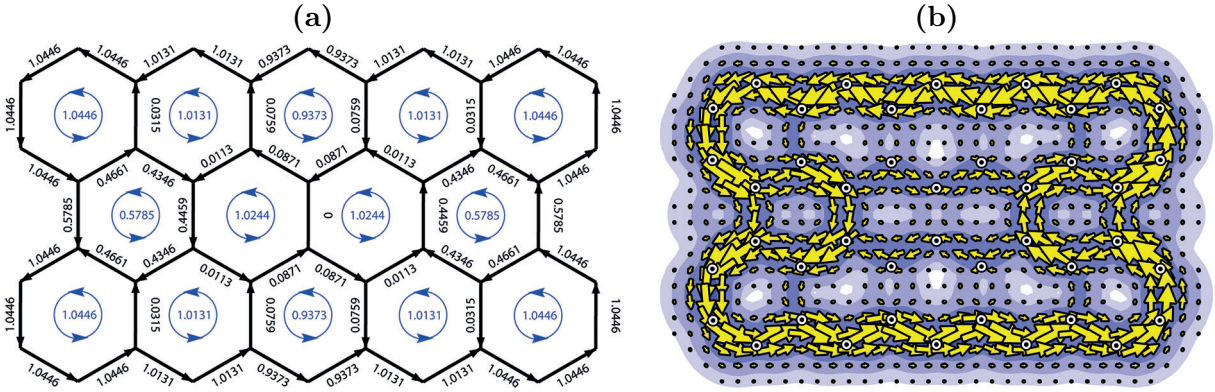


Figure 6.14: The current-density maps for 545-perylene showing currents calculated through (a) the Hückel-London model and (b) the pseudo-π method ($j_{\max} = 0.099$ a.u.)

First, note the similarity in HL ring-current strengths for rings **c** and **ii**. The near equivalence results in significant cancellation of the bond-current along the interface. This leads to a reduced current of 0.0113 and 0.0871 along the interface of the top and middle rows. There is a similar approximate reproduction of the absolute current magnitude

across these same bonds in the pseudo-π calculation (Figure 6.14).

This observation offers an explanation for the peculiar appearance of current at N=5 and also partially validates Hypothesis 1. The pattern does indeed result from cancelling subsets of current from the monomer and central contributors in the larger systems. Furthermore, the HL model quantifies the diatropic current that appears at the interface between the top and central rows. For N=6, ring **iii** supports a diatropic bond-current appearing similar to benzene; for N=7, this diatropic current appears similar to naphthalene; and finally for N=8, this ring-current appears similar to anthracene. Aside from the case of N=6, similar observations can be made for N= $7-9$ in the *ab initio* approach, see Figure 6.13.

6.3.4.2 Dominance of the Molecular Orbitals

Currents in both HL and *ab initio* models are reliant on the occupation of MOs. However, *ab initio* results come from a frontier orbital theory approach and HL results are subject to cancellation and are not limited to the frontier. Table 6.5 has identified several MOs responsible for certain current patterns and in so doing raises the question of why these orbitals in particular dominate the map. As N increases, the number of molecular orbitals in the system also increases and coincides with a decrease in the HOMO-LUMO gap. This will have a profound effect on the ring-current, identical to the effect discussed earlier in Chapter 4, due to the dependence of the current magnitude on the energy gap between occupied and unoccupied levels (see equation (2.13)).

MOs for an N-perylene can be 'mapped' onto the orbitals of an [N+1]-perylene. In the examples to be discussed, the nodal changes along the z-axis are kept constant and mapping of orbitals is in accordance with the nodal changes along the defined y-axis (with molecular axes defined in Figure 6.3). Figure 6.15 illustrates this effect using perylene and bisanthrene orbitals. The perylene $B_{3g}(2)$ orbital has three z-axis nodal planes and one y-axis plane. In bisanthrene this 'parent' orbital can retain the single y-axis node, leading to retention of the parent orbital symmetry, or increase the nodal count by 1, resulting in the $B_{1u}(4)$ orbital.

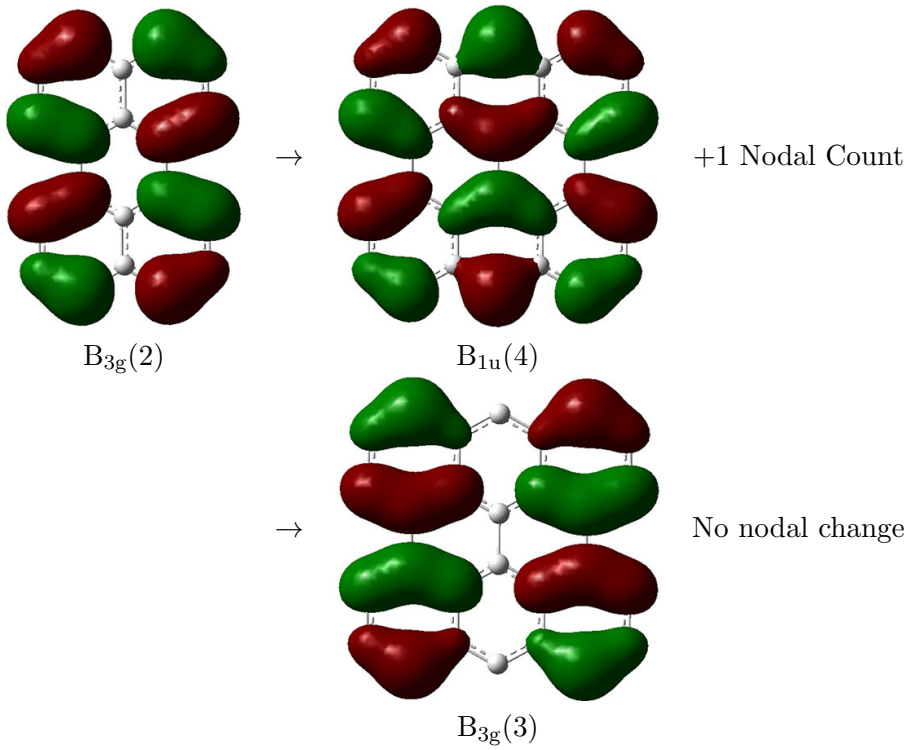


Figure 6.15: Examples of molecular orbitals which change with increase in the size of the extension series of perylene. The first change from $B_{3g}(2)$ to $B_{1u}(4)$ is accomplished by an increase of one nodal plane in the y-axis. The second change from $B_{3g}(2)$ to $B_{3g}(3)$ involves no change in the number of nodes.

The analysis can be extended to introduce rules for each orbital symmetry based on the character table. In all mapped orbitals, nodal planes parallel to the horizontal z-axis are preserved and thus characters under the $C_2(z)$ and $\sigma_{(xz)}$ symmetry elements are identical. Instead only nodal planes perpendicular to the z-axis need be considered. If there is no nodal change, the symmetry element of the new MO will be identical to that of the parent. If the horizontal node count changes by one, the sign of characters under the $C_2(x)$, $C_2(y)$, i and $\sigma_{(xy)}$ symmetry elements will invert. Taking this into consideration, orbital symmetries change as defined in Table 6.7.

Considering these rules, the orbital spectrum can be modified to include lines to indicate the change in energy of the occupied orbitals as N increases for the extension. Figure 6.16 focuses on the frontier orbital region and the two lowest unoccupied molecular orbitals.

Table 6.7: The orbital symmetries of the mapping procedure between orbitals in an N-perylene and those in an [N+1]-perylene. Orbital symmetries either remain constant in the node preserved case or increase by one in the y-axis node adding case. In both instances the z-axis nodes remain constant between mapping.

N-Perylene		**[N+1]-Perylene MO**	
		Node Adding	**Node Preserving**
A_g	$\rightarrow$	B_{2u}	A_g
B_{1u}	$\rightarrow$	B_{3g}	B_{1u}
B_{2u}	$\rightarrow$	A_g	B_{2u}
B_{3g}	$\rightarrow$	B_{1u}	B_{3g}

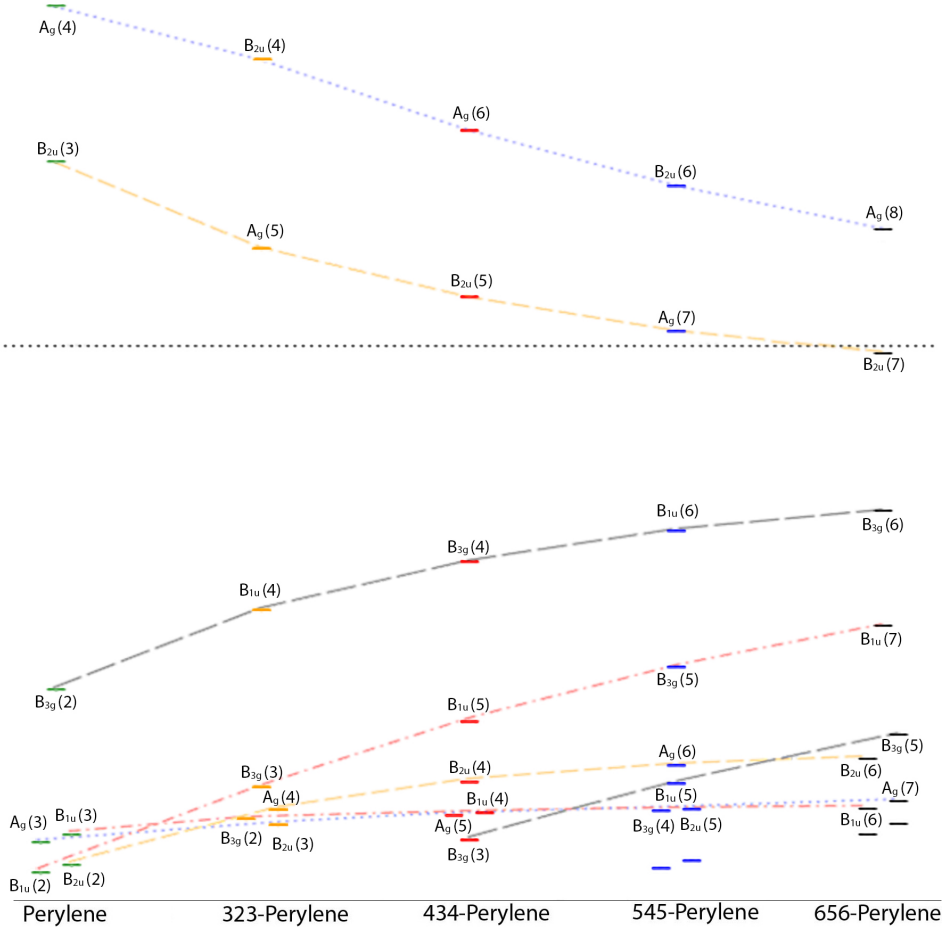


Figure 6.16: A section of the molecular orbitals diagram between the values of -0.1 and -0.4 a.u. of the of the pseudo-π orbital energies for the perylene extensions N$= 2-6$. Connecting lines follow orbitals with one extra y-axis node compared to the N-1 perylene. Labels of the molecular orbitals are listed near the level. Energy levels are calculated at the DFT/B3LYP 6-31G** level of theory. Those levels that are nearly degenerate are horizontally offset for clarity.

Table 6.5 identified subsets of occupied MOs that were the major components in either the monomer-dominated or spoke-bond-dominated current. Combining the knowledge of the orbital labels with the orbital energy spectrum identifies patterns that explain why these MOs are of importance.

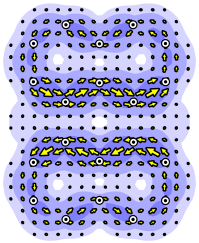
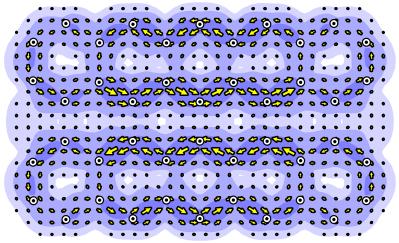
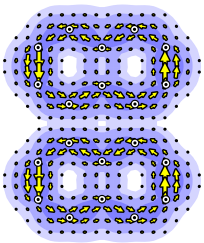
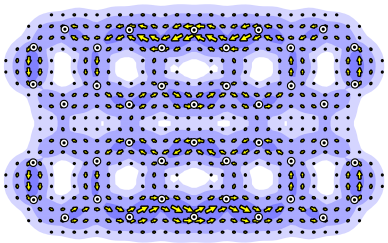
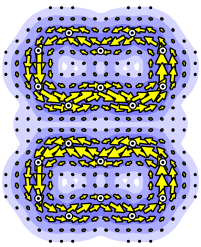
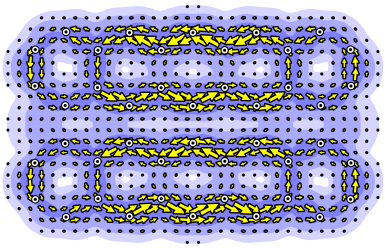
First, consider the monomer-contributing orbitals. For clarity these are listed below.

Table 6.8: Molecular orbitals reproduced from Table 6.5 that are considered as monomer-contributing orbitals.

N	**Monomer MOs**		
2	$B_{3g}(2)$	$A_g(3)$	$B_{1u}(3)$
3	$B_{1u}(4)$	$B_{2u}(3)$	$B_{3g}(2)$
4	$B_{3g}(4)$	$A_g(5)$	$B_{1u}(4)$
5	$B_{1u}(6)$	$B_{2u}(5)$	$B_{3g}(4)$
6	$B_{3g}(6)$	$A_g(7)$	$B_{1u}(6)$

In all cases, there are three major contributing orbitals to the monomer map: the HOMO, and a near-degenerate pair. Through inspection of Figure 6.16, the location and trends of these orbitals can be investigated. By definition, the HOMO orbital is always at the frontier of molecular orbitals and here always has a significant contribution to the ring-current. However, to give an accurate reproduction of the pattern of the monomer the combination of the degenerate pair is needed. As seen in Figure 6.16, the energies of the degenerate pair remain roughly constant when the mapping procedure of N-perylene orbitals to [N+1]-perylene orbitals is performed. When N$= 2 - 4$ the degenerate orbitals are close to the frontier level, hence the monomer-like pattern dominates. However, by N ≥ 5, these degenerate levels are buried and have weaker contributions. This is evident when comparing the HOMO canonical orbital contribution with that of the total monomer. At N=2 the HOMO only partially reproduces the monomer subset. At N=5, the HOMO canonical contribution reproduces the majority of the pattern, with a reduced contribution to the total current-density from the degenerate pair. The contribution of the degenerate pair *is* still important, but, combined with other effects, leads to a reduction in the monomer-like current map (see Table 6.9).

Table 6.9: The current contribution from the orbitals in the monomer subset of Table 6.5 for N = 2 and 5. Orbital labels below the current map indicate the orbital/ orbitals of discussion, with j_{max} values reported below the label. The map Monomer MOs is the result of the combination of the contributions from HOMO and Near Degenerate Orbitals.

	N= 2	**N= 5**
HOMO		
	$B_{3g}(2)$ 0.045 a.u.	$B_{1u}(6)$ 0.037 a.u.
Near Degenerate Orbitals		
	$A_g(3)$, $B_{1u}(3)$ 0.055 a.u.	$B_{2u}(5)$, $B_{3g}(4)$ 0.036 a.u.
Monomer MOs		
	0.074 a.u.	0.065 a.u.

Next, consider the major spoke-bond-contributing orbitals from Table 6.5.

Table 6.10: Molecular orbitals reproduced from Table 6.5 that are considered as major spoke-bond-contributing orbitals.

N	**Spoke bond MOs**		
2	$B_{1u}(2)$	$B_{2u}(2)$	
3	$A_g(4)$	$B_{3g}(3)$	
4	$B_{1u}(5)$	$B_{2u}(4)$	
5	$A_g(6)$	$B_{3g}(5)$	
6	$B_{1u}(7)$	$B_{2u}(6)$	$A_g(6)$

At N=2, these orbitals are buried as the [HOMO-4] and [HOMO-5] respectively and, combined, contribute only weak spoke-bond current. However, as N increases these orbitals rise in energy faster than those in the Monomer MOs subset, and move above the monomer contributing degenerate pair closer to the frontier. Therefore, one can identify a two-fold complementary effect:

i) A reduction in the degenerate pair contribution.

ii) An increase in the strength of the spoke bond contribution.

Therefore, the replacement of a monomer current map with a perimeter current map can be rationalised from the occupation of a subset of the molecular orbitals. The MOs within each subset of an N-perylene can be mapped to complementary orbitals in an [N+1]-perylene according to the number of nodes in the y-axis. From current-density calculations, the dominance of the MOs evolves over the N-perylene series, with dominant orbitals lying closer to the frontier. Now one question remains: can the rise in energy between orbitals shown in Figure 6.16 be rationalised? To answer this, consider the symmetry of the orbitals that link the monomer and perylene-extension orbitals in 6.1.1.

6.3.4.3 Subsets based on monomer contributors

To understand how the orbitals change in energy, two MO diagrams are constructed. The two energy level diagrams to consider are those of naphthalene and 212-perylene, which has a monomer-based ring current (Figure 6.18); and pentacene and 545-perylene, which has a perimeter based ring current (Figure 6.19).

For a series of M-linear-polyacenes, where M corresponds to the number of rings, the ring current of the polyacene can be accurately represented by the contribution of two molecular orbitals. Comparing the M and M+1 polyacene MOs, similarities in orbital nodal characteristics can again be identified. When M is increased by one, the number of nodes in these orbitals also increases, and thus remains close to the frontier. Assigned orbital symmetries will reflect these changes, analogous to those in Table 6.7. For polyacenes up to tetracene, the π-current density can be reproduced by considering the occupation of the only two MOs:

$$\begin{aligned} &\text{If M} = 2p \quad \text{then} \quad \mathrm{B_{3g}(p)} \quad \mathrm{A_g(p+1)} \\ &\text{If M} = 2p+1 \quad \text{then} \quad \mathrm{B_{1u}(p+1)} \; \mathrm{B_{2u}(p+1)} \end{aligned} \tag{6.1}$$

However, as M increases, more orbitals become necessary for accurate reproduction of the current-density and the rules in equation (6.1) no longer apply. For naphthalene, the combination of the HOMO and [HOMO-1] orbitals ($B_{3g}(1)$ and the $A_g(2)$) are sufficient. For pentacene, the orbitals assigned through the above method would be the HOMO and the [HOMO-2] ($B_{1u}(3)$ and $B_{2u}(3)$) which partially reproduce the total π-current density, with major discrepancies in the terminal rings, see Figure 6.17. This trend only continues to worsen as M increases.

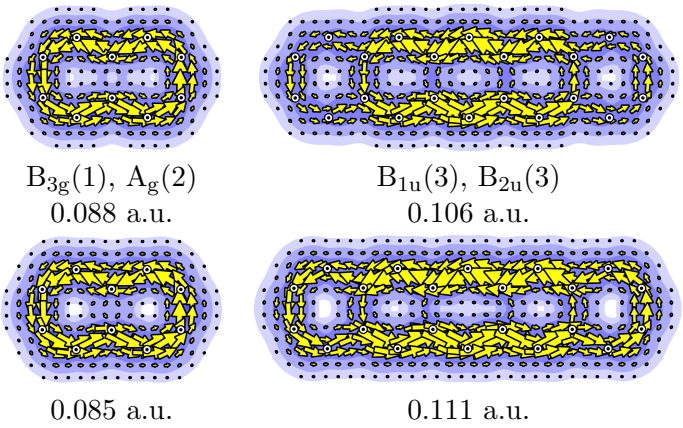


Figure 6.17: Pseudo-π current density maps identifying the contributions arising from orbitals prescribed by equation (6.1) (top) and the contribution from all π-orbitals (bottom) for naphthalene, left, and pentacene, right.

From section 6.1.1, the two monomer orbitals defined by equation (6.1) split into four orbitals of the perylene extension. When N= $2-4$ the four split orbitals all lie at the forefront of the perylene MO frontier. At N ≥ 5, other orbitals intercalate into the energy spectrum and the prescribed orbitals are no longer necessarily close to the frontier. Partitioning of the current into the four prescribed split orbitals and the rest, the current-densities of these subsets can be calculated. The contributions are illustrated in Table 6.11.

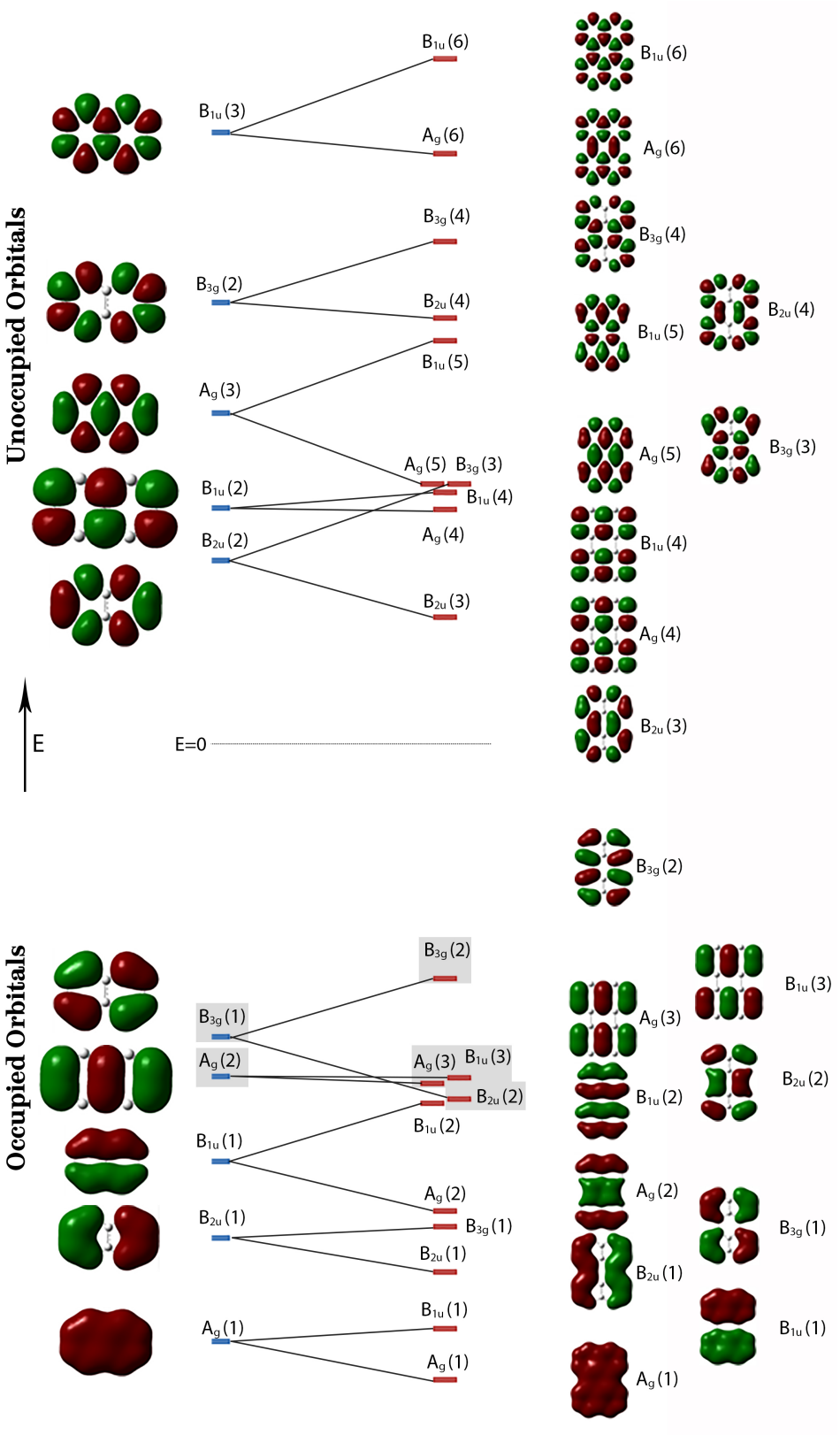


Figure 6.18: Molecular-orbital correlation diagrams of naphthalene, left, and perylene, right. Perylene MOs are identified from the (+)(−) contributions from two monomer MOs. In this case the full spectral range is shown for perylene and naphthalene, plotted on an energy axis calculated at the DFT/B3LYP/6-31G** level. Those MOs above (below) the line at E=0 are antibonding (bonding). Boxes highlight the orbitals identified through equation (6.1) and corresponding perylene (+)(−) split orbitals.

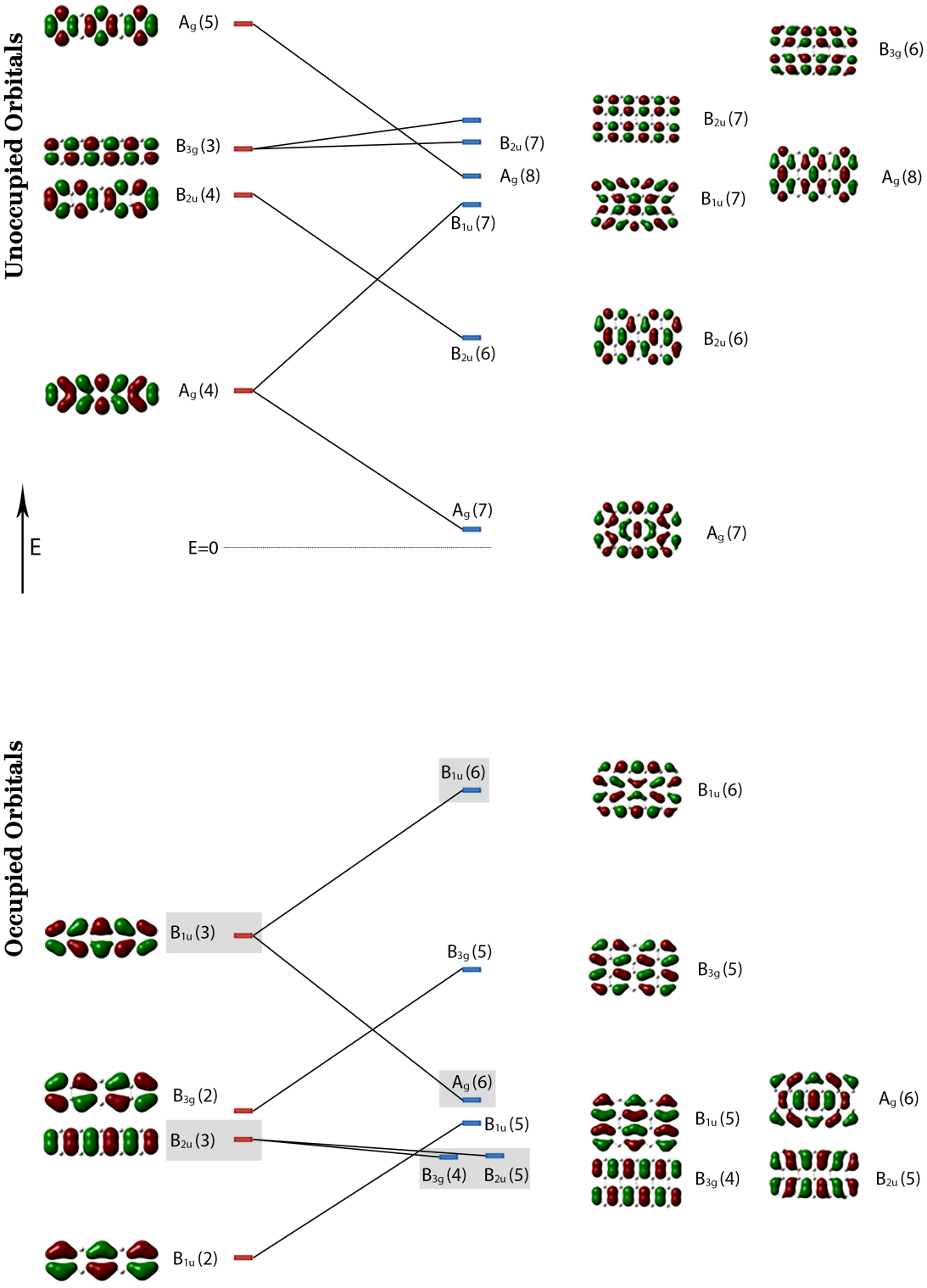
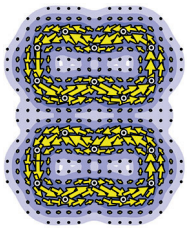
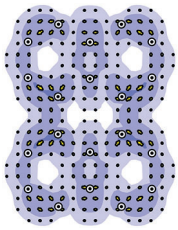
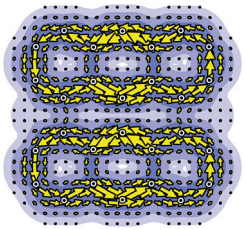
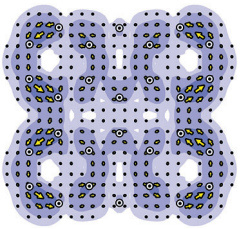
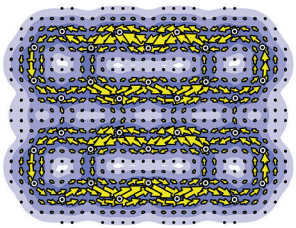
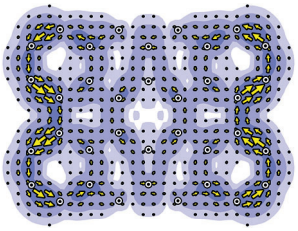
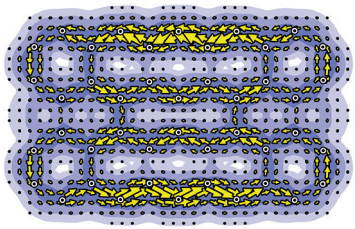
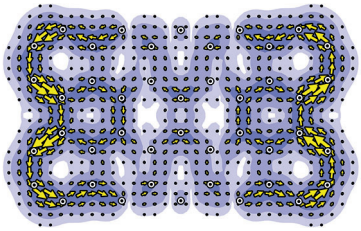
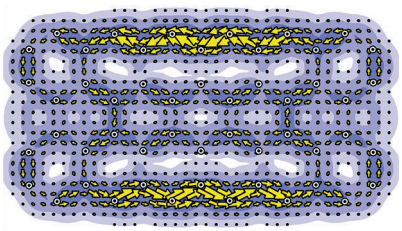
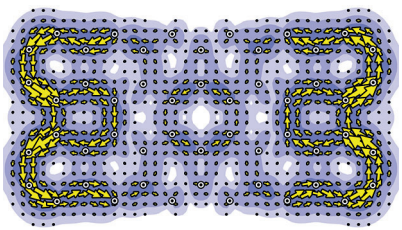


Figure 6.19: Molecular-orbital correlation diagrams for pentacene, left, and 545-perylene, right. Only orbitals which are near to the frontier (in the range -0.36 to 0.26 a.u.) are shown due to the large number of π-MOs in both 545-perylene and pentacene, plotted on an energy axis calculated at the DFT/B3LYP/6-31G** level. Those MOs above (below) the line at E=0 are antibonding (bonding). Boxes highlight the orbitals identified through equation (6.1) and corresponding perylene $(+)(-)$ split orbitals.

Table 6.11: The subsets of the perylene extensions based on the major orbital contributions from the monomer (left) and remaining orbitals (right). Orbitals which contribute to the subset and $j_{\max}$ values are reported below each map.

N	(+)(−) Split Monomer MOs	Remaining MOs
2		
	$A_g(3)$, $B_{3g}(2)$, $B_{1u}(3)$, $B_{2u}(2)$	$A_g(1\text{-}2)$, $B_{3g}(1)$, $B_{1u}(1\text{-}2)$, $B_{2u}(1)$
	0.082 a.u.	0.018 a.u.
3		
	$A_g(4)$, $B_{3g}(2)$, $B_{1u}(4)$, $B_{2u}(3)$	$A_g(1\text{-}3)$, $B_{3g}(1,3)$, $B_{1u}(1\text{-}3)$, $B_{2u}(1\text{-}2)$
	0.085 a.u.	0.032 a.u.
4		
	$A_g(5)$, $B_{3g}(4)$, $B_{1u}(4)$, $B_{2u}(4)$	$A_g(1\text{-}4)$, $B_{3g}(1\text{-}3)$, $B_{1u}(1\text{-}3,5)$, $B_{2u}(1\text{-}3)$
	0.085 a.u.	0.052 a.u.
5		
	$A_g(6)$, $B_{3g}(4)$, $B_{1u}(6)$, $B_{2u}(5)$	$A_g(1\text{-}5)$, $B_{3g}(1\text{-}3,5)$, $B_{1u}(1\text{-}5)$, $B_{2u}(1\text{-}4)$
	0.081 a.u.	0.071 a.u.
6		
	$A_g(7)$, $B_{3g}(6)$, $B_{1u}(6)$, $B_{2u}(6)$	$A_g(1\text{-}6)$, $B_{3g}(1\text{-}5)$, $B_{1u}(1\text{-}5,7)$, $B_{2u}(1\text{-}5)$
	0.088 a.u.	0.091 a.u.

From these subsets, it is clear that when the system is small, $2 \leq N \leq 4$ the four $(+)(-)$ split monomer orbitals result in an accurate approximation for the current-density map to the full π-system. This is not unexpected, considering that at N=2 this set accounts for 2/5 of the total number of orbitals in the system, and are incidentally the four highest occupied MOs. However, as the total number of MOs increases, the contribution from these four orbitals becomes diluted.

For $N \geq 5$, the current-density map for the $(+)(-)$ split monomer contributions is less like the total π picture, indicating dominant orbitals have been excluded. For example, examination of Table 6.5 identifies the $B_{3g}(5)$ orbital, in 545-perylene, as a contributor to the stronger ring current in the spoke bonds. Using the MO diagram in Figure 6.19 one can identify this orbital as the $(-)$ split from a monomer MO that was not included in the two orbital prescription. The proximity of this orbital to the frontier, and hence large current contribution, arises from the raised energy level of the monomer parent, the $B_{3g}(2)$, which pushed the $(-)$-contribution closer to the frontier of the perylene MOs.

In the general sense, a rule of thumb can be defined. If the two orbitals of the monomer, identified through equation (6.1), are sufficient to approximate the monomer current, then the four split orbitals will describe the perylene extension map as well.

6.3.5 Hypothesis 1 Revisited

Returning now to Hypothesis 1, the current-density maps of the extended perylenes can be understood as the resultant of competition between orbital contributions. Early in the series $1 \leq N \leq 4$ the current-density maps appear as two localised monomer maps rationalised by the dominance of only a select few molecular orbitals. These MOs could be 'mapped' back via simple symmetry arguments to the major linear polyacene contributing MOs. The dominance of only a select few MOs mean a central ring-current is weak, leading to the observed strong current along the interface of the rows.

For $N \geq 5$ a larger set of MOs are needed to accurately partition the map into major contributors. MO contributions for the central rings now become more important with larger contributions that has the effect of reducing the current along the row interfaces.

The combined effect of reduced monomer MO contributions and an increased contribution from central ring MOs leads to the change from a monomeric total current map to a more perimeter current map. Further investigation is needed to define the origin of the diatropic current observed in the centre of the central row for N $\geq$ 7.

6.4 Conclusion

Perylene, and its various bicycles and derivatives, are examples in the literature that epitomise the failure of conjugated circuit, and in a broader sense Kekulé-structure-based, models. CC models of bicycles of perylene in which the naphthalene 'monomer' changes to pentalene, heptalene and octalene, provide a muted reproduction of the HL and *ab initio* current maps. For dipentalene and diheptalene, all models depict a strong paratropic current map circulating around the whole perimeter. This is also the case of perylene where, aside from the over-simplification of an empty centre ring, the CC model correlates with HL and pseudo-π methods. However in the case of dioctalene, the over-simplification in the CC models is evident with the three main models denoting the three cases of aromaticity. Randić gives a non-existent ring-current; Ciesielski et al. gives a diatropic, localised monomer ring-current, which incidently is identical to that in the HL and pseuod-π models; finally the Mandado model predicts a localised paratropic monomer ring-current. A more uniform CC model is still needed, which will be discussed in the next part of the thesis.

For the systems referred to as the extensions of perylene, in which the monomer is extended to an N-benzenoid linear polyacene, conjugated-circuit models completely fail to reproduce the pattern of the HL and *ab initio* methods. This failure is associated with the presence of fixed single bonds, (PBO = 0), joining the two monomer polyacenes.

Ab initio and Hückel-London calculations indicate an increasing center strength contribution. Both models demonstrate the presence of current density that evolves over the range of the N-perylenes. At small N, 1 $\leq$ N $\leq$ 4, the current map is dominated by a localised monomer current map. When N $\geq$ 5 the contribution of the center rings is sufficient to alter the current map to one dominated by the perimeter.

The *ab initio* current-density can be separated into subsets of canonical molecular orbitals. The subsets are those contributing to the monomer, those contributing to the spoke bond and finally, those that are $(+)(-)$ splits of the major contributing monomer orbitals. From inspection of the energy level diagrams, the subsets can all be identified from the symmetry groups of the monomer. It turns out for N in the range, $1 \leq \mathrm{N} \leq 4$, the subset of $(+)(-)$ split orbitals of the monomers major orbitals accurately reproduce the total π current map. But beyond this limit, reproduction is poor. The rationale proposed for this observation is simply that more MOs are needed to reproduce the map as the total number of MOs increases, and so the total number of current-bearing MOs increases in the system.

For the other subsets an increase and decrease can be observed in the strength of the current in the spoke bond and monomer subsets respectively. This results in the disappearance of the monomer-dominated ring current and the appearance of the perimeter-based map. As N increases, the orbitals which would contribute to a monomer-based ring-current become buried leading to a decreased contribution. Coinciding with this reduction, those molecular orbitals responsible for current across the spoke bonds increase in energy, moving closer to the frontier. The effect is an increased current contribution and the emergence of a perimeter-arcing current.

Part III

The Future of Conjugated-Circuit Models

The third part of the thesis focuses on the future of the conjugated-circuit models. Two attempts to improve conjugated-circuit models are proposed, with the aim to include non-Kekuléan graphs, and to improve the accuracy of the conjugated-circuit picture as an approximation of Hückel-London model. The first is an extension of valence-bond theory incorporating 'conjugated circuits' found in Dewar structures. The second is an extension of the weighted Aihara formalism, and utilises coefficients from characteristic polynomials.

Chapter 7

The Use of Dewar Structures

7.1 Introduction

In order for conjugated-circuit models to be useful as models of ring-current based aromaticity, some shortcomings need to be addressed. Unfortunately, as discussed throughout this document, these are numerous. The present chapter details an attempt to include non-Kekuléan benzenoids in CC models and at the same time circumvent the problems caused by fixed single or double bonds, which lead to difficulties in systems such as perylene, as discussed in Chapter 6. The first approach to be discussed uses the idea of including first-excited structures in the CC model, which is adapted from an old proposal for an improved Pauling Bond Order (PBO).[114]

For a bond between atoms r and s, the Pauling Bond Order, PBO_{rs}, is defined as:

$$\mathrm{PBO}_{rs} = \frac{m\left(\mathrm{G} - r - s\right)}{\mathrm{K(G)}} \tag{7.1}$$

where $m\left(\mathrm{G} - r - s\right)$ is the number of perfect matchings in which bond rs appears double, i.e. the matching number of the edge rs in the graph, and K(G) is the total number of perfect matchings of the molecular graph. PBO gives a useful qualitative account of benzenoid bond-lengths,[229] and offers qualitative comparison with experimental bond lengths, for example in fullerenes[230] and quasi-single bonds.[231] Of importance to the present work is a demonstration that PBO has a direct relationship with the perimeter ring current of benzenoids in the Randić CC model.[115] However, PBO also has a documented history of only partial success in other examples such as the chevrons,[218] a family of benzenoids, and fluoranthene,[220] a non-alternant analogue of perylene. These difficulties have led to attempts to give improved definitions of the bond order, two examples of which involve weighted contributions from Clar[232] and Fries structures.[233]

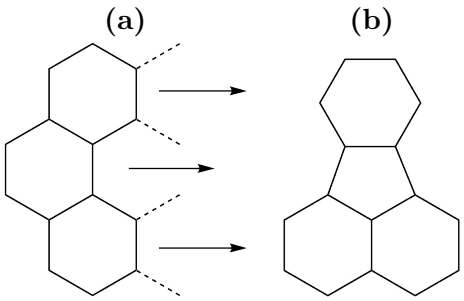


Figure 7.1: Two example systems where a PBO analysis fails to correlate with experimental measurements. (a) the chevron benzenoid series (b) fluoranthene.

Here, the solution proposed by Pauling in 1980,[234] and taken up again by Dias in 2011[235] will be examined. The new feature in this formulation involved the direct incorporation of Dewar structures. Dewar structures are named after James Dewar who proposed an alternative structure of benzene which became known as 'Dewar Benzene'[9] (although this name has itself been contested).[236]

The implications of the inclusion of these graphs becomes apparent when one partitions matchings of the graph into *perfect* and '*imperfect*' matchings. The matching polynomial,[237] $\alpha\,(\mathrm{G}, x)$, of an N sized graph can be constructed to incorporate information on these structures. It is defined as,[161]

$$\alpha\,(\mathrm{G}, x) = \sum_{k=0}^{\lfloor \mathrm{N}/2 \rfloor} (-1)^k\, m(\mathrm{G}, k)\, x^{\mathrm{N}-2k} \tag{7.2}$$

where $m(\mathrm{G}, k)$ is the number of k-matchings of G. In this language, a perfect matching is an N/2 matching, and, for example, $m(\mathrm{G}, 1)$ is the number of edges of the graph. For even graphs, two coefficients are important, $m(\mathrm{G}, [\mathrm{N}/2])$ and $m(\mathrm{G}, [\mathrm{N}/2 - 1])$, which correspond respectively to the number of Kekulé structures and K-2 structures. The latter will now be referred to as the $\mathrm{K}^{(2)}$ structures, defined as the number of perfect matchings for the set of graphs in which two vertices are removed in all possible ways. To illustrate with an example, the matching polynomial of benzene is:

$$\alpha(\mathrm{G}, x) = x^6 - 6x^4 + 9x^2 - 2$$

hence, benzene has two Kekulé and nine 'first-excited' structures. Dewar structures are a

sub-set of the K-2 structures (Figure 7.2) where those first-excited structures that contain radicals on adjacent vertices are discounted. Thus, the number of Dewar structures, DS, for benzene is three (Figure 7.2 (b)).

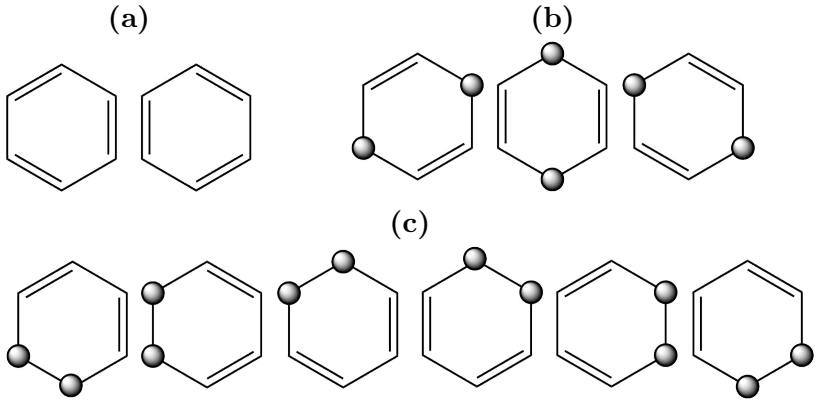


Figure 7.2: The three classifications of structures considered in this chapter illustrated using the example of benzene. (a) The perfect matchings of benzene, known as Kekulé structures; (b) the category of first-excited structures where radical positions are on non-adjacent atoms known as Dewar structures; (c) the remaining first-excited structures that, in addition to those in (b), form the $\mathrm{K}^{(2)}$ structures.

For a PAH, the number of DS can be found from

$$\begin{aligned} \mathrm{DS(G)} &= \mathrm{K}^{(2)}(\mathrm{G}) - \left(\frac{\mathrm{N}}{2}\right)\mathrm{K(G)} \\ &= m(\mathrm{G}, [\mathrm{N}/2-1]) - \left(\frac{\mathrm{N}}{2}\right) m(\mathrm{G}, [\mathrm{N}/2]). \end{aligned} \tag{7.3}$$

The present chapter considers mainly bipartite graphs, where vertices can be categorised as starred or unstarred, such that no two adjacent vertices belong solely to the same starred or unstarred set. For a neutral benzenoid with perfect matchings, the two radical positions in the K-2 (and hence DS structures), must occupy an starred and an unstarred vertex. The maximum number of biradical positions of a graph to be considered is therefore equal to,

$$\mathrm{BR(G)} = n_{\mathrm{starred}} \times n_{\mathrm{unstarred}} \tag{7.4}$$

where n_{starred} and $n_{\mathrm{unstarred}}$ correspond to the numbers of starred and unstarred positions respectively. BR(G) can be reduced by simple symmetry arguments depending on the

point group and symmetry elements of the graph. Radical positions that are related through a $\sigma_{(yz)}$ operation will lead to mirror image structures. Consider the example of anthracene. The 76 K-2 structures and 48 DS are obtained by comparing matchings compatible with the 49 possible pairs of biradical positions, located on the seven starred and seven unstarred vertices. By symmetry, one can reduce this to 28 positions through examination of the four symmetry distinct starred and seven unstarred vertices, as defined by the labels in Figure 7.3. The result for anthracene is that only 46 K-2 and 30 Dewar structures need to be considered. A simple analysis after this reduction is then performed to calculate all structures by taking the mirror images of the appropriate positions. Simplification of these structures can be applied to any system with a symmetry element which bisects vertices such as the $\sigma_{(yz)}$ operation in anthracene.

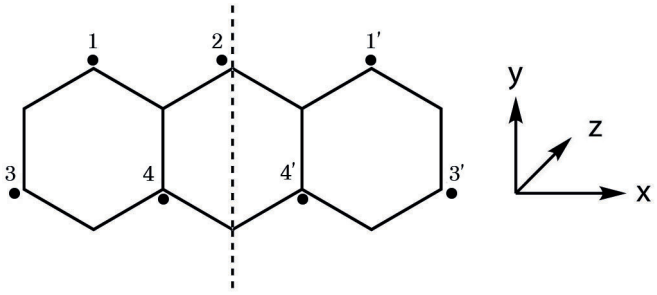


Figure 7.3: The reduced set of radical positions in the example of anthracene obtained through application of the $\sigma_{(yz)}$ operation.

Finally, the number of radical positions varies depending on the parity of the system. For Kekuléan structures the two important coefficients are the $m(\mathrm{G}, [\mathrm{N}/2])$ and $m(\mathrm{G}, [\mathrm{N}/2-1])$. In odd systems, by definition there is no $m(\mathrm{G}, [\mathrm{N}/2])$ coefficient, thus the first coefficient of equation (7.2) will correspond to the $\mathrm{K}^{(\eta)}$ structures. Here, η corresponds to the nullity of the graph, which is of the same parity as N. An example is phenalene with 13 vertices and $\eta = 1$, thus the first-excited $\mathrm{K}^{(\eta)}$ structures support one radical position.

Now that the technical details have been discussed, the use of first-excited structures for calculation of the modified Pauling Bond Order and improving the Randić conjugated-circuit model will be considered.

7.2 Dewar-Based Pauling Bond Order

Before discussion of ring-current models, the proposed improvement to PBO for geometry analysis is examined and critically analysed. The proposal was made by Dias in 2011 with a comparison of *ab initio* and experimental bond-lengths for alternant and non-alternant PAHs. To achieve this, equation (7.1) is modified to include the scaled contribution from first-excited structures,[235]

$$\mathrm{PBO}_{rs} = \frac{m(\mathrm{G}-r-s) + \omega\,\mathrm{DS}(\mathrm{G}-r-s)}{\mathrm{K}(\mathrm{G}) + \omega\,\mathrm{DS}(\mathrm{G})} \tag{7.5}$$

where ω is a parameter to account for the smaller contribution from the number of Dewar structures in G, DS(G). Both $m(\mathrm{G}-r-s)$ and $\mathrm{DS}(\mathrm{G}-r-s)$ are found through removal of vertices r and s and all incident edges.

7.2.1 The Origin of the ω Parameter

It is now useful to examine the importance of the value ω since it will appear in the subsequent analysis. Dias chooses the value of 0.03 based on the initial analysis of the bond lengths in perylene performed by Pauling.[235] As mentioned previously, there are two bonds in perylene which have a fixed-single bond Pauling Bond Order (called spoke bonds in Chapter 6). However, experimentally these have length 1.471 Å,[238] shorter than the expected single bond length (1.504 Å for a conjugated system of alternating single and double bonds).[239] Pauling Bond Order can itself be used to predict a bond length, BL, through the following equation:[239,240]

$$\mathrm{BL}_{rs} = 1.504 - (1.504 - 1.334)\,\frac{1.84\,\mathrm{PBO}_{rs}}{0.84\,(\mathrm{PBO}_{rs}+1) + 0.16} \tag{7.6}$$

The value of ω used as the ratio for first-excited structures was found through solving equation (7.6) with BL_{rs} taken to be the length of the spoke bond of perylene. As Pauling states:[234] "*I have accepted the usual value 1.470 Å for the bonds g* (Pauling's labelling scheme for the spoke bonds) *which corresponds to 12 % contribution of the excited structures and to the ratio 0.030.*" From equation (7.6), 1.470 Å corresponds to a PBO of 0.12, which from equation (7.5) can then be solved for ω.[241]

$$\begin{aligned} 0.12 &= \frac{0 + \omega\, 49}{9 + \omega\, 98} \\ \omega &= 0.029 \end{aligned} \tag{7.7}$$

In the case of perylene, there are 194 first-excited structures, with the spoke bond double in 49. Therefore, Pauling has normalised the calculation by considering the combined number of times either spoke bond is double, hence 98, a conclusion also reached by Dias.[235] The rationalisation for this choice of normalisation is unclear. Instead, normalisation by the *total* number of first-excited structures seems more intuitive:

$$\begin{aligned} 0.12 &= \frac{0 + \omega\, 49}{9 + \omega\, 194} \\ \omega &= 0.04199. \end{aligned} \tag{7.8}$$

Furthermore, the parameter of 0.03 was derived only for this one system. While perylene is one case where unmodified PBO is erroneous, there is a plethora of other examples such as any of the alternant systems investigated in Chapter 6 or zethrene (discussed in detail later), which contains both fixed single and/or double bonds. One could even investigate cases as simple as the linear polyacenes, where PBO calculated bond lengths are inconsistent with experimentally determined lengths.

7.2.2 Modified PBO of Polyacenes

Now, how well does the modified PBO compare to experiment when applied to other systems? For example, consider the case of naphthalene, anthracene and tetracene, using the bond labelling scheme in Figure 7.4.

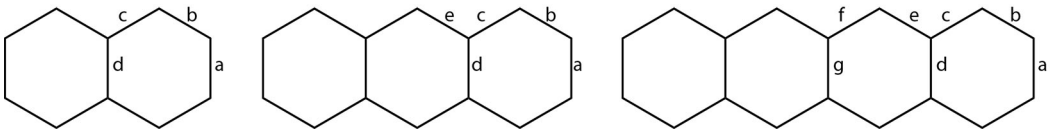


Figure 7.4: Labelling conventions for naphthalene, anthracene and tetracene (left to right).

The details of the observed bond lengths, PBO, and modified PBOs are given in Table 7.1. This table shows that the PBO deviates largely from the experimentally determined bond lengths, most notably for bond **a**. One should also consider the large differences

between bonds **a**, **c** and **d**. A PBO_K (PBO using purely Kekulé structures) analysis indicates these bonds are equivalent, a feature not reproduced in the experimental data (where bond **a** is shorter than the others in naphthalene and anthracene and longer in tetracene). Furthermore, PBO_{DS} (PBO using purely Dewar structures) on its own is not an accurate reproduction of the experimental results, either underestimating and overestimating the lengths of various bonds.

Table 7.1: Bond length data for naphthalene, anthracene and tetracene for the bonds labelled according to Figure 7.4 detailing: experimental bond lengths and corresponding PBO; calculated from Kekulé (PBO_K) and Dewar structures (PBO_{DS}) alone, and the modified Pauling Bond Order calculated from equation (7.5) with $\omega = 0.03$ (PBO_{Dias}). δ_{PBO} and δ_{BL} correspond to the difference between experimental and Dias PBO and BL respectively.

	Bond	Experimental[242]		PBO_K	PBO_{DS}	PBO_{Dias}	δ_{PBO}	δ_{BL}
		BL (Å)	PBO_{Exp}					
Naphthalene	**a**	1.401	0.455	0.333	0.438	0.348	0.107	-0.0188
	b	1.372	0.654	0.667	0.375	0.626	0.028	-0.0036
	c	1.423	0.331	0.333	0.375	0.339	-0.008	0.0016
	d	1.412	0.391	0.333	0.125	0.305	0.086	-0.0161
	Bond	**Experimental[243]**		**PBO_K**	**PBO_{DS}**	**PBO_{Dias}**	**δ_{PBO}**	**δ_{BL}**
		BL (Å)	**PBO_{Exp}**					
Anthracene	**a**	1.419	0.352	0.250	0.396	0.289	0.063	-0.0123
	b	1.366	0.701	0.750	0.458	0.673	0.028	-0.0035
	c	1.433	0.280	0.250	0.375	0.283	-0.003	0.0005
	d	1.436	0.266	0.250	0.167	0.228	0.038	-0.0082
	e	1.399	0.468	0.500	0.375	0.467	0.001	-0.0001
	Bond	**Experimental[244]**		**PBO_K**	**PBO_{DS}**	**PBO_{Dias}**	**δ_{PBO}**	**δ_{BL}**
		BL (Å)	**PBO_{Exp}**					
Tetracene	**a**	1.479	0.086	0.200	0.382	0.272	-0.186	0.0443
	b	1.385	0.559	0.800	0.527	0.692	-0.133	0.0178
	c	1.431	0.290	0.200	0.355	0.261	0.029	-0.0059
	d	1.439	0.252	0.200	0.191	0.196	0.056	-0.0123
	e	1.398	0.474	0.600	0.391	0.517	-0.043	0.0067
	f	1.409	0.408	0.400	0.409	0.404	0.004	-0.0007
	g	1.475	0.101	0.200	0.127	0.171	-0.071	0.0178

Modified PBO calculated using equation (7.5) can be seen to offer an improvement

over conventional PBO. Differences between experimental data and those calculated through equation (7.5) are given in the δ values. Most δ_{PBO} values are below 0.1, and the average (absolute) deviation is 0.055, corresponding to an average deviation in bond length, δ_{BL}, of 0.01 Å. Thus, modified PBO offers some minor improvement when compared with experiment. Reproduction is still not perfect. Consider bonds **a** and **b** in tetracene. The δ_{PBO} values are -0.186 and -0.133 respectively showing that Dias is overestimating the bond order by 19% and 13 %, significantly larger than the average.

Implicit to equation (7.5) are two eventualities where inclusion of Dewar structures will worsen the conventional $\mathrm{PBO_K}$. These occur when either:

$$\mathrm{PBO_{DS}} < \mathrm{PBO_K} < \mathrm{PBO_{Exp}}$$

$$\text{or} \qquad \mathrm{PBO_{DS}} > \mathrm{PBO_K} > \mathrm{PBO_{Exp}}$$

In either of these cases a PBO calculated through equation (7.5) will be further from experimental data. From this equation, $\mathrm{PBO_{Dias}}$ is a value that lies in between the Kekulé and DS bond orders. Therefore, for any bond where $\mathrm{PBO_K}$ and $\mathrm{PBO_{DS}}$ do not lie either side of the $\mathrm{PBO_{Exp}}$ there will be no improvement offered by use of the Dias equation and in fact, PBO values will worsen. Two examples where this can be observed are in bond **d** of anthracene and bond **a** of tetracene. In summary, the linear polyacenes investigated demonstrate the Dias formula offers an improvement over unmodified PBO, but reproduction is still not perfect.

7.2.3 An Investigation into the ω Parameter

Having established the origins of the ω parameter, it is now possible to use the Dias equation to relate ω to the experimentally determined bond length. Equation (7.6) can be rearranged into an expression for PBO_{rs},

$$\mathrm{PBO}_{rs} = \frac{1.504 - \mathrm{BL}_{rs}}{0.84\,\mathrm{BL}_{rs} - 0.95056} \tag{7.9}$$

substitution of (7.9) into equation (7.5) and rearranging to find ω_{rs} leads to

$$\omega_{rs} = \frac{0.95056\,m_{\mathrm{K}} + 1.504\,\mathrm{K(G)} - \mathrm{BL}_{rs}\,(\mathrm{K(G)} + 0.84\,m_{\mathrm{K}})}{(\mathrm{DS(G)} + 0.84\,m_{\mathrm{DS}}) - 1.504\,\mathrm{DS(G)} - 0.95056\,m_{\mathrm{DS}}} \tag{7.10}$$

where m_{K} and m_{DS} replace the terms from (7.5) for $m(\mathrm{G}-r-s)$ and $\mathrm{DS}(\mathrm{G}-r-s)$, respectively. The utility of equation (7.10) is in the generation of individual ω_{rs} values for the bond rs according to a chosen bond length. If an experimental value of BL_{rs} is substituted into (7.10), corresponding ω_{rs} values will indicate the extent to which Dewar structures need to be included in the calculation.

Now consider both perylene and zethrene, two systems where $\mathrm{PBO}_{\mathrm{K}}$ yields bonds with fixed single and/or fixed double character. The calculated ω_{rs} values for the different bonds labelled in Figure 7.5 are detailed in Table 7.2.

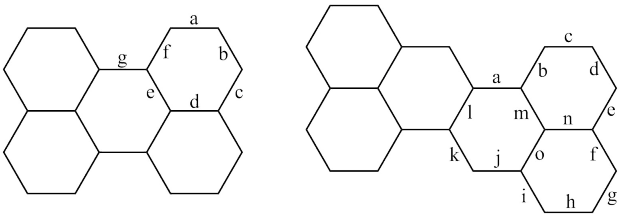


Figure 7.5: The labelling convention used for the unique bonds in perylene and zethrene

Table 7.2 demonstrates that ω_{rs} values differ for each bond, with little consistency in magnitude or sign. For some bonds, the contribution from Dewar structures should be subtracted, whilst in others it should be added. The value calculated for bond **g** (Table 7.2) of perylene differs from that calculated by Pauling (equation (7.8)). A change of 0.001 Å in bond length implies a variation in ω of 6.6 %. Furthermore, a discrepancy can be seen for bond **g** of perylene from the 0.03 value defined by Pauling. The rounded value of 0.042, defined in equation (7.8), relies on a rounded PBO value indicating a dependence on the precise value of PBO and the ease with which ω can change. The inconsistency in ω is worse for zethrene with ω values ranging from -0.084 to 0.1156. The conclusion here is that the chosen value of 0.03 is not appropriate for all bonds and all systems.

Table 7.2: Bond length data for perylene and zethrene for the bonds labelled according to Figure 7.5 detailing: experimental bond lengths and corresponding PBO_{Exp} calculated using equation (7.9); the matching numbers of the bonds in the Kekulé and Dewar structures, and the modified Pauling bond order calculated using the Dias equation (7.5); δ_{PBO} corresponds to the difference between the experimental and Dias PBO values; finally ω_{rs} corresponds to the ω value needed for equation (7.5) to equate to the experimental PBO value for a given bond *rs*.

	Bond	Experimental[238] BL (Å)	Experimental[238] PBO_{Exp}	m_K	m_{DS}	PBO_{Dias}	δ_{PBO}	ω_{rs}
Perylene	**a**	1.415	0.374	3	93	0.391	-0.017	0.0178
	b	1.369	0.677	6	92	0.591	0.086	-0.0024
	c	1.398	0.474	3	69	0.342	0.132	-0.0552
	d	1.421	0.341	3	50	0.304	0.037	-0.0045
	e	1.428	0.305	3	62	0.328	-0.023	-0.0909
	f	1.394	0.499	6	71	0.549	-0.05	0.0584
	g	1.471	0.116	0	49	0.099	0.017	0.0393

	Bond	Experimental[245] BL (Å)	Experimental[245] PBO_{Exp}	m_K	m_{DS}	PBO_{Dias}	δ_{PBO}	ω_{rs}
Zethrene	**a**	1.485	0.064	0	70	0.103	-0.039	0.0126
	b	1.377	0.616	6	156	0.525	0.091	0.0059
	c	1.404	0.437	3	170	0.398	0.039	0.1949
	d	1.360	0.751	6	196	0.584	0.167	-0.0086
	e	1.403	0.443	3	127	0.335	0.108	-0.0244
	f	1.414	0.379	3	137	0.350	0.030	-0.0646
	g	1.359	0.759	6	176	0.555	0.205	-0.0075
	h	1.398	0.474	3	190	0.428	0.046	0.1156
	i	1.376	0.624	6	126	0.481	0.143	0.0035
	j	1.438	0.256	0	140	0.206	0.050	0.0536
	k	1.352	0.821	9	187	0.718	0.103	0.0131
	l	1.46	0.160	0	91	0.134	0.025	0.0468
	m	1.415	0.374	3	137	0.350	0.024	-0.0843
	n	1.423	0.331	3	105	0.302	0.029	0.0011
	o	1.426	0.315	3	97	0.291	0.025	0.0072

In spite of its shortcomings for the qualitative correction of bond lengths/ bond order, the Dias equation (7.5) prompts the consideration of using Dewar structures in conjugated-circuit ring current calculations. This will be done in subsequent sections for linear polyacenes, perylene, zethrene and finally for some non-Kekuléan systems.

7.3 Dewar Structures in Ring-current Calculations

It would be feasible to adapt equation (7.5) to the calculation of the Randić ring current inspired by the documented relationship between PBO and perimeter currents in benzenoids.[115] In order to account for conjugated circuits in Dewar structures, the definition of CCs must be extended from perfect matchings to encompass first-excited Dewar structures. This is done by considering any 'Kekulé' structure present in the radical-removed fragment of each Dewar structure. To illustrate this idea, all symmetry-distinct first-excited structures of anthracene are displayed in Figure 7.6.

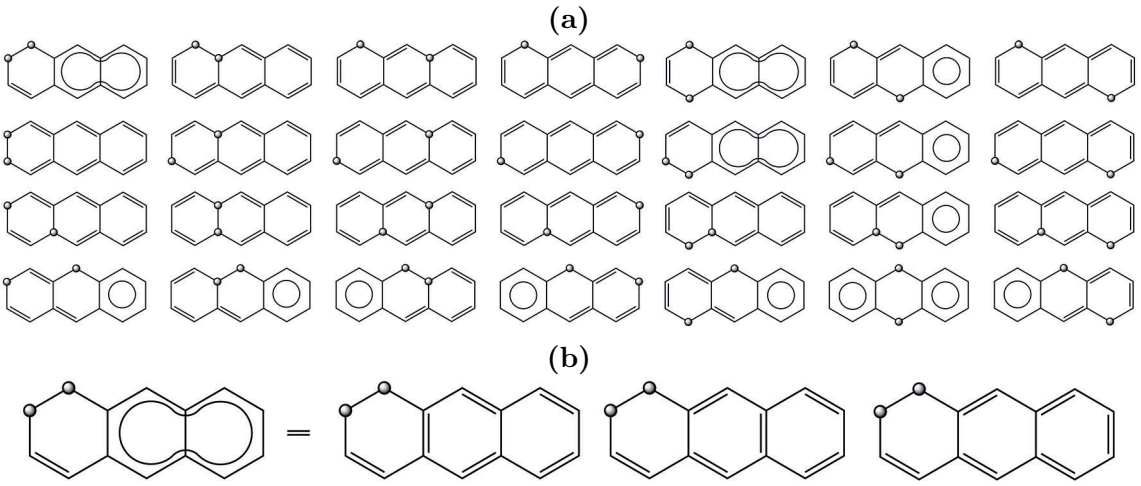


Figure 7.6: (a) The positions of unpaired electrons in anthracene for the $K^{(2)}$ structures, of which DS are a subset. A Clar-like notation is used to indicate multiple 'Kekulé' structures with a fixed allocation of radical sites, (b) the Kekulé structures identified in the first $K^{(2)}$ structure.

Figure 7.6 includes both Dewar and $K^{(2)}$ structures, which, at first, will both be considered. For each structure identified, a conjugated-circuit method can be applied to the $G - r - s$ fragments. Two types of conjugated circuit need to be defined. CCs identified through conventional Kekulé structures will be denoted as primary-CCs and those identified through Dewar structures will be denoted as secondary-CCs. If the Randić model is considered, the top left $K^{(2)}$ structure of Figure 7.6(a) will be equivalent to a conventional naphthalene current in $G - r - s$. Applying this to all structures results in Figure 7.7 that details the Randić ring currents for the four rows of Figure 7.6.

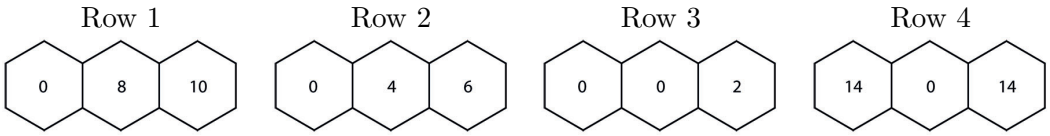


Figure 7.7: The resulting Randić based ring-current, calculated using the Randić model for any secondary-conjugated-circuits identified in Figure 7.6.

One notices that the symmetry distinct ring-currents in Figure 7.7 are asymmetric. This must be reversed by applying the $\sigma_{(yz)}$ operation to rows 1 to 3.

Performing this analysis is simple in the case of anthracene but when systems become larger, the number of $K^{(2)}$ structures rapidly increases to the extent where a pencil and paper method is arduous. Instead, the Randić CC model equation (1.20) can be modified to incorporate both Kekulé and Dewar structures. One plausible form is:

$$J_C = \frac{2m[G - C]^2 + \omega\, 2m[(G - r - s) - C]^2}{m[G] + \omega\, m[G - r - s]} \tag{7.11}$$

From now onwards, equation (7.11) will rely on the value of $\omega = 0.03$, and will be referred to as the '*RD equation*'. The RD equation can then be applied to both $K^{(2)}$ and DS structures to calculate the ring-current for a cycle. The individual cycle contributions are summarised in Table 7.3, using labelling conventions as used Table 3.1 from Chapter 3.

Table 7.3: The cycles and overall Randić current contribution as a combination of both the standard Randić contribution and secondary conjugated-circuits that are identified in the first-excited structures: $K^{(2)}$ and Dewar structures. Numerical results assume $\omega = 0.03$ calculated using the RD equation.

Cycle	**$K^{(2)}$ Structures**	**Dewar Structures**
C_1	$J_{C_1} = \frac{2 \times 1^2 + \omega\ 2 \times (9 + 2^2)}{4 + \omega\ 76} = \frac{130}{314}$	$J_{C_1} = \frac{2 \times 1^2 + \omega\ 2 \times (5 + 2^2)}{4 + \omega\ 48} = \frac{118}{272}$
C_3	$J_{C_3} = \frac{2 \times 1^2 + \omega\ 2 \times (6)}{4 + \omega\ 76} = \frac{118}{314}$	$J_{C_3} = \frac{2 \times 1^2 + \omega\ 2 \times (2)}{4 + \omega\ 48} = \frac{106}{272}$
C_4	$J_{C_4} = \frac{2 \times 1^2 + \omega\ 2 \times (3)}{4 + \omega\ 76} = \frac{109}{314}$	$J_{C_4} = \frac{2 \times 1^2 + \omega\ 2 \times (1)}{4 + \omega\ 48} = \frac{103}{272}$
C_6	$J_{C_6} = \frac{2 \times 1^2 + \omega\ 2 \times (0)}{4 + \omega\ 76} = \frac{100}{314}$	$J_{C_6} = \frac{2 \times 1^2 + \omega\ 2 \times (0)}{4 + \omega\ 48} = \frac{100}{272}$

The total Randić current is the summation of the contribution from relevant cycles. The current maps, scaled to the largest magnitude, are reported in Figure 7.8.

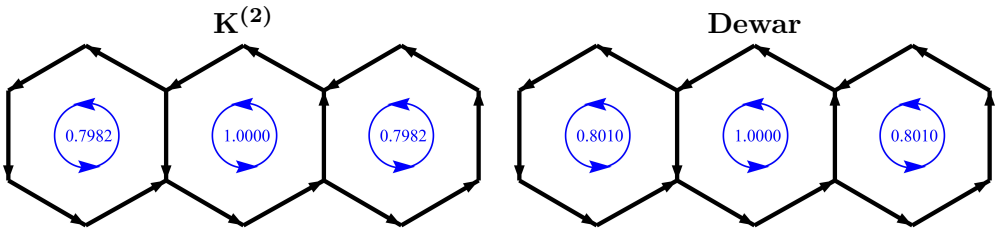
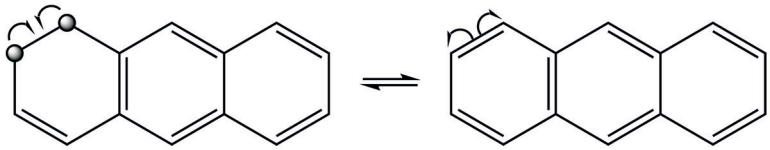


Figure 7.8: The scaled Randić current calculated through the combination of primary-conjugated-circuits (from Kekulé structures) and secondary-conjugated-circuits identified from $K^{(2)}$ structures (left) or Dewar structures (right) via application of the RD equation.

Future sections will discuss only Dewar structures. From a chemical perspective, excluding $K^{(2)}$-specific structures is intuitive. Structures where radicals are adjacent to one another can simply be considered as a radical split of a bond in a Kekulé structure, which seems chemically implausible.



Therefore, these structures will be removed from subsequent analyses.

7.4 Ring-Current Examples

7.4.1 N-Linear Polyacenes

The first series that will be considered is that of the linear polyacenes. Previous investigation by Dias provides an equation to determine the number of Dewar structures, DS, for this series of benzenoids.[246] It was found that the number of Dewar structures of graph G, an N-linear polyacene, is:

$$\mathrm{DS(G)} = \frac{1}{24} \times \left(2\mathrm{N}^4 + 24\mathrm{N}^3 + 34\mathrm{N}^2 + 12\mathrm{N}\right) \tag{7.12}$$

Compare equation (7.12) to the equation for the number of standard Kekulé structures in linear polyacenes:

$$\mathrm{K(G)} = \mathrm{N} + 1 \tag{7.13}$$

where in both cases, N corresponds to the number of benzenoid rings in the linear polyacene. Simple examination of the two equations leads to the conclusion: the number of Dewar Structures will be much larger than the number of Kekulé structures for a given polyacene.

As discussed in the case of antikekulene in Chapter 5, an analytical formula for ring currents can be found for a series where the number of Kekulé (or in this case Dewar structures) can be counted. For primary-CCs, the Randić ring-current in the Q^{th} ring for the N-polyacene, $\mathrm{J(N}, Q)$ can be represented by the following equation.[94]

$$\mathrm{J(N}, Q) = 2Q \times (\mathrm{N} - Q + 1) \tag{7.14}$$

Using a differencing technique, as employed by Dias for (7.12), an analytical ring-current equation can be obtained for the DS of the linear polyacenes.[247] This is,

$$\mathrm{J(N}, Q) = \frac{1}{5!} \times \left(c_1\mathrm{N}^5 + c_2\mathrm{N}^4 + c_3\mathrm{N}^3 + c_4\mathrm{N}^2 + c_5\mathrm{N}^1 + c_6\right) \tag{7.15}$$

where $c_1 = 8Q$

$$c_2 = -40Q(Q-1)$$

$$c_3 = 80Q\left(Q^2 - 2Q + 2\right)$$

$$c_4 = -80Q\left(Q^3 - 3Q^2 + 6Q - 1\right)$$

$$c_5 = 8Q\left(6Q^4 - 20Q^3 + 70Q^2 - 50Q + 13\right)$$

$$c_6 = -8Q(Q-1)\left(2Q^4 - 4Q^3 + 26Q^2 - 24Q + 19\right).$$

Equation (7.15) shows that the Randić secondary-conjugated-circuit contribution to current will increase as a function of N^5. Comparing this with the normal Randić equation leads to the observation that the contribution from secondary-CCs increases faster than that of the primary-CCs. Interestingly, equation (7.15) contains the standard

Randić formula as a factor.

$$\mathrm{J}(\mathrm{N},Q) = \frac{1}{15} \times [Q(\mathrm{N}-Q+1)]\left(\mathrm{N}^4 + c_1\mathrm{N}^3 + c_2\mathrm{N}^2 + c_3\mathrm{N}^1 + c_4\right) \tag{7.16}$$

where $c_1 = 4(-Q+1)$

$c_3 = 2\left(3Q^2 - 6Q + 8\right)$

$c_4 = -Q^3 + 12Q^2 - 32Q - 6$

$c_5 = 2Q^4 - 4Q^3 + 26Q^2 - 24Q + 19$

Equations (7.14) and (7.15) can be displayed graphically, using values of N = 1 to 7 and $Q = 1$ to N (see Figure 7.9).

N	Dewar Current (7.15) Q						
	1	**2**	**3**	**4**	**5**	**6**	**7**
1	1						
2	1	1					
3	1	0.400	1				
4	1	0.548	0.548	1			
5	1	0.710	0.484	0.710	1		
6	1	0.846	0.555	0.555	0.846	1	
7	1	0.959	0.670	0.533	0.670	0.959	1

N	Randić Current (7.14) Q						
	1	**2**	**3**	**4**	**5**	**6**	**7**
1	1						
2	1	1					
3	1	1.333	1				
4	1	1.5	1.5	1			
5	1	1.6	1.8	1.6	1		
6	1	1.666	2	2	1.666	1	
7	1	1.714	2.143	2.286	2.143	1.714	1

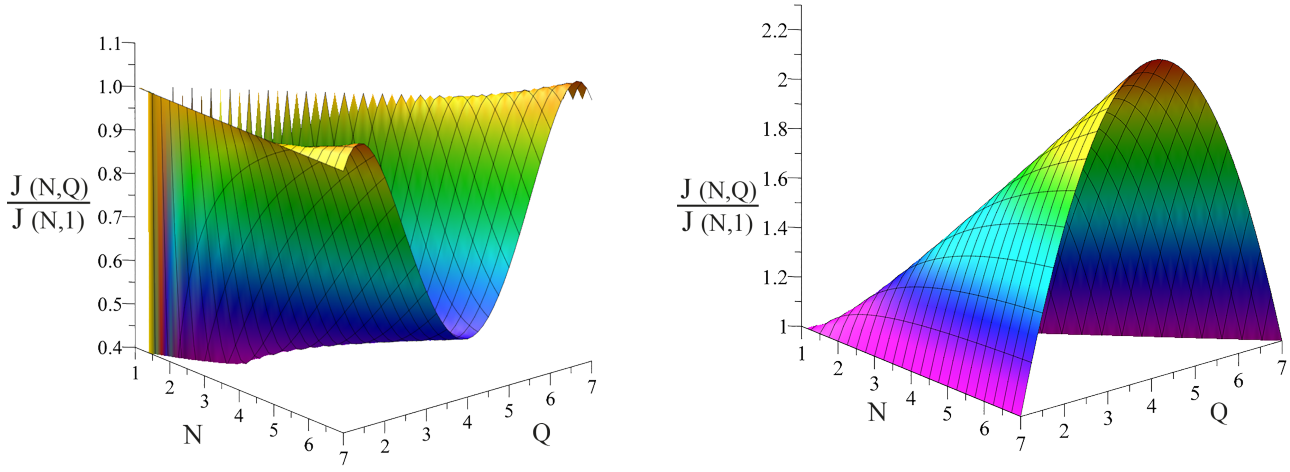


Figure 7.9: The magnitudes (top) and graphical representations (bottom) of the ring current for the (left) the Dewar Structure and (right) the Randić ring-current models of an N-polyacene. Magnitudes are scaled to the terminal ring. Q refers to the ring number in the range of 1 to N.

The graphs and ring-current magnitudes in Figure 7.9 both demonstrate the first problem with including Dewar structures. The number of secondary-CCs contributions rises rapidly as N increases, owing to the N^5 order of the number of secondary-CCs. This trend is reduced in significance when considering the scaled current. Furthermore, the Dewar structure contribution has the opposite trend to those expected from other ring-current models:[94] Dewar structures tend to show terminal rings carry more current than central rings. If interpreted in terms of local aromaticity, this trend is not reciprocated in HL or *ab initio* ring-current models, but is predicted by some other aromaticity indices.[94,248] Combining both forms of ring current models via equation (7.11) leads to magnitudes in Figure 7.10, which are then compared to the HL model.

Hückel-London

N \ Q	1	2	3	4	5	6	7
1	1						
2	1	1					
3	1	1.180	1				
4	1	1.222	1.222	1			
5	1	1.231	1.278	1.231	1		
6	1	1.231	1.290	1.290	1.290	1	
7	1	1.230	1.291	1.303	1.291	1.230	1

RD Equation Current

N \ Q	1	2	3	4	5	6	7
1	1						
2	1	1					
3	1	1.248	1				
4	1	1.272	1.272	1			
5	1	1.220	1.239	1.220	1		
6	1	1.175	1.134	1.134	1.175	1	
7	1	1.163	1.068	1.007	1.068	1.163	1

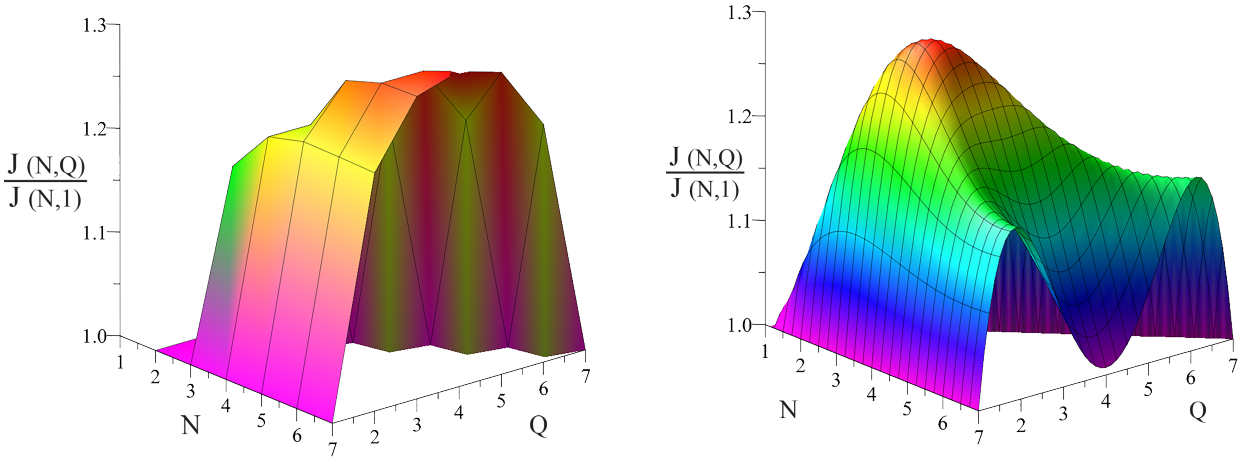


Figure 7.10: The magnitudes (top) and graphical representations (bottom) of the ring current for the (left) Hückel-London and (right) the RD equation (7.11) models of an N-polyacene. Magnitudes are scaled to the terminal ring. Q refers to the ring number in the range of 1 to N.

The goal for the improvement of the conjugated circuit models is to reproduce the trends of the HL model:
(1) the plateau of ring current magnitude for central rings when N > 5 and
(2) the magnitude of currents in central rings remaining larger than terminal rings.
Figure 7.10 shows that the ring current calculated through the RD equation fails to show either trend. Whilst the RD equation should not be immediately discarded, it indicates that further improvements will be necessary.

A significant issue is the value of ω. At $\omega = 0.03$, the scaling of Dewar structures quickly outweighs the Kekulé structure contributions as N increases beyond 5. This feature is shown by the dip in Figure 7.10 (right) comparing Q = 2 and 4 for N=7. This central dip only continues to worsen as N increases. To visualise this effect further, Figure 7.11 displays the ring-currents of the central ring scaled to the terminal ring across all N-linear polyacenes up to N=9, analogous to Figure 9 in reference [94].

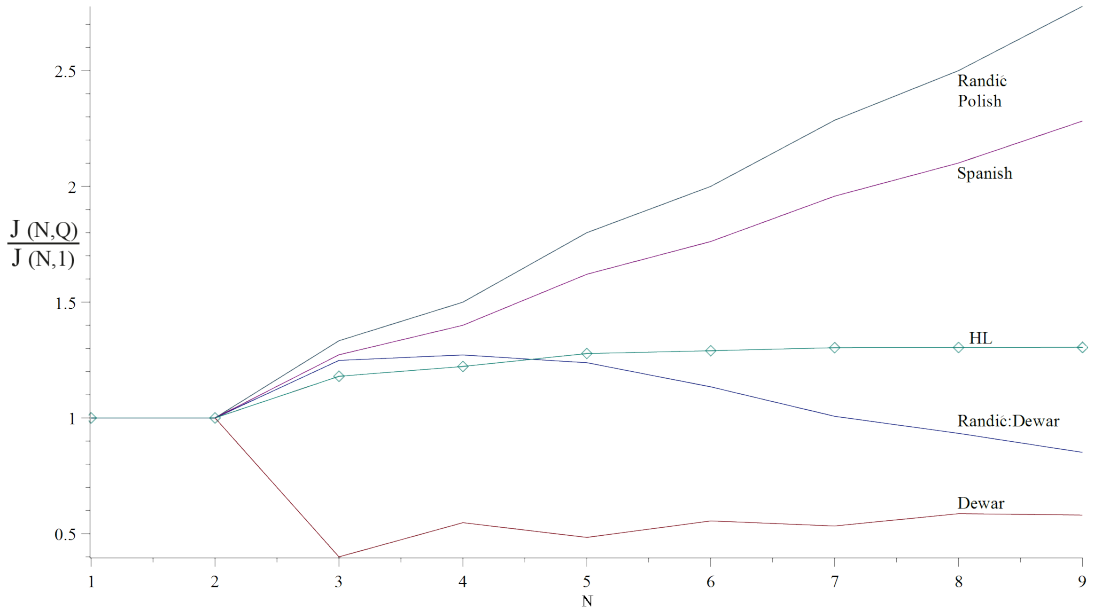


Figure 7.11: The major graph-theoretical ring-current models showing ring current magnitudes for the central ring of the N-linear polyacene, with magnitudes scaled to that of the terminal ring. Randić:Dewar refers to the current from the RD equation. Randić and Ciesielski et al. models are superimposed since the scaled currents are equivalent.

Figure 7.11 illustrates a clear issue with the RD equation. At small values of N

the curve follows the trend of the Randić current. But, once past a critical value of N, where 0.03 no longer sufficiently dampens the contribution of Dewar ring currents, the magnitude tends towards that of the Dewar current. As such the central ring supports currents weaker than those in the terminal ring, a pattern not present in the HL model. This is true for all systems that use the RD equation to calculate a ring-current. The RD equation will always give a trend line in the intermediate region between the Randić and Dewar trends, moving closer to the Dewar line as the system size increases. This is exemplified again in Chapter 8 when 'zig-zag' fibonacenes are discussed.

7.4.1.1 RD Current in Catafusenes

Observations of the series of linear polyacenes and other catafusenes (benzenoid graphs containing no internal vertices) leads to the following theorem.

Theorem 7.4.1 *All secondary-conjugated-circuits identified in a catafusene will be of size* $4n + 2$.

From the literature, primary-CCs are all of size $4n+2$.[207] Theorem 7.4.1 can be rationalised by consideration of the positioning of radical positions in catafusenes and through comparison with a perifusene (a benzenoid with at least one internal vertex).

For catafusenes, the lack of internal vertices means any vertex that supports a radical position will result in the destruction of any face the vertex was a part of. Consider triphenylene, illustrated in Figure 7.12. Fixing one radical and then varying the position of the second leads to the three possible eventualities for the current in catafusene biradicals.

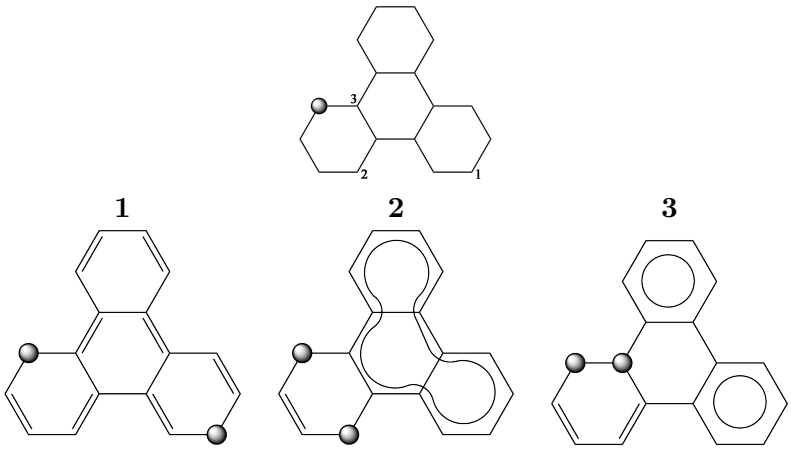


Figure 7.12: Three examples of radical positions for triphenylene that result in three possibilities of secondary-CCs from the labelling in the top diagram. Position 1 leads to no secondary-CC; position 2 leads to a single secondary-CC and finally position 3 leads to two disjoint secondary-CCs.

Every vertex in a catafusene is on the perimeter, thus any removal will act to break that cycle into individual fragments. There will be three eventualities depending upon position, all of which are illustrated in Figure 7.12. Either no conjugated-circuits will remain in $\mathrm{G} - r - s$, or the parent catafusene is split into smaller catafusene fragments.

1. $m[(\mathrm{G} - r - s)] = 1$ and the fragment contains no secondary-CCs.
2. $m[(\mathrm{G} - r - s)] > 1$ resulting in a single secondary-CC system.
3. $m[(\mathrm{G} - r - s)] > 1$ resulting in multiple disjoint secondary-CCs systems.

Removal of a vertex in catafusene benzenoids will not create any new faces. Therefore, there is no possible way to create a $4n$ circuit through the process of vertex removal. If any secondary-CCs remain in $\mathrm{G} - r - s$, they were originally a part of the parent catafusene set and are of size $4n + 2$ and will simply be classed as smaller catafusenes.

Now compare with a perifusene. Any internal vertex is the union of three hexagons and can support a radical position. After removal, the perimeter of the three hexagons is on 12 vertices corresponding to a $4n$ secondary-CC, subject to the position of additional radicals. This explains why primary-CCs identified in *all* benzenoid graphs are constructed from $4n + 2$ circuits; whereas only catafusene benzenoids are constructed from all-$4n + 2$ secondary-CCs.

7.4.2 Zethrene and the Extensions of Perylene

Next the RD equation is applied to examples where the CC models fail to give an accurate depiction of HL current patterns. The examples chosen for the following section are the benzenoids zethrene, perylene and the next two structures of the extended perylene series defined in Chapter 6. The structures and face labelling convention (analogous to that in Chapter 6) are shown in Figure 7.13.

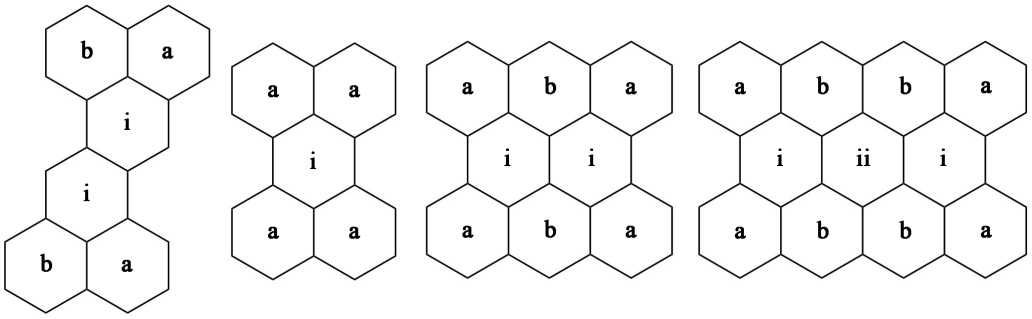


Figure 7.13: The structures and face labels of zethrene, perylene, 323-perylene and 434-perylene (left to right).

The case of perylene and extensions has also been investigated by Dias who devised an analytical equation for the number of Dewar structures in the [N(N − 1)N]-perylene series.[246] For this series, the number of Dewar structures is:

$$\mathrm{DS(G)} = \left(\frac{1}{120}\right)\ \left(\mathrm{N}^7 + 15\mathrm{N}^6 + 105\mathrm{N}^5 + 495\mathrm{N}^4 + 934\mathrm{N}^3 + 750\mathrm{N}^2 + 220\mathrm{N}\right) \qquad (7.17)$$

One can also construct an analytical expression for the number of Kekulé structures. For the same generation, the number of Kekulé structures is:

$$\mathrm{K(G)} = (\mathrm{N}+1)^2 \qquad (7.18)$$

This final equation is also true for zethrene where N=2. This follows from the fixed single and fixed double bonds in face **i** and its symmetrical equivalent. The resultant CC pattern is that of two isolated naphthalene currents, made up of rings **a** and **b**. Ring-current magnitudes, in all cases scaled to the magnitude in ring **a**, are shown in Table 7.4 with ring-currents calculated using the Randić model (for primary- and secondary-CCs); the HL model; and the RD equation.

Table 7.4: Ring current magnitudes for zethrene, perylene, 323- and 434-perylene with rings labelled as in Figure 7.13. Ring current magnitudes are all scaled to the magnitude in ring **a**.

Zethrene

	a	**b**	**i**
Randić	1	1	0
Dewar	1	1.3220	0.8008
HL	1	1.0651	0.4222
RD Eqn	1	1.0909	0.2261

Perylene

	a	**i**
Randić	1	0
Dewar	1	0.6282
HL	1	0.2460
RD Eqn	1	0.0723

323-Perylene

	a	**b**	**i**
Randić	1	1.3333	0
Dewar	1	0.5946	0.6137
HL	1	1.0350	0.4560
RD Eqn	1	1.0082	0.2701

434-Perylene

	a	**b**	**i**	**ii**
Randić	1	1.5	0	0
Dewar	1	0.5786	0.4500	0.8783
HL	1	0.9785	0.5436	0.8327
RD Eqn	1	0.7721	0.3559	0.6946

The Dewar and RD equation ring-current models offer some improvement by the inclusion of faces that are void of current in conventional CC models. The problem is that the pattern of current differs from that calculated through the HL model. Once again, the form of the modified Dias equation dampens the Dewar contribution only weakly because of the factor ω. Since the number of Dewar structures increases at a rate of N^7 (compared to the N^2 rate for Kekulé structures), Dewar contributions quickly become dominant and distort the pattern.

However, the ring-current pattern calculated through use of the RD equation, does offer some improvement over conventional CC models. First, in the case of zethrene, CC models predict rings **a** and **b** to be equivalent. This is corrected by using the RD equation, where stronger current is found in ring **b** (in agreement with HL and *ab initio* maps). Secondly, the central row in perylene now has a non-zero predicted current flow, again in agreement with HL and *ab initio* maps.

7.4.3 Non-Kekuléan Structures

To complete the ring-current analysis using this model two further examples will be considered. These belong to the non-Kekuléan family of molecules: phenalene, the smallest non-Kekuléan benzenoid, and the recently synthesised[249] even-vertex triangulene.[250]

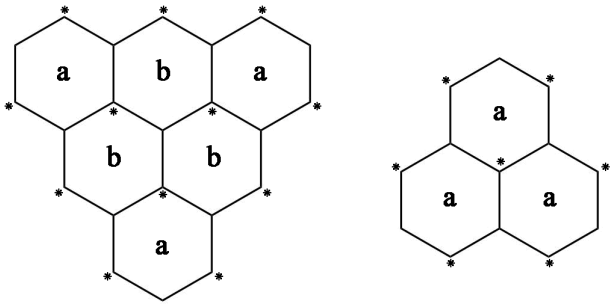


Figure 7.14: The structures of triangulene (left) and phenalene (right), identifying starred and unstarred vertices along with the labelling convention used for the subsequent ring-current analysis.

Phenalene is the smallest non-Kekuléan benzenoid, as it is the smallest with an odd number of vertices. Thus, phenalene supports an odd number of radical positions, with the first-excited structures being those with a single radical vertex. Phenalene is bipartite, but only the starred vertices (labelled in Figure 7.14) can support a first-excited state radical. The resulting Kekulé structures of the radical-removed fragment are shown in Figure 7.15.

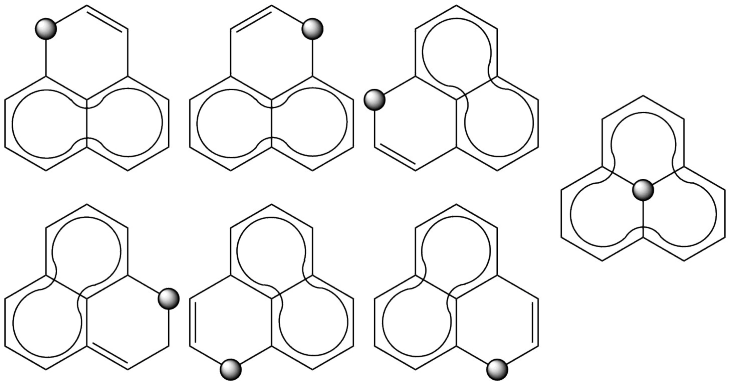


Figure 7.15: The Kekulé structures that can be drawn in the radical removed structures of phenalene. Cyclic paths denote the delocalisation across all bonds contained within the cyclic path. Clar-like notation again signifies the presence of multiple Kekulé structures in each fragment.

Triangulene has an even number of vertices but no Kekulé structures.[11] The even number of vertices necessitates triangulene must support an even number of radical vertices. The difference in the number of starred and unstarred vertices implies that the two radicals must be positioned on starred vertices (labelled in Figure 7.14). Localisation on unstarred vertices leads to higher order radical structures.

Both phenalene and triangulene possess no primary-CCs meaning conventional conjugated-circuit models have no way to approximate the ring-current. Isolation of vertices means secondary-CCs can be identified and therefore the RD equation can be used to approximate a ring-current map. Raw and scaled ring-current magnitudes are displayed in Table 7.5.

Table 7.5: Raw and scaled ring-current magnitudes for phenalene and triangulene calculated using various models, displaying raw current magnitudes and those scaled to ring **a**. Cycle labelling corresponds to those in Figure 7.14. Scaled currents are normalised to the magnitude in ring **a**.

Phenalene			**Triangulene**				
	Raw	**Scaled**		**Raw**		**Scaled**	
	a	**a**		**a**	**b**	**a**	**b**
Randić	0	0	**Randić**	0	0	0	0
Dewar	14	1	**Dewar**	676	588	1	0.8698
HL	0.6695	1	**HL**	0.6548	0.6251	1	0.9546
RD Eqn	0.7	1	**RD Eqn**	1.1046	0.9608	1	0.8698

As can be seen, inclusion of secondary-CCs offers an improvement over conventional CC models. The scaled ring-currents can also be seen to approximate closely to that of the scaled HL. Some improvements are still needed to the Dewar model, particularly related to the ω value. Ultimately, current maps are qualitatively correct now supporting current, in contrast with the inability of the CC models to give any flow at all.

7.5 Conclusion

The first attempt to improve the CC models involves the inclusion of first-excited structures. In graph theoretical terms this corresponds to the presence of radicals in: $K^{(2)}$ structures where all possible biradical structures are considered; or Dewar structures where adjacent biradicals are removed from the $K^{(2)}$ structures. Originally applied to the improvement of Pauling Bond Order, the Dias equation accounts for Kekulé-based conjugated circuits (primary-CCs) and Dewar-based conjugated-circuits (secondary-CCs). The postulated equation relied on a fixed parameter ω which dampens the contribution from Dewar structures.

In terms of PBO, the Dias equation offers some improvement of bond orders when judged against experimental bond length/ bond order data. The most egregious examples of the failure of CC models, perylene, zethrene and non-Kekuléan structures, also demonstrate an overall improvement, eliminating the problematic fixed single and double bonds. When considering ring-currents, inclusion of secondary-CCs leads to some role for cycles previously not active in current CC models. In all cases investigated, while not reproducing HL identically, the RD equation offers some improvement. Non-Kekuléan structures and 'empty rings' now have a qualitatively correct assignment of current.

Perhaps the main problem with the RD equation is the ω parameter. Historically, the value of ω was taken to be 0.03. However, this was only devised through consideration of one bond of perylene, and involved a questionable mode of normalisation. Investigation of the parameter on several benzenoids has found this value to be not appropriate for many bonds or systems. The result is that for any fixed value, the contribution from Dewar structures quickly becomes the dominant contribution in the series investigated. This can be rationalised by the formulae for the number of Dewar structures which rise to the order of N^5 and N^7 for polyacenes and perylenes respectively. There is clear scope for improvement, which may come from a better, more flexible choice of ω parameter devised through consideration of more systems. Alternatively, different formulation could be postulated for the RD formula through the incorporation of other CC models.

Chapter 8

The Myrvold-Fowler Model[1]

8.1 Introduction

The final model to be discussed was recently proposed as part of a long standing collaboration between the Fowler group in Sheffield and computer scientist Prof. Wendy Myrvold from the University of Victoria (BC). An examination of the Aihara formalism (detailed in full in Chapter 3) identified a Hückel-London calculation involving the use of characteristic polynomials. The idea of the Myrvold-Fowler models, henceforth shortened to the MF models, relies on the use of these polynomials, but using only select coefficients from the polynomials of the graph, and the cycle-removed graph, G−C. The intention is to take more forms of the Aihara cycle expansion into account in a new CC-like model.

The general characteristic polynomial for an n-vertex graph is defined as

$$\phi_{\mathrm{G}}(x) = x^{\mathrm{n}} + c_{\mathrm{n}-1}x^{\mathrm{n}-1} \ldots + c_2x^2 + c_1x^1 + c_0 \tag{8.1}$$

and the characteristic polynomial for the graph G−C, existing on m-vertices, is defined as

$$\phi_{\mathrm{G\text{-}C}}(x) = x^{\mathrm{m}} + d_{\mathrm{m}-1}x^{\mathrm{m}-1} \ldots + d_2x^2 + d_1x^1 + d_0. \tag{8.2}$$

For a bipartite graph, with even n, all coefficients c_k with odd k vanish, and likewise for odd n, all coefficients c_k with even k vanish. The goal of creating formulations described below was to model the calculated Hückel-London ring current via cycle contributions, summed over all possible cycles.

[1]Prof. Wendy Myrvold is thanked for the creation of programs used in this chapter. In addition, work in this chapter is also detailed in the upcoming paper, which also details the Aihara formalism in Chapter 3: Myrvold. W., Kaur. P., Clarke. J., and Fowler. P.W., *In Preparation.*

Three equations were constructed, referred to as the *One-Term*:

$$J_C = -2 \times \left(\frac{S_C}{S_0}\right) \left[\frac{d_0}{c_0}\right], \tag{8.3}$$

the *Two-Term*:

$$J_C = -2 \times \left(\frac{S_C}{S_0}\right) \left[\frac{d_0}{c_0} + \frac{d_2}{c_2}\right], \tag{8.4}$$

and finally the *Adjusted-Two-Term*, henceforth referred to as Adjusted, equation:

$$J_C = -2 \times \left(\frac{S_C}{S_0}\right) \left[\frac{d_0}{c_0} + 4 \times \frac{d_2}{c_2}\right], \tag{8.5}$$

where in all cases, positive (negative) current magnitudes denote diatropic (paratropic) oriented currents. The value of 4 in the Adjusted model is taken as a parameter roughly optimised through a trial-and-error approach to fit to the HL model for benzenoids with up to seven hexagonal faces. In alternant, Kekuléan systems, the c_0 and d_0 terms correspond to K^2 of G or G−C, respectively. For a non-Kekuléan system, the d_0 and c_0 terms are replaced by the first non-zero terms in the characteristic polynomials. To generalise, d_0 and c_0 terms are the first non-zero terms of the characteristic polynomial, with d_2 and c_2 terms the next coefficients of the characteristic polynomial with the same parity of the order x as for the d_0 and c_0 terms.

8.1.1 Explicit examples: Three benzenoid graphs

Now consider the three benzenoid graphs consisting of three hexagons, where each is examined in depth and compared to the Hückel-London and Randić ring-current models.

8.1.1.1 Anthracene

First consider anthracene, as performed in Chapter 3.4.1, the MF models can be used to demonstrate the striking similarity to the HL results. Using an identical cycle labelling system and recalling that $C_1 = C_2$ and $C_4 = C_5$, the characteristic polynomials of the graphs and the unique cycles are:

$\phi_{\mathbf{G}}$	$x^{14} - 16x^{12} + 98x^{10} - 296x^8 + 473x^6 - 392x^4 + 148x^2 - 16$
$\phi_{\mathbf{G-C_1}}$	$x^8 - 8x^6 + 18x^4 - 13x^2 + 1$
$\phi_{\mathbf{G-C_3}}$	$x^8 - 6x^6 + 11x^4 - 6x^2 + 1$
$\phi_{\mathbf{G-C_4}}$	$x^4 - 3x^2 + 1$
$\phi_{\mathbf{G-C_6}}$	1

Input into the MF models results in the following cyclic ring-current magnitudes.

Label	One-Term	Two-Term	Adjusted	Hückel-London
$\mathbf{C_1}$	0.125	0.3001	0.8277	0.4058
$\mathbf{C_3}$	0.125	0.2061	0.4493	0.2824
$\mathbf{C_4}$	0.25	0.3311	0.3311	0.3183
$\mathbf{C_6}$	0.375	0.375	0.375	0.3603

Then the total ring-current in the terminal and central faces can be summarised by the summation of contributing cycles.

	Raw		Scaled	
	Terminal	Central	Terminal	Central
Randić	6	8	1	1.3333
Hückel-London	1.0844	1.2794	1	1.1798
One-Term	0.75	1	1	1.3333
Two-Term	1.0068	1.2432	1	1.2348
Adjusted	1.7770	1.9730	1	1.1103

Examination of the ratio of currents demonstrates that both the Two-Term and Adjusted models result in a ring-current ratio quantitatively consistent with the HL model. The One-Term and Randić models are equivalent in the scaled form.

8.1.1.2 Phenalene

Next consider the non-Kekuléan graph phenalene. Breaking the system down into constituent cycles, there are three unique cycles, labelled C_1 to C_3 (see Figure 8.1).

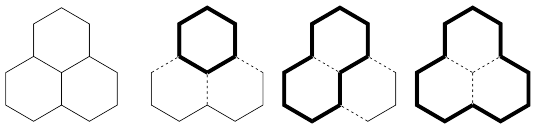


Figure 8.1: The graph of phenalene (left) and the three unique cycles, indicated by the bold bonds, labelled mid-left to right as C_1, C_2 and C_3.

The characteristic polynomials of the corresponding graph and cycle-removed graphs and the corresponding cycle contributions are:

$\boldsymbol{\phi_G}$	$x^{13} - 15x^{11} + 84x^9 - 226x^7 + 309x^5 - 207x^3 + 54x$
$\boldsymbol{\phi_{G-C_1}}$	$x^7 - 6x^5 + 10x^3 - 4x$
$\boldsymbol{\phi_{G-C_2}}$	$x^3 - 2x$
$\boldsymbol{\phi_{G-C_3}}$	x

Label	One-Term	Two-Term	Adjusted	Hückel-London
$\mathbf{C_1}$	0.148	0.2448	0.5346	0.3684
$\mathbf{C_2}$	0.148	0.1675	0.2254	0.2290
$\mathbf{C_3}$	−0.111	−0.111	−0.111	−0.1569

which when summed over all contributing cycles, i.e. $C_1 + 2C_2 + C_3$ results in the overall MF magnitudes. By symmetry, only one face needs to be considered.

	Terminal
Randić	0
Hückel-London	0.6695
One-Term	0.3333
Two-Term	0.4686
Adjusted	0.8744

Since there is no other ring to offer as a scaling, all models which predict some degree of current therefore scale to 1. Thus, all MF models are superior to the conventional CC models.

8.1.1.3 Phenanthrene

The final three benzenoid graph is phenanthrene. In this case, there are four unique cycles, labelled C_1 to C_4 (see Figure 8.2).

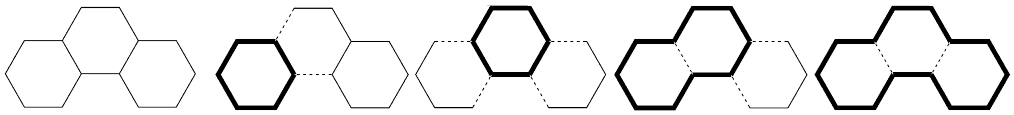


Figure 8.2: The graph of phenanthrene (left) and the four unique cycles, indicated by the bold bonds, labelled mid-left to right as C_1, C_2, C_3 and C_4.

The characteristic polynomials of the corresponding graph and cycle-removed graphs and the corresponding cycle-current contributions for the various models are:

$\phi_{\mathbf{G}}$	$x^{14} - 16x^{12} + 98x^{10} - 297x^8 + 479x^6 - 407x^4 + 166x^2 - 25$
$\phi_{\mathbf{G-C_1}}$	$x^8 - 8x^6 + 19x^4 - 16x^2 + 4x$
$\phi_{\mathbf{G-C_2}}$	$x^8 - 6x^6 + 11x^4 - 6x^2 + 1x$
$\phi_{\mathbf{G-C_3}}$	$x^4 - 3x^2 + 1$
$\phi_{\mathbf{G-C_4}}$	1

Label	One-Term	Two-Term	Adjusted	Hückel-London
$\mathbf{C_1}$	0.32	0.5128	1.0911	0.6361
$\mathbf{C_2}$	0.08	0.1523	0.3692	0.2338
$\mathbf{C_3}$	0.16	0.2323	0.4492	0.2405
$\mathbf{C_4}$	0.24	0.24	0.24	0.2600

Again using symmetry arguments, the calculation reduces to the summation of the central and terminal faces. The Two-Term and Adjusted formulae again display similar scaling to the HL model.

	Raw		Ratio	
	Terminal	Central	Terminal	Central
Randić	12	8	1	0.6666
Hückel-London	1.1366	0.9748	1	0.8576
One-Term	0.72	0.64	1	0.8888
Two-Term	0.9851	0.8569	1	0.8699
Adjusted	1.7802	1.5075	1	0.8468

8.2 Examination of Ring-Current Models

8.2.1 Linear Polyacenes

The discussion of anthracene can be extended to all linear polyacenes. Taking Figure 7.11, the three MF models can be added, such that the new Figure 8.3 compares all relevant graph theory models.

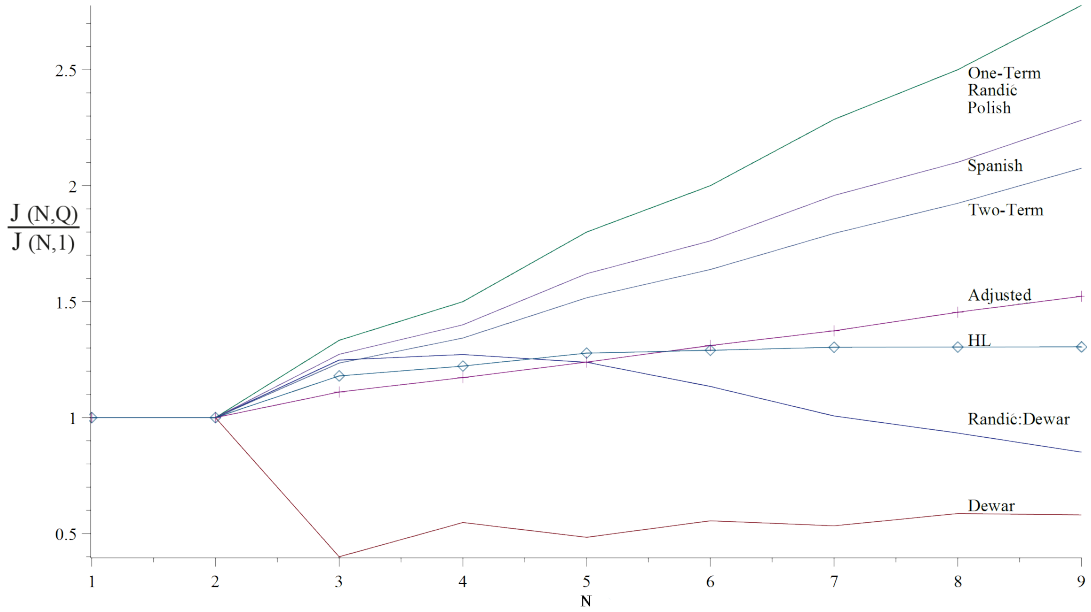


Figure 8.3: Comparison of the major graph-theoretical ring-current models showing ring current magnitudes for the central ring of the N-linear polyacene, scaled to that of the terminal ring. Randić:Dewar refers to the current equation (7.11). Randić, Ciesielski et al. and One-Term models are superimposed since the scaled currents are equivalent. For simplicity, the Mandado curve refers to the use of equation (1.22).

Figure 8.3 shows several nuances in the behaviour of the three models. First, the Randić, Ciesielski et al. and One-Term models are all equivalent for linear-polyacenes scaled to terminal rings. This full equivalence is limited to the linear polyacenes. Secondly, the Adjusted equation shows the best overall tracking of the HL model. The Two-Term equation, is also better than the three published CC models. However, no model possesses the plateau in current magnitude observed in the HL model when N increases (see Figure 8.3). Of the three proposed MF models, the Adjusted model is the clearly the best owing to the closer approximation to this plateau. Furthermore, comparison of the

Adjusted model to the RD equation, shows the Adjusted model is consistently better at approximating the HL current pattern.

In addition, it is also useful to consider how the magnitude of current changes through the faces of the polyacene. Figure 8.4 displays the current magnitude for each face of 6-polyacene, calculated using the various models with magnitudes normalised to the terminal ring.

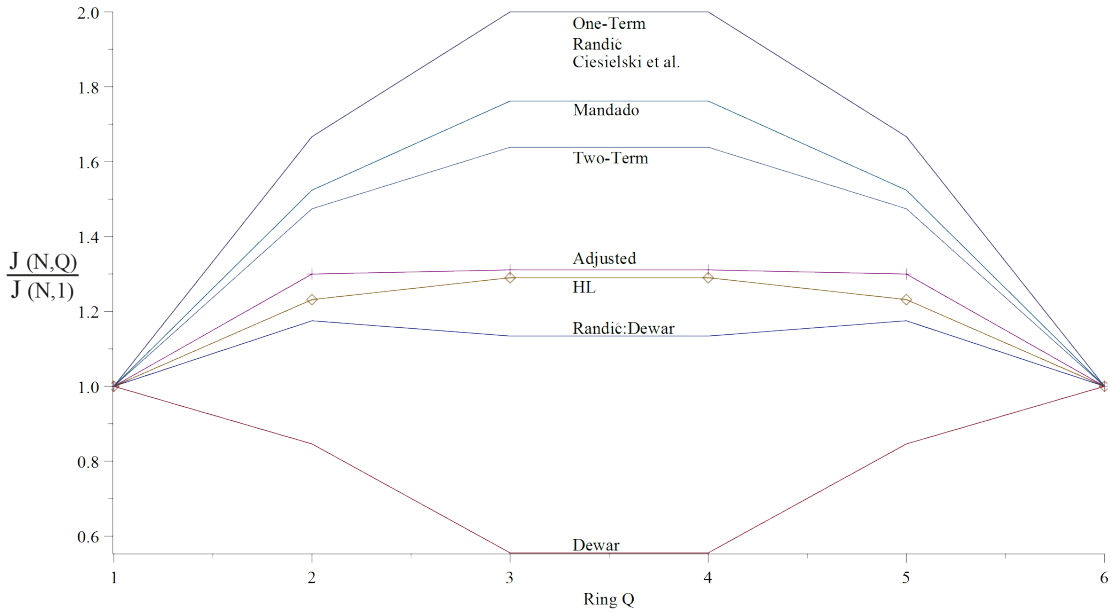


Figure 8.4: Comparison of the major graph-theoretical ring-current models showing ring current magnitudes of the faces of 6-polyacene, scaled to that of the terminal ring. Randić:Dewar refers to the current from equation (7.11). Randić, Ciesielski et al. and One-Term models are superimposed since the scaled currents are equivalent. For simplicity, the Mandado curve refers to the use of equation (1.22).

From Figure 8.4, it is clear that the Adjusted model is the best approximation of HL current across the faces, displaying the characteristic central ring plateau. The Adjusted model displays the closest overall consistency to the trends observed in the HL model. The other MF and CC models rise in terms of scaled magnitude at a much faster rate than the Adjusted model and, at large values of N, do not show a plateau in the inner faces of the polyacene. In addition, the RD and Dewar models also fail to display appropriate scaling at large values of N, showing the decrease in current discussed earlier in Chapter 7. Slight deviations from HL results are seen, particularly for anthracene, where the

Adjusted trend is below HL, and 9-polyacene, where the trend is above HL. However, the Adjusted model is superior in terms of scaled results to any other model investigated.

8.2.2 Linear Fibonacenes

The second series of systems to be considered are the linear fibonacenes, a series where a linear segment contains no more than two hexagons.[104,251] In contrast to the single-isomer linear polyacenes, N-fibonacenes with more than three rings can exist as multiple isomers. For the present case only the 'zig-zag' fibonacene isomer will be considered, the general structure of which is illustrated in Figure 8.5.

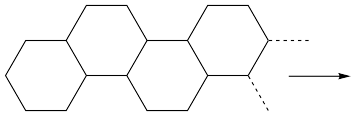


Figure 8.5: The generation of a 'zig-zag' fibonacene where subsequent rings are added in a manner to extend the zig-zag.

Figure 8.6 compares the various models for the ring-currents, where all current magnitudes are normalised to the current of the terminal ring.

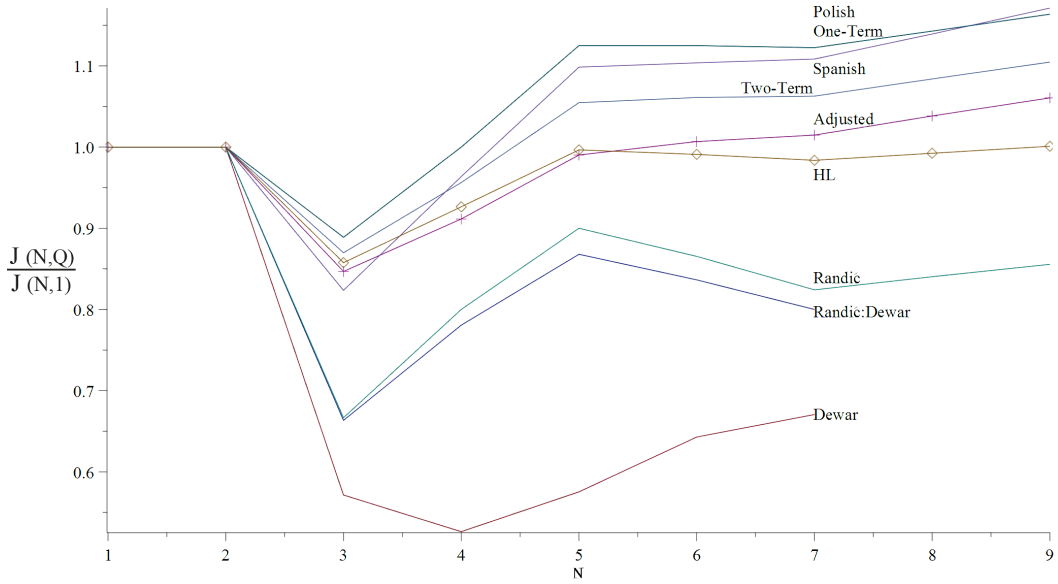


Figure 8.6: Comparison of the major graph-theoretical ring-current models showing ring current magnitudes for the central ring of the N-'zig-zag' fibonacene, with magnitudes scaled to that of the terminal ring. Randić:Dewar refers to the current from equation (7.11). Ciesielski et al. and One-Term models are superimposed since the scaled currents are equivalent.

Once again, there are interesting patterns that should be investigated. First, the ratio of the Adjusted formula is clearly closer to that of the HL than any of the other models investigated so far. At N > 5 the Adjusted model deviates from the HL model, with current magnitudes increasing rather than dipping, but this is only a minor difference. Second, the poor scaling of the RD equation, compared to both the Adjusted and HL models, should be noted. By definition, the RD equation is a compromise between Randić and Dewar models and, while appropriate for the calculation of small linear-polyacenes, it is not appropriate for linear-fibonacenes. Finally, the Two-Term offers improvement over conventional CC models, but its own utility is surpassed by the superior Adjusted model. Next, consider how the ring-current changes in magnitude throughout the different faces of the 6-fibonacene (see Figure 8.7).

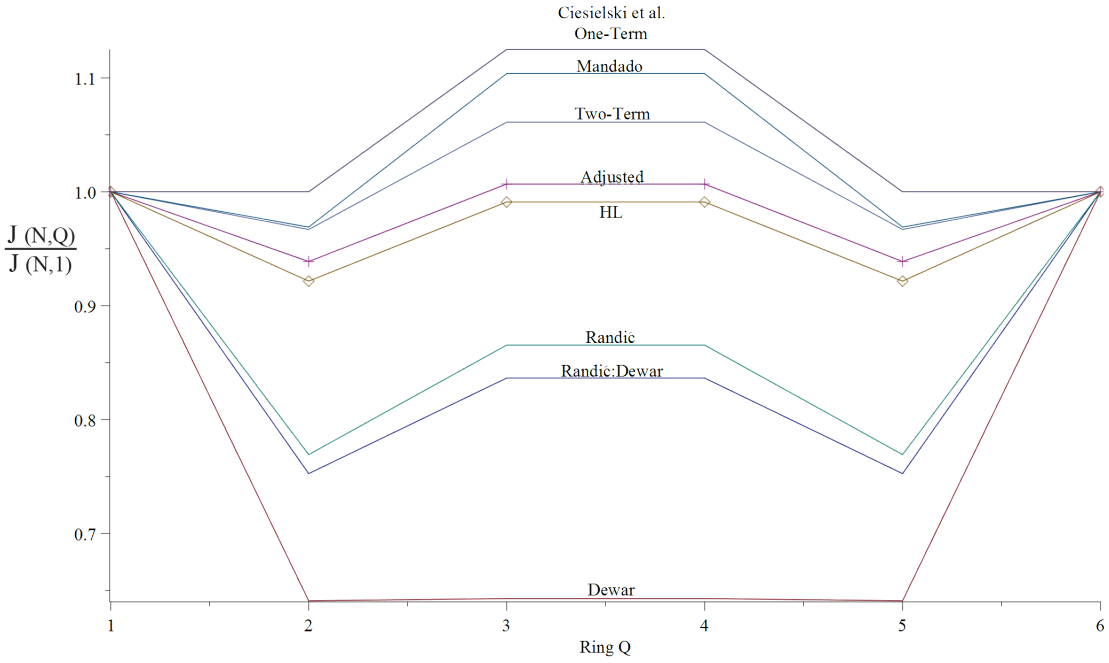


Figure 8.7: Comparison of the major graph-theoretical ring-current models showing ring current magnitudes for the individual faces 6-'zig-zag'-fibonacene, scaled to that of the terminal ring. Randić:Dewar refers to the current from equation (7.11). Ciesielski et al. and One-Term models are superimposed since the scaled currents are equivalent.

Figure 8.7 provides the best evidence for the utility of the Adjusted formula. Ring-current magnitudes follow the pattern of the HL model to a high degree of reproducibility

that continues for the majority of fibonacenes investigated. As seen with the N-polyacenes, the Adjusted model displays the best overall scaled ring current trends, consistently reproducing those in the HL model. However, there are still small deviations between HL theory and the adjusted model observed at large values of the N-fibonacene. With respect to the other MF, CC and Dewar-based models, the Adjusted model is the superior model.

8.2.2.1 Differentiation between Isomers

One further point should be raised that emphasises the success of the new models. Through conventional CC models, there is no differentiation between fibonacene isomers, a result of the equivalence in $m(\mathrm{G}-\mathrm{C})$ in all CC models. However, isomeric difference is a feature present in HL and *ab initio* maps.[104] In agreement with these more accurate methods, the RD, Two-Term and Adjusted MF models are all able to differentiate between rings of a given position in different isomers. Two isomers exist for 4-fibonacene corresponding to the 'zig-zag' isomer considered above, and a curved system shown in Figure 8.8.

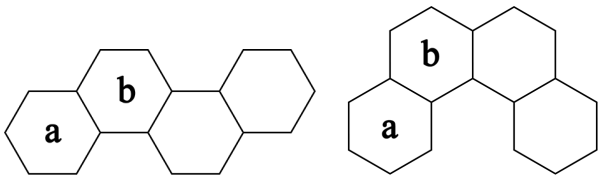


Figure 8.8: The two isomers of 4-fibonacene, (left) the 'zig-zag' isomer and (right) the curved isomer. **a** and **b** correspond to the labelling of faces which are then related by symmetry to the other faces in the specific isomer.

Scaling all current magnitudes to that of face **a** (resulting in all ring currents in these faces being 1), the current magnitudes for face **b**, calculated through various models, are summarised in Table 8.1.

Table 8.1: Ring-current magnitudes for the two isomers, defined as the zig-zag and curved, for 4-fibonacene, calculated through various graph-theoretical models. In both cases, ring current magnitudes are scaled to that in ring **a** that, for simplicity, is not reported here since this is one for both models.

Label	One-Term	Two-Term	Adjusted	Randić:Dewar	HL	Randić
Zig-Zag	1	0.965	0.9287	0.7859	0.9337	0.8
Curved	1	0.9563	0.9115	0.7807	0.9264	0.8

One can see that the One-Term and the Randić models both fail to distinguish between the isomers. This is caused by inclusion of only the final term of the characteristic polynomial, hence the number of Kekulé structures, which is constant for all fibonacene isomers of the same N. Subtle differences emerge in the second terms of the characteristic polynomial and the number of Dewar structures. The result is different contributions of similar shaped cycles between the two isomers. Once again, the Adjusted model can be said to offer the 'best' approximation to the HL model. However, the real success is the ability of the RD, Two-Term and Adjusted models to quantify the different current between the isomers.

8.2.3 Zethrene and perylene extensions

Turning attention to zethrene and the extensions of perylene, as described in Chapters 6.3 and 7.3, allows the MF models to be tested on systems containing fixed bond orders. In all cases ring-current magnitudes are scaled to the ring labelled **a**, in accordance with the conventions used previously in Figure 7.13.

First consider the example of zethrene. All of the newly proposed models, with the exception of the One-Term, accurately depict the **i** faces of zethrene possessing a diatropic current and appropriately distinguish the **a** and **b** faces. The absence of current in face **i** in the One-Term model is attributed to these cycles not being involved in any Kekulé structure and thus, G−C will be non-Kekuléan. Therefore, according to equation (8.3) the magnitude of the d_0 coefficient will be zero. The Two-Term and Adjusted formulae predict some degree of current owing to the inclusion of the second coefficient d_2 resulting in, for the Adjusted model, an accurate representation of the ring-current.

Table 8.2: The ring-current magnitudes for the benzenoids zethrene, perylene, 323- and 434-perylene, labelled according to Figure 7.13 and scaled to face **a**. RD Eqn refers to the current calculated using the RD equation (7.11).

Zethrene

	a	**b**	**i**
Randić	1	1	0
One-Term	1	1	0
Two-Term	1	1.0510	0.2298
Adjusted	1	1.101	0.4545
RD Eqn	1	1.0909	0.2261
HL	1	1.0651	0.4222

Perylene

	a	**i**
Randić	1	0
One-Term	1	0
Two-Term	1	0.1352
Adjusted	1	0.2752
RD Eqn	1	0.0723
HL	1	0.2460

323-Perylene

	a	**b**	**i**
Randić	1	1.3333	0
One-Term	1	1.3333	0
Two-Term	1	1.1706	0.2633
Adjusted	1	1.0258	0.4979
RD Eqn	1	1.0082	0.2701
HL	1	1.0350	0.4560

434-Perylene

	a	**b**	**i**	**ii**
Randić	1	1.3333	0	0
One-Term	1	1.5	0	0
Two-Term	1	1.2189	0.2929	0.5370
Adjusted	1	1.0035	0.5174	0.9487
RD Eqn	1	0.7721	0.3559	0.6946
HL	1	0.9785	0.5436	0.8327

Now consider the series of extensions of perylene. The MF models, excluding the One-Term for the same reasons as zethrene, approximate the HL current to a reasonable level. In all cases, the central faces **i** or **ii**, empty in the CC models, are now predicted to possess diatropic currents of approximate scaled magnitudes to the HL model. Once again, the Adjusted formula offers the 'better' approximation, closer to the scaled HL. This comparison also extends to the RD equation. The Adjusted MF model can be seen to offer 'better' scaled currents than the RD equation for all of the perylene systems investigated.

8.2.4 Non-Bipartite Graphs

Finally, two examples of non-bipartite graphs will be discussed in detail. First, consider pentalene, a typical example of an antiaromatic system as prescribed through various models, for example NICS[103] and circuit resonance energies.[72] Unfortunately, it is also an example of the breakdown of the MF models. Table 8.3 reports the ring-current magnitudes calculated through various models.

Table 8.3: The ring-current magnitudes from the four literature graph-theoretical models and the four proposed models. (Left) the models identifying pentalene as antiaromatic; (right) the models predicting pentalene as aromatic.

Model	Magnitude	Model	Magnitude
Hückel-London	-2.1372	**One-Term**	0
Randić	-2	**Two-Term**	0.3311
Ciesielski et al.	-2	**Adjusted**	1.3244
Mandado	-0.5		
RD Equation	-0.8368		

Table 8.3 assumes pentalene is constructed from regular pentagons with fixed bond lengths of 1.4 Å. Characteristic polynomials will no longer be of one parity in x, as is the case for bipartite systems. Here, the MF currents are formulated by only considering coefficients of the same parity in x, for example taking c_0 as the coefficient from the x^1 term and c_2 as the coefficient from the x^3 term. Alternative formulation can be conceived by taking the next available coefficient from the polynomials, for example by taking the coefficients from the x^1 and x^2 terms as c_0 and c_2 values respectively. The results from the latter formulation, not reported here, have the affect of changing the magnitude of current, but not the overall tropicity found in the MF models.

As evident from table 8.3, the three MF models all denote pentalene as an aromatic system possessing a diatropic current. This is in contrast to the various other models based on multiple criteria[103,252] and even includes the conjugated-circuit models. Moreover, the RD equation successfully depicts pentalene as antiaromatic, in spite of the lack of any secondary-conjugated circuits.

The question is now why this is happening, the answer to which lies in a dissection of the individual cycle contributions. There are two unique cycles which contribute to each

pentagon face: the sole pentagon and the perimeter. These are referred to as C_1 and C_2 respectively. Comparison of the cyclic contributions from the MF, HL and Randić cyclic models rationalise the magnitudes in Table 8.4.

Table 8.4: A cyclic breakdown of the sole pentagon, C_1, and the perimeter cycle, C_2, which result in the total current magnitude for the graph-theoretical ring-current models. S_C/S_0 represents the normalised area of the pentagon, ≈ 0.66221

Label	One-Term	Two-Term	Adjusted	Hückel-London	Randić
C_1	$\frac{1}{2}\frac{S_C}{S_0}$	$\frac{S_C}{S_0}$	$\frac{5}{2}\frac{S_C}{S_0}$	$0.6149\frac{S_C}{S_0}$	0
C_2	$-\frac{1}{2}\frac{S_C}{S_0}$	$-\frac{1}{2}\frac{S_C}{S_0}$	$-\frac{1}{2}\frac{S_C}{S_0}$	$-3.8422\frac{S_C}{S_0}$	-2
Total	0	$\frac{1}{2}\frac{S_C}{S_0}$	$\frac{2S_C}{S_0}$	$-3.2273\frac{S_C}{S_0}$	-2

Inspection of Table 8.4 identifies where the discrepancy in the MF models arises. First, in the Randić model, C_1 is non-conjugated so the resultant ring current arises solely from the 4n perimeter of two fused pentagons. Secondly, the pentagon contributes a diatropic current for all non-conjugated-circuit models. In the HL model the diatropic pentagon is ultimately cancelled by a stronger paratropic perimeter current resulting in overall paratropicity. In contrast, in the MF models the perimeter cycle contribution fails to offer the same suppression as in the HL model. As such the perimeter cycle only weakens the diatropic contribution from the pentagon in the cases of the Two-Term and Adjusted models or matches the pentagon contribution in the case of the One-Term model. The result in all three MF models is the incorrect assignment of aromaticity.

The final example to be discussed is fluoranthene. Mentioned in Chapters 6 and 7, fluoranthene suffers from fixed single bonds joining the naphthalene unit to the benzene unit through the single pentagon face **i** (see Figure 8.9).

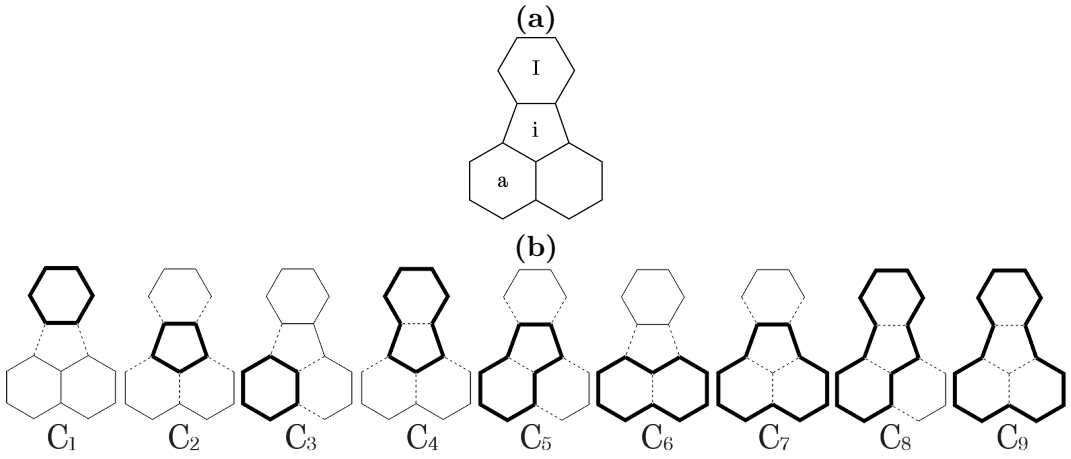


Figure 8.9: (a) The structure of fluoranthene and the face labelling scheme. (b) The cycle labelling scheme where bold lines identify the cycle in question.

The ring-current magnitudes, as calculated through the various graph-theoretical models are reported in Table 8.5.

Table 8.5: Current magnitudes calculated using a series of graph-theoretical models scaled to the ring of the largest magnitude.

Face	Hückel-London	One-Term	Two-Term	Adjusted	Randić	RD Eqn
I	0.8711	0.7501	0.8101	0.8780	1	1
a	1	1	1	1	0.8889	0.8833
i	0.0501	0	0	0	0	0

Magnitudes in Table 8.5 identify several features. First, fluoranthene can be considered a non-alternant analogue of perylene. As such, the CC models will inevitably fail to predict any current modulus in ring **i**. Second, all MF models and the RD equation also fail to quantify current magnitude in ring **i**. However, the Adjusted model scales the **a** and **I** rings to a similar scale as in the HL model, which is a minor improvement over the Randić and RD models. It should be noted that, from the HL model, the predicted ring-current in ring **i** is weak, only 5% of that in ring **a**. A cycle contribution decomposition in Table 8.6 identifies why the MF models fail to predict current in ring **i**.

Table 8.6: Cycle contributions calculated using a series of graph-theoretical models. Cycle are labelled as illustrated in Figure 8.9.

Cycle	Hückel-London	One-Term	Two-Term	Adjusted	Randić
$\mathbf{C_1}$	0.8333	0.5	0.763	1.552	18
$\mathbf{C_2}$	0.0121	0	0	0	0
$\mathbf{C_3}$	0.468	0.2222	0.3874	0.8828	8
$\mathbf{C_4}$	0.0148	0	0	0	0
$\mathbf{C_5}$	0.513	0.4444	0.5545	0.8848	8
$\mathbf{C_6}$	0.0087	0	0	0	0
$\mathbf{C_7}$	-0.0061	0	0	0	0
$\mathbf{C_8}$	0.0083	0	0	0	0
$\mathbf{C_9}$	-0.0052	0	0	0	0

The HL cycle contribution from cycles identified as conjugated-circuits are larger in magnitude than any other contribution (C_1, C_3 and C_5). However, it is the contribution from non-conjugated circuits that leads to the HL current in face **i**. The major contributions are approximated through the MF models and Randić model, which both only recognise the larger contributing conjugated circuits. Any cycle containing face **i** is absent of current in the MF models. It turns out this discrepancy is due to the mismatch of coefficients used in equations (8.3)−(8.5), which is attributed to the non-bipartite nature of the graph. Finally, the absence of face **i** current in the RD equation can be attributed to the lack of any secondary-CCs involving the pentagon.

8.3 Conclusion

Three ring current models are proposed that utilise the coefficients of the characteristic polynomial, combining the Ciesielski et al. and Aihara models. All three involve the computation of coefficients from the characteristic polynomial: the final term and the second to last term of the same parity. The third model, referred to as the Adjusted model, includes a fitted value to approximate the inclusion of the second scaled coefficient term. This model offers significant improvements over all published conjugated-circuit models and that of the proposed equation (7.11), acting as an appropriate approximation to the HL model for the benzenoid series investigated.

The models can be applied to systems previously excluded from CC models including non-Kekuléan and those containing fixed-single or fixed-double bonds. In the cases of the benzenoids investigated, the Adjusted model provides an accurate approximation of the HL models. This includes reproducing the HL trend of the mid ring plateau when scaled to the terminal ring.

However, MF model ring currents for the two non-benzenoid examples, pentalene and fluoranthene, fail to depict an accurate assessment of ring current aromaticity. Pentalene is anti-aromatic, supporting paratropic ring-currents calculated through both *ab initio* and Hückel-London approaches. However, the MF models predict pentalene to support a diatropic ring-current. Furthermore, fluoranthene is considered a non-alternant perylene analogue and as such conventional conjugated-circuit models suffer the problem of PBO-fixed single bonds. Both RD and MF models fail to quantify current in this central ring, rationalised by a lack of primary and secondary-CCs involving the pentagon and an explicit exclusion of coefficient terms in the MF equations (8.3)−(8.5). Therefore, further investigation is needed in the applicability of the MF models to other non-benzenoid systems. For the time being, the Adjusted MF model can only be applied with confidence to benzenoid systems.

Part IV

Summary, Future Work and Bibliography

Chapter 9

Summary and Future Work

The central issue of this research was an investigation of graph-theoretical evaluations of ring-currents, namely the Hückel-London and conjugated-circuit models. The former is a historically well-established model that has been shown to accurately reproduce current maps of *ab initio* quality. In contrast, the latter is a younger conception with an aim to approximate HL quality maps through considering only dominant contributions. These approximations have resulted in many documented systems that display significant deviations from the ring-current depictions of the higher accuracy models. There are currently four literature models of the conjugated-circuit models, which vary according to area inclusion and inherent normalisation. The models work by partitioning conjugated-circuits, identified through alternating single and double bonds in a given Kekulé structure, into individual cycle contributions, which are then summed to find the overall current map. Through employment of the Aihara variant of Hückel-London theory, which also partitions current into cycle contributions, comparisons can be drawn between conjugated circuit contributions and HL contributions. It is clear the reason for the deviation in maps is a result of the failure in the underlying conjugated-circuit theory that excludes cycles that are considered non-conjugated, but in the HL model sum to dominate the current.

The Aihara Hückel-London model was detailed in full. Cyclic contributions can be evaluated by manipulation of characteristic polynomials of the graph and cycle vertex and edge removed graph. This model itself has led to multiple theorems related to Hückel-London theory that have explained observations from maps. These include: occupied and virtual current equivalence in bipartite graphs; and the lack of all current in non-bonding orbitals. Manipulation of characteristic polynomials has the potential to produce

analytical formulae for Hückel-London ring currents. The present research has limited this to mono-cyclic heterocycles. In this chapter, HL ring current was found to be robust against changes to electronegativities imposed when heteroatoms are introduced. However, the analysis was limited by assuming $\beta_{\mathrm{CX}} = \beta_{\mathrm{CC}}$ which requires further investigation into the affect of resonance integral changes. Furthermore, preliminary work on other systems such as Kekulé benzene has shown that the change in currents over the HL ring-current can be mapped using the Aihara formalism as a function of changing β and area parameters. This model has proved to be a powerful tool for computation of *ab initio* quality maps at a reduced computational cost.

The ability to construct analytical ring-current equations in the Hückel-London model is limited by system size and ability to express eigenvalues compactly and analytically. Any system where $\phi_{\mathrm{G}}(x)$ contains quintic or higher order polynomial factors, it is impossible to express eigenvalues analytically. This is not true for conjugated-circuit models. If K(G) can be expressed analytically for a series of structures, then it is possible for the conjugated-circuit model current to also be expressed analytically. As shown in Chapter 5, the Randić ring current formulae for the antikekulene homologues and derivatives, were found to be functions of the Fibonacci and Lucas number sequences. A lack of comparable *ab initio* maps made a definitive assessment of aromaticity problematic owing to issues with optimisation of these hypothetical systems. Ideally this should be investigated further to assess the disputed antiaromaticity associated with antikekulene, and investigate the equiaromaticity found through a conjugated circuit analysis for antikekulene derivatives.

Attention was turned to benzenoids that contain fixed single or double Pauling Bond Orders. These systems have been shown to possess inaccurate CC current maps, when compared against *ab initio* and Hückel-London quality maps. Examples of these types of systems include perylene and zethrene, where central faces are void of current. Investigations of perylene derivatives, where the top and bottom rows are changed to other bicycles, and extensions, where the perylene benzenoid rows are extended, resulted in conjugated circuit maps that differed from the corresponding HL or *ab initio* maps. The

ab initio and HL models depicted a strong monomer current in perylene extensions up to 5 hexagons in the top row, after which the current altered to become a perimeter-dominated map. Mapping contributions from various molecular orbitals identified a change in the dominant contributions accounted for in *ab initio* and HL models. However, the absence of MO occupation in conjugated circuit theory means this trend is not reciprocated.

The primary aim was to find new ways to improve the conjugated-circuit models, avoiding the aforementioned inconsistencies. To achieve this two new models were proposed, referred to as the Randić-Dewar model and the Adjusted Myrvold-Fowler models. Both new models offer advantages over conventional CC models by inclusion of fully or partially non-Kekuléan systems. The Randić-Dewar model adds, to the conventional Randić model, a parameterised contribution from the so-called secondary-conjugated-circuits, defined as those CCs identified in the first-excited Dewar structures. The proposed current contribution has the form:

$$\mathrm{J_C} = \frac{2\mathrm{m[G-C]}^2 + \omega\, 2\mathrm{m[(G-}r-s\mathrm{)-C]}^2}{\mathrm{m[G]} + \omega\ \ \mathrm{m[G-}r-s\mathrm{]}} \tag{9.1}$$

The parameter, ω was taken to be 0.03 for historical reasons. However, this numerical parameter arises *only* from consideration of the fixed single bonds in perylene and by only counting a select few of the first-excited structures. Furthermore, the parameter is currently insufficient at appropriately dampening contributions from Dewar structures. At large system sizes, the Dewar contribution outweighs the Randić contribution, owing to the rapid increase in the number of Dewar structures compared to Kekulé structures. The result is that in larger systems investigated, such as large linear polyacenes or fibonacenes, the magnitude from application of equation (9.1) becomes approximate to $\mathrm{m[(G-}r-s\mathrm{)-C]}^2$. Thus, further investigation is needed into the parameterisation to prevent over-exaggeration of Dewar structures. This could be achieved by testing parameters on a wider range of systems, both benzenoids and non-benzenoids. In addition, a more detailed investigation into non-benzenoid systems is needed to maximise the potential of this model. The formulation in equation (9.1) is one possible form that combines Randić and Dewar structures. Further conceivable equations involve different

modes of normalisation and accountability of cycle area.

The second proposed model is called the Adjusted Myrvold-Fowler model and is based on computation of the coefficients from the characteristic polynomials of the graph and the cycle-removed graph. Inspired by the Aihara model of Hückel-London model, this model includes an optimised parameter of the cycle-removed graph (see equation (9.2)).

$$\mathrm{J_C} = -2 \times \left(\frac{S_\mathrm{C}}{S_0}\right) \left[\frac{d_0}{c_0} + 4 \times \frac{d_2}{c_2}\right]. \tag{9.2}$$

This model involves the inclusion of *all* possible cycles not just conjugated circuits, similar to the Aihara formalism. In general, investigations of a series of benzenoid systems (linear polyacenes and fibonacenes) identified this model as the best approximation of the ring-current magnitude for benzenoids, closely reproducing trends observed in the Hückel-London model and importantly includes non-Kekuléan systems. However, this benefit is not universal. The classically antiaromatic pentalene is predicted aromatic; and fluoranthene, a non-alternant perylene analogue, suffers identical problems of an 'empty' centre ring as the CC models. The conclusion is that further optimisation is necessary for non-alternant systems, including in depth inspection of necessary coefficients in this class of graph.

The work in this thesis has been limited to the application to non-Kekuléan systems. As discussed in Chapter 1.4, this is but one of the many problems associated with the conjugated-circuit models. Other major problems include the application to charged systems and the various classifications of aromaticity. Preliminary work has attempted to address charged systems utilising the Dewar model, where radical vertices instead localise anionic or cationic charges. However, this investigation is only preliminary and the extent of its utility requires further investigation. There exist two examples where attempts have been made to turn CC models into a MO-like model proposed by Randić[120,121] and Mandado.[123] Although, neither have gained significant traction, investigations on applicability are ongoing.

As applied in Chapter 4, the Aihara HL model can easily be applied to heterocyclic systems. For conjugated-circuit models, an extension to heteroaromaticity is not obvious

owing to the absence of the Hückel electronegativity and bond strength parameters. The Adjusted-MF model *can* model these systems due to accountability of some terms of the characteristic polynomial which will contain certain parameters. While not a full application, the Adjusted model could be made applicable to heteroaromatic systems.

To summarise, the research presented in this document has the potential to improve the fragile conjugated-circuit models. The new models proposed have provided the opportunity to extend the conjugated-circuit models to the calculation of non-Kekuléan structures. However, further work is certainly needed for both the Myrvold-Fowler models and the Randić-Dewar model.

Bibliography

[1] The Chemical Society, University of Sheffield. *Aromaticity: an International Symposium held at Sheffield on 6th-8th July 1966.* The Chemical Society, 1st edition, **1966**.

[2] Bergmann, E. D., Pullman, B. *Aromaticity, Pseudo-Aromaticity, Anti-Aromaticity, The Jerusalem symposium on Quantum Chemistry and Biochemistry III.* Academic Press Inc, 1st edition, **1971**.

[3] *Chemical Reviews* Special Issue on 'Aromaticity', **2001**, (issue 5), *101.*

[4] *Chemical Reviews* Special Issue on 'Delocalization-Pi and Sigma', **2005**, (issue 10), *105.*

[5] *Chemical Society Review* Themed Collection on 'Challenges in Aromaticity: 150 Years after Kekulé's Benzene', **2015**, *44.*

[6] Faraday, M. *Philos. Trans. Roy. Soc. Lond.*, **1825**, *115*, 440.

[7] Kekulé, A. *Bull. Soc. Chim. Par.*, **1865**, *3*, 98.

[8] Kekulé, A. *Justus Liebigs Ann. Chem.*, **1872**, *162*, 77.

[9] Dewar, J. *Proc. Roy. Soc. Edinb.*, **1869**, *6*, 82.

[10] Rocke, A. J. *Angew. Chem. Int. Ed.*, **2015**, *54*, 46.

[11] Clar, E. *The Aromatic Sextet.* John Wiley & Sons, 1st edition, **1972**.

[12] Jensen, W. B. *J. Chem. Educ.*, **2009**, *86*, 423.

[13] Armit, J. W., Robinson, R. *Justus Liebigs Ann. Chem.*, **1925**, *127*, 1604.

[14] Smith, M. B., March, J. *March's Advanced Organic Chemistry Reactions, Mechanisms, and Structure.* John Wiley & Sons, Inc, 5th edition, **2001**.

[15] Atherton, J. C. C., Jones, S. *Tetrahedron*, **2003**, *59*, 9039.

[16] de la Mare, P. B. D., Klassen, N. V., Koenigsberger, R. *J. Chem. Soc. (Resumed)*, **1961**, 5285.

[17] Schleyer, P. v. R., Jiao, H. *Pure Appl. Chem.*, **1996**, *68*, 209.

[18] Mitchell, R. H. *Chem. Rev.*, **2001**, *101*, 1301.

[19] Hoffmann, R. *Am. Sci.*, **2015**, *103*, 18.

[20] Binsch, G. *Naturwissenschaften*, **1973**, *60*, 369.

[21] Balaban, A. T., Oniciu, D. C., Katritzky, A. R. *Chem. Rev.*, **2004**, *104*, 2777.

[22] Subramanian, G., Schleyer, P. v. R., Jiao, H. *Organometallics*, **1997**, *16*, 2362.

[23] Gutman, I., Milun, M., Trinajstić, N. *J. Am. Chem. Soc.*, **1977**, *99*, 1692.

[24] Aihara, J., Kanno, H., Ishida, T. *J. Phys. Chem. A*, **2007**, *111*, 8873.

[25] Fowler, P. W., Rees, C. W., Soncini, A. *J. Am. Chem. Soc.*, **2004**, *126*, 11202.

[26] Boese, R., Maulitz, A. H., Stellberg, P. *Chemische Berichte*, **1994**, *127*, 1887.

[27] Williams, R. V. *Chem. Rev.*, **2001**, *101*, 1185.

[28] Clarke, J., Fowler, P. W., Gronert, S., Keeffe, J. R. *J. Org. Chem.*, **2016**, *81*, 8777.

[29] Klein, D. J., Schmalz, T. G., Hite, G. E., Seitz, W. A. *J. Am. Chem. Soc.*, **1986**, *108*, 1301.

[30] Bühl, M., Hirsch, A. *Chem. Rev.*, **2001**, *101*, 1153.

[31] Rzepa, H. S. *Chem. Rev.*, **2005**, *105*, 3697.

[32] Jiao, H., Schleyer, P. v. R. *Angew. Chem. Int. Ed. (English)*, **1993**, *32*, 1763.

[33] Boldyrev, A. I., Wang, L. *Chem. Rev.*, **2005**, *105*, 3716.

[34] Mercero, J. M., Boldyrev, A. I., Merino, G., Ugalde, J. M. *Chem. Soc. Rev.*, **2015**, *44*, 6519.

[35] Breslow, R. *Acc. Chem. Res.*, **1973**, *6*, 393.

[36] Bultinck, P. *Faraday Disc.*, **2007**, *135*, 347.

[37] Schleyer, P. v. R. *Chem. Rev.*, **2001**, *101*, 1153.

[38] Krygowski, T. M., Cyrański, M. K. *Chem. Rev.*, **2001**, *101*, 1385.

[39] Schaad, L. J., Andes Hess, B. J. *Chem. Rev.*, **2001**, *101*, 1465.

[40] Cyrański, M. K. *Chem. Rev.*, **2005**, *105*, 3773.

[41] Gomes, R. A. N. F., Mallion, R. B. *Chem. Rev.*, **2001**, *101*, 1349.

[42] Zhao, L., Grande-Aztatzi, R., Foroutan-Nejad, C., Ugalde, J. M., Frenking, G. *Chemistry Select*, **2017**, *2*, 863.

[43] Bird, C. W. *Tetrahedron*, **1996**, *52*, 9945.

[44] Minkin, V. I., Glukhovtsev, M. N., Simkin, B. Y. *Aromaticity and Antiaromaticity Electronic and Structural Aspects*. John Wiley & Sons Inc, 1st edition, **1994**.

[45] Garratt, P. J. *Aromaticity*. John Wiley & Sons, 1st edition, **1986**.

[46] Lazzeretti, P. *Prog. Nucl. Magn. Reson. Spectrosc.*, **2000**, *36*, 1.

[47] Gershoni-Poranne, R., Stanger, A. *Chem. Soc. Rev.*, **2015**, *44*, 6597.

[48] Salem, L. *The Molecular Orbital Theory of Conjugated Systems.* W. A. Benjamin, Inc., **1966**.

[49] Haigh, C. W., Mallion, R. B. *Progress in Nuclear Magnetic Resonance Spectroscopy*, **1979**, *13*, 303.

[50] Hinchliffe, A., Munn, R. W. *Molecular Electromagnetism.* John Wiley & Sons, **1985**.

[51] Bothner-By, A. A., Pople, J. A. *Ann. Rev. Phys. Chem.*, **1965**, *16*, 43.

[52] Pople, J. A. *J. Chem. Phys.*, **1964**, *41*, 2559.

[53] Lonsdale, K. *J. Chem. Soc. (Resumed)*, **1938**, 364.

[54] Musher, J. I. *J. Chem. Phys.*, **1965**, *43*, 4081.

[55] Dauben, H. J., Wilson, J. D., Laity, J. L. *Nonbenzenoid Aromatics: Chapter 3: Diamagnetic Susceptibility Exaltations as a Criterion for Aromaticity*, volume 2, 167. **1971**.

[56] Dauben, H. J., Wilson, J. D., Laity, J. L. *J. Am. Chem. Soc.*, **1968**, *90*, 811.

[57] Pople, J. A., Untch, K. G. *J. Am. Chem. Soc.*, **1966**, *88*, 4811.

[58] Aihara, J., Horikawa, T. *Bull. Chem. Soc. Jpn.*, **1983**, *56*, 1853.

[59] Pople, J. A. *J. Chem. Phys.*, **1956**, *24*, 1111.

[60] Pauling, L. *J. Chem. Phys.*, **1936**, *4*, 673.

[61] Lampman, G. M., Pavia, D. L., Kriz, G., Vyvyan, J. R. *Spectroscopy.* Brooks/Cole, Cengage Learning, 4th edition, **2010**.

[62] Rice, J. E., Lee, T. J., Remington, R. B., Allen, W. D., Clabo, D. A., Schaefer, H. F. *J. Am. Chem. Soc.*, **1987**, *109*, 2902.

[63] de Castro, B. R. M., Gomes, J. A. N. F., Mallion, R. B. *J. Mol. Struct. Theochem*, **1992**, *260*, 133.

[64] Jiao, H., Schleyer, P. v. R. *AIP Conference Proceedings*, **1995**, *330*, 107.

[65] Katritzky, A. R., Barczynski, P., Musumarra, G., Pisano, D., Szafran, M. *J. Am. Chem. Soc.*, **1989**, *111*, 7.

[66] Schleyer, P. v. R., Maerker, C., Dransfeld, A., Jiao, H., van Eikema Hommes, N. J. R. *J. Am. Chem. Soc.*, **1996**, *118*, 6317.

[67] Chen, Z., Wannere, C. S., Corminboeuf, C., Puchta, R., Schleyer, P. v. R. *Chem. Rev.*, **2005**, *105*, 3842.

[68] Schleyer, P. v. R., Manoharan, M., Wang, Z.-X., Kiran, B., Jiao, H., Puchta, R., van Eikema Hommes, N. J. R. *Org. Lett.*, **2001**, *3*, 2465.

[69] Fallah-Bagher-Shaidaei, H., Wannere, C. S., Corminboeuf, C., Puchta, R., Schleyer, P. v. R. *Org. Lett.*, **2006**, *8*, 863.

[70] Aihara, J. *Chem. Phys. Lett.*, **2002**, *365*, 34.

[71] Aihara, J., Oe, S. *Bull. Chem. Soc. Jpn.*, **2003**, *76*, 1363.

[72] Aihara, J. *Bull. Chem. Soc. Jpn.*, **2004**, *77*, 101.

[73] Steiner, E., Fowler, P. W. *Phys. Chem. Chem. Phys.*, **2004**, *6*, 261.

[74] Lazzeretti, P. *Phys. Chem. Chem. Phys.*, **2004**, *6*, 217.

[75] Stanger, A. *J. Org. Chem.*, **2005**, *71*, 883.

[76] Gershoni-Poranne, R., Stanger, A. *Chem. Eur. J.*, **2014**, *20*, 5673.

[77] Gauss, J. *J. Chem. Phys.*, **1993**, *99*, 3629.

[78] London, F. *J. Phys. Radium*, **1937**, *8*, 397.

[79] Pople, J. A. *Mol. Phys.*, **1958**, *1*, 175.

[80] McWeeny, R. *Mol. Phys.*, **1958**, *1*, 311.

[81] Haigh, C., Mallion, R. B., Armour, E. A. G. *Mol. Phys.*, **1970**, *18*, 751.

[82] Mallion, R. B. *Mol. Phys.*, **1973**, *25*, 1415.

[83] Mallion, R. B. *Proc. Roy. Soc. Lond. A Mat.*, **1975**, *341*, 429.

[84] Dickens, T. K., Mallion, R. B. *Croat. Chem. Acta*, **2013**, *86*, 387.

[85] Coulson, C. A. *Proc. Roy. Soc. Lond. A Mat.*, **1939**, *169*, 413.

[86] Pasquarello, A., Schlüter, M., Haddon, R. C. *Phys. Rev. A*, **1993**, *47*, 1783.

[87] Pasquarello, A., Schlüter, M., Haddon, R. C. *Science*, **1992**, *257*, 1660.

[88] Ceulemans, A., Chibotaru, L. F., Fowler, P. W. *Phys. Rev. Lett.*, **1998**, *80*, 1861.

[89] Kirchhoff, G., O'Toole, J. B. *IRE Transactions on Circuit Theory*, **1958**, *5*, 4.

[90] Randić, M. *Chem. Phys. Lett.*, **1976**, *38*, 68.

[91] Randić, M. *J. Am. Chem. Soc.*, **1977**, *99*, 444.

[92] Randić, M. *Tetrahedron*, **1977**, *33*, 1905.

[93] Gomes, J., Mallion, R. *Revista Portuguesa de Quimica*, **1979**, *21*, 82.

[94] Fowler, P. W., Myrvold, W. *J. Phys. Chem. A*, **2011**, *115*, 13191.

[95] Gutman, I., Randić, M. *Chem. Phys.*, **1979**, *41*, 265.

[96] Randić, M., Vukičević, D., Novič, M., Plavšić, D. *Int. J. Quant. Chem.*, **2012**, *112*, 2456.

[97] Hückel, E. *Z. Phys.*, **1931**, *70*, 204.

[98] Hückel, E. *Z. Phys.*, **1931**, *72*, 310.

[99] Hückel, E. *Z. Phys.*, **1932**, *76*, 628.

[100] Randić, M. *Chem. Phys. Lett.*, **2010**, *500*, 123.

[101] Randić, M. *J. Comp. Chem. Japan*, **2017**, *16*, 42.

[102] Klein, D. J., Randić, M., Babić, D., Trinajstić, N. *Int. J. Quant. Chem.*, **1994**, *50*, 369.

[103] Cyrański, M. K., Krygowski, T. M., Katritzky, A. R., Schleyer, P. v. R. *J. Org. Chem.*, **2002**, *67*, 1333.

[104] Fowler, P. W., Cotton, S., Jenkinson, D., Myrvold, W., Bird, W. H. *Chem. Phys. Lett.*, **2014**, *597*, 30.

[105] Steiner, E., Fowler, P. W. *Chem. Comm.*, **2001**, 2220–2221.

[106] Gomes, J. A. N. F. *Croat. Chem. Acta*, **1980**, *53*, 561.

[107] Randić, M. *Chem. Rev.*, **2003**, *103*, 3449.

[108] Randić, M., Novič, M., Vračko, M., Vukičević, D., Plavšić, D. *Int. J. Quant. Chem.*, **2012**, *112*, 972.

[109] Randić, M., Novič, M., Plavšić, D. *J. Math. Chem.*, **2012**, *50*, 2755.

[110] Ciesielski, A., Krygowski, T. M., Cyrański, M. K., Dobrowolski, M. A., Aihara, J. *Phys. Chem. Chem. Phys.*, **2009**, *11*, 11447.

[111] Dickens, T. K., Gomes, J. A. N. F., Mallion, R. B. *J. Chem. Theory Comp.*, **2011**, *7*, 3661.

[112] Mandado, M. *J. Chem. Theory Comp.*, **2009**, *5*, 2694.

[113] Baer, F., Kuhn, H., Regel, W. *Z. Naturforsch. A*, **1967**, *22*, 103.

[114] Pauling, L., Brockway, L. O., Beach, J. Y. *J. Am. Chem. Soc.*, **1935**, *57*, 2705.

[115] Fowler, P. W., Myrvold, W., Jenkinson, D., Bird, W. H. *Phys. Chem. Chem. Phys.*, **2016**, *18*, 11756.

[116] Randić, M. *Chem. Phys. Lett.*, **2014**, *601*, 1 .

[117] Gutman, I. *MATCH Commun. Math. Comput. Chem.*, **1977**, *3*, 121.

[118] Randić, M., Guo, X. *Int. J. Quant. Chem.*, **1994**, *49*, 215.

[119] Gutman, I., Furtula, B., Radenković, S. *Z. Naturforsch. A*, **2004**, *59*, 699.

[120] Randić, M. *J. Phys. Chem.*, **1982**, *86*, 3970.

[121] Randić, M., Nettleton, F. E. *Int. J. Quant. Chem.*, **1986**, *30*, 203.

[122] Randić, M., Plavšić, D., Trinajstić, N. *J. Mol. Struct. Theochem*, **1989**, *185*, 249.

[123] Ramos-Berdullas, N., Radenković, S., Bultinck, P., Mandado, M. *J. Phys. Chem. A*, **2013**, *117*, 4679.

[124] Wiberg, K. B. *Chem. Rev.*, **2001**, *101*, 1317.

[125] Havenith, R. W. A., Lugli, F., Fowler, P. W., Steiner, E. *J. Phys. Chem. A*, **2002**, *106*, 5703.

[126] Keith, T. A., Bader, R. F. W. *Chem. Phys. Lett.*, **1993**, *210*, 223.

[127] Keith, T. A., Bader, R. F. W. *J. Chem. Phys.*, **1993**, *99*, 3669.

[128] Lazzeretti, P., Malagoli, M., Zanasi, R. *Chem. Phys. Lett.*, **1994**, *220*, 299.

[129] Steiner, E., Fowler, P. W. *J. Phys. Chem. A*, **2001**, *105*, 9553.

[130] Pople, J. A. *Disc. Faraday Soc.*, **1962**, *34*, 7.

[131] Hameka, H. F. *Mol. Phys.*, **1958**, *1*, 203.

[132] Schindler, M., Kutzelnigg, W. *J. Chem. Phys.*, **1982**, *76*, 1919.

[133] Schindler, M., Kutzelnigg, W. *J. Am. Chem. Soc.*, **1983**, *105*, 1360.

[134] Lazzeretti, P. *Mol. Phys.*, **1996**, *89*, 157.

[135] Steiner, E., Fowler, P. W., Havenith, R. W. A. *J. Phys. Chem. A*, **2002**, *106*, 7048.

[136] Fowler, P. W., Steiner, E., Zanasi, R., Cadioli, B. *Mol. Phys.*, **1999**, *96*, 1099.

[137] Steiner, E., Fowler, P. W. *Int. J. Quant. Chem.*, **1996**, *60*, 609.

[138] Zanasi, R., Lazzeretti, P., Malagoli, M., Piccinini, F. *J. Chem. Phys.*, **1995**, *102*, 7150.

[139] Soncini, A., Fowler, P. W. *Chem. Phys. Lett.*, **2004**, *396*, 174.

[140] Fowler, P. W., Steiner, E. *Chem. Phys. Lett.*, **2002**, *364*, 259.

[141] Steiner, E., Fowler, P. W., Soncini, A., Jenneskens, L. W. *Faraday Disc.*, **2007**, *135*, 309.

[142] Soncini, A., Domene, C., Engelberts, J. J., Fowler, P. W., Rassat, A., van Lenthe, J. H., Havenith, R. W. A., Jenneskens, L. W. *Chem. Eur. J.*, **2005**, *11*, 1257.

[143] Oziminski, W. P., Palusiak, M., Dominikowska, J., Krygowski, T. M., Havenith, R. W. A., Gibson, C. M., Fowler, P. W. *Phys. Chem. Chem. Phys.*, **2013**, *15*, 3286.

[144] Radenković, S., Bultinck, P., Gutman, I., Durdević, J. *Chem. Phys. Lett.*, **2012**, *552*, 151.

[145] Havenith, R. W. A., Fowler, P. W., Jenneskens, L. W. *Org. Lett.*, **2006**, *8*, 1255.

[146] Fowler, P. W., Havenith, R. W. A., Jenneskens, L. W., Soncini, A., Steiner, E. *Angew. Chem. Int. Ed.*, **2002**, *41*, 1558.

[147] Lillington, M., Fowler, P. W., Diudea, M. V. *Pol. J. Chem.*, **2007**, *81*, 653.

[148] Dickens, T. K., Mallion, R. B. *Croat. Chem. Acta*, **2015**, *88*, 221.

[149] Gershoni-Poranne, R., Gibson, C. M., Fowler, P. W., Stanger, A. *J. Org. Chem.*, **2013**, *78*, 7544.

[150] bse.pnl.gov (Last accessed 20/11/2017) with references therein for carbon and hydrogen.

[151] Feller, D. *J. Comp. Chem.*, **1996**, *17*, 1571.

[152] Schuchardt, K., Didier, B., Elsethagen, T., Sun, L., Gurumoorthi, V., Chase, J., Li, J., Windus, T. *J. Chem. Inf. Model.*, **2007**, *47*, 1045.

[153] Dunning, T. H. *J. Chem. Phys.*, **1989**, *90*, 1007.

[154] Guest, M., Bush, J., I, van Dam, H., Sherwood, P., Thomas, J., van Lenthe, J., Havenith, R. W. A., Kendrick, J. *Mol. Phys.*, **2005**, *103*, 719.

[155] Havenith, R. W. A., Fowler, P. W. *Chem. Phys. Lett.*, **2007**, *449*, 347.

[156] Havenith, R. W. A., Meijer, A., Irving, B., Fowler, P. W. *Mol. Phys.*, **2009**, *107*, 2591.

[157] Fowler, P. W., Gibson, C. M., Bean, D. E. *Proc. Roy. Soc. A*, **2014**, *470*, 20130617.

[158] Soncini, A., Teale, A. M., Helgaker, T., De Proft, F., Tozer, D. J. *J. Chem. Phys.*, **2008**, *129*, 74101.

[159] Aihara, J. *Phys. Chem. Chem. Phys.*, **2016**, *18*, 11847.

[160] Aihara, J. *Bull. Chem. Soc. Jpn.*, **2016**, *89*, 1425.

[161] Gutman, I., Polansky, O. E. *Mathematical Concepts in Organic Chemistry*. Springer-Verlag, 1st edition, **1986**.

[162] Aihara, J. *J. Am. Chem. Soc.*, **1976**, *98*, 6840.

[163] Aihara, J. *J. Am. Chem. Soc.*, **1979**, *101*, 558.

[164] Aihara, J. *J. Am. Chem. Soc.*, **1979**, *101*, 5913.

[165] Aihara, J. *Bull. Chem. Soc. Jpn.*, **2004**, *77*, 651.

[166] Aihara, J. *Bull. Chem. Soc. Jpn.*, **2008**, *2*, 241.

[167] Aihara, J. *Pure Appl. Chem.*, **1982**, *54*, 1115.

[168] Aihara, J. *J. Am. Chem. Soc.*, **1981**, *103*, 5704.

[169] Aihara, J., Horikawa, T. *Chem. Phys. Lett.*, **1983**, *95*, 561.

[170] Aihara, J. *J. Am. Chem. Soc.*, **1976**, *98*, 2750.

[171] Van-Catledge, F. A. *J. Org. Chem.*, **1980**, *45*, 4801.

[172] Coulson, C. A., Rushbrooke, G. S. *Math. Proc. Cambridge*, **1940**, *36*, 193.

[173] Mallion, R. B., Rouvray, D. H. *J. Math. Chem.*, **1990**, *5*, 1.

[174] Aihara, J., Sekine, R., Ishida, T. *J. Phys. Chem. A*, **2011**, *115*, 9314.

[175] Kruszewski, J., Krygowski, T. M. *Tetrahedron Lett.*, **1972**, *13*, 3839.

[176] Frizzo, C., Martins, M. P. *Struct. Chem.*, **2012**, *23*, 375.

[177] Bird, C. W. *Tetrahedron*, **1992**, *48*, 335.

[178] Aihara, J., Kanno, H., Ishida, T. *J. Am. Chem. Soc.*, **2005**, *127*, 13324.

[179] Islas, R., Chamorro, E., Robles, J., Heine, T., Santos, J., Merino, G. *Struct. Chem.*, **2007**, *18*, 833.

[180] Schleyer, P. v. R., Jiao, H., Goldfuss, B., Freeman, P. K. *Angew. Chem. Int. Ed. (English)*, **1995**, *34*, 337.

[181] Wu, J. I., Pühlhofer, F. G., Schleyer, P. v. R., Puchta, R., Kiran, B., Mauksch, M., van Eikema Hommes, N. J. R., Alkorta, I., Elguero, J. *J. Phys. Chem. A*, **2009**, *113*, 6789.

[182] Gerschgorin, S. *Izv. Akad. Nauk. SSSR. Otd. Fiz-Mat. Nauk.*, **1931**, *7*, 749.

[183] Gerschgorin, S. *Izv. Akad. Nauk. SSSR. Otd. Fiz-Mat.*, **1931**, *1*, 749.

[184] Kreyszig, E. *Advanced Engineering Mathematics*. John Wiley & Sons, New York, 7th edition, **1993**.

[185] Varga, R. S. *Gerschgorin and His Circles*. Springer-Verlag Berlin Heidelberg, **2004**.

[186] Frost, A. A., Musulin, B. *J. Chem. Phys.*, **1953**, *21*, 572.

[187] Fowler, P. W., Soncini, A., Jenneskens, L. W. *Struc. Bond.*, **2005**, *115*, 57.

[188] Abraham, R. J., Sheppard, R. C., Thomas, W. A., Turner, S. *Chem. Comm. (Lon.)*, **1965**, 43.

[189] Elvidge, J. A. *Chem. Comm. (Lon.)*, **1965**, 160.

[190] Gutman, I. *Z. Naturforsch. A*, **1984**, *39*, 152.

[191] Streitweiser, A. J. *Molecular Orbital Theory for Organic Chemists*. Wiley, New York, **1962**.

[192] Pearson, R. G. *Proc. Nat. Acad. Sci. USA*, **1975**, 2104.

[193] Fowler, P. W., Bean, D. E., Seed, M. *J. Phys. Chem. A*, **2010**, *114*, 10742.

[194] Sekine, R., Nakagami, Y., Aihara, J. *J. Phys. Chem. A*, **2011**, *115*, 6724.

[195] Hajgató, B., Deleuze, M. S., Ohno, K. *Chem. Eur. J.*, **2006**, *12*, 5757.

[196] Steiner, E., Fowler, P. W., Jenneskens, L. W., Acocella, A. *Chem. Comm.*, **2001**, 659.

[197] Jiao, H., Schleyer, P. v. R. *Angew. Chem. Int. Ed. (English)*, **1996**, *35*, 2383.

[198] Aihara, J. *Bull. Chem. Soc. Jpn.*, **1993**, *66*, 57.

[199] Dickens, T. K., Mallion, R. B. *Chem. Phys. Lett.*, **2011**, *517*, 98.

[200] Schulman, J. M., Disch, R. L., Jiao, H., Schleyer, P. v. R. *J. Phys. Chem. A*, **1998**, *102*, 8051.

[201] Babić, D., Trinajstić, N. *J. Mol. Struct. Theochem*, **1994**, *314*, 321.

[202] Diederich, F., Staab, H. A. *Angew. Chem. Int. Ed. (English)*, **1978**, *17*, 372.

[203] Fonari, A., Röder, J. C., Shen, H., Timofeeva, T. V., Vollhardt, K. P. C. *Synlett*, **2014**, *25*, 2429.

[204] Miyoshi, H., Nobusue, S., Shimizu, A., Tobe, Y. *Chem. Soc. Rev.*, **2015**, *44*, 6560.

[205] Gutman, I., Cyvin, S. J. *J. Mol. Struct. Theochem*, **1993**, *288*, 85.

[206] Christoph, H., Grunenberg, J., Hopf, H., Dix, I., Jones, P., Scholtissek, M., Maier, G. *Chem. Eur. J.*, **2008**, *14*, 5604.

[207] Gutman, I., Cyvin, S. J. *J. Mol. Struct. Theochem*, **1989**, *184*, 159.

[208] Vajda, S. *Fibonacci and Lucas Numbers and the Golden Section*. Dover Publications, **2007**.

[209] Hillman, A. P. *Fibonacci Quarterly*, **1965**, *3*, 157.

[210] OEIS.org (Last accessed 09/11/2017), hexagon N=2p number sequence reference A049682.

[211] Aihara, J. *J. Am. Chem. Soc.*, **1985**, *107*, 298.

[212] Schulman, J. M., , Disch, R. L. *J. Am. Chem. Soc.*, **1996**, *118*, 8470.

[213] Frisch, M. J., Trucks, G. W., Schlegel, H. B., Scuseria, G. E., Robb, M. A., Cheeseman, J. R., Scalmani, G., Barone, V., Mennucci, B., Petersson, G. A., Nakatsuji, H., Caricato, M., Li, X., Hratchian, H. P., Izmaylov, A. F., Bloino, J., Zheng, G., Sonnenberg, J. L., Hada, M., Ehara, M., Toyota, K., Fukuda, R., Hasegawa, J., Ishida, M., Nakajima, T., Honda, Y., Kitao, O., Nakai, H., Vreven, T., Jr., J. A. M., Peralta, J. E., Ogliaro, F., Bearpark, M., Heyd, J. J., Brothers, E., Kudin, K. N., Staroverov, V. N., Kobayashi, R., Normand, J., Raghavachari, K., Rendell, A., Burant, J. C., Iyengar, S. S., Tomasi, J., Cossi, M., Rega, N., Millam, J. M., Klene, M., Knox, J. E., Cross, J. B., Bakken, V., Adamo, C., Jaramillo, J., Gomperts, R., Stratmann, R. E., Yazyev, O., Austin, A. J., Cammi, R., Pomelli, C., Ochterski, J. W., Martin, R. L., Morokuma, K., Zakrzewski, V. G., Voth, G. A., Salvador, P., Dannenberg, J. J., Dapprich, S., Daniels, A. D., Farkas, Ö., Foresman, J. B., Ortiz, J. V., Cioslowski, J., Fox, D. J. *Gaussian 09 Revision D.01*, **2009**.

[214] Lazzeretti, P; Zanasi, R., SYSMO package (University of Modena), 1980. Additional routines by Fowler, P., Steiner, E., Havenith, R. W. A., Soncini, A.

[215] Gutman, I., Radenković, S. *Paradise Lost-Electron Conjugation in Homologs and Derivatives of Perylene*, 297–320. Springer International Publishing, Cham, **2016**.

[216] Dickens, T. K., Mallion, R. B. *J. Phys. Chem. A*, **2011**, *115*, 351.

[217] Nikolić, S., Randić, M., Klein, D. J., Plavšić, D., Trinajstić, N. *J. Mol. Struct*, **1989**, *198*, 223.

[218] Radenković, S., Gutman, I., Antić, M. *Chem. Phys. Lett.*, **2014**, *614*, 104 .

[219] Rong-Si, C., Cyvin, S. J., Cyvin, B. *Polycycl. Aromat. Compd.*, **1999**, *13*, 1.

[220] Vukičević, D., Durdević, J., Gutman, I. *Polycycl. Aromat. Compd.*, **2012**, *32*, 36.

[221] Haigh, C. W., Mallion, R. B. *Croat. Chem. Acta*, **1989**, *62(1)*, 1.

[222] Gutman, I., Turković, N., Jovičić, J. *Monatshefte für Chemie / Chemical Monthly*, **2004**, *135*, 1389.

[223] Dickens, T. K., Mallion, R. B. *J. Phys. Chem. A*, **2011**, *115*, 351.

[224] Radenković, S., Tošović, J., Durdević Nikolić, J. *J. Phys. Chem. A*, **2015**, *119*, 4972.

[225] Fowler, P. W., Rassat, A. *Phys. Chem. Chem. Phys.*, **2002**, *4*, 1105.

[226] Heilbronner, E. *J. Chem. Educ.*, **1989**, *66*, 471.

[227] Clar, E. *Polycyclic Hydrocarbons - Volume 2*. Springer-Verlag Berlin Heidelberg, **1964**.

[228] Dewar, M. J. S. *The Molecular Orbital Theory of Organic Chemistry*. McGraw-Hill Book Company, **1969**.

[229] Goddard, R., Haenel, M. W., Herndon, W. C., Krueger, C., Zander, M. *J. Am. Chem. Soc.*, **1995**, *117*, 30.

[230] Narita, S., Morikawa, T., Shibuya, T. *J. Mol. Struct. Theochem*, **2000**, *532*, 37.

[231] Morikawa, T., Narita, S. *Polycycl. Aromat. Compd.*, **2003**, *23*, 307.

[232] Randić, M. *J. Mol. Struct. Theochem*, **1991**, *229*, 139.

[233] Sedlar, J., Andelić, I., Gutman, I., Vukičević, D., Graovac, A. *Chem. Phys. Lett.*, **2006**, *427*, 418 .

[234] Pauling, L. *Acta Cryst. B*, **1980**, *36*, 1898.

[235] Dias, J. R. *J. Phys. Chem. A*, **2011**, *115*, 13619.

[236] Baker, W., Rouvray, D. H. *J. Chem. Educ.*, **1978**, *55*, 645.

[237] Gutman, I. *MATCH Commun. Math. Comput. Chem.*, **1979**, *6*, 75.

[238] Camerman, A., Trotter, J. *Proc. Roy. Soc. Lond. A Mat.*, **1964**, *279*, 129.

[239] Pauling, L. *The Nature of the Chemical Bond*. Cornell University Press, 3rd edition, **1960**.

[240] Pauling, L., Wheland, G. W. *J. Chem. Phys.*, **1933**, *1*, 362.

[241] Personal notebooks from L.Pauling, scarc.library.oregonstate.edu/coll/pauling/rnb /index.html (a. 14/08/2017), Nov 1979, 34, p 65.

[242] Pawley, G. S., Yeats, E. A. *Acta Cryst. B*, **1969**, *25*, 2009.

[243] Cruickshank, D. W. J. *Acta Cryst. B*, **1956**, *9*, 915.

[244] Robertson, J. M., Sinclair, V. C., Trotter, J. *Acta Cryst. B*, **1961**, *14*, 697.

[245] Shan, L., Liang, Z., Xu, X., Tang, Q., Miao, Q. *Chem. Sci.*, **2013**, *4*, 3294.

[246] Dias, J. R. *J. Phys. Chem. A*, **2013**, *117*, 4716.

[247] Dias, J. R. *Mol. Phys.*, **2015**, *113*, 3389.

[248] Bultinck, P., Rafat, M., Ponec, R., Van Gheluwe, B., Carbó-Dorca, R., Popelier, P. *J. Phys. Chem. A*, **2006**, *110*, 7642.

[249] Pavliček, N., Mistry, A., Majzik, Z., Moll, N., Meyer, G., Fox, D. J., Gross, L. *Nat. Nanotechnol.*, **2017**, *12*, 308.

[250] Clar, E. *Polycyclic Hydrocarbons - Volume 1*. Springer-Verlag Berlin Heidelberg, **1964**.

[251] Došlić, T. *MATCH Commun. Math. Comput. Chem.*, **2011**, *65*, 775.

[252] Zywietz, T. K., Jiao, H., Schleyer, P. v. R., de Meijere, A. *J. Org. Chem.*, **1998**, *63*, 3417.